



NASA/ OHIO SPACE GRANT CONSORTIUM

2020-2021 ANNUAL STUDENT RESEARCH SYMPOSIUM PROCEEDINGS XXIX



NASA's Ingenuity helicopter unlocked its rotor blades, allowing them to spin freely, on April 7, 2021, the 47th Martian day, or sol, of the mission. Credit: NASA/JPL-Caltech

Photo Courtesy of NASA

March 26, 2021
Symposium was virtual due to COVID-19
Cleveland, Ohio



Follow OSGC on:



*Just click on any name, and it will link you
to the page immediately!*

TABLE OF CONTENTS

Table of Contents	<u>Page(s)</u> 2
Foreword	6
Membership	7
Acknowledgments.....	8
Symposium Presentations	9

<u>Fellows</u>	<u>University</u>	<u>Page</u>
Bradley, Jacob M.	Kent State University	11
Coffey, Joshua F.	University of Cincinnati	20
DeBortoli, Nicholas S.	University of Dayton.....	23
DeGroote, Nicholas S.	University of Cincinnati	25
DiLillo, Ana M.....	Cleveland State University	33
Emshoff, Brandon L.....	The Ohio State University	37
Hubbard, Erin P.	Cleveland State University	41
Kosir, Shane T.	University of Dayton.....	44
Mason, Taylor W.	Miami University	47
Pearl, David L.	Miami University	53

<u>Scholars</u>	<u>College/University</u>	<u>Page</u>
Beckett, Joseph G.	University of Dayton.....	58
Berry, Brian J.	University of Dayton.....	63
Birchfield, Karlee D.	University of Cincinnati	65
Broski, Noah A.	The Ohio State University	69
Bryson, Elizabeth M.	Baldwin Wallace University.....	71
Castma, Joseph C.	Youngstown State University	76
Cephas, Zackry D.	Wilberforce University	78
Clarchick, Victoria L.	Marietta College	81
Connolly, Jacob A.	The University of Toledo	86
Covington, Kayla M.	The University of Toledo	90
Cresanto, Alexis C.	Youngstown State University	93
D'Alesandro, Sabrina R.	Wright State University	97

<u>Scholars</u>	<u>College/University</u>	<u>Page</u>
DeAngelis, Mark A.	The Ohio State University	101
Decato, Kevin H.	The University of Toledo	105
Deisler, William A.	Ohio Northern University	108
Devillier, Amanda M.	University of Cincinnati	111
DeVriendt, Brooke E.	Ohio Northern University	113
Doong, Kristel H.	The University of Akron.....	116
El Rassi, Hiba	The University of Akron.....	118
Floring, Grace N.	Case Western Reserve University.....	121
Gilligan, Rebecca N.	University of Cincinnati	126
Godawski, Jason T.	Miami University	131
Grant, Devin R.	Central State University	135
Gravenstein, Amy R.	The University of Akron.....	137
Hartswick, Delenn R.	Baldwin Wallace University.....	140
Heitmeyer, Daniel R.	University of Cincinnati	142
Heppe, Brandon J.	Cleveland State University	145
Herbruck, Sarah C.	Miami University	148
Howell, Catherine E.	The University of Akron.....	150
Hughes, Allayah C.	Wilberforce University	154
Lemieux, Sebastian J.	University of Cincinnati	156
Long, Naja T.	University of Dayton.....	161
Malek, Elizabeth C.	Wright State University	163
Marshall, David K.	The Ohio State University	166
Mills, Kristina G.	Cedarville University	170
Mitchell, Sara A.	Cedarville University	172
Mullin, William A.	The Ohio State University	174
Myers, Zane R.	Ohio Northern University	180
Paar, Maja F.	Case Western Reserve University.....	183
Pineault, Hannah J.	The University of Akron.....	185
Plentovich, Nicholas W.	Cleveland State University.....	189
Praprost, Christina D.	Miami University	193
Puckett, Markus R.	Central State University	196

<u>Scholars</u>	<u>College/University</u>	<u>Page</u>
Rathkamp, Joseph R.	Ohio Northern University	198
Rickman, William L.....	Miami University	200
Roman, Sarah J.	Kent State University	202
Sais, Andrew J.	The Ohio State University	204
Shasteen, Hayley D.....	Kent State University	211
Shelton, Armani D.	Central State University	219
Stoeffler, Branden S.....	Ohio Northern University	221
Stropki, Kevin C.	Cleveland State University	223
Tyszkiewicz, Jack C.....	The Ohio State University	225
Vadala, Christopher P.	Kent State University	233
Vitale Jacob C.	Cleveland State University	235
Watts, Ryan T.	Ohio Northern University	239
Wells, Kaden C.	University of Cincinnati	242
Wood, Madison M.	Kent State University	244
Worrell, Sarah N.	Kent State University	246
Zirckel, Matthew J.	Kent State University	249

<u>Community College Scholars</u>	<u>Community College</u>	<u>Page</u>
Ali, Muhammed Z.	Lorain County Community College	252
Ciminillo Delamotte, Grace A. ...	Columbus State Community College	261
Dorsey, Tyler J.	Cincinnati State Technical and Community College	264
Dunson, Brandon L.	Sinclair Community College.....	266
Frith, Kyle H.	Columbus State Community College	269
Jackson, Mystal E.	Lorain County Community College	272
Palmer, Ryan M.	Lorain County Community College	275
Thompson, Blaine C.	Lorain County Community College	278
Williams, Emily T.....	Lorain County Community College	280
Zirkle, Andrea L.....	Lorain County Community College	283

<u>Education Scholars</u>	<u>College/University</u>	<u>Page</u>
Brautigam, Lillian C.	Ohio Northern University	285
Carter, Savannah E.	Ohio Northern University	287

<u>Education Scholars</u>	<u>College/University</u>	<u>Page</u>
Christman, Emma N.....	Marietta College.....	290
Hoon, Nicolette M.	Cleveland State University.....	292
Joy, Derek G.	Youngstown State University.....	296
Kaminski, Margaret M.	Kent State University.....	300
Lafferty, Kaitlyn D.....	Marietta College.....	302
Lockwood, Grace S.....	Cedarville University.....	304
Palmer, Josephine M.....	Ohio Northern University.....	306
Sukalac, Emily A.	Baldwin Wallace University.....	308
Vollmar, Jenna L.....	University of Cincinnati.....	311
Wallbrown, Alexa E.....	Kent State University.....	313
Wright, Adison M.	Wright State University.....	317

FOREWORD

The Ohio Space Grant Consortium (OSGC), a member of the NASA National Space Grant College and Fellowship Program, awards graduate fellowships and undergraduate scholarships to students working toward degrees in Science, Technology, Engineering and Mathematics (STEM) disciplines at OSGC-member universities. The awards are made to United States citizens, and the students are competitively selected. Since the inception of the program in 1989, over 1,320 undergraduate scholarships and 181 graduate fellowships have been awarded.

Matching funds are provided by the 24 member universities/community colleges, the Ohio Aerospace Institute (OAI), and the Ohio Department of Higher Education (State of Ohio). Note that this year ~ \$500,000 will be directed to scholarships and fellowships representing contributions from NASA, the Ohio Aerospace Institute, State of Ohio, member universities, foundations, and industry.

By helping more students to graduate with STEM-related degrees, OSGC provides more qualified technical employees to industry. The research conducted for the Master's fellowship must be of interest to NASA. A prime aspect of the scholarship program is the undergraduate research project that the student performs under the mentorship of a faculty member. This research experience is effective in encouraging U. S. undergraduate students to attend graduate school in STEM. The Education scholarship recipients are required to attend a workshop conducted by NASA personnel where they are exposed to NASA educational materials and create a lesson plan for use in their future classrooms.

Due to COVID-19, the Annual Student Research Symposium scheduled for Friday, March 26, 2021, at the Ohio Aerospace Institute was made virtual through WebEx. A recording of the virtual Symposium is available on the OSGC website at: <http://osgc.org/event-material/>

Research reports of students from the following schools are contained in this publication:

Affiliate Members

- The University of Akron
- Baldwin Wallace University
- Case Western Reserve University
- Cedarville University
- Central State University
- Cleveland State University
- University of Dayton
- Kent State University
- Marietta College
- Miami University
- Ohio Northern University
- The Ohio State University
- Ohio University
- University of Cincinnati
- The University of Toledo
- Wilberforce University
- Wright State University
- Youngstown State University

Community Colleges

- Cincinnati State Technical and Community College
- Columbus State Community College
- Lakeland Community College
- Lorain County Community College
- Sinclair Community College

MEMBER INSTITUTIONS

Affiliate Members

- Baldwin Wallace University..... James W. McCargar, Ph.D.
- Case Western Reserve University Roger D. Quinn, Ph.D.
- Cedarville University Robert Chasnov, Ph.D., P.E.
- Central State University Augustus Morris, Jr., Ph.D., P.E.
- Cleveland State University Wei Zhang, Ph.D.
- Kent State University..... Joseph D. Ortiz, Ph.D.
- Marietta College..... Prof. Craig Rabatin, P.E.
- Miami University James Moller, Ph.D., P.E.
- Ohio Northern University..... Jed E. Marquart, Ph.D., P.E.
- The Ohio State University Dr. Mo Samimy
- Ohio University..... Dr. Shawn Ostermann
- The University of Akron..... Dr. Julie Zhao
- University of Cincinnati Dr. Kelly Cohen
- University of Dayton..... Dr. Robert J. Wilkens
- The University of Toledo Dr. Lesley M. Berhan
- Wilberforce University Deok Hee Nam, Ph.D.
- Wright State University Mitch Wolff, Ph.D.
- Youngstown State University Byung-Wook Park, Ph.D.

Campus Representative

Community Colleges

- Cincinnati State Technical and Community College Professor Abigail Yee
- Columbus State Community College..... Professor Jeffery M. Woodson, M.S., I.E.
- Cuyahoga Community College Prof. Michelle S. Davis
- Lakeland Community College..... Professor Tom Ciferno
- Lorain County Community College..... Regan L. Silvestri, Ph.D.
- Sinclair Community College Eric C. Dunn

Campus Representative

NASA Glenn Research Center - Representatives

- Dr. M. David Kankam
- Ms. Susan M. Kohler



ACKNOWLEDGMENTS

Thank you to all who helped with the OSGC's 29th Annual Research Symposium!

Keynote Speaker:

- ★ Douglas H. Wheelock (Colonel, U.S. Army, Ret.) NASA Astronaut, for providing inspirational anecdotes of his experiences and an engaging discourse about aerospace.
- ★ John Stephen, Virtual Appearances Specialist NASA Johnson Space Center, for coordinating Colonel Wheelock's appearance.

Campus Representatives – 4-Year Universities

- Dr. James W. McCargar, Baldwin Wallace University
- Dr. Roger Quinn, Case Western Reserve University
- Robert Chasnov, Ph.D., P.E., Cedarville University
- Augustus Morris, Jr., Ph.D., P.E., Central State University
- Wei Zhang, Ph.D., Cleveland State University
- Dr. Joseph D. Ortiz, Kent State University
- Dr. Andrew Beck, Marietta College
- James Moller, Ph.D., P.E., Miami University
- Jed E. Marquart, Ph.D., P.E., Ohio Northern University
- Dr. Mo Samimy, The Ohio State University
- Dr. Shawn Ostermann, Ohio University
- Dr. Julie Zhao, The University of Akron
- Dr. Kelly Cohen, University of Cincinnati
- Dr. Robert J. Wilkens, University of Dayton
- Dr. Lesley M. Berhan, The University of Toledo
- Deok Hee Nam, Ph.D., Wilberforce University
- Mitch Wolff, Ph.D., Wright State University
- Kevin J. Disotell, Ph.D., Youngstown State University

Campus Representatives - Community Colleges

- Professor Abigail Yee, Cincinnati State Technical and Community College
- Professor Jeffery M. Woodson, M.S., I.E., Columbus State Community College
- Professor Michelle S. Davis, Cuyahoga Community College
- Professor Tom Ciferno, Lakeland Community College
- Regan L. Silvestri, Ph.D., Lorain County Community College
- Eric C. Dunn, Sinclair Community College

Special thanks go out to the following:

- Dr. John Sankovic, President and CEO – OAI, for supporting the OSGC and hosting this event.
- Mark Cline, Senior Manager, Information Technology – OAI, whose expertise made the virtual forum not only possible, but a huge success!
- Dr. Andrew Gyekenyesi, Director of Research – OAI, for stepping up as Interim Director of the OSGC during times of transition.
- Jessica Tremayne, Marketing Communications and PR Manager – OAI, for moderating the event.

29th Annual OSGC Student Research Symposium

The 2021 Student Research Symposium went virtual due to the COVID-19 pandemic. The benefits of such a venue is the entire symposium was recorded and may be viewed at <http://osgc.org/event-material/>



2021 OSGC STUDENT RESEARCH SYMPOSIUM
Hosted By: Ohio Aerospace Institute (OAI)
22800 Cedar Point Road • Cleveland, OH 44142
• (440) 962-3000
Friday, March 26, 2021

AGENDA

9:00 AM – 9:10 AM	Welcome and Introductions (10 minutes) <i>John Sankovic</i> President and CEO, Ohio Aerospace Institute
9:10 AM – 9:15 AM	Welcome and Introductions (5 minutes) <i>Andrew Gyekenyesi</i> Interim Director, Ohio Space Grant Consortium and Director of Research/Chief Scientist, Ohio Aerospace Institute
9:15 AM – 9:35 AM	Keynote Speech (15 minutes, 5 minute Q&A) Douglas H. Wheelock (Colonel, U.S. Army, Ret.) NASA Astronaut
9:35 AM – 9:40 AM	Break (5 minutes)
9:40 AM – 10:35 AM	Student Presentations – Block 1 (55 minutes) <ul style="list-style-type: none">•Derek G. JoySenior, AYA Science Education, Youngstown State University•Sara A. MitchellSenior, Geology, Cedarville University•William A. MullinSenior, Aero/Astro Engineering, The Ohio State University•Nicolette M. Hoon.....Junior, Multi-Age Education, Cleveland State University•Shane T. KosirMaster's 2, Chemical Engineering, University of Dayton
10:35 AM – 10:40 AM	Break (5 minutes)
10:40 AM – 11:45 AM	Student Presentations – Block 2 (65 minutes) <ul style="list-style-type: none">•Madison M. WoodJunior, Geology, Kent State University•Christopher P. VadalaSenior, Biology, Kent State University•Joseph G. Beckett.....Junior, Mechanical Engineering, University of Dayton•Erin P. Hubbard.....Master's 1, Mechanical Engineering, Cleveland State University•Nicholas S. DeGroote ...Master's 1, Aerospace Engineering, University of Cincinnati• Muhammed Ali Pre-Medical Sciences, <u>Sophomore</u>, Lorain County Community College
11:45 AM – 12PM	Closing Remarks <i>Andrew Gyekenyesi</i> Interim Director, Ohio Space Grant Consortium and Director of Research/Chief Scientist, Ohio Aerospace Institute <i>Tim Hale</i> Interim Program Manager, Ohio Space Grant Consortium
12:00 PM	Symposium Adjourns

Fellows

How Pore-Scale Topology Of Sedimentary Rocks Control Transition Of Non-Fickian To Fickian Contaminant Transport And The Upscaling Of Dispersion Phenomenon

Student Researcher: Jacob M. Bradley

Advisor: Dr. Kuldeep Singh

Kent State University

Department of Geology

Abstract

Hydraulic heterogeneity in aquifers contributes to non-Fickian transport characteristics, i.e., which cannot be defined by the continuum-scale advection-dispersion equation (ADE). We investigate the role of first-order heterogeneity, i.e., pore geometry's effect on the dispersion phenomenon of porous media. The research questions addressed are; *how can we determine dispersion coefficient and Dispersivity as a function of pore-scale geometry and various flow rate?* In this computational study, a series of intra-pore geometries are designed and quantified by a dimensionless pore geometry factor (β), which captures a broad range of pores that likely exists due to diagenetic processes. Navier-Stokes and Advection-Diffusion equations are solved to examine the transport phenomenon via breakthrough curve (BTC) and residence time distribution (RTD). We determine a length-scale when non-Fickian features transition to the Fickian transport regime by sequentially extending the number of pores. Our results indicate that not only is the velocity distribution and its variance (σ^2) are dependent on the pore geometry, but its impact is amplified with flow rate. Consequently, the magnitude of non-Fickian becomes significant for complex pore shapes and require a longer length-scale for the Fickian transport. Thus, a larger velocity variance due to the effect of intra-pore geometry and flow rate contributes to a larger dispersion where variations are found to be a function of β and flow rate. We determine various constitutive equations to predict the length-scale needed for Fickian dispersion, the magnitude of non-Fickian features, the Fickian dispersion and Dispersivity coefficients as a function of pore geometry factor (β) for various flow regimes bridging the gap between the pore-scale and the continuum-sale.

Project Objectives:

Solute transport is known to exhibit non-Fickian transport characteristics, i.e., which cannot be defined by the continuum-scale advection-dispersion equation (ADE). The non-Fickian characteristics are likely associated with large variability in pore fluid velocity. For example, large variability in velocity can be caused by diverging-converging pore channel geometry, which is further influenced by the flow rate. The usage of ADE to predict solute transport often results in under-estimated coefficients of solute transport for heterogeneous porous media. Thus, the impact of a single pore-scale heterogeneity, e.g., intra-pore geometry, on predicting solute transport in upscaled models or at the continuum-sale is still not well understood. The purpose of this study is to investigate how the heterogeneity in intra-pore geometry due to geologic diagenesis controls the flow behavior and Fickian dispersion phenomenon for solute transport.

Methodology:

To study how the flow and transport phenomenon modifies due to pore geometries at pore-scale, a series of 15 diverging-converging intra-pore geometries are designed, which account for a wide range of sediment grain shapes and result in pore topology spanning from 'cavity' pore to 'slit' pore (Figure 1). We quantify these intra-pore geometries by a dimensionless hydraulic shape factor (β) based on the

hydraulic radius theory (Bear, 1972; Chaudhary et al., 2013). COMSOL Multiphysics software (2008) is used to numerically solve Navier-Stokes and Advection-Diffusion equations to examine the flow and transport phenomenon calculating velocity variance, permeability, 'breakthrough curves' (BTC) and 'residence time distributions' (RTD). Pore domains are systematically extended in the direction of flow to determine the length-scale or the representative elementary volume (REV) when non-Fickian transport transitions to Fickian transport. Fickian dispersion coefficients, ' D_H ' were determined using the second moment method that use the temporal variance in BTC data. These Fickian dispersion coefficients are used to calculate the longitudinal Dispersivity. Sensitivity analysis investigates the role of varying intra-pore topology and flow rate on permeability, length-scales for Fickian dispersion, and characteristics of Fickian dispersion and Dispersivity as a function of intra-pore geometry and flow rate. Our analysis employs the physics of fluid and solute transport by computing velocity distribution, velocity variance, residence time distribution to determine potential constitutive relations that can predict the Fickian transport phenomenon as a function of intra-pore-scale geometry and flow rate.

Results and Discussion:

Through an analysis of the flow fields, we found that the permeability follows an inverse power-law relationship with the hydraulic shape factor β with an exponent of $3/2$. The variance of the velocity field σ^2 is found to have power-law dependence on intra-pore geometry with an exponent of $7/4$ (Figure 2a), and another power-law dependence on the flow rate (Re) with an exponent of 2 (Figure 2b). We further combine these define relations to obtain a universal relationship that can account for variance in velocity as a function of pore geometry and the flow rate combined (Figure 2c). Thus, our new defined relationship serves to quantify the relative impacts of the first order heterogeneity or the intra-pore geometry on velocity variance for various flow rate scenarios in porous media.

The velocity field variance controls non-Fickian transport characteristics and its transition to Fickian transport behavior. We find larger velocity variance increases the magnitude of non-Fickian characteristics. Thus, larger length-scales are required for the transport to transition to a Fickian regime. Both the magnitude of non-Fickian characteristics (Figure 3a) and the length-scale required for Fickian transport (Figure 3b) are dependent on β , and the effects of which get amplified with the flow rate, Re . For example, up to a physical length of 1.1 meters or 500 pores is needed for the slit pore to attain Fickian behavior at Pe of 1000.

Fickian dispersion is found to be exponentially dependent on intra-pore geometry, with exponents ranging from 0.05 to 0.31 (Figure 4a). Flow rate further amplifies Fickian dispersion where the exponents, Γ is a measure of this amplified response and dependent on $\ln(Re)$ (Figure 4b). Thus, we can define new equations that can predict Fickian dispersion coefficients as a function of intra-pore geometry and flow rate.

As an investigation of how Fickian dispersion evolves with the flow rate, a range of advective flow regimes spanning Pe between 1 to 1000 are considered. We find that the Fickian dispersion follows a power-law relation of the form Pe^δ (Figure 5a). Here the exponent, δ is found to be linearly dependent on β , which has a range of $\delta = 1.16$ from one end of intra-pore geometry, i.e., the cavity pore ($\beta = 5.9$) to $\delta = 1.8$ for the slit pore ($\beta = 23.98$). Prediction of δ has been a contentious debate, where previous studies have reported a wide range in δ . Using linear dependence δ on β , we normalize the effect of pore geometry to the intermediate pore shape or the 'bead pack' pore with $\beta = 13.9$ and determine a universal power-law relation with an exponent of $3/2$ (Figure 5b). Thus, the usage of these relationships will provide the possibility of predicting dispersion as a function of dispersion for various advection rates (Pe).

Using the theory of hydrodynamic dispersion of porous media, we calculate longitudinal Dispersivity, which is a manifestation of the characteristics of intra-pore geometry, i.e., the structure of

porous media. We found that longitudinal Dispersivity is exponentially dependent on intra-pore geometry by a factor spanning from 0.05 to 0.22 and can be predicted as a function of β . Longitudinal Dispersivity is further amplified by the flow rate from which the exponents, Ψ , follow a natural logarithmic relation with Re similar to that found between Γ and Re .

The relation between longitudinal Dispersivity and length-scale has been a long-standing debate. However, we determined that longitudinal Dispersivity follows a linear relationship with length-scale when including literature reported Dispersivity data and from this study (Figure 6). We emphasize that variations in intra-pore geometry alone that exist at pore-scale can require length-scales up to 1 meter for the Fickian transport to manifest. One meter is a vast domain for CFD studies, and which only accounts for the first-order effects or intra-pore geometry effects. The length-scale needed to determine Fickian transport may likely be larger for second-order and third-order heterogeneity effects related to pore-size and connectivity variations.

Significance:

This study demonstrates the impact of the ‘first-order’ heterogeneity found at pore-scale, e.g., intra-pore geometry, and how these effects get amplified with changes in flow rate to predict the flow and solute transport for upscaled models, e.g., pore-network models. Furthermore, 1) the length-scales when ADE can be used will be determined for various intra-pore geometries and flow scenarios, and 2) the relationship of Fickian dispersion coefficients ‘ D_a ’, ‘ D_H ’, and longitudinal Dispersivity ‘ α_L ’ as a function of β and Re may be directly used in up-scaled pore-network models. This concept can be applied in many fields to predict solute transport in aquifers, petroleum migration, and secondary recovery techniques (Bear, 1972). In comparison, determining the length-scales for ADE to be valid at various Reynold’s numbers can be used for predicting solute transport at high flows in the subsurface, e.g., near the head of pumping wells and residence times of solutes as they migrate across an aquifer (Bear, 1972). Lastly, our findings provide a foundation for future work to investigate how length-scales and Fickian dispersion coefficients evolve with increasing heterogeneity such as tortuosity.

Figures and Tables:

Figure 1: Diverging-converging intra-pore geometry design: (a) Half 2D sections of intra-pore geometries formed from various grain shapes (solid color lines) resulting in different β values, (b) 3-D rendition of intra-pore shapes to two linearly connect pores for a few pore domains. Note, the dashed rectangle over pore with $\beta = 23.98$ marks the link to its 2D section shown in (a).

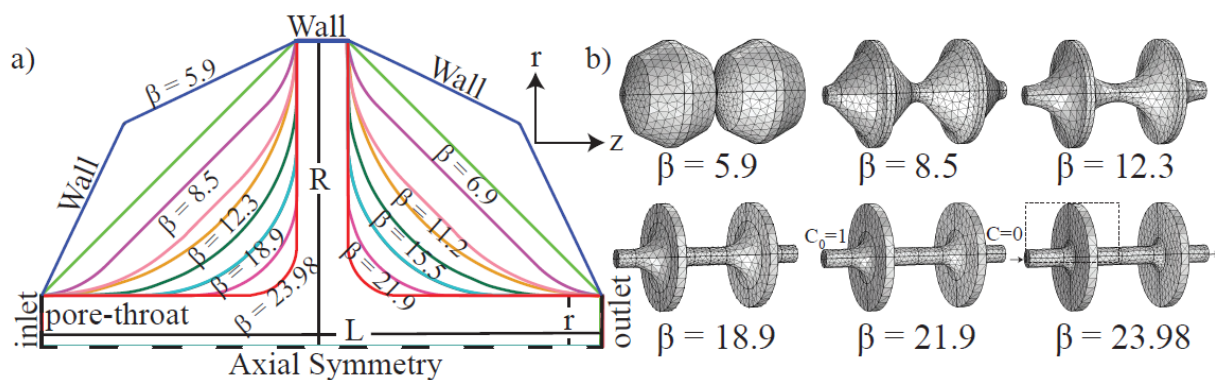


Figure 2: Velocity variance depends on intra-pore geometry factor β by a power-law with an exponent of $7/4$ ($R^2 > 0.99$), which is independent of flow rate, Re (a). The velocity variance is dependent on Re by another power-law with an exponent of 2 ($R^2 > 0.99$) (b). The combined effects of pore geometry β and Re on velocity variance (σ^2) ($R^2 = 0.99$) (c).

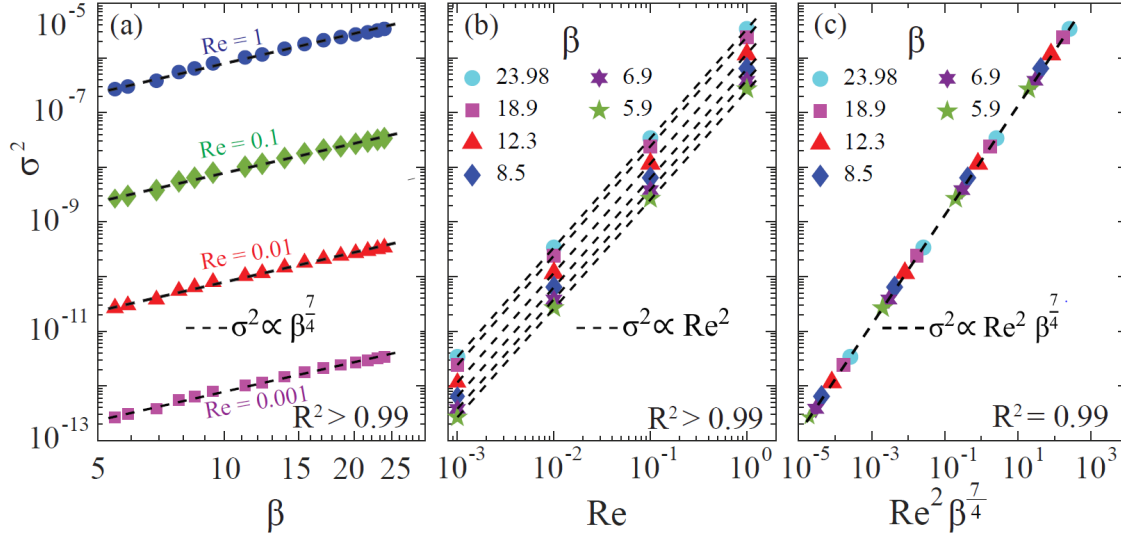


Figure 3: The magnitude of non-Fickian characteristics and the effects of intra-pore geometry for various Re - Pe flow scenarios (a). The length-scale (L) for the Fickian transport depends on intra-pore geometry and amplified differently based on the flow regime, Re - Pe (b).

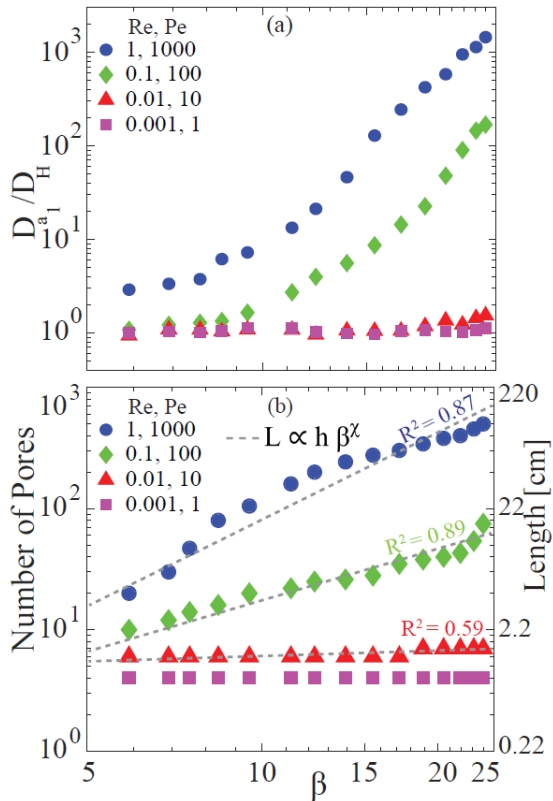


Figure 4: The exponential dependence of the Fickian dispersion (D_H) on the hydraulic shape factor (β) for various Re-Pe flow scenarios (a). The exponent (Γ) in D_H and β relationship is dependent logarithmically on flow rate (b).

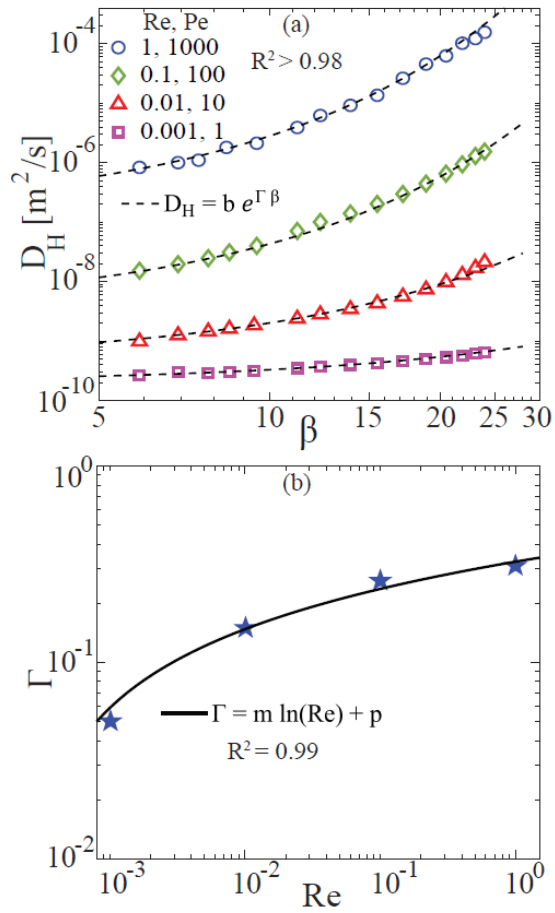


Figure 5: Normalized Fickian dispersion coefficients (D_H / D_m) as a function of Pe-Re from all pores. Dashed lines show fits of the equations of Bachmat, (1965) and Bear, (1966). The black dashed lines outline the equation for end member pores, i.e., the cavity pore ($\beta = 5.9$), the bead pack pore ($\beta = 13.9$), and the slit pore ($\beta = 23.98$) (a). The effects pore geometry normalized to the bead pack pore with a university power-law exponent of 3/2 in contrast with various previous studies (b).

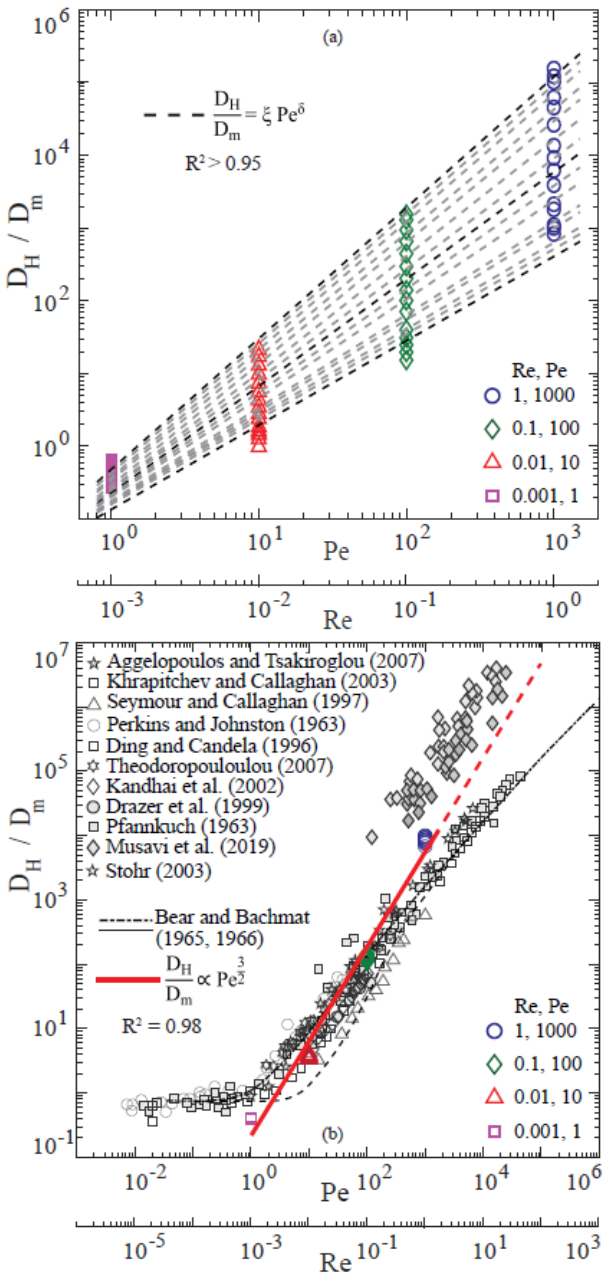
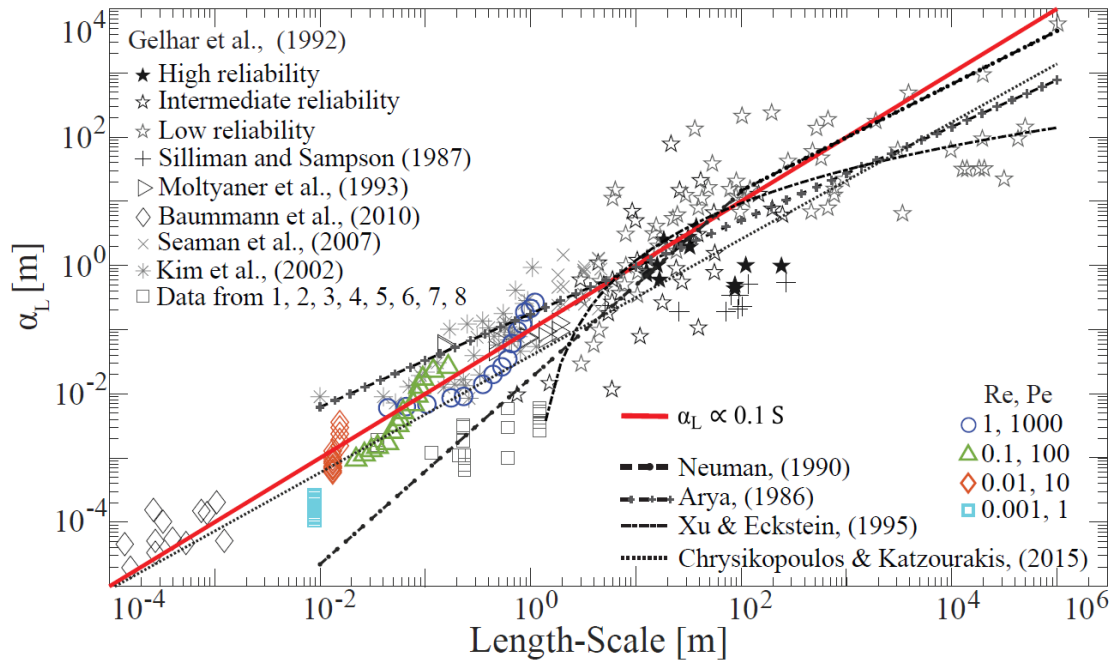


Figure 6: Comparison of our defined 1:1 relationship (red line) for our span of intra-pore geometries with different regressions proposed from previous studies. Low reliable dispersivity data were acquired from these sources: 1) Baker, (1977), 2) Coats and Smith, (1964), 3) Delshad, (1986), 4) Kasraie and Ali, (1984), 5) Ptak and Teutsch, (1994), 6) Robertson et al., (1991), 7) Schulze-Makuch and Cherkauer, (1997). Note, length-scale on the x-axis is physical length.



Acknowledgements:

I am deeply indebted to my advisor, Dr. Kuldeep Singh, for his infinite guidance, inspiring encouragement, constructive criticism, and technical suggestions throughout the duration of this investigation. Without his constant help and support, I would have not been able to conquer the many challenges and obstacles that I faced during my study. I would like to express my sincere gratitude to OSGC for awarding me the Fellowship grant to continue and wrap up my studies. In addition, I want to say thank you to the Department of Geology at Kent State University (KSU) for the opportunity to enable myself to conduct this investigation.

References:

Aggelopoulos, C., & Tsakiroglou, C. (2007). The Longitudinal Dispersion Coefficient of Soils as Related to the Variability of Local Permeability. *Water, Air and Soil Pollution*, 185. <https://doi.org/10.1007/s11270-007-9445-6>

Aris, R., & Taylor, G. I. (1956). On the dispersion of a solute in a fluid flowing through a tube. *Proceedings of the Royal Society of London. Series A. Mathematical and Physical Sciences*, 235(1200), 67–77. <https://doi.org/10.1098/rspa.1956.0065>

Arya, A. (1986). *Dispersion and reservoir heterogeneity*. United States.

Arya, A., Hewett, T. A., Larson, R. G., & Lake, L. W. (1988). Dispersion and Reservoir Heterogeneity. *SPE Reservoir Engineering*, 3(01), 139–148. <https://doi.org/10.2118/14364-PA>

- Bachmat, Y. (1965), Basic transport coefficients as aquifer characteristics, I.A.S.H. Symposium Hydrology of Fractured Rocks, Dubrovnik.
- Baker, L. E. (1977). Effects of Dispersion and Dead-End Pore Volume in Miscible Flooding. *Society of Petroleum Engineers Journal*, 17(03), 219–227. <https://doi.org/10.2118/5632-PA>
- Bear, J., & Bachmat, Y. (1966). Hydrodynamic dispersion in non-uniform flow through porous media, taking into account density and viscosity differences. *PN*, 4, 66.
- Bear, J. (1972). *Dynamics of fluids in porous media*. America Elsevier Publishing Company.
- Blunt, M. J., Bijeljic, B., Dong, H., Gharbi, O., Iglauer, S., Mostaghimi, P., Paluszny, A., & Pentland, C. (2013). Pore-scale imaging and modelling. *Advances in Water Resources*, 51, 197–216. <https://doi.org/https://doi.org/10.1016/j.advwatres.2012.03.003>
- Chaudhary, K., Cardenas, M. B., Deng, W., & Bennett, P. C. (2013). Pore geometry effects on intrapore viscous to inertial flows and on effective hydraulic parameters. *Water Resources Research*, 49(2), 1149–1162. <https://doi.org/https://doi.org/10.1002/wrcr.20099>
- Chaudhary, K., Cardenas, M. B., Deng, W., & Bennett, P. C. (2013). Pore geometry effects on intrapore viscous to inertial flows and on effective hydraulic parameters. *Water Resources Research*, 49(2), 1149–1162. <https://doi.org/https://doi.org/10.1002/wrcr.20099>
- Coats, K. H., & Smith, B. D. (1964). Dead-End Pore Volume and Dispersion in Porous Media. *Society of Petroleum Engineers Journal*, 4(01), 73–84. <https://doi.org/10.2118/647-PA>
- COMSOL Multiphysics (2008), COMSOL Multiphysics Version 3.5a.
- Delshad, M. (1986). *A study of transport of micellar fluids in porous media*.
- Ding, A., & Candela, D. (1996). Probing nonlocal tracer dispersion in flows through random porous media. *Phys. Rev. E*, 54(1), 656–660. <https://doi.org/10.1103/PhysRevE.54.656>
- Drazer, G., Rosen, M., & Zanette, D. H. (2000). Anomalous transport in activated carbon porous samples: power-law trapping-time distributions. *Physica A: Statistical Mechanics and Its Applications*, 283(1), 181–186. [https://doi.org/https://doi.org/10.1016/S0378-4371\(00\)00149-7](https://doi.org/https://doi.org/10.1016/S0378-4371(00)00149-7)
- Gelhar, L. W., Welty, C., & Rehfeldt, K. R. (1992). A critical review of data on field-scale dispersion in aquifers. *Water Resources Research*, 28(7), 1955–1974. <https://doi.org/https://doi.org/10.1029/92WR00607>
- Kandhai, D., Hlushkou, D., Hoekstra, A. G., Slood, P. M. A., Van As, H., & Tallarek, U. (2002). Influence of Stagnant Zones on Transient and Asymptotic Dispersion in Macroscopically Homogeneous Porous Media. *Phys. Rev. Lett.*, 88(23), 234501. <https://doi.org/10.1103/PhysRevLett.88.234501>
- Kasraie, M., & Ali, S. M. F. (1984). *Role of Immobile Phase Saturations in Tertiary Oil Recovery*. <https://doi.org/10.2118/12635-MS>

- Khrapitchev, A. A., & Callaghan, P. T. (2003). Reversible and irreversible dispersion in a porous medium. *Physics of Fluids*, 15(9), 2649–2660. <https://doi.org/10.1063/1.1596914>
- Mousavi Nezhad, M., Rezaia, M., & Baioni, E. (2019). Transport in Porous Media with Nonlinear Flow Condition. *Transport in Porous Media*, 126(1), 5–22. <https://doi.org/10.1007/s11242-018-1173-4>
- Neuman, S. P. (1990). Universal scaling of hydraulic conductivities and dispersivities in geologic media. *Water Resources Research*, 26(8), 1749–1758. <https://doi.org/https://doi.org/10.1029/WR026i008p01749>
- Perkins, T. K., & Johnston, O. C. (1963). A Review of Diffusion and Dispersion in Porous Media. *Society of Petroleum Engineers Journal*, 3(01), 70–84. <https://doi.org/10.2118/480-PA>
- Pfannkuch, H.-O. (1963). *Contribution a l'etude des déplacements de fluides miscibles dans un milieu poreux.*
- Ptak, T., & Teutsch, G. (1994). Forced and natural gradient tracer tests in a highly heterogeneous porous aquifer: instrumentation and measurements. *Journal of Hydrology*, 159(1), 79–104. [https://doi.org/https://doi.org/10.1016/0022-1694\(94\)90250-X](https://doi.org/https://doi.org/10.1016/0022-1694(94)90250-X)
- Robertson, W. D., Cherry, J. A., & Sudicky, E. A. (1991). Ground-Water Contamination from Two Small Septic Systems on Sand Aquifers. *Groundwater*, 29(1), 82–92. <https://doi.org/https://doi.org/10.1111/j.1745-6584.1991.tb00500.x>
- Schulze-Makuch, D., & Cherkauer, D. S. (1997). Method developed for extrapolating scale behavior. *Eos, Transactions American Geophysical Union*, 78(1), 3. <https://doi.org/https://doi.org/10.1029/97EO00005>
- Seymour, J. D., & Callaghan, P. T. (1997). Generalized approach to NMR analysis of flow and dispersion in porous media. *AIChE Journal*, 43(8), 2096–2111. <https://doi.org/https://doi.org/10.1002/aic.690430817>
- Stöhr, M., Roth, K., & Jähne, B. (2003). Measurement of 3D pore-scale flow in index-matched porous media. *Experiments in Fluids*, 35(2), 159–166. <https://doi.org/10.1007/s00348-003-0641-x>
- Theodoropoulou, M. (2007). Dispersion of Dissolved Contaminants in Groundwater: from Visualization Experiments to Macroscopic Simulation. *Water, Air, and Soil Pollution*, 181, 235–245. <https://doi.org/10.1007/s11270-006-9296-6>
- Xu, M., & Eckstein, Y. (1995). Use of Weighted Least-Squares Method in Evaluation of the Relationship Between Dispersivity and Field Scale. *Ground Water*, 33, 905–908. <https://doi.org/10.1111/j.1745-6584.1995.tb00035.x>

Possible Supplemental Power Extraction from Rotating Detonation Engine using Magnetohydrodynamics

Student Researcher: Joshua F. Coffey

Advisor: Dr. Ephraim Gutmark

University of Cincinnati
Aerospace Engineering & Engineering Mechanics

Abstract

Detonation based engines, where the combustion wave moves with a velocity greater than the speed of sound, and rotating detonation engines (RDE) in particular, where the detonation wave moves around an annular combustor have become a focus of research recently due to their potential advantages over traditional deflagration-based (subsonic combustion velocity) engines. Detonations, due to the shock waves that form, result in much higher temperatures than are seen in traditional engines. While this may make the implementation of detonation engines more difficult, it does present an opportunity in the form of electrical power that can be harvested from the detonation products. At the high temperatures present during detonation, mainly right behind the shock wave, ionization can occur and, when coupled with a magnetic field, a current is induced that, if extracted, could be used to power other systems in an air or spacecraft.

Project Objectives

The goal of this project was to design and test a system that could be added to an existing RDE at the University of Cincinnati (UC) that could determine how much power is available to be extracted. When a conducting fluid, like the ionized gas in a detonation wave, moves through a constant magnetic field, an electromotive force (emf) is induced that leads to the generation of an electrical current as described by Faraday's Law of induction in the field of magnetohydrodynamics, which is the combination of fluid dynamics and Maxwell's equations governing electromagnetism [1]. This current will be in a direction perpendicular to both the magnetic field and velocity of the gas flow and is dependent on the magnitude of both as described by the equation $\mathbf{J} = \sigma(\mathbf{u} \times \mathbf{B})$ where \mathbf{J} is the current density, σ is the electrical conductivity of the gas, \mathbf{u} is the velocity of the gas flow, and \mathbf{B} is the magnetic field felt by the gas. The electromotive force that drives the current is of the order $|\mathbf{u} \times \mathbf{B}|$ and can be calculated using the equation $\epsilon = h|\mathbf{B}| |\mathbf{u}|$ where ϵ is the emf and h is the channel width through which the detonation travels [2]. It is this quantity that this project sought to calculate.

Methodology

This project was split into three parts: testing the rotating detonation combustor present at the Gas Dynamics and Propulsion Lab (GDPL) to measure the wave speed \mathbf{u} , designing a system that could feasibly be built at the GDPL to generate a magnetic field, and calculating the emf that could result when both of these systems were combined.

The velocities of the detonation wave were gathered for several conditions, determined by the mass flow rate of the oxidizer, in this case air, and the equivalence ratio, which is a function of the amount of fuel, gaseous hydrogen, that was used. The fuel and oxidizer were chosen to be what they were mainly due to their frequent use in other detonation literature, although the use of air as oxidizer was serendipitous as

it has been shown that in a rotating detonation engine, the use of air as opposed to oxygen results in an increase in electrical conductivity [3]. The combustor in use at UC is of annular design and has a channel width of 2.54 cm. The velocity was calculated in LabVIEW based on when the detonation passes three ion probes that are present at three equidistant locations around the circumference of the combustor.

The magnetic field was modelled in COMSOL and was based on the idea of using several Neodymium magnets of dimension 40mm x 40mm by 20mm that are currently in use in the GDPL. Two orientations of magnetic field were considered, to be generated in the two possible directions perpendicular to the detonation wave at any point in the combustor and resulted in magnetic fields between 0.1 and 0.4 T.

Results

As can be seen in figure 1, as equivalence ratio and oxidizer mass flow rate increased, so too did the velocity until a point at which it plateaued. This is as expected based on previous detonation research [4]. Figure 2 follows a similar trend, as expected, with emf increasing with oxidizer flow rate and magnetic flux density. These values are useful in giving an idea of the potential current that can be drawn from this type of system, since emf is of order $|\mathbf{u} \times \mathbf{B}|$ and current is equal to $\sigma(\mathbf{u} \times \mathbf{B})$. These results will lead into the continued research currently planned to measure both the emf generated by the system and the electrical conductivity of the system.

Figures

Figure 1. Velocity vs. Equivalence Ratio

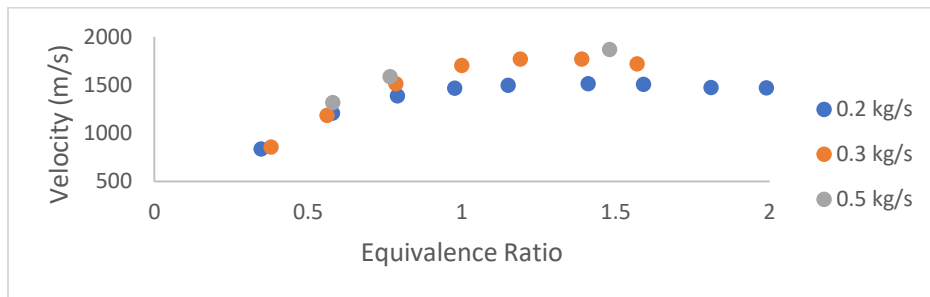
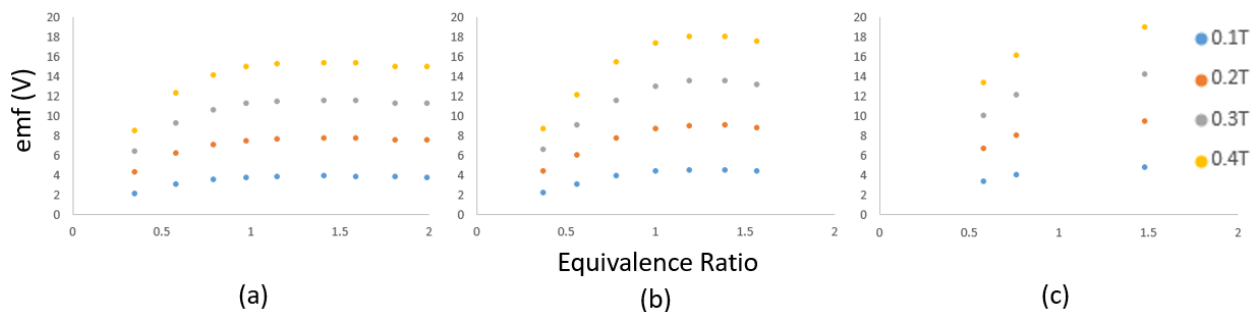


Figure 2. emf vs. Equivalence Ratio at (a) 0.2 kg/s, (b) 0.3 kg/s, and (c) 0.5 kg/s



Acknowledgments and References

This work was supported by the Ohio Space Grant Consortium. Thanks to the RDE researchers at GDPL, led by Dr. Anand, for their assistance throughout this project, Drs. Nagy and Velicheti for their help with the electronics portion of this project, and project advisor Dr. Gutmark.

- 1) P. A. Davidson, *Introduction to Magnetohydrodynamics*, Cambridge University Press, 2017, 2nd Edition
- 2) E. L. Popov, et al., "MHD Effects in Continuous Spin Detonation" *Doklady Physics*, 2019, Volume 64, No. 2, pp. 77–79
- 3) J. Braun, et al., "One-Dimensional Analysis of the Magnetohydrodynamic Effect in Rotating Detonation Combustors" *AIAA Journal*, 2016, Volume 54, No. 12, pp. 3761-3767
- 4) V. Anand, "Investigation of Rotating Detonation Combustor Operation with H₂-Air Mixtures" *International Journal of Hydrogen Energy*, 2016, Volume 41, No. 2, pp. 1281-1292

Optimizing Radiative Fin Planar Shape and Thickness for Maximum Heat Loss while Minimizing Mass

Student Researcher: Nicholas S. DeBortoli

Advisor: Dr. Rydge Mulford

University of Dayton
Mechanical Engineering

Abstract

Spacecraft in planetary orbits experience large fluctuations in heat inputs. However, spacecraft waste heat is generally rejected from a constant surface area, constant emissivity surface called a radiator. As such, onboard heaters are used to control spacecraft temperatures, consuming non-negligible portions of limited volume, mass, and power budgets. One proposed method to rectify heater power consumption on board spacecraft is to develop dynamic radiators which morph to adopt the ideal emitting surface area. In this work, finite volume methods are used to find the optimal planar shape for maximum heat loss per unit volume of a dynamic radiative fin suspended in space. In order to optimize a fin for maximum heat loss, two variables were considered: planar area shape and thickness profile. A finite difference model was created for various fin shapes to calculate heat rate. These shapes ranged from a rectangular fin to a triangular fin, with combinations of these two shapes (pentagon) also considered. Temperature profiles across the width and length of the fin were generated. Optimization routines were then used to find the optimal shape, both on the face and along the thickness, for maximum heat loss per unit volume. Completion of this work constitutes considerable progress towards the development of an effective dynamic radiator for use in a variety of applications. Subsequent work has begun involving the modeling of these dynamic radiators attached in parallel on small spacecraft.

Project Objectives

- Develop a dynamic radiative fin with the highest rate of heat transfer per unit volume
- Optimize fin's planar face shape and thickness profile
- Create prototypes of optimal fins to be analyzed and experimented upon
- Perform system's level analysis of a small spacecraft in orbit with a dynamic radiator onboard
- Reduce the need for heaters onboard small spacecraft

Methodology Used

In order to develop an optimized dynamic radiator, the ideal planar fin shape had to first be determined. To do so, a finite volume approach was used, discretizing the fin geometries in two dimensions along the face. The geometries were discretized into a mesh of 1000 elements using a Python package. A constant temperature boundary condition (345 K) was established along the base of the fin to simulate heat input from a spacecraft. From there, the temperatures of each node were determined using the following equation:

$$\frac{k\left(\frac{w_m}{L_m}T_m + \frac{w_n}{L_n}T_n + \frac{w_o}{L_o}T_o\right) - 2A\varepsilon\sigma T_i^4}{\frac{w_m t_m}{L_m} + \frac{w_n t_n}{L_n} + \frac{w_o t_o}{L_o}} = T_i$$

Equation 1. Governing Finite Difference Equation

k = fin thermal conductivity [30] (W/m^2)

ε = fin emissivity [0.9]

σ = Stefan-Boltzmann constant [$5.67 \cdot 10^{-8}$] ($W/m^2 K^4$)

A = Emitting surface area (m^2)

w_m, w_n, w_o = width of element sides (m)

L_m, L_n, L_o = length between element centroids (m)

t_m, t_n, t_o = average thickness at each element side (m)

T_m, T_n, T_o = neighboring element temperature (K)

T_i = central element temperature (K)

Once each node's temperature was determined using linear algebra methods, the temperature profile was compared to an initial guess to verify that the calculation was correct. If the difference between the calculated profile and the guess was not within a predetermined convergence criterion (10^{-7}), the process was repeated, using the new profile as the initial guess. In order to validate the results from this study, a uniform thickness, square fin profile was compared against results in literature. The error between the results was 0.13%, thus validating the results. Now that the profiles have converged, optimization methods will be used to determine the ideal triangular, rectangular, and pentagonal geometries for the fin shape, as well as the ideal thickness profile.

Results

The comparison of a triangular, rectangular, and pentagonal fin, each with the same volume and base width can be seen in Figure 1. Each of these fins also has the same, constant thickness profile. As can be seen, the maximum heat rate per unit volume can be found in the rectangular fin. With this being said, it is only a slight improvement over the pentagonal fin (1.2%).

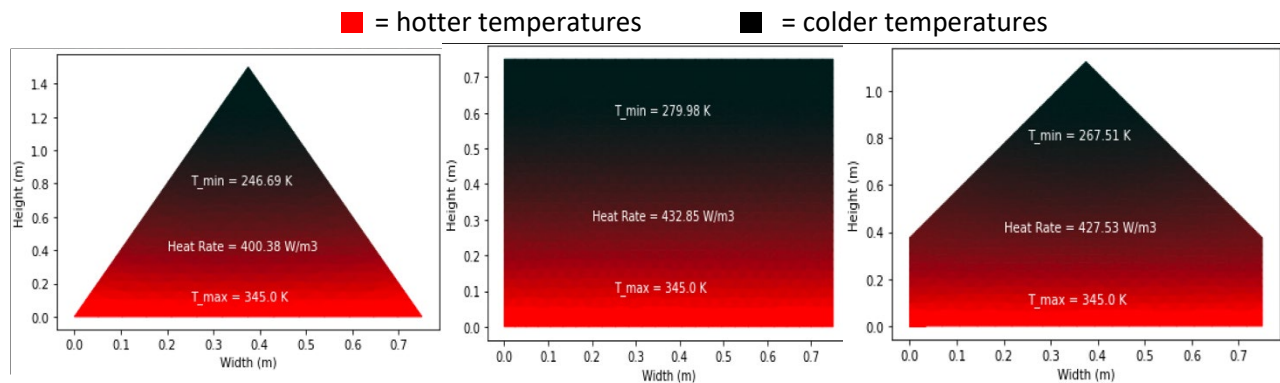


Figure 1. Temperature Profiles of Three Uniform-Thickness Radiative Fins

Discussion

When comparing fins with a constant thickness, the rectangular fin was the best performer. With all three fins having the same mass, this demonstrates that better capabilities can be achieved in a rectangular fin than in a triangular fin with the same volume and mass. With mass being such an enormous consideration in spacecraft design, this is important knowledge to have when designing radiators. Furthermore, these results only consider fins with uniform thickness. To complete this study, optimization needs to be run along the fins' thickness profiles. Finally, this work is only for static fins suspended in space. Once the ideal radiative fin shape is determined, transient, dynamic fin analysis will be run with these ideal fins attached to a small spacecraft.

Acknowledgments

The author would like to thank the OSGC and the University of Dayton for their continued support throughout this research project. Furthermore, the author thanks Dr. Rydge Mulford for his mentorship, assistance, and support throughout this project.

References

- [1] Mulford, Rydge B, et al. "Heat Transfer, Efficiency and Turn-down Ratio of a Dynamic Radiative Heat Exchanger." *International Journal of Heat and Mass Transfer*, vol. 143, 17 July 2019, pp. 1–11
- [2] Weston, S., 2018, *State of the Art Small Spacecraft Technology*, NASA/TP-2018-220027, NASA, Moffett Field. CA.

Cooperative Multi-Agent UAS Task Assignment for Disaster Response Scenario

Student Researcher: Nicholas DeGroot

Advisor: Kelly Cohen

University of Cincinnati

Department of Aerospace Engineering and Engineering Mechanics

Abstract

Task assignment problems have evolved as computation methods and resources have allowed, utilizing Unmanned Aerial Systems (UAS) as a resource for accomplishing a variety of complex tasks. The ability of UAS to operate in complex environments, cover large areas, and be deployed quickly opens the door for a variety of applications, with one such being disaster response. In this research, a scenario is considered where UAS are used to help dispatch aid to a region after a natural disaster such as a hurricane. A heterogeneous fleet of both fixed-wing and multirotor UAS is available to be allocated to the region of interest, with the goal of accomplishing all known tasks in the minimum amount of time. The multiple-depot multiple travelling salesman problem (MDMTSP) is initially used as a benchmark to show the effectiveness of the algorithm. Several variations are then added to the MDMTSP to better represent the challenges of disaster response task assignment including search tasks, heterogeneous sensors, fuel constraints, and Dubins vehicles. Future goals of the project focus on applying the developed algorithm in a hardware test and performing a real-world flight test demonstration.

Project Objectives

Unmanned aerial systems (UAS) have shown to be a valuable asset for first responders in a disaster response situation. They can improve situational awareness of the disaster environment by providing real-time imagery, damage assessment, identifying blocked roads, or detecting people who are trapped or otherwise in need of help. Many examples are available which show how UAS have been used effectively to respond to disasters. For example, the Northrop Grumman Global Hawk was used after Typhoon Haiyan in 2013, a senseFly swinglet CAM was used after the Haiti earthquake in 2012, and several variants of UAS have been used to monitor radiation levels in Fukushima starting in 2011 [1].

This project ultimately seeks to provide a method which allows for tasks to be assigned in real-time to a fleet of UAS operating in a disaster response environment. The environment will likely be chaotic, where situations may change rapidly with limited time to react to new information. The available resources will also likely be limited, whether those resources are UAS, sensors, supplies, or anything else. Therefore, the solution should be adaptable, scalable, and robust. This means it should apply to many different scenarios, with a highly variable number of UAS and tasks, while also being able to account for sudden changes that occur to either the fleet or the tasks. Multiple tasks are to be assigned to multiple UAS in a way which minimizes the time required to accomplish all known tasks. This forms a non-deterministic polynomial-time hard (NP-Hard) cooperative multiple task assignment problem (CMTAP) [2].

This type of problem presents several challenges. As stated above, the problem is NP-Hard, meaning the time required to find a solution increases exponentially with the addition of new tasks. Coupling issues also present themselves between task assignment and path planning. The time required for a UAS to accomplish a set of tasks is dependent on both the assigned tasks, and the route between those tasks.

Also, the task assignment and path planning subtasks cannot be easily decoupled, making large-scale problems difficult to solve in a reasonable amount of time. In its simplest form, this problem can be viewed as a variation of the Multiple Depot Multiple Travelling Salesman Problem (MDMTSP) with a MinMax objective function [3]. This objective function attempts to minimize the cost of the UAS in the fleet with the *maximum* cost. A mathematical description of the MDMTSP is shown below in Equation 1.

$$J_k = \sum_{e_{ij} \in A} w_{ijk} d_{ij} \quad (1)$$

$\min J_{k^+}$ where

$$k^+ = \operatorname{argmax}_{k \in \{1, \dots, m\}} J_k$$

Where:

J_k is the value of the objective function

w_{ijk} is a binary variable when k travels from task i to j

A is the set of edges connecting tasks

e_{ij} is an edge in A

d_{ij} is the distance between tasks

m is the number of UAS

Methodologies Used

After conducting a literature review for ways to solve CMTAP problems, a market-based approach was selected for use in this project. Market-based algorithms simulate the process of people buying and selling items with the idea that the free market will find a near-optimal solution over time. The market involves four different steps which are detailed below: auction, trade, switch, and relinquishment. This process is repeated for a specified number of iterations, or until a solution has been converged upon.

Auction: Tasks are put up for bid, and each UAS in the fleet bids on the current task up for auction. For the MinMax objective function, bids are based on the estimated time for the UAS to accomplish *all* of its tasks and return to its depot. The task is then assigned to the lowest bidder, and the auction continues until all tasks known by the market are assigned.

Trade: After all tasks have been auctioned, two UAS are randomly selected for a trade, designated here as UAS 1 and UAS 2. UAS 1 analyzes all the tasks currently assigned to UAS 2 and sees if it is able to accomplish any of those tasks for a lower cost. If UAS 1 can accomplish the task for a lower cost, then the task is removed from UAS 2 and assigned to UAS 1.

Switch: Two UAS are randomly selected for a switch, designated as UAS 1 and UAS 2. A polygon is formed from the routes of each respective selected UAS with vertices at the task locations. If a task currently assigned to either UAS 1 or UAS 2 lies within the polygon for the other UAS, then the task assignment is switched. The task switch step was developed from observing that UAS who have intersecting routes typically have a sub-optimal task assignment.

Relinquishment: Each UAS in the fleet chooses a number of tasks to send back to the market for auction. Tasks are relinquished based on their marginal cost to each UAS. Marginal cost is defined as the

additional time required to accomplish all tasks with and without the task currently being analyzed assigned.

The market-based task assignment method was chosen based on several criteria, the first of which being scalability. Exact solvers are typically unable to provide solutions to this type of problem in real time. This is especially true when the goal is to run the algorithm on-board a UAS on hardware with limited processing power such as single-board computers. Instead, a market-based provides a solution with a heuristic method that seeks to find a near-optimal solution but at a greatly reduced execution time.

The market-based algorithm also has a distributed nature where each UAS is responsible for calculating both its own bids, and which of its current tasks it will relinquish. The market can be implemented in two ways depending on the desired application. The first involves a centralized auctioneer who is responsible for running the market, receiving bids, and sending notifications to UAS about the results of the market. This has the advantage of minimizing the amount of inter-UAS communication by only requiring communication from each UAS to the auctioneer. It does however have the disadvantage of being completely reliant on the auctioneer, lowering the robustness and fault tolerance of the system. Alternatively, a copy of the market can be run on each UAS, with information being shared across the fleet. This method improves the robustness of the system by removing the reliance on an auctioneer, but at the detriment of increasing the amount of inter-UAS communication.

Market-based task assignment also makes the implementation of both heterogeneous UAS and heterogeneous tasks relatively simple. UAS are aware of the sensors they possess, as well the sensors required to accomplish a task. Therefore, only the bids of individual UAS are affected by heterogeneity because a UAS can simply choose to not bid on a task if it does not have the required sensors.

As stated previously, the simplest form of task assignment addressed by this research is the MDMTSP. In this case, all tasks are simply a set of waypoints which need to be visited. For this problem, the ordering of the tasks assigned to each UAS, and therefore the value of the global objective function, involves solving a single Travelling Salesman Problem (TSP). The TSP is NP-Hard in itself, so computation time will increase quickly for large problems. A 2-opt heuristic method was selected to solve the TSP subproblem because it quickly provides good results for the scale of the problems being considered in this research. It is also worth noting that the implementation of the MDMTSP is identical for one or more depots because UAS bid on tasks in the same way regardless of starting location. They are unaware of the positions of the other UAS in the fleet and know only about their bids.

Results Obtained

The MDMTSP is used extensively in this section as it provides a good way to benchmark the developed algorithm against other methods in the literature. A literature review did not find any results that would serve as an appropriate benchmark for this research involving CMTAP, heterogeneous UAS, and heterogeneous tasks. As such, the MDMTSP is used as a benchmark for the market-based algorithm, and to build confidence in its performance for more complex situations.

Results are compared to the work by Kivelevitch and Carlsson et al., who have both studied the MDMTSP extensively [3][4]. Several scenarios are considered with between 1 and 50 depots, and between 100, and 500 tasks. The location of both the depots and the tasks were selected from a uniform random distribution between 0 and 100 units. A sample of several of the benchmarks

Table 1: A sample comparison between the results from the developed algorithm and the results from Kivelevitch and Carlsson et al. Note: All times are in seconds

<u>Case</u>	<u>Depots, Agents, Tasks</u>	<u>Kivelevitch Average Max</u>	<u>Carlsson Average Max</u>	<u>DeGroot Average Max</u>	<u>Kivelevitch Average Time</u>	<u>DeGroot Average Time</u>
d1v10c100	1, 10, 100	71.504	80.305	73.150	6.109	0.941
d5v5c100	5, 5, 100	191.134	229.966	187.209	4.597	2.174
d10v10c100	10, 10, 100	110.068	282.258	111.391	6.318	1.069
d10v10c200	10, 10, 200	137.543	175.119	144.779	10.465	7.439
d20v20c200	20, 20, 200	80.937	118.888	80.630	23.678	4.253
d50v50c500	50, 50, 500	58.165	122.607	59.888	259.220	26.871

conducted is shown in Table 1. The results in Table 1 are for a 10-run average, as all of the included methods use some randomness in their approach to finding a solution. The average values for the maximum UAS cost in the fleet, along with the average execution times are shown. All benchmarks were performed on an Intel Core i5-8400 processor @2.6 GHz. In general, the method in this research finds average solutions approximately in-line with the method developed by Kivelevitch, and substantially better than the method from Carlsson.

Run times for the developed method are under 10 seconds for all scenarios but the 50 depot, 50 UAS, 500 task, where the time climbs to 26.871 seconds. All tests showed the developed algorithm improving on the time by Kivelevitch, with the largest difference again coming for the 50 depot, 50 UAS, 500 task scenario. A benchmark was unable to be performed on the runtime for Carlsson’s algorithm, but the results would almost certainly yield a faster time due to the algorithm being implemented in a compiled programming language.

A visual example of the results obtained by the market-based algorithm for the 10 depot, 10 UAS, 100 task case is shown in Figure 1. The results include attributes indicative of what would be expected for a near-optimal solution, with no intersections between the routes of the UAS, and the difference between the route lengths only varying by about 10 percent. The locations of each UAS are also labeled on the figure.

Scenarios with search tasks were also considered. A search task is defined following a path required to traverse a search area using a back-and-forth scan pattern. A search area is an arbitrary polygon defined by a set of vertices. The direction of the search lines is determined by first fitting a minimum rotated rectangle around the search area polygon, then making the search path lines parallel to the longest side of the rectangle, reducing the total number of turns required by the UAS [5]. Bids for the assignment of search tasks are based on the closest waypoint in the search area to the previous task. There are four possible entry points into the search area, which are optimized by brute force after the task has been assigned. The concept of a search task along with an example implementation is shown in Figure 2.

Situations involving both heterogeneous tasks and fuel constraints adhere to the same basic principle. If a UAS is unable to accomplish the current task, then it will not bid on the task, trade for the task, or switch to the task. For heterogeneous tasks, each UAS has a list of available sensors, and each task has a

list of sensors required to accomplish the task. If the sensors on the UAS are not equal to the sensors required for the task, then the task is infeasible and will not be bid on. An example of task assignment with heterogeneous tasks is shown in Figure 3.

Fuel constraints consider the maximum endurance for a UAS and the estimated cost for accepting a new task. If the cost for accepting a new task violates the constraint on endurance, the UAS will not bid on the task. In this case however, a UAS can still acquire a task which was once too expensive in later iterations through a combination of task trading, switching and relinquishment, allowing for the possibility of escaping local minima. An example of task assignment with fuel constraints is shown in Figure 4.

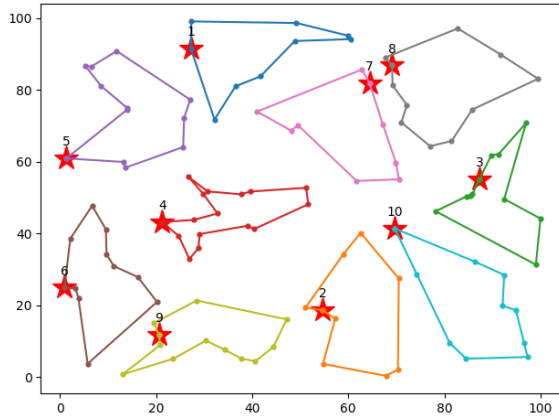
Vehicles with constraints of their turn radius were also accounted for in the algorithm. A Dubins Vehicle is used to provide a simplistic model of the trajectories of fixed-wing aircraft [6]. The implementation of Dubins Vehicles into the task assignment algorithm use a Dubins Path solver which finds the minimum length path from a starting location and heading to a final location and heading [7][8]. The cost estimate for the single TSP is still based on Euclidean distance. Otherwise, another dimension would need to be added to the distance matrix because the length of the Dubins path is dependent on the locations of the UAS's current task and its next task. The bids for each UAS however, are based on the distance returned by the Dubins solver for the solution found to the TSP. A task assignment solution with one Dubins vehicle is shown in Figure 5.

Significance and Interpretation of Results

In conclusion, this research has developed a framework which allows for the assignment of multiple tasks to multiple UAS. Benchmarking the algorithm with the MDMTSP has shown the results to be in-line with methods representing the current state of the art, with run times typically on the order of a few seconds. Several different types of tasks have been implemented at the time of writing, including search tasks. Constraints involving heterogeneous UAS, heterogeneous tasks, fuel, and vehicle dynamics have also been accounted for.

Future work will focus on applying the task assignment algorithm in changing environments. This includes situations where new tasks may appear or disappear, or new UAS become available or unavailable. The goal is to eventually perform a hardware integration with the algorithm running on-board each UAS in the fleet to show how the solution can be implemented in a real-world flight test. The framework can then be used to expand the accessibility of research regarding multi-agent systems. The task assignment algorithm can be built upon further with additions such as the integration of hardware sensors until a system can be deployed in a standalone fashion.

Figures/Charts



UAS 1 Cost: 102.285
 UAS 2 Cost: 100.700
 UAS 3 Cost: 102.144
 UAS 4 Cost: 99.197
 UAS 5 Cost: 102.499
 UAS 6 Cost: 101.436
 UAS 7 Cost: 96.021
 UAS 8 Cost: 97.954
 UAS 9 Cost: 93.5497
 UAS 10 Cost: 103.363
 Max UAS Cost: 103.363

Figure 1: A visual example of the results obtained from the market-based algorithm for the 10 depot, 10 UAS, 100 task scenario

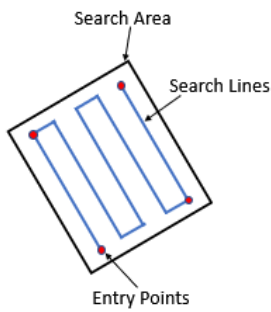
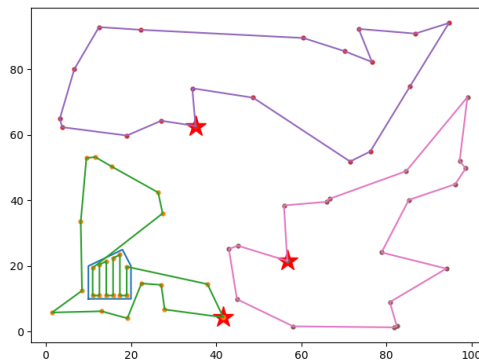


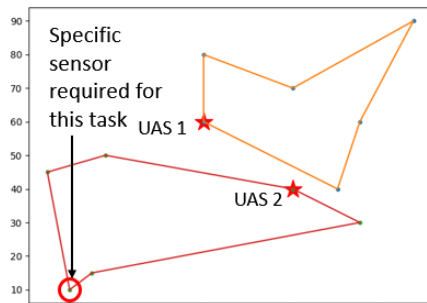
Figure 2: Example search area



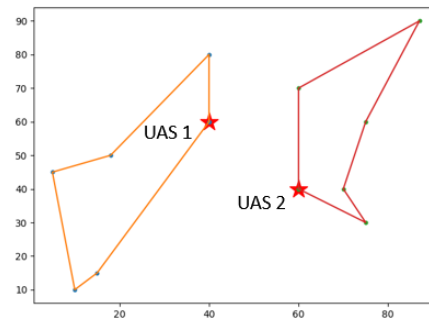
3 UAS
50 Point Visit Tasks
1 Search Task

 UAS 1 Cost: 255.928
 UAS 2 Cost: 268.432
 UAS 3 Cost: 242.186

Figure 2: An example showing how search tasks are structured is shown on the left. A task assignment with 3 UAS, 50 waypoints, and 1 search task is shown on the right



UAS 1 Cost: 164.943
 UAS 2 Cost: 179.403



UAS 1 Cost: 165.035
 UAS 2 Cost: 145.735

Figure 3: The difference in task assignment when only one UAS is able to accomplish a particular task

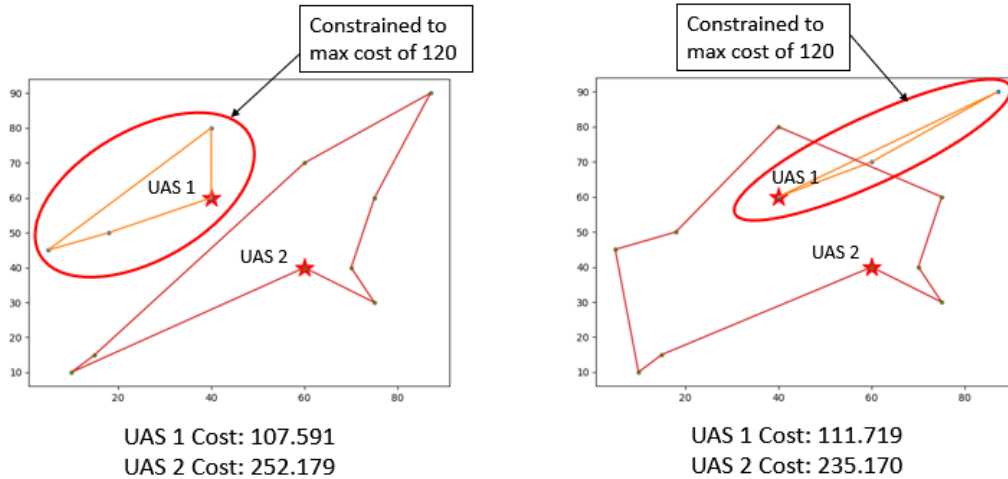


Figure 4: Results from two runs of the task assignment algorithm when enforcing fuel constraints

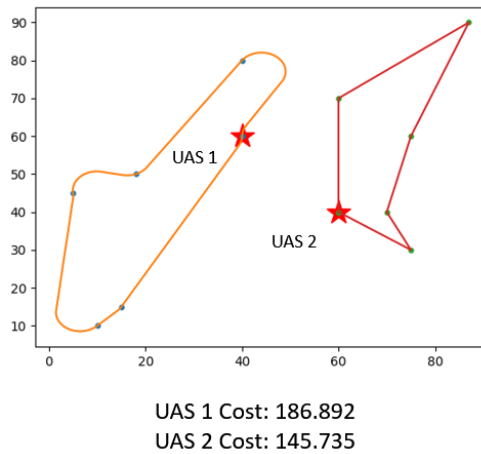


Figure 5: An example task assignment when UAS 1 is a Dubins vehicle

References

1. Kim, Karl & Davidson, Jennifer. (2015). Unmanned Aircraft Systems Used for Disaster Management. Transportation Research Record: Journal of the Transportation Research Board. 2532. 83-90. 10.3141/2532-10.
2. Martinez, Sonia. (2010). UAV Cooperative Decision and Control: Challenges and Practical Approaches (Shima, T. and Rasmussen, S.; 2008) [Bookshelf]. Control Systems, IEEE. 30. 104 - 107. 10.1109/MCS.2010.935899.
3. Kivelevitch, Elad & Cohen, Kelly & Kumar, Manish. (2013). A Market-Based Solution to the Multiple Depots, Multiple Traveling Salesmen Problem with Profits. AIAA Infotech at Aerospace (I at A) Conference. 10.2514/6.2013-4666.
4. Carlsson, John & Ge, Dongdong & Subramaniam, Arjun & Ye, Yinyu. (2009). Solving min-max multi-depot vehicle routing problem. 10.1090/fic/055/03.

5. DeGroote, N. S., Barnes, E., Burton, J., Terry, M., Ouwerkerk, J. N., and Cohen, K., "A Solution for the Challenges Presented by the 2020 AUVSI SUAS Competition," AIAA Scitech 2021 Forum, <https://doi.org/10.2514/6.2021-0522>.
6. Dubins, L.E. (July 1957). "On Curves of Minimal Length with a Constraint on Average Curvature, and with Prescribed Initial and Terminal Positions and Tangents". American Journal of Mathematics. **79** (3): 497–516. [doi:10.2307/2372560](https://doi.org/10.2307/2372560). [JSTOR 2372560](https://www.jstor.org/stable/2372560)
7. Xu, Wenda & Wei, Junqing & Dolan, John & Zhao, Huijing & Zha, Hongbin. (2012). A Real-Time Motion Planner with Trajectory Optimization for Autonomous Vehicles. Proceedings - IEEE International Conference on Robotics and Automation. 10.1109/ICRA.2012.6225063.
8. Shkel, A.M. & Lumelsky, Vladimir. (2001). Classification of the Dubins set. Robotics and Autonomous Systems. 34. 179-202. 10.1016/S0921-8890(00)00127-5.

Noncovalent Glyco-SWCNT Complexes and Interactions with Lectins

Student Researcher: Ana M. DiLillo

Advisor: Dr. Geyou Ao

Cleveland State University

Department of Chemical and Biomedical Engineering

Abstract

Single-wall carbon nanotubes (SWCNTs) have unique optical, electronic, and chemical properties which can be utilized for a wide range of applications, such as biosensing and imaging advancement in the near-infrared spectral range. These applications are facilitated *via* stable dispersion of SWCNTs by biopolymers in an aqueous environment. In this work, we study the behavior of synthetic glycopolymers (i.e., polymers with carbohydrate pendant groups) and their ability to stabilize SWCNTs *via* noncovalent complexation resulting in water soluble, glycopolymer-wrapped SWCNT (Glyco-SWCNT) hybrids. Particularly, disaccharide lactose-containing polymers of various chain lengths will be tested to optimize dispersion stability, quality, and yield of SWCNTs. These Glyco-SWCNT complexes will be utilized to explore the multivalent interactions between carbohydrates and various carbohydrate-binding proteins (lectins) *via* optical spectroscopy with the goal of determining the selectivity and sensitivity of targeted interactions between carbohydrates and proteins. If successful, these Glyco-SWCNT complexes can be utilized as fluorescent probes to detect specific carbohydrate-protein interactions in biology that are important for many cellular events, such as cancer development and metastasis.

Project Objectives

The scope of this project is to enhance SWCNT dispersion quality and yield *via* synthetic glycopolymers and investigate the interactions between the carbohydrate pendant groups and lectins. A deeper understanding of the carbohydrate-protein interactions allows us to determine effects on dispersion stability, binding kinetics, and binding affinity on Glyco-SWCNT complexes. The carbohydrate-protein interaction plays a significant role in a wide range of cellular processes, such as cancer and host-pathogen interaction.¹ Through the optimization of Glyco-SWCNT complexes and their targeted lectin binding, we can determine applicability as a future biosensor for cellular events. These complexes can be further developed to target specific glycosylation profiles allowing the unique NIR signature of SWCNTs to act as a noninvasive image medium for the affected cells.

Methodology

Synthetic glycopolymers with pendant lactose groups were synthesized using cyanoxyl free radical-mediated polymerization (CFRMP) scheme.² CoMoCAT SWCNT powder was dispersed using synthetic glycopolymers by tip sonication. A total dispersion volume of 1 mL was comprised of SWCNTs and synthetic glycopolymer in deionized water. After tip sonication, dispersion was separated into 9 equal samples that were then centrifuged to collect supernatant. Supernatant was diluted in phosphate buffer solution (PBS) in preparation for lectin addition and absorbance data was gathered using NS3 NanoSpectralyzer (Applied NanoFluorescence, LLC) to determine SWCNT concentration.

Arachis hypogaea (PNA), Concanavalin A (ConA), and Bovine Serum Albumin (BSA) were purchased through Sigma Aldrich. A mass ratio analysis on SWCNT:PNA was conducted to determine optimal

incubation time and concentration for lectin addition. The optical spectroscopy characterization of glyco-SWCNTs including vis-NIR absorbance and fluorescence was measured using NS3 NanoSpectralyzer prior to lectin addition and at intervals after addition. Additionally, sequential vis-fluorescence of the FITC marked PNA was conducted to gather kinetic information. Assuming the reaction model for single-site surface adsorption, a kinetic parameter (k_s) was found using the following equation:³

$$I(t) = M(1 - e^{-k_s t}) + I_0$$

where I_0 and I are fluorescence intensity of FITC at 525 nm wavelength before and after adding PNA. Lastly, samples of glyco-SWCNTs in PBS were mixed with PNA, ConA, and BSA aliquots, respectively, at a constant molar concentration of proteins and the mixtures were incubated for a certain amount of time. After incubation, samples were centrifuged to collect supernatant. Optical characterization of supernatant was conducted for vis-NIR absorbance and fluorescence using NS3 NanoSpectralyzer.

Results Obtained

A mass ratio analysis of SWCNTs:PNA showed a steady decrease in concentration of SWCNTs in the supernatant after incubation until reaches a saturation level at SWCNTs:PNA=1:8 (Figure 1). The decrease in nanotube concentrations is due to the glyco-SWCNTs creating crosslinks *via* the bound lectin. The crosslinks result in agglomeration of the glyco-SWCNTs, which can then be removed by centrifugation.⁴

The synthetic glycopolymers utilized have pendant lactose groups attached, which is a disaccharide comprised of galactose and glucose. PNA is a lectin with a strong binding affinity to galactose and ConA has a strong binding affinity for mannose and glucose. Figure 2 depicts the time resolved fluorescence intensity change of the FITC marker, which diminishes as the protein binds to the glyco-SWCNTs. The increased rate of binding for PNA depicts that galactose binds more readily with proteins. This can be due to steric influences of glycopolymer wrapping resulting in galactose being more readily available to the lectins.

Additionally, a non-carbohydrate binding protein BSA was explored to verify the crosslinking of glyco-SWCNTs by proteins and the effects on NIR-fluorescence. BSA does not display agglomeration, which demonstrates that crosslinking is not occurring as shown in Figure 3a. The increase in NIR fluorescence intensity of SWCNTs near 995 nm corresponding to the E_{11} peak of (6,5) species indicates that BSA may interact with the bare surface of SWCNTs leading to an increased surface coverage of SWCNTs (Figure 3b). On the other hand, the decrease in NIR fluorescence intensity of Glyco-SWCNTs when mixed with PNA and ConA is likely due to the crosslinking between glyco-SWCNTs creating tension that pulls the synthetic glycopolymers off the SWCNT surface (Figure 3b).

Significance and Interpretation of Results

At this time, the results obtained are depicting that glyco-SWCNT complexes can in fact bind with different lectins. This binding causes crosslinking between neighboring glyco-SWCNTs that result in the formation of agglomeration. The wrapping structure of the glycopolymers results in varied carbohydrate interaction depending on hydrophobic and steric interferences. These results are promising for the future of designing novel biosensors to probe targeted carbohydrate-protein interactions for understanding basic molecular mechanisms in many cellular events. As the library of glyco-SWCNT complexes expands, the kinetic information for target lectins can also be explored further. This research will continue to develop

with the addition of more lectins being tested as targets for the specific synthetic glycopolymers used here.

Figures

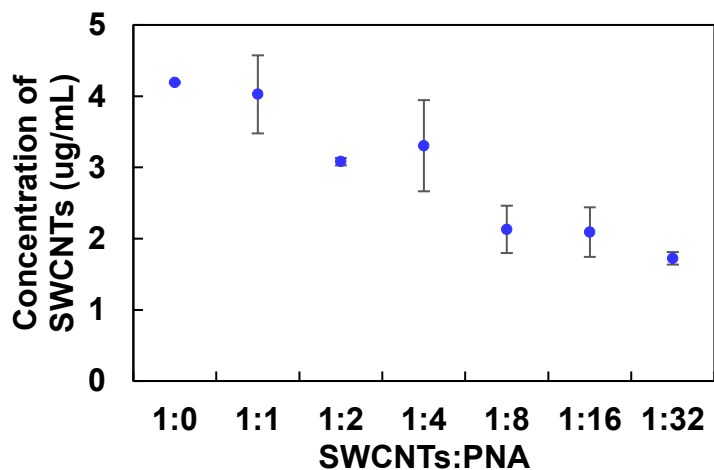


Figure 1: Concentration of SWCNTs as a function of SWCNTs:PNA mass ratio when incubating Glyco-SWCNTs with PNA.

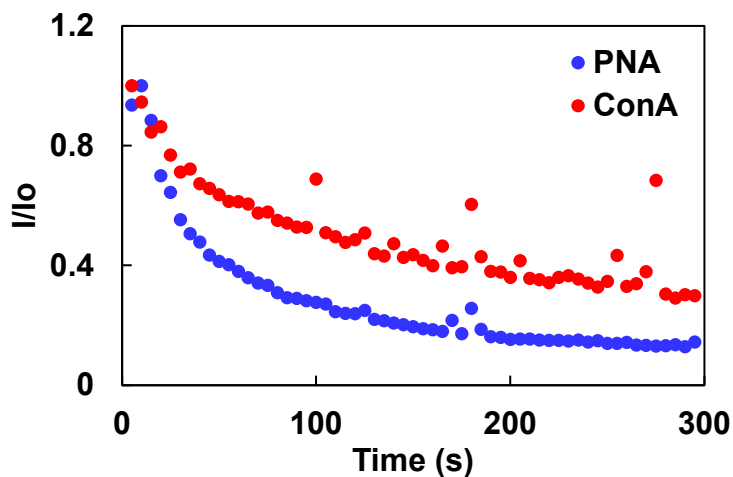


Figure 2: Fluorescence intensity ratio over time for addition of PNA and ConA to Glyco-SWCNT complexes in PBS.

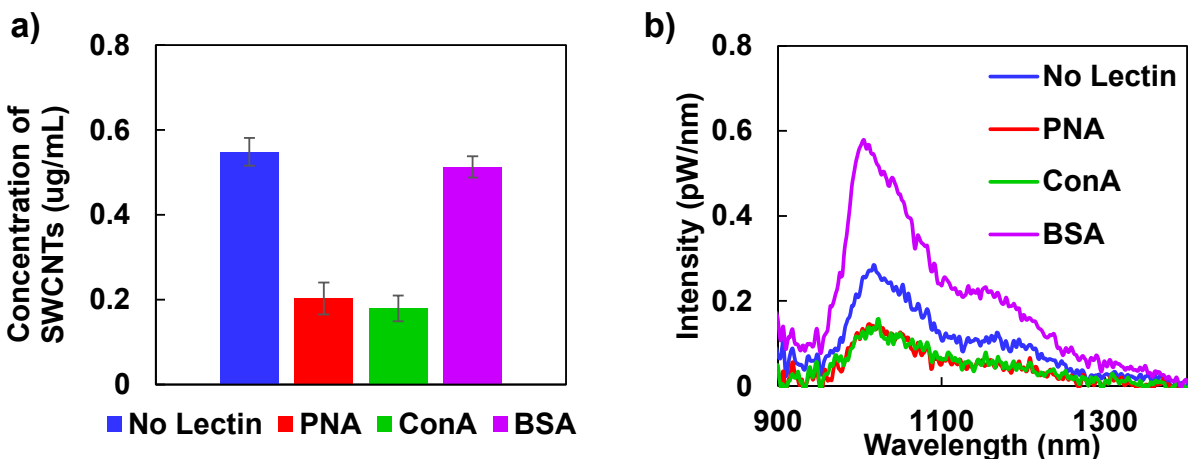


Figure 3:(a) Concentration of SWCNTs remaining in supernatant after incubating Glyco-SWCNTs with various proteins (i.e., PNA, ConA, and BSA). (b) NIR fluorescence spectra of supernatant of Glyco-SWCNTs after incubation with proteins.

Acknowledgements

A.M.D. acknowledges the NASA/Ohio Space Grant Consortium Master's Fellowship 2020-2021, NSF REU support, and CSU Summer Undergraduate Summer Research Award. We acknowledge Ka Keung Chan and Dr. Xue-Long Sun in the Department of Chemistry at CSU for synthesizing glycopolymers and helpful discussion.

References

1. Dai, Z. *et al.* Nanoparticle-Based Sensing of Glycan - Lectin Interactions. 10018–10019 (2006).
2. Cantwell, M. A., Chan, K. K., Sun, X.-L. & Ao, G. Carbohydrate- and Chain Length-Controlled Complexation of Carbon Nanotubes by Glycopolymers. *Langmuir* (2020) doi:10.1021/acs.langmuir.0c01498.
3. Reuel, N. F. *et al.* Transduction of glycan-lectin binding using near-infrared fluorescent single-walled carbon nanotubes for glycan profiling. *Journal of the American Chemical Society* 133, 17923–17933 (2011).
4. Liyanage, S. H. & Yan, M. Quantification of binding affinity of glyconanomaterials with lectins. *Chemical Communications* 56, 13491–13505 (2020).

Classification of Manned Aircraft in a Cluttered Low-Altitude Radar Environment Using Artificial Neural Networks

Student Researcher: Brandon L. Emshoff

Advisors: Dr. James Gregory and Dr. Matthew McCrink

The Ohio State University
Mechanical and Aerospace Engineering

Abstract

As small unmanned aerial systems (sUAS) become more prevalent in airspace already occupied by manned aircraft and begin beyond visual line of sight (BVLOS) operations, airspace surveillance systems capable of deconflicting the shared airspace become more important, especially in rural, uncontrolled airspace. Radar presents itself as a suitable surveillance system for the low-altitude environment where sUAS and manned aircraft are likely to interact. Radar can see all cooperative and non-cooperative – without automatic dependent surveillance-broadcast (ADS-B) out – aircraft in this environment. Radar is also centralized and independent of sUAS and manned aircraft operations. A downside to radar, though, is that at low altitudes radar clutter becomes an issue, though this issue can be mitigated. Thus, to tackle this issue, a machine-learning, artificial neural network algorithm was created to declutter the low-altitude radar feed to provide better situational awareness for the deconfliction of sUAS and manned aircraft. Truth data sets obtained from ADS-B and onboard flight recorders were used to correlate radar tracks to build a training data set that allows the model to ingest strictly radar data to make a classification. This algorithm is both lightweight and accurate in its classifications, removing greater than 94% of the clutter tracks seen by the radar, therefore increasing the usability of the radar feed.

Project Objectives (a discussion of your objectives)

Many previous attempts have been made to deconflict the shared airspace between sUAS and manned aircraft. These attempts have successfully implemented different methods to achieve this desired deconfliction. Vision-based systems equipped directly to each sUAS have been shown to allow for the detection and deconfliction at short ranges between sUAS and slow-moving and low-altitude aircraft and obstacles [1, 2]. The fusion of onboard and offboard sensors have also been utilized by Cornic, et al. for detect and avoid capabilities with sUAS [3]. Radar alone has also been used with extended Kalman filtering models to identify aircraft at medium to high altitudes, though the authors expressly mention the need for alternative means of low-altitude detection measures [4]. Finally, staring radars at low altitudes have been proven to track and classify small targets, albeit at very limited range [5]. While all these methods have shown promising results, they have all major drawbacks that limit their success and ability to be relied upon for large-scale solutions. Because of these limitations, this project focuses on developing a method for low-altitude detection of aircraft that can be used to help deconflict the shared airspace between manned aircraft and sUAS. Radar was chosen as the detection method of choice because it can see both cooperative and non-cooperative aircraft. Radar is also independent from sUAS and manned aircraft platforms and provides a centralized system for gathering airspace data. This project aims to reduce the inherent issues with radar clutter tracks when utilizing active radar at low altitude by using machine learning algorithms, specifically artificial neural networks.

Methodology Used

A neural network model was chosen because of the past success of this model type in other classification applications [6, 7]. The model consists of 20 input neurons, 40 hidden layer neurons, and a

single output neuron that labels the track as either an aircraft or clutter. 5,204 radar tracks – around 15% of which are aircraft and the other 85% being clutter – collected over the course of three days were used to train and test the model. The model was trained over 50 epochs (iterations), with each epoch consisting of a training session on 50 random examples from the set. Data for this study was collected using radar installations at three different locations to maximize the coverage and visibility of our surveillance system. The relative locations of these radar installations can be seen in Figure 1. ADS-B sensors at these locations also collected data on cooperative aircraft operating within the coverage area to be used as truth data sources for our radar tracks. When ADS-B data correlates with radar data, those radar tracks are labeled as aircraft. Flight recorder data obtained by flying with a local crop-dusting company that operates within our coverage area and was also used to correlate radar tracks. All other radar tracks that could not be correlated to known truth data was labeled as clutter tracks. These labeled tracks were then reduced to 20 feature variables, as seen in Table 1, for ingestion into the neural network model.

Table 1. Feature set used for the model

Parameter	Extracted Feature
Time (sec)	duration
Altitude (m)	mean altitude
	range of altitude
	binned altitude [0, 400)
	binned altitude [400, 800)
	binned altitude [800, 1500)
	binned altitude [1500, 2500)
Latitude (deg)	binned altitude [2500, 10000)
	mean latitude
	range of latitude
Longitude (deg)	mean longitude
	range of longitude
Heading (deg)	standard deviation of heading
Velocity (m/s)	mean velocity
	binned velocity [0, 20)
	binned velocity [20, 40)
	binned velocity [40, 80)
	binned velocity [80, 120)
	binned velocity [120, 500)

Results Obtained

After training the model, a final classification accuracy of 94.4% on data previously unseen by the model was achieved. The model loss drops quickly, indicating that the neural network converges quickly to a model of the system. This convergence denotes a feature set rich in information required to separate the clutter from the aircraft tracks. Figure 2 shows the model loss and model accuracy over the course of the 50 epochs during training. Upon further inspection of the confusion matrix, shown in Figure 3, generated with the testing data set, the model eliminates 95.6 % of the clutter tracks from the set. It also correctly classifies 37 of the 41 aircraft tracks correctly.

Significance and Interpretation of Results

The purpose of this research was to create a model that can scrutinize noisy low-altitude radar data and provide an output that is usable by sUAS operators for deconfliction with manned aircraft. By removing greater than 95% of the clutter tracks, this system shows great promise. When manned aircraft and human lives are at stake, the number of false positives is not as important as false negatives. If the number of false positives does not severely clutter the surveillance broadcast, a few false positives that

slip by are not of much concern. The final number of tracks that would be reported to operators in this case was 55, of which 37 were confirmed aircraft, which is much better than the unfiltered, original case.

This model in its current state does not handle data in real time, thus future work into this classifier will focus on enabling real time processing of radar data to provide as a full service to operators. The model is also planned to include more classification cases than just radar or clutter. Determining whether a clutter track is weather-based or ground-based, as well as predicting the type of aircraft detected by radar is being explored. Also, currently, the amount of data available for real crop-duster flights is also extremely limited, so a model of radar performance is being created such that simulated crop-duster flights can be used as supplemental data for that unique aircraft case. The work done to date is a very promising start, however, and has provided much insight into the complex problems associated with classifying noisy radar return data.

Figures/Charts

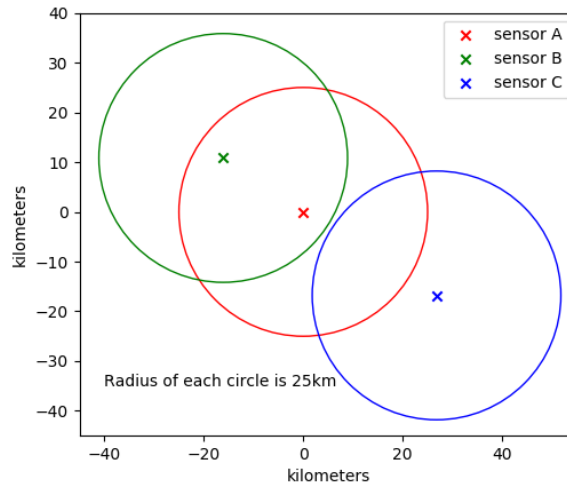


Figure 1. Relative sensor locations and coverage area

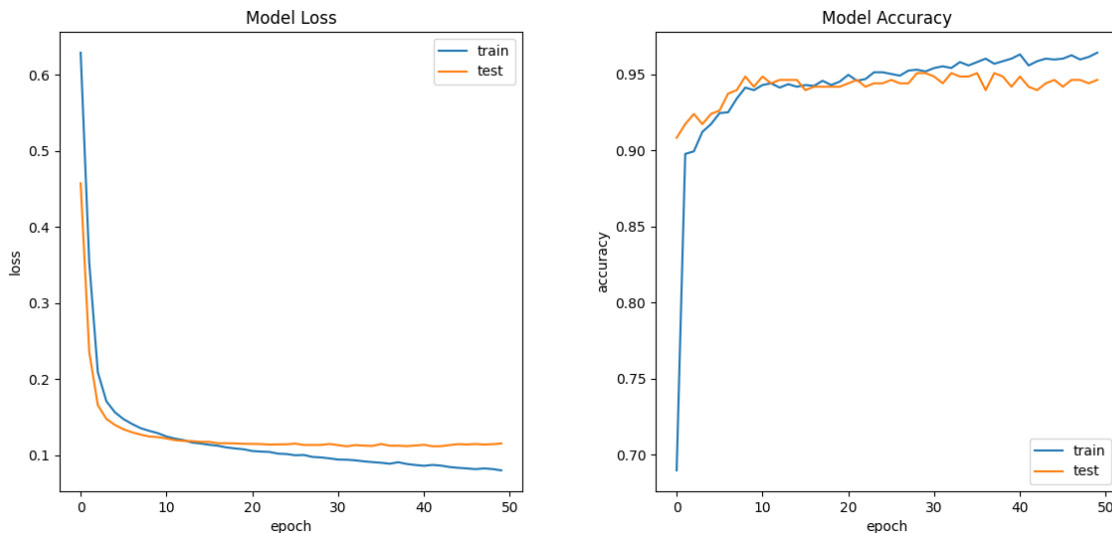


Figure 2. Classifier training and testing metrics

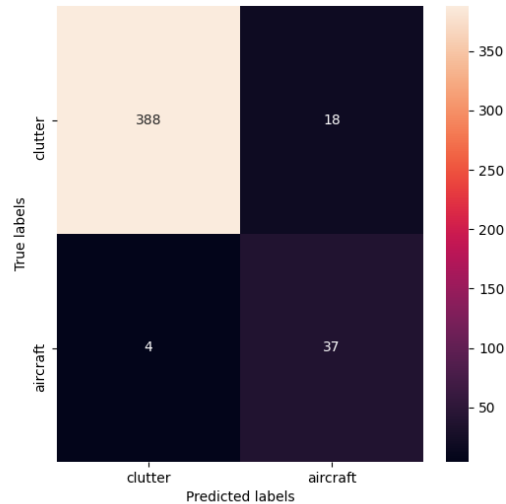


Figure 3. Confusion matrix for classifier algorithm on test set

Acknowledgments and References

The author would like to thank Dr. Matthew McCrink and Dr. James Gregory for their guidance during the research process. The author would also like to thank Achal Singhal for assisting with data collection and general troubleshooting issues and Fisher Ag for allowing the collection of flight data during their spraying season. Finally, the author would like to thank the Ohio Space Grant Consortium and The Ohio State University for providing funding to make this research possible.

1. Cho, S., Huh, S., Shim, D.H., Choi, H.S., "Vision-based Detection and Tracking of Airborne Obstacles in a Cluttered Environment," *Journal of Intelligent & Robotic Systems*, Volume 69, No. 1-4, Jan. 2013, pp. 475-488. doi: 10.1007/s10846-012-9702-9.
2. Mueller, M., Sharma, G., Smith, N., Ghanem, B., "Persistent Aerial Tracking System for UAVs," *International Conference on Intelligent Robots and Systems*, Oct. 2016, pp. 1562-1569.
3. Mcfadyen, A., Mejias, L., "A survey of autonomous vision-based see and avoid for unmanned aircraft systems." *Progress in Aerospace Sciences*, Volume 80, 2016, pp. 1-17.
4. Cornic, P., Garrec, P., Kemkemian, S., Ratton, L., "Sense and Avoid Radar using Data Fusion with Other Sensors," *IEEE Aerospace Conference*, 2011, pp. 1-14. doi: 10.1109/AERO.2011.5747514.
5. Jahangir, M., Baker, C.J., "L-band staring radar performance against micro-drones," *19th International Radar Symposium*, 2018, pp. 1-10. doi: 10.23919/IRS.2018.8448107.
6. Guyon, I. "Applications of neural networks to character recognition," *International Journal of Pattern Recognition and Artificial Intelligence*, Volume 5, 1991, pp. 353-382.
7. Baxt, W. G. "Use of an artificial neural network for data analysis in clinical decision-making: the diagnosis of acute coronary occlusion," *Neural Computation*, Volume 2, No. 4, 1990, pp. 480-489.

Uncertainty Quantification of Wind-tunnel Tests of a Low-Rise Building Model Using the NIST Aerodynamic Database

Student Researcher: Erin P. Hubbard

Advisor: Dr. Wei Zhang

Cleveland State University
Department of Mechanical Engineering

Abstract

Wind-induced roof damage of low-rise buildings and the cascading failures that follow such damage have resulted in vast economic losses in the United States (National Oceanic Data Center, 2018). These types of events and their impact on structures are simulated in boundary-layer wind tunnels. It has been documented that pressure statistics on reduced-scale building models differ considerably among different boundary-layer wind tunnels. Flow facility capability, model design and manufacturing, instrumentation, test setup and procedures, and specific data reduction methodology as well as researchers' experience are among the many factors that affect measured data and results in wind-tunnel experiments. To identify which sources may drive variation in the pressure statistics obtained from wind-tunnel tests, a detailed uncertainty quantification analysis is performed via Monte Carlo simulation using the NIST aerodynamic database. This work will demonstrate how measurement uncertainty propagates to quantities of interest in a wind-tunnel test, provide an improved understanding of critical measurements and uncertainty sources in tests of this type, and may reveal hints as to why differences exist between pressure statistics results in various facilities.

Objectives

Boundary-layer (BL) wind tunnel tests of wind loading on building models have served as primary means to determine the minimal design wind loads by the American Society of Civil Engineers (ASCE) provisions. It is well known that wind-tunnel results, e.g. surface pressure on building models, often show considerable discrepancies even significant efforts are put in model preparation, experimental setup, equipment/instrumentation calibration and data reduction methodology (Fritz et al, 2008). Though these variations are acknowledged, the reasons why they may be present remain unknown. Uncertainty in the wind pressure data results are by and large unreported (Ho et al. 2005), making meaningful comparisons impossible as a first step to determining whether or not the disagreement is statistically significant. Uncertainty quantification quickly becomes a critical piece of the puzzle when seeking these answers since "the uncertainty is as important a part of the result as the estimate itself. ...An estimate without a standard error is practically meaningless" (Jefferys 1967 in Higdon et al. 2006).

In view that BL wind tunnel test cases and results are used to determine minimal design wind loads and also to validate computational fluid dynamics (CFD) simulation, it is imperative to provide uncertainty quantification of the wind-tunnel test data and results. The main objectives of this work are 1) to provide an uncertainty propagation analysis using the publicly available NIST aerodynamic database to quantify uncertainties in velocity profile and pressure statistics, 2) to provide a breakdown of uncertainty source contributions and identify leading sources, and 3) to provide uncertainty propagation tools to make estimates readily available to publish alongside future CSU test results.

Methodology

This study will estimate uncertainty, particularly systematic uncertainty, in pressure statistics using the

Monte Carlo method of uncertainty propagation from wind-tunnel experiments archived in the NIST aerodynamic database. The test cases were performed at University of Western Ontario's (UWO) Boundary-Layer Wind Tunnel Laboratory, using a 1:100 scaled model of a low-rise building in suburban terrain.

The Monte Carlo Method (MCM) of uncertainty propagation is a fully probabilistic approach to UQ in which random draws are made from assumed error distributions for all pertinent uncertainty sources, errors are added to appropriate seed data values, and data is reduced to results of interest. This procedure is repeated through n iterations until the probability distribution of the outcomes is stable and well-defined. For example, for outcome distributions of a Gaussian nature, convergence criteria can be selected for the sample standard deviation s such that $\frac{|s_n - s_{n-1}|}{s_n} < 0.001$, indicating that the n^{th} Monte Carlo sample caused less than 0.1% change to the sample standard deviation from the previous iteration. A probabilistic interval can then be defined as the uncertainty in the result (typically a 95% level of coverage). The process is depicted in Fig. 1. To determine uncertainty source sensitivities, the Monte Carlo simulation can be run the same way with each uncertainty source being applied one at a time to discover the relative impact of each on the calculated result.

Results

The uncertainty in several variables of interest will be quantified, such as the inflow wind speed profile, inflow turbulence intensity profile, and building pressure statistics. A sensitivity analysis of input uncertainties will provide insight into the dominant uncertainty sources. If time allows, a second uncertainty propagation simulation will be performed for a similar wind-tunnel test by the Tokyo Polytechnic University (TPU). With uncertainty estimates for both wind-tunnel tests in hand, meaningful conclusions may be drawn about the agreement or disagreement of the building pressure statistics. If uncertainty levels are unacceptably high, the sensitivity test results will help guide decisions being made in the planning phase of an upcoming wind tunnel test that involves a similar setup to the UWO test. These UQ results can ensure the adequate capture of critical parameters in future tests. Additionally, an uncertainty propagation code will be created that, with a few tweaks to the simulation, produce uncertainty estimations applicable to other similar wind-tunnel tests.

Conclusions

Wind tunnel tests of building models remain an important research approach to improve design of minimal wind loading. Using the NIST aerodynamic database, this work will demonstrate how the uncertainty propagates with given error sources of wind-tunnel measurements. The work is still in progress. Results are expected to quantify uncertainty in critical parameters, identify significant uncertainty sources, and reveal hints as to why differences exist between reported pressure statistics.

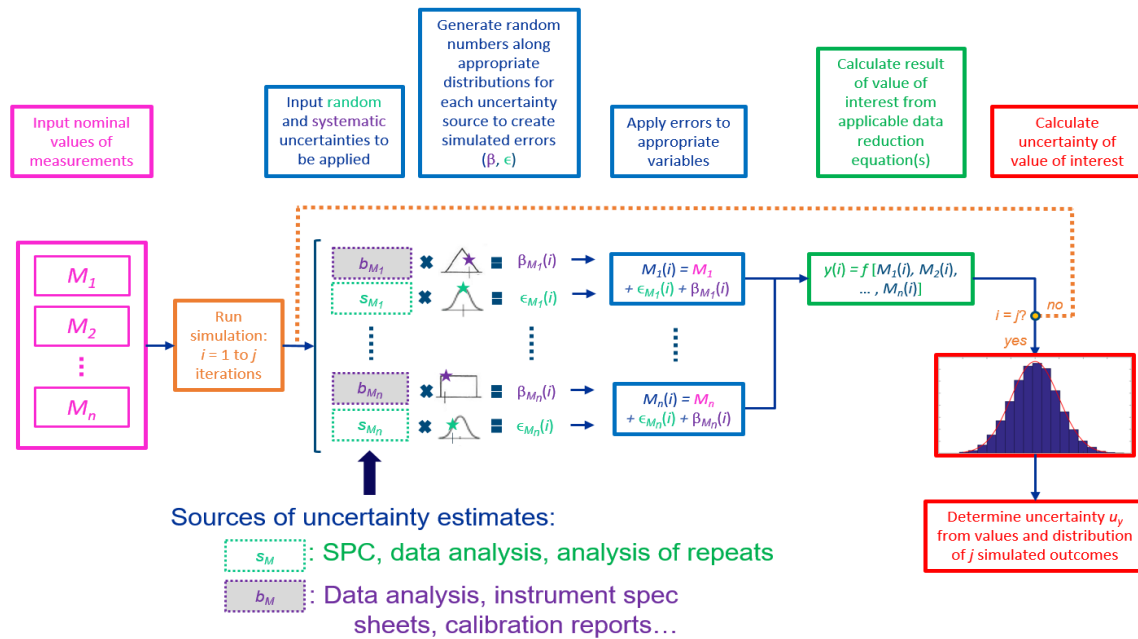


Figure 1. Monte Carlo method of uncertainty propagation (based on Stephens et.al, 2016)

Acknowledgements

E. Hubbard acknowledges the generous support of the Ohio Space Grant Consortium (OSGC) Master's Fellowship. W. Zhang acknowledges the National Science Foundation (NSF) CAREER grant (Award# 1944776) and the OSGC Faculty Research Initiation Grant Project (FRIGP).

References

- Fritz, W.P., Bienkiewicz, B., Cui, B., Flamand, O., Ho, T.C.E., Kikitsu, H. Letchford, C.W., and Simiu, E., 2008. International Comparison of Wind Tunnel Estimates of Wind Effects on Low-Rise Buildings: Test-Related Uncertainties. *Journal of Structural Engineering*, ASCE 134(12): 1887-1890.
- Higdon, D., Klein, R., Anderson, M., Berliner, M., Covey, C. Ghattas, O., Graziani, C. Habib, S., Sefcik, J., Stark, P., and Steward, J., 2006. Uncertainty Quantification and Error Analysis. Workshop on Scientific Challenges in National Security: the Role of Computing at the Extreme Scale, Los Alamos National Laboratory, 10-00262.
- Ho, T.C.E., Surry, D., Morrish, D., and Kopp, G.A. 2005. The UWO Contribution to the NIST Aerodynamic Database for Wind Loads on Low Buildings: Part 1. Archiving Format and Basic Aerodynamic Data. *Journal of Wind Engineering and Industrial Aerodynamics*, 93(1):1-30.
- National Oceanic and Atmospheric Administration National Climatic Data Center, "Billion-Collar Weather and Climatic Disasters: Overview," 2018.
- Stephens, J., Hubbard, E., Walter, J., and McElroy, T., 2016. Uncertainty Analysis of the NASA Glenn 8x6 Supersonic Wind Tunnel. Contractor Report, National Aeronautics and Space Administration, NASA/CR-2016-219411: 91.

Optical Dilatometry Measurements for the Quantification of Sustainable Aviation Fuel Materials Compatibility

Student Researcher: Shane T. Kosir

Advisor: Dr. Joshua Heyne

University of Dayton
Department of Chemical and Materials Engineering

Introduction and Objectives

Sustainable aviation fuel (SAF) offers a near-term opportunity to reduce aviation's greenhouse gas emissions. Many currently-approved SAFs are limited to a maximum blend ratio of 50% with conventional jet fuel due to materials compatibility issues (i.e., O-ring volume swell). Specifically, aircraft have been found to leak significant quantities of fuel over the timescale of hours when volume swell is not sufficient [1]. Aromatics provide the majority of volume swell for conventional jet fuel but are generally undesirable due to their low specific energy (SE) and tendency to form soot. Previous high-performance jet fuel optimization efforts indicate that blends consisting primarily of cycloalkanes can meet volume swell requirements while achieving 1.9% and 5.1% SE [MJ/kg] and energy density [MJ/L] gains relative to conventional jet fuel [2]. Given these optimization results, it is proposed that cycloalkanes can overcome the blend limit and add to the value proposition of sustainable aviation fuels. Here, optical dilatometer measurements of volume swell for sustainable aviation fuels are reported. These measurements will serve to screen candidate SAFs, many of which have high cycloalkane concentrations, at an early stage of the approval process. Two prescreening tiers are proposed: Tier α and Tier β [3]. The focus of this report will be Tier α , which will couple optical dilatometry measurements with two-dimensional gas chromatography (GCxGC) data to predict volume swell with ~ 1 mL of fuel.

Methodology

The optical dilatometer used for this study is shown in Fig. 1. It consisted of an LED light source, an optical cell, an optical stage, and a digital camera connected to a computer. Nitrile rubber O-rings (NBR) provided by the University of Dayton Research Institute (UDRI) were used in this study. A 1 mm cross-section of the O-ring was cut using a scalpel and placed at the bottom of the optical cell. Time was taken as zero, t_0 , when 5 mL of the solvent was injected into the optical cell. Pictures were taken starting at the time when the O-ring was positioned at the center of the optical cell, t_{pp} . Images were taken every 20 seconds for the first four minutes, followed by intervals of 10 minutes until the O-ring volume converged, as determined by image processing. The O-ring was determined to be converged when its volume remained invariant over the last 30 images. Once the O-ring volume had converged, images were processed to determine the cross-sectional area of the O-ring as a function of time. O-ring area was linearly extrapolated from t_0 to t_{pp} . Volume swell was calculated using the equation shown in Fig. 2, which assumes isotropic swelling [4]. In this equation, μ is the volume swell (%), A_{ij} is the cross-sectional area of current image, and A_0 is the cross-sectional area at t_0 . The final volume swell was taken as the average volume swell of the last 30 images.

Results and Discussion

The volume swell dependence on isomer variation within molecular group/carbon number (MG/C#) bins has been investigated. Three constitutional isomers (*n*-, *iso*-, and *tert*-butylcyclohexane) and two stereoisomers (*cis*- and *trans*- decalin) were studied. Fig. 2 shows the volume swell of these molecules plotted against aromatic concentration with molar volumes listed in the plot. Volume swell for 11 conventional jet fuels is also depicted to establish the conventional swell range. Volume swell for the isomers increased with decreasing molar volume except for *n*-butylcyclohexane, which outswelled

isobutylcyclohexane. The constitutional isomers swelled an average of $4.0 \pm 0.8\%$, with the standard deviation representing 20% of the average swell value. The stereoisomers swelled an average of $15.2 \pm 3.8\%$, with the standard deviation representing 25% of the average swell value. These standard deviations illustrate the potential for isomers to influence the GCxGC prediction methodology, which depends on minimal variance within MG/C# bins. The constitutional isomers swelled in the order: low branching < no branching < high branching. This order requires further validation before it can be generalized to additional molecules. These results also indicate that decalin has the potential to significantly increase volume swell compared to substituted monocycloalkanes of the same carbon number.

Fig. 3 depicts the composition and volume swell of the fuels used for this report. Fuel compositions were measured by GCxGC at UDRI. Fuels below the red line, which represents the ASTM D1655 25% upper aromatic limit, are of interest. A large amount of the composition space below the red line remains to be measured. The 8% lower aromatic limit, from ASTM D7566, is represented by the green line. Conventional fuels are represented by circles and SAFs are represented by triangles in Fig. 3. Of the five SAFs screened, four fell below the conventional swell range and one fell above it. Underswelling is somewhat surprising given that three of the SAFs with low swell values had high concentrations of cycloalkanes. H29, the SAF that overswelled, is represented by the blue pentagon. H29 swelled at 16.1%, about three times the magnitude of its neighboring molecules. The high swell of H29 indicates that there may be molecules that swell disproportionately high within MG/C# bins.

A neural network was trained using the automatic machine learning (AutoML) feature in H2O Flow, an open-source machine learning software. Volume swell for the 19 fuels served as the dependent variable and the GCxGC compositional data served as the training features. A total of 80 MG/C# bins were used to train the model, with the composition represented by the volume percentage of each bin in the fuel. The following molecular groups were contained in the bins: aromatics, diaromatics, cycloaromatics, iso-alkanes, *n*-alkanes, monocycloalkanes, dicycloalkanes, tricycloalkanes, and alkenes. Predicted versus actual volume swell values are depicted in Fig. 4. The neural network achieved a five K-fold cross-validated mean absolute error (MAE) of 1.9%, which is 30% of the average volume swell. The high MAE is largely due to underprediction of H29; without H29, the MAE was 1.2, or 19% of the average swell value. The accuracy of the neural network can be improved by including additional fuels to train the model. Different analytical techniques such as GC-MS or GCxGC-VUV can be used in addition to GCxGC to identify high-swelling compounds.

Figures

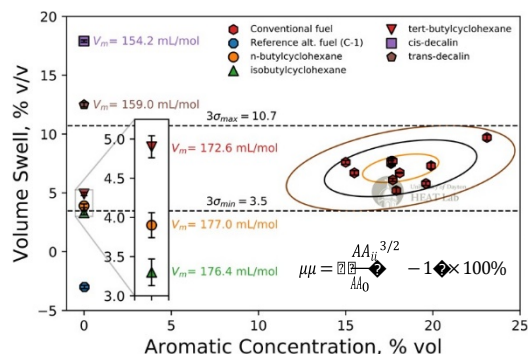
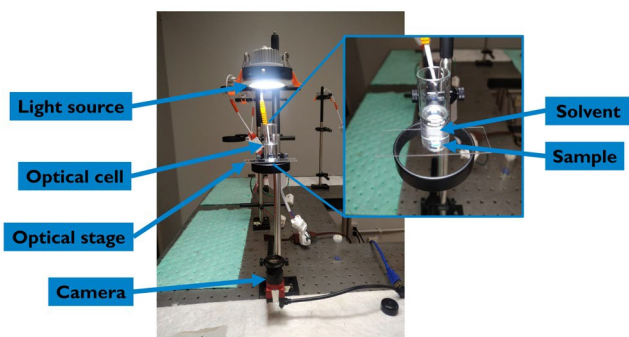


Fig. 1 (left). Diagram of the optical dilatometer used in this study.

Fig. 2 (right). Volume swell versus aromatic concentration for constitutional isomers and stereoisomers.

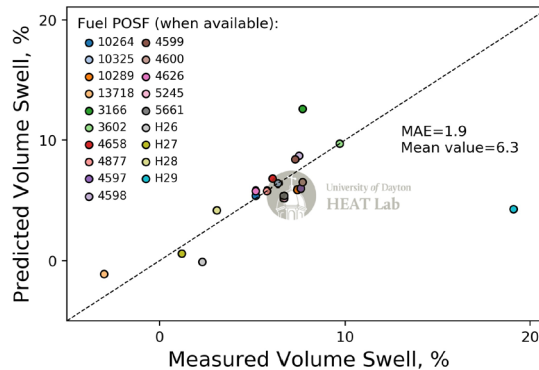
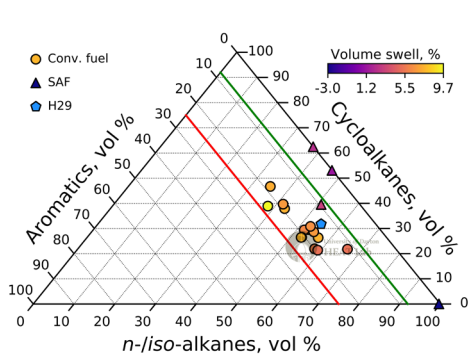


Fig. 3 (left). Triplot representing the composition and swell of fuels used in this study.

Fig. 4 (right). Predicted versus measured volume swell for neural network predictions.

Acknowledgments

The authors would like to thank the Ohio Space Grant Consortium for their support, as well as Dr. John Graham of UDRI for his help with materials procurement and experimental/theoretical input.

References

- [1] Klingshirn CD, DeWitt M, Striebich R, Anneken D, Shafer L, Corporan E, et al. Hydroprocessed Renewable Jet Fuel Evaluation, Performance, and Emissions in a T63 Turbine Engine. *J Eng Gas Turbines Power* 2012;134.
- [2] Kosir S, Heyne J, Graham J. A machine learning framework for drop-in volume swell characteristics of sustainable aviation fuel. *Fuel* 2020;274. <https://doi.org/10.1016/j.fuel.2020.117832>.
- [3] Yang Z, Kosir S, Stachler R, Shafer L, Anderson C, Heyne JS. A GCxGC Tier α combustor operability prescreening method for sustainable aviation fuel candidates. *Fuel* 2021;292. <https://doi.org/10.1016/j.fuel.2021.120345>.
- [4] Graham JL, Striebich RC, Myers KJ, Minus DK, Harrison WE. Swelling of nitrile rubber by selected aromatics blended in a synthetic jet fuel. *Energy and Fuels* 2006;20:759–65. <https://doi.org/10.1021/ef050191x>.

Experimental Evaluation of a Two-Actuator Beam System for the Development of Effective Vibrotactile Feedback in Large Touch Displays

Student Researcher: Taylor W. Mason

Advisor: Jeong-Hoi Koo

Miami University

Department of Mechanical and Manufacturing Engineering

Abstract

The vibrational sensation felt on the surface of a screen, known as vibrotactile feedback, is a key feature of many modern touch displays. This sense of touch enhances user feedback and improves object usability. Most actuators are primarily used for small displays in hand-held devices to effectively create touch feedback. However, the current actuators are not suitable for large touchscreen displays because they cannot create sufficiently large vibrotactile sensations. Devices such as tablets, information kiosks, and automotive dashboard panels are examples of large touchscreens that typically lack the capability of generating vibrotactile feedback for the users. Using a newly developed actuator meant for large touch displays, this research studies its effectiveness in a two degree of freedom actuator-beam system. The system was excited at its resonant frequencies as well as other prominent frequencies found in experimental testing. These results showed that the vibration in the system could be significantly changed based on the number of actuators being activated and the excitation frequency. In future studies, this will be applied to a multi-actuator-plate system to create a dynamic haptic experience that can be applied to large touch screens.

Introduction

As touchscreens are becoming increasingly popular, larger devices are getting their interfaces changed to become touch-oriented. Many small touchscreen devices utilize haptic actuators to generate vibrations on the surface of their screens which provide tactile feedback to the users, known as vibrotactile haptic feedback. This feedback creates engaging user interfaces without the need for mechanical buttons [1]. Studies have shown that the implementation of such haptic modules in touch displays increases input speed and input accuracy, as well as tactile feedback and user satisfaction [2]. While this feedback is quite common in small devices, most currently used haptic actuators fail to effectively provide vibrotactile feedback in large displays. Some examples of large touchscreens that typically lack the capability of generating vibrotactile feedback for the users include tablets, information kiosks, and automotive dashboard panels.

A new haptic actuator based on electrostatic actuators was developed for use in large touch displays. Unlike typical electrostatic actuators, this actuator utilizes a moving mass and two electrodes to increase vibration intensity. The mass is connected to a base using thin radial beam springs. On either side of the mass is a copper electrode, which creates an electrostatic attractive force on the mass. To ensure the forces from the electrodes do not interfere, the electrodes are activated in an alternating fashion. This ensures maximum oscillation of the mass which increases vibration intensity. The exploded view and working principle of the actuator can be seen below in *Figure 1*. This actuator was shown to be effective in a previous study that tested its single degree of freedom performance [3]. The actuator produced a maximum peak to peak acceleration (a metric for vibrational output) of 14.32 g-forces in the single degree of freedom testing and a maximum of 3.88 g-forces in the preliminary two degree of freedom panel

testing. These results show promising potential for the use of the new electrostatic resonant actuator in generating vibrotactile feedback for large touch displays.

To further study the new actuator and work towards applying it to large touch displays, a preliminary two actuator beam system was created. This study proposes using different actuation frequencies, time offsets between the actuators, and actuator vibration amplitudes as a means to control the vibration in the beam. This knowledge will then be applied and extended to a large touchscreen plate with multiple actuators. *Figure 2* shows future applications of this study, with 4 actuators being applied to a large touch display. Applying the results and knowledge gained from the actuator-beam study, the vibrotactile feedback performance will be evaluated and controlled in the large touchscreen displays.

Project Objectives

The primary goal of this research was to evaluate the vibrotactile performance in a two-actuator-beam system. To accomplish this goal, vibrational testing was done with the actuators to determine their maximum steady-state peak to peak acceleration and resonant frequency. The results were plotted and interpreted to see how different actuator activation conditions affected the vibration response of the system.

Methodology Used

The first step was to identify the critical parameters of the actuator-beam system such as resonant frequencies and damping ratio. The system can be seen in *Figure 3*. This system uses a thin 1x12-inch aluminum beam with an actuator supporting each end. This beam was marked into 0.5-inch segments to ensure consistent accelerometer placement in the experiments. The resonant frequencies were found by inputting a sine sweep function into a single actuator and using an accelerometer to record the response. The sweep covered the range of 10-300 Hz over 25 seconds. Using the accelerometer actuator's input and accelerometer's output, the frequency response function of the beam was calculated. The frequency response function showed the resonant frequencies of the system and could also be used to estimate the damping ratios using the half-power method.

After the system identification was complete, an experimental study was conducted to measure the vibration in the beam under different actuator activation conditions. Using a custom controller, the frequency, start delay, and activation duration of each actuator could be independently controlled. These parameters were studied in different combinations to see their effect on vibrotactile performance in the beam. In the first experiment, a single actuator was activated and the acceleration at resonant frequencies was determined in an attempt to find unique mode shapes in the response. The next experiment was identical, but two actuators were activated simultaneously.

Results Obtained

After plotting the frequency response function, the resonant frequencies in the range of interest for this system were determined to be 171.4 Hz and 202.2 Hz. Using the half-power method, the damping ratios for these modes were estimated as 0.0034 and 0.0031.

The system was excited at the resonant frequencies by a single actuator and the peak to peak acceleration was recorded every half-inch along the beam. These frequencies produced unique acceleration responses, as seen in *Figure 4* below. Based on the results, the response in the beam varies greatly depending on location and frequency. Each frequency results in different high and low acceleration points, making exciting the beam at either frequency useful depending on what haptic sensation is wanted to be achieved at a given location.

In the next experiment, both actuators were used simultaneously at the same frequency. Similar to the last experiment, the acceleration was recorded along the beam for each testing case. The actuators were first driven at the resonant frequencies, but this proved to be ineffective when using both actuators simultaneously. The frequency was experimentally changed until new peak frequencies were found using both actuators, which occurred at 181 Hz and 216 Hz. The results were plotted together in *Figure 5*. When finding the resonant frequencies of the beam a sine sweep function in a single actuator was used, which may not represent the resonant frequency when using both actuators. This likely accounts for the difference in resonant frequency found when using both actuators compared to a single actuator.

Significance and Interpretation of Results

Compiling the results, findings showed the vibration response in the beam can be controlled by changing the number of actuators used and the frequency at which the actuators were driven. *Figures 6* and *Figure 7* compare the vibration response when using one or both actuators excited at 171 Hz and 181 Hz, respectively. By activating a single actuator then later activating the second actuator, the vibration response of the beam can be increased or decreased depending on the frequency. This effect can be seen in reverse such that activating both actuators then reducing to just one actuator also causes an increase or decrease in vibration response (depending on frequency). Therefore, results confirmed that this process can be used to control the beam's vibration response depending on the desired haptic effect.

Future studies will test activation of the actuators at different frequencies and time delays to see their effect on the system's vibration. This will then be applied to a four actuator-plate system as seen in *Figure 2*. Using a combination of actuators with different activation parameters, the system's vibration will be controlled to create a dynamic vibrotactile haptic feedback experience in large touch displays.

Figures/Charts

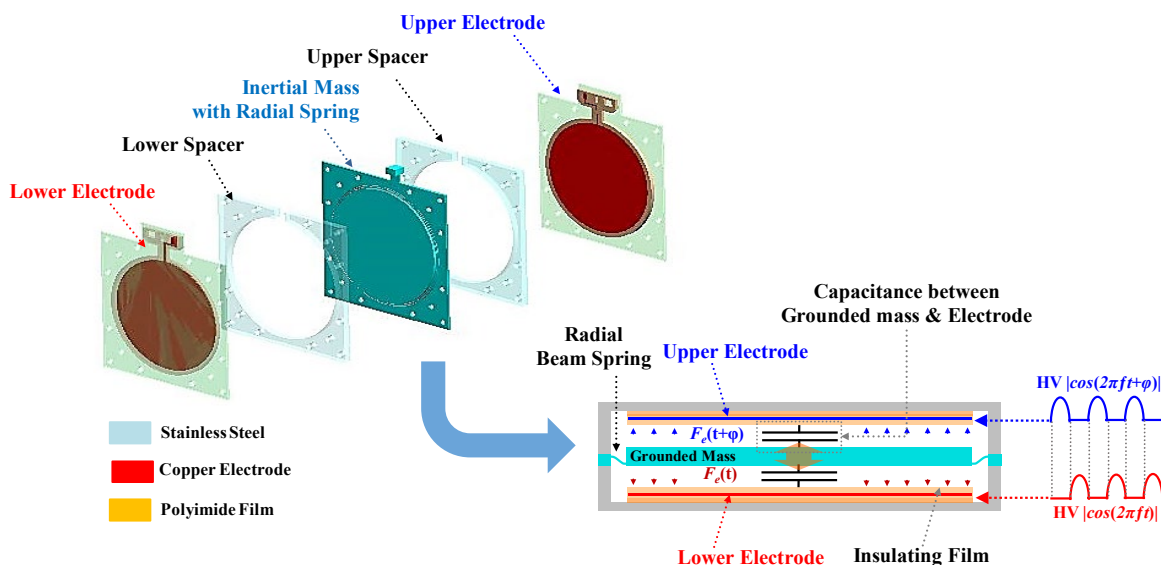
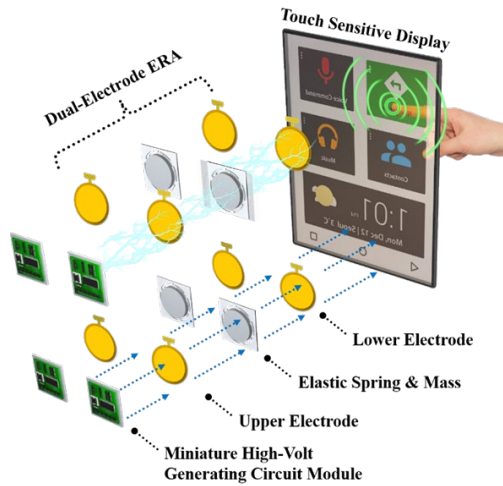
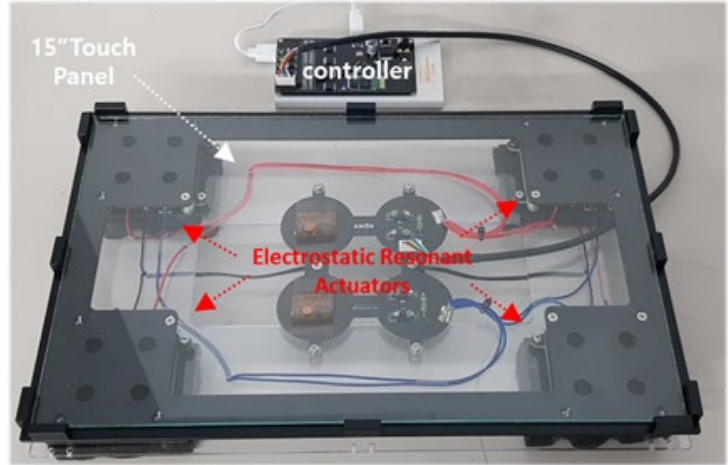


Figure 1. Exploded view model and working principle design of the proposed ERA module.



(a)



(b)

Figure 2. An illustration showing: (a) the concept of multiple actuators implemented in a touch-sensitive display; (b) 4 actuators applied to a glass plate system

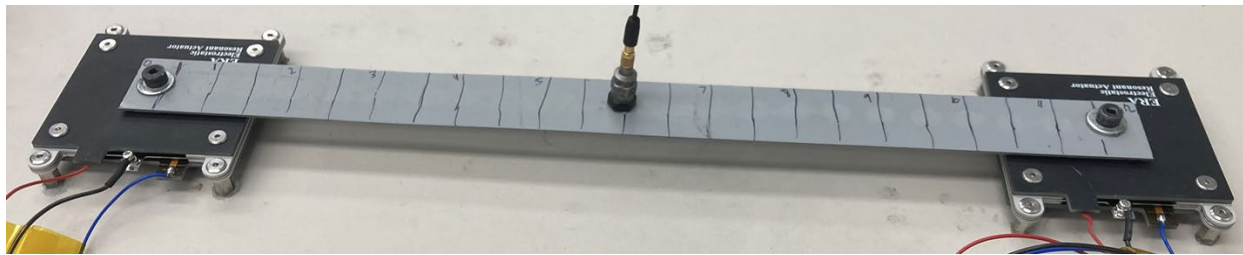


Figure 3. Actuator-beam system uses for preliminary vibration testing.

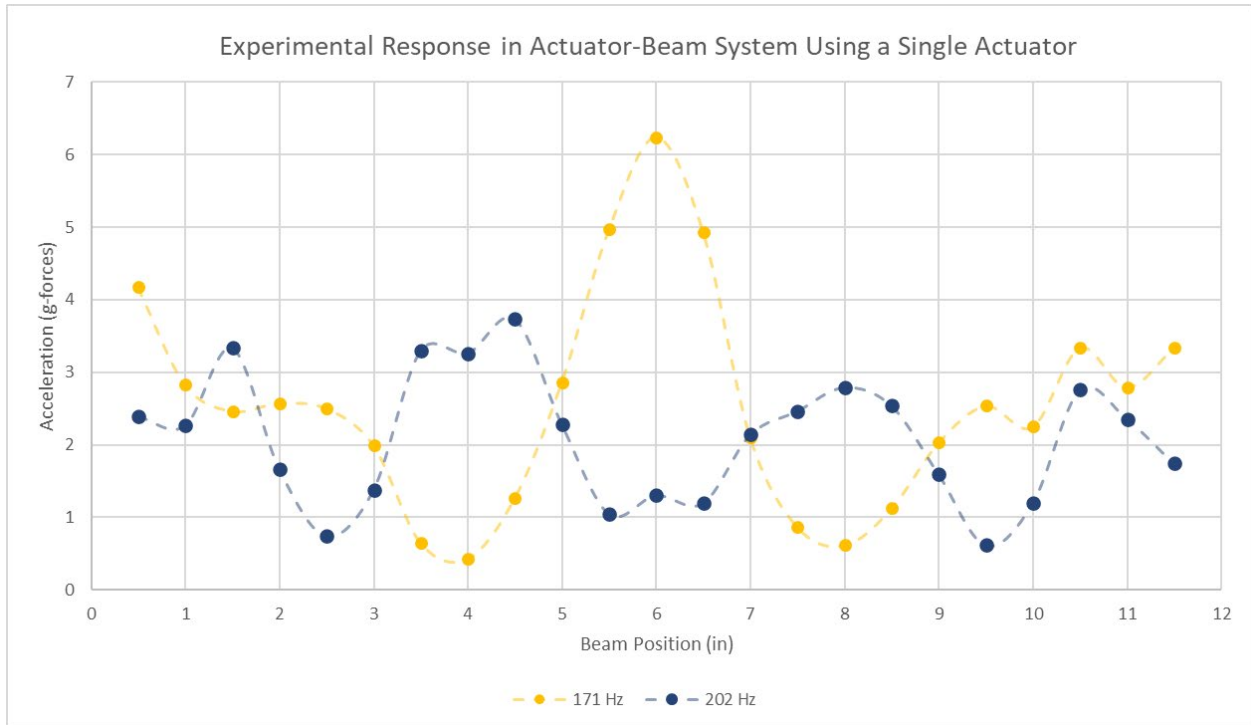


Figure 4. Experimental Response in the actuator-beam system using only the left side actuator.

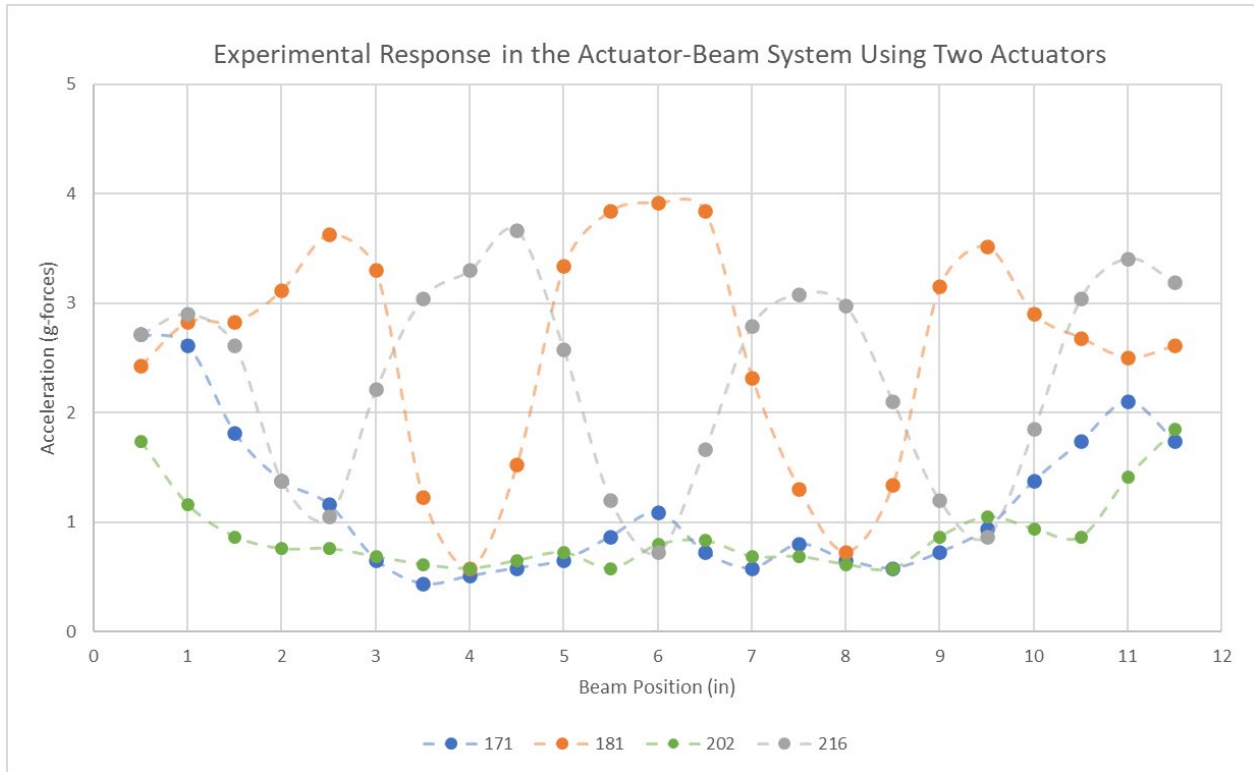


Figure 5. Experimental response in the beam using both actuators at the same frequency.

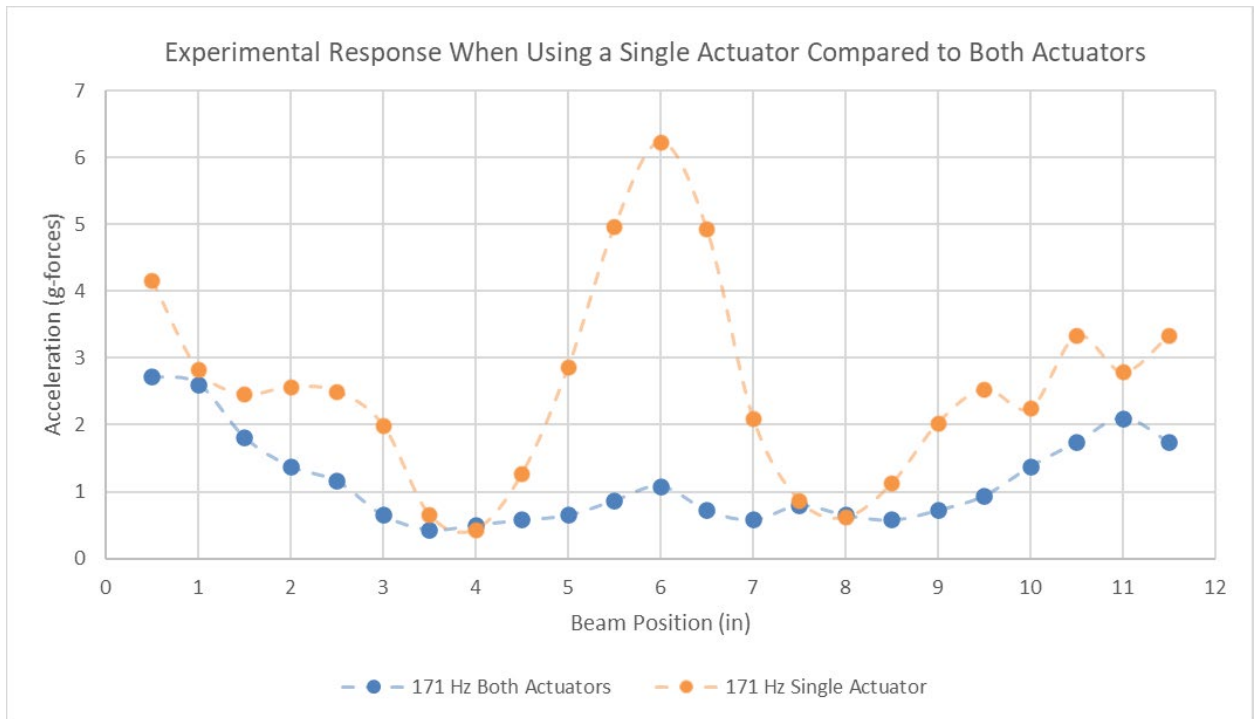


Figure 6. Experimental response in the beam using one actuator at 171 Hz compared to using both actuators at 171 Hz.

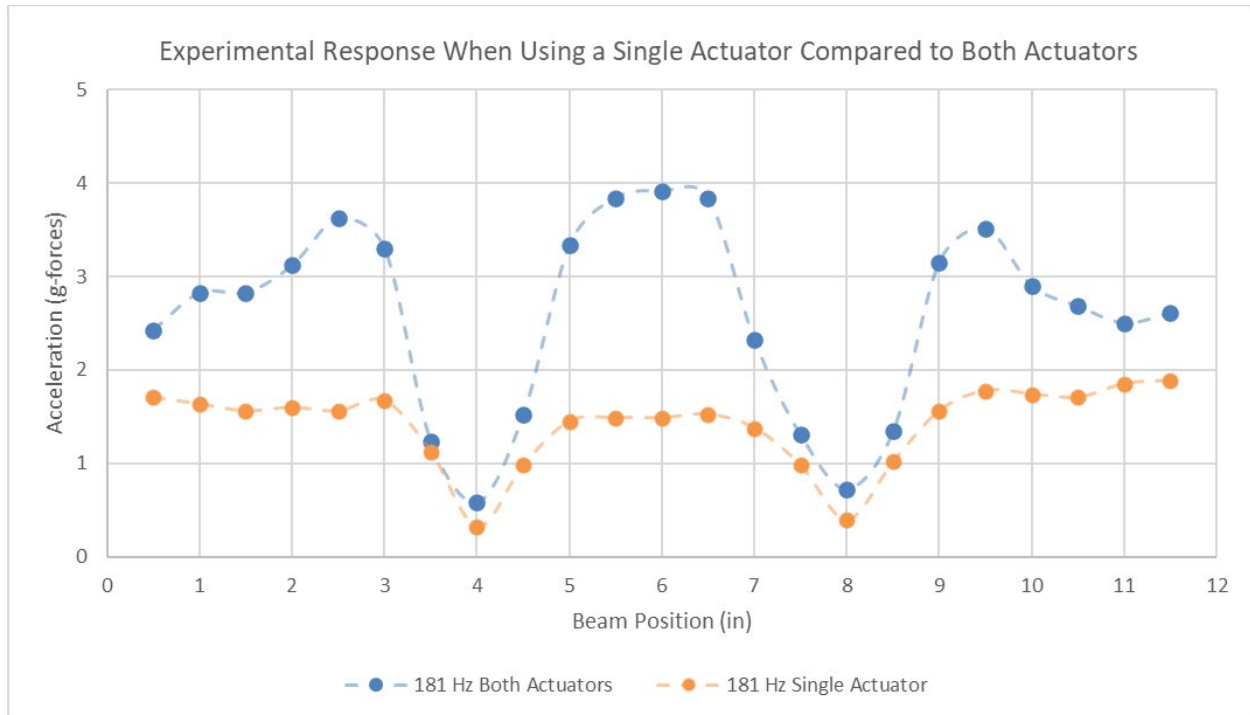


Figure 7. Experimental response in the beam using one actuator at 181 Hz compared to using both actuators at 181 Hz.

Acknowledgments and References

I would like to thank OSGC for providing this experience and making this research possible. I'd also like to thank Dr. Jeong-Hoi Koo for advising and assisting me with this research, as well as teaching me the research process.

1. M. Silfverberg, "Using Mobile Keypads with Limited Visual Feedback: Implications to Handheld and Wearable Devices," *Mobile HCI 2003*, ed. L. Chittaro, LNCS 2795: 76-90 (2003).
2. Banter, Bruce. "Touch Screens and Touch Surfaces Are Enriched by Haptic Force-Feedback." *Information Display*, vol. 26, no. 3, 2010, pp. 26–30.
3. T. Mason, J.-H. Koo, Y.-M. Kim, and T.-H. Yang, "Experimental Evaluation on the Effect of Electrode Configuration in Electrostatic Actuators for Increasing Vibrotactile Feedback Intensity," *Applied Sciences*, vol. 10, no. 15, Art. no. 15, Jan. 2020, doi: 10.3390/app10155375.

A Novel Characterization of Friction Stir Welds under Active Temperature Control

Student Researcher: David L Pearl

Advisor: Dr. Carter Hamilton

Miami University College of Engineering and Computing
Department of Mechanical and Manufacturing Engineering

Abstract

Aluminum alloys 2024-T4 and 7075-T6 were joined by FSW under active PID temperature control at different set points. Analysis of precipitation and local hardness was estimated through use of PALS, thermal flow modeling, and tensile testing. Comparing temperature profiles from the simulation with PALS profiles in cross-section enabled a correlation between precipitation and expected local hardness, further explaining the precipitation process in a FSW. Tensile failures occurred in the stir zone, due to design of tensile specimens, and correlated with a dip in positron lifetimes in the center of the SZ. Close correlation between PALS maximums and minimums, and regions on the temperature profiles leads to inferences regarding precipitate formation. SEM fractography confirms ductile failures in the SZ. Results were limited to 2024 due to limitations on PALS collection in 7075.

Project Objectives

The study found a distinct gap in literature for the application of PALS analysis to FSW, and specifically to active temperature control of the process. Applying temperature control in this manner enables comparison of the process at different temperature levels, against an uncontrolled, constant-parameter trial. The effectiveness and potential for using an active temperature control of the process was studied to observe the effects that controlling the process would have.

Methodology Used

Welds were completed in collaboration with the Friction Stir Research Laboratory (FSRL) at Brigham-Young University in Provo, Utah. Similar alloy welds in 2024-T4 and 7075-T6 were chosen in 3 levels: low control (LC), high control (HC), and an uncontrolled trial (UC). Temperatures for each level were chosen based on literature, with the goal of completing a low temperature limit for the tool and setup. One tool was used, and the controller was a simplified PID controller developed by FSRL for their other research into temperature controllers and modeling of FSW. Most studies measure the process temperature at a location 5-10 mm away from the weld centerline, resulting in inaccuracies in defining the absolute maximum weld temperature. These inaccuracies were avoided by using a tool with a thermocouple hole bored from the shank, ending within millimeters of the end of the tool. The thermocouple was mounted on the spindle and connected wirelessly to a telemetry system. Thus, the PID controller received an accurate picture of the system with short delay, enabling an accurate control of the system by tuning the spindle speed. Once completed, the welds were analyzed for defects by spectral analysis, and subjected to tensile testing in the perpendicular direction, SEM fractography, and samples were sent to another collaborator for PALS analysis. A numerical model was also developed and helped complete the picture of the process by providing cross-sections of the weld temperature under steady-state.

Results Obtained

Difficulties with worldwide pandemic restrictions limited the results received from overseas collaborators in Krakow, Poland. The student researcher had planned to accompany the specimens and assist in PALS testing, as well as creating microhardness profiles and analyzing precipitates through TEM.

However, the student was not able to travel, and as labs closed across the world, luckily received the PALS profiles for all three of the 2024 trials. Combined with the temperature cross-section and tensile testing, a more complete picture can be generated of the zones and precipitation within the 2024 weld. Without a PALS profile, analysis of the 7075 experiments is much less conclusive. Temperature cross-sections and tensile testing are helpful but form a far from complete picture of the precipitation in the weld.

Significance and Interpretation of Results

2024

Starting with PALS (S-parameter) data, the 2024 cross-section closely matches an expected microhardness cross-section. This agrees with literature [1]. By defining weld zones such as Stir Zone (SZ), Thermo-Mechanically Affected Zone (TMAZ), Heat Affected Zone (HAZ), and Base Material (BM) based on patterns from literature, correlations with precipitate formation, dissolution, and growth can be drawn. For example, while the high temperature SZ is expected to show complete dissolution and grain refinement, the TMAZ shows increased hardness even without complete dissolution. Slight deformation and an increased precipitate density likely caused this increase. The HAZ is most interesting, as it classically is the weakest region, showing tensile failures [2]. Without deformation to decrease precipitate size, the microstructure exhibits that of overaging, with larger precipitates and thus fewer barriers to failure. According to the PALS plot, the LC trial will have the strongest SZ, and this is confirmed in the tensile testing, where the LC trial shows the highest average UTS.

7075

Without PALS, conclusions are necessarily much looser in 7075. Starting with the temperature plots and comparing to 2024, the dissolution and precipitate formation temperatures are much lower compared to the process temperature, enabling all three trials to exceed dissolution temperatures. However, the HAZ would be expected to extend further, as the region of elevated temperature likely would extend. The TMAZ would be the most interesting zone to examine under PALS or microhardness, as the temperature would be much higher (relatively) at the edge of the SZ, so increased precipitate formation would likely occur, perhaps strengthening the TMAZ even further. In tensile testing, the UC trial showed a lower standard deviation across the length of the weld than either of the controlled trials. This points to strain rate as a potentially relevant variable in the process, as the UC trial could also be defined as having constant spindle speed, rather than constant temperature.

Figures/Charts

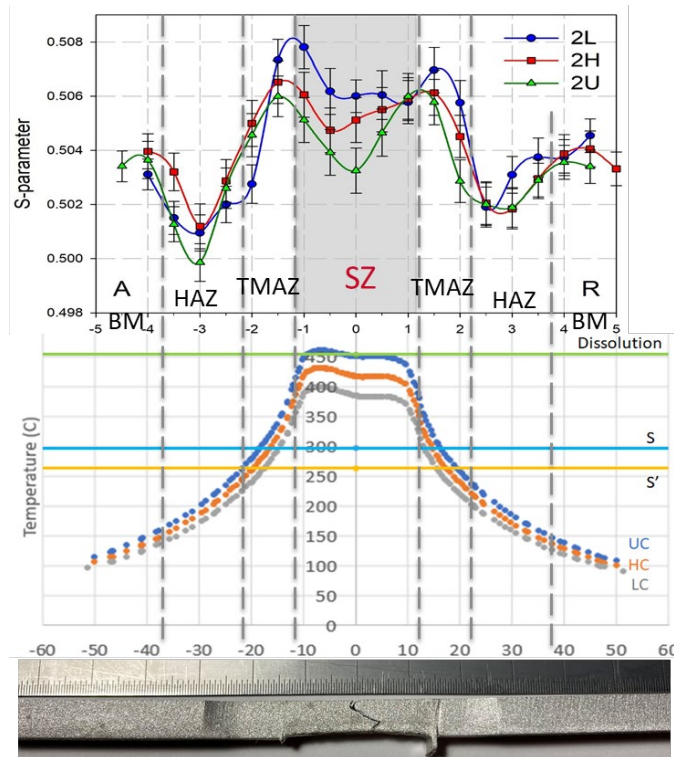


Figure 1. Comparison of weld locations in PALS, temperature, and tensile testing results- 2024.

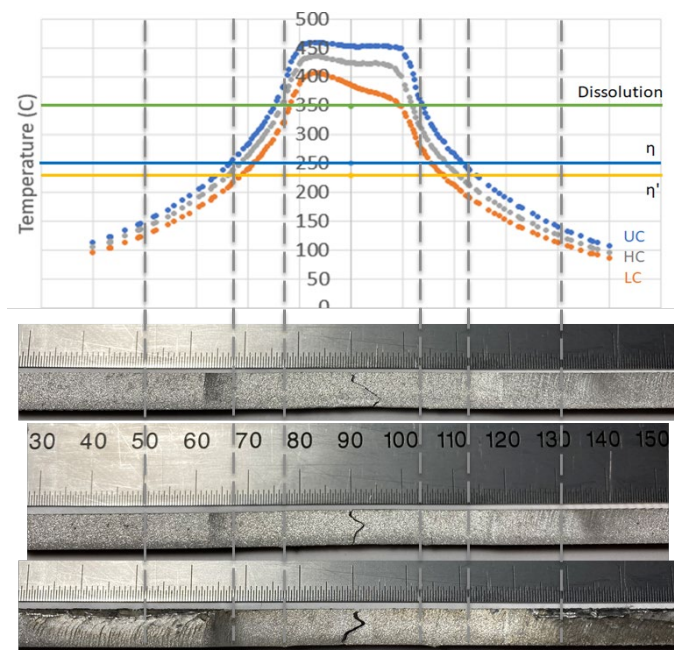


Figure 2. Comparison of weld locations in temperature and tensile testing results- 7075.

Acknowledgments

The author would like to thank his adviser, Dr. Carter Hamilton, for continual support and guidance throughout the length of this project, as well as support and assistance from Mr. John Hunt and Dr. Yuri Hovanski at the FSRL at BYU. In addition, the rest of the MME department at Miami University have been incredibly helpful in completing any testing or answering any questions regarding this project. Finally, the author is thankful for the help of his family and friends, for supporting him through the duration of this project and assisting even when they did not understand the purpose.

References

- [1] H. G. Priesmeyer and G. Bokuchava. Positron annihilation as an additional source of information about plastic deformation in structural materials. *Materials Science and Engineering A*, 437, pp. 54-59. 2006.
- [2] H. J. Liu, J. C. Hou, H. Guo. Effect of welding speed on microstructure and mechanical properties of self-reacting friction stir welded 6061-T6 aluminum alloy. *Materials and Design* 50 (2013). 872-878.

Scholars

Toward DLP 3D-Printed Soft Robots: A Stereo DIC Investigation of the Mechanics of Ultra-Stretchable Self-Healing UV-Curable Photopolymers

Student Researcher: Joseph G. Beckett

Advisor: Dr. Robert L. Lowe

University of Dayton

Department of Mechanical and Aerospace Engineering

Abstract

Digital light processing (DLP) additive manufacturing (AM) is a recent development in 3D printing where full layers of photo-curable polymers (photoresins) are irradiated and cured with projected ultraviolet (UV) light to create a three-dimensional part layer-by-layer. Recent breakthroughs in polymer chemistry have led to a growing number of ultra-stretchable UV-curable elastomeric photoresins, some capable of over 450% elongation at fracture. Coupled with the practical manufacturing advantages of DLP AM, these novel elastomeric photoresins are compelling candidates for numerous exciting applications, ranging from regenerative medicine (e.g., vascular grafts and tissue scaffolds) to soft robotics (the focus of this research). In general, soft robotics refers to the use of “soft” materials (i.e., those with a high degree of flexibility, stretchability, and conformability, such as natural rubber) in robotic devices, producing conformal mechanisms that safely interact with humans and are adept at grasping and manipulating assorted objects.

To advance the role of DLP AM in this novel and promising technological space, a fundamental understanding of the mechanical behavior (i.e., deformation and fracture) of UV-curable elastomeric materials over a broad range of loading conditions is requisite. At present, however, this remains an open problem. Thus, the research described herein takes a first step toward addressing this critical technological gap by (a) designing and implementing a stereo digital image correlation (DIC) system optimized for large-deformation soft materials testing; (b) conducting an inaugural experimental test program on a novel self-healing ultra-stretchable UV-curable elastomer synthesized at the Air Force Research Laboratory (AFRL); (c) using the resulting mechanical test data to develop working analytical and computational models that facilitate the design, optimization, control, and virtual testing of a prototype soft robot; and (d) validating the models using 3D DIC strain measurements of a prototype soft robotic actuator.

Project Objectives

The scope of this research is to design and implement a custom stereo digital image correlation (DIC) system optimized for testing large-deformation soft materials, a class of materials that have presented challenges to traditional DIC measurement techniques (e.g., pattern breakdown, significant de-correlation from reference image) [1]. DIC is a game-changing optical measurement technique that analyzes a series of images to track the motion of a high-contrast speckle pattern applied to the surface of a test specimen undergoing deformation [2]. Stereo (or three-dimensional) DIC utilizes a series of synchronized images from a pair of cameras to produce high-precision 3D surface strain and displacement fields [3]. These full-field deformation measurements are substantially richer than those obtained from traditional

extensometers and strain gauges, which only provide an average strain over a given length or the strain at a single point.

Upon completion, this stereo DIC system used in combination with an extended-height Instron load frame will enable a fundamental understanding of the deformation and fracture of novel self-healing ultra-stretchable UV-curable elastomers synthesized at AFRL. The resulting test data will be used to create robust constitutive models and finite-element analysis tools that will later be validated through 3D DIC measurements of a prototype soft robotic actuator.

Methodology Used

To effectively design a cost-effective stereo DIC system, a literature review was conducted on stereo DIC and existing techniques for large-deformation DIC. The focus was placed on stereo DIC because of its ability to reduce errors from out-of-plane motion, misalignment, vibrations, and heat waves, which are all common sources of error in 2D DIC studies [4]. Furthermore, the ability to conduct component-level analyses is another important advantage of 3D DIC. The technical DIC knowledge gained from the literature allowed baseline specifications of the main components of the system (i.e., cameras, lenses, sample preparation supplies) to be determined. Specifications that would limit the system's ability to overcome the challenges posed by large-deformation DIC of soft materials were adjusted to better address known challenges. These optimized system requirements were used to select suitable components for the system. Minor components of the system (i.e., mounting equipment, lighting) were selected to meet the needs of the other components. At this point, funds were acquired, and the system was purchased.

As the components were selected, various open-source DIC codes were researched. Trial DIC analyses were conducted on sample data from the Society for Experimental Mechanics DIC Challenge data to observe the effects of various DIC analysis parameters on the spatial resolution and noise levels of the results. Soon after, while lab access was restricted due to the COVID-19 pandemic, a prototype 2D DIC testing apparatus was constructed and gradually refined to produce preliminary 2D DIC images. The prototype system was comprised of a vise, clamps, an incandescent lamp, and wooden supports to secure a cell phone camera above the vise. Samples of elastic household materials were tested to simulate the underlying conditions needed for the operation of a successful laboratory-scale DIC system. Image series from these tests were processed using Ncorr, an open-source 2D DIC software with proven accuracy [5]. Lateral strain and displacement fields from a test using the prototype system are shown in Figs. 1 and 2, respectively.

Results and Discussion

The insights gained from the literature review and prototype DIC system enabled the creation of an operational stereo DIC system for large-deformation soft materials testing (Fig. 3). The machine vision cameras selected for the system use the Sony IMX267 sensor. This sensor utilizes recent breakthroughs in CMOS imaging technology to offer a global shutter, high quantum efficiency, low noise, and square pixels which makes it well suited for DIC [4]. The sensor's wide aspect ratio also makes this sensor a strong candidate for large-deformation DIC. The 8.9 MP sensor allows for high resolutions along the longitudinal axis of strain during tensile testing while the wide aspect ratio maximizes the portion of the frame that contains the deforming sample. Tensile tests were emphasized during the design process because large-deformation tensile testing requires large fields of views to capture elongating samples.

Increased field of views decrease the resolution of the region of interest which negatively impacts the spatial resolution of the strain mapping.

Edmund Optics High Performance (HP) Series 35 mm fixed focal length lenses were selected to provide sufficient resolution and to prevent vignetting on the large sensor. Low distortion was not a primary concern during the lens selection because stereo calibration of the cameras corrects a vast majority of the distortion error. For the system lighting, LED panels with diffusers were implemented to provide uniform, flicker-free light. LEDs also minimize heat emitted from the light source, which is known to distort DIC images [4]. For image patterning, ink stamps will be utilized to provide a pattern that penetrates the sample. This will prevent the pattern from detaching from the surface of specimens at large strains or higher strain rates.

The Digital Image Correlation Engine (DICE) was selected from among many candidate open-source DIC software packages for its ability to conduct 2D and 3D DIC analyses as well as its robust documentation, proven accuracy, and effective virtual strain gauge and extensometer tools [6]. Initial procedures for using DICE and the machine vision camera software were drafted as a part of this project, and will be actively refined with continued use.

For future development of this research, the system will be carefully validated and verified using error values provided by DICE in combination with comparing DIC strain readings to those provided by a physical extensometer. Subsequently, an Instron 3365 extended-height load frame along with the stereo DIC system will be used to conduct a series of mechanical tests of a novel AFRL-synthesized self-healing photopolymer under a wide variety of loading conditions (e.g., uniaxial tension, uniaxial compression, pure shear, etc.). These tests will be conducted at varied strain rates, and some will be carried out under cyclic loading. The resulting data will be used with in-house software to create robust constitutive models and finite-element analysis (FEA) tools that will be validated using 3D DIC surface strain measurements of a prototype soft robotic actuator.

Figures



Figure 1. 2D strain field projected onto deforming sample (prototype DIC system).

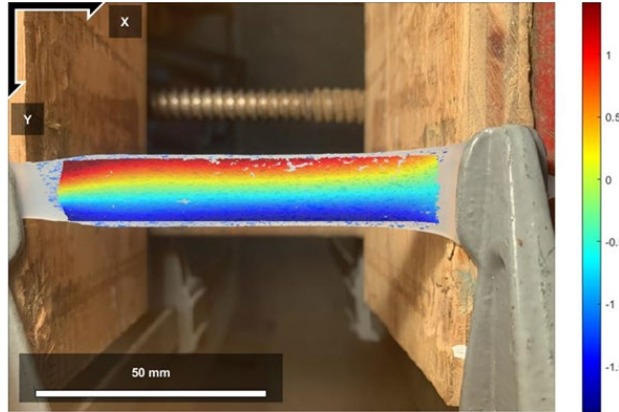


Figure 2. 2D displacement field projected on deforming sample (prototype DIC system).

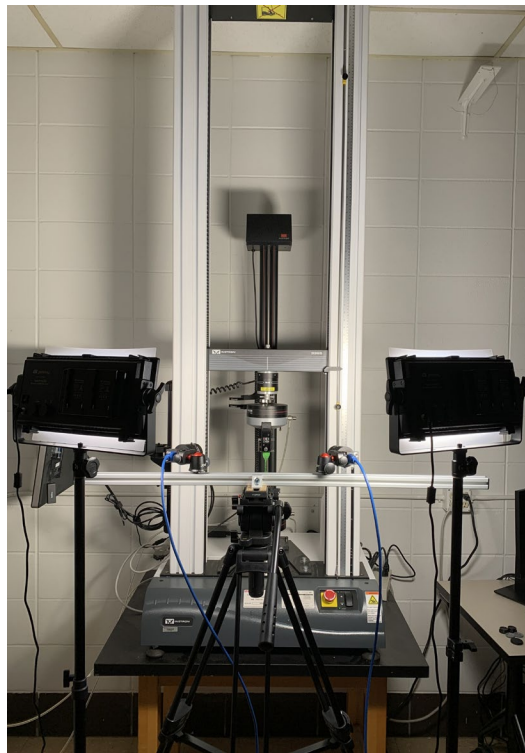


Figure 3. Operational laboratory-scale stereo DIC System optimized for large-deformation soft materials testing.

Acknowledgments

The author would like to thank the Ohio Space Grant Consortium, the University of Dayton School of Engineering, the University of Dayton Honors Program, and the Berry Summer Thesis Institute for supporting this work and funding a portion of the stereo DIC system. The author would also like to thank Dr. Robert Lowe and the other Behavior of Advanced Materials and Structures (BAMS) Lab researchers for their support of this work.

References

1. Z. Tang et al., Large deformation measurement scheme for 3D digital image correlation method. *Optics and Lasers in Engineering* **50**, 122–130, 2012.
2. T.C. Chu et al., Applications of digital-image-correlation techniques to experimental mechanics. *Experimental Mechanics* **25**(3), 232–244, 1985.
3. P.F. Luo et al., Accurate measurement of three-dimensional deformations in deformable and rigid bodies using computer vision. *Experimental Mechanics* **33**(2), 123–132, 1993.
4. E.M.C. Jones et al., A good practices guide for digital image correlation. International Digital Image Correlation Society, 2018.
5. J. Blaber et al., Ncorr: Open-source 2D digital image correlation Matlab software. *Experimental Mechanics* **55**, 1105–1122, 2015.
6. Turner et al., *Digital Image Correlation Engine*. Computer software. Version 00. USDOE, 2015.

Alternative Foam Insulation for Space Applications

Student Researcher: Brian Berry

Advisor: Dr. Rydge Mulford

University of Dayton
Mechanical Engineering

Abstract

This research focuses on alternative insulation materials for space crafts. I obtained polyurethane foam to measure the thermal conductivity and compare this to current space standards.

Objectives

My objectives were to measure the thermal conductivity of tannin foam and image the pore structure. The tannin foam initially intended to be tested was not possible to obtain due to COVID-19, the lab at NASA Goddard which originally planned to supply the foam is not operating during COVID. I adjusted my objectives to test thermal conductivity of another insulator. Tannin is a natural material based from the bark of a tree (Celzard, 2014), if the material is a suitable insulator then the prospect of producing space craft materials in space would become feasible. The thermal conductivity of the foam would inform us if the foam is a good enough insulator to be utilized in space. Imaging the foam would allow us to examine the microstructure of the pores and with alterations in the production of the foam we could adjust the pores to enhance the thermal conductivity. Since we were not able to obtain tannin foam samples within our research period, I ran tests to find the thermal conductivity of another foam. After measuring polyurethane foam, we could reproduce the tests using the tannin foam in the future.

Methodology

Using a KD2-Pro instrument with a KS1 instrument needle I measured the thermal conductivity of the polyurethane foam. Completely inserting the needle into the ¼" thick edge of the foam making sure the needle is not exposed to air and parallel to the material. I took 14 different measurements, measuring on all four sides and 7 different locations, 2 measurements at each location.

Results Obtained

Using the KD2-Pro I obtained a thermal conductivity between the range $0.0519-0.0605 \frac{W}{m \cdot K}$ for the polyurethane foam. The average thermal conductivity from the sample was $0.0542 \frac{W}{m \cdot K}$, with a standard deviation of $0.00241 \frac{W}{m \cdot K}$.

Interpretation of Results

Current space craft insulator applications have a thermal conductivity range from $0.0260 - 0.0519 \frac{W}{m \cdot K}$ (Gilmore, 1994). The results show it is a reasonable insulator, just on the outer range of the thermal conductivity for space crafts. In the future I can use the results from the polyurethane foam as a control for testing the tannin-based foams.

Figures

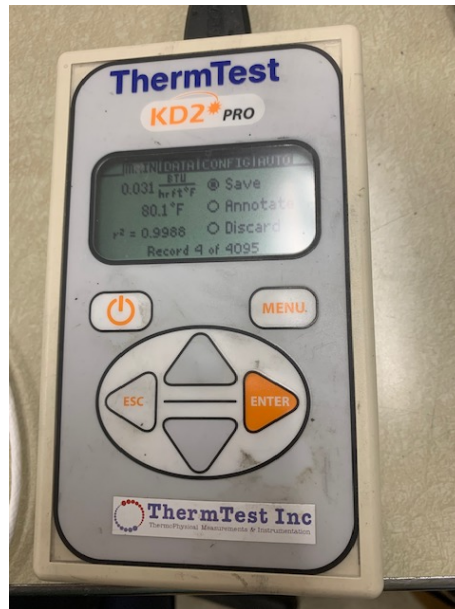


Figure 1: KD2-Pro Instrument

Acknowledgements

Dr. Rydge Mulford for stepping up to help with the research, as well as helping adjust to the many problems we encountered on the way. Bishal Gautam for teaching me how to use the KD2 Instrument.

References

1. Celzard, A., Szczurek, A., Jana, P., Pizzi, A., Stauber, M., Bourbigot, S. . . . Fierro, V. (2014). Latest progresses in the preparation of tannin-based cellular solids. *Cellular Plastics*, 51, 1-14.
2. Gilmore, D. G., & Bello, M. (1994). Satellite thermal control handbook. In *Satellite thermal control handbook* (pp. 4-79-4-80). El Segundo, CA: The Aerospace Corporation Press.

Thermal Analysis of Laser Powder Bed Fusion using Finite Element Modeling

Student Researcher: Karlee D. Birchfield

Advisor: Dr. Yao Fu

University of Cincinnati

Department of Aerospace Engineering and Engineering Mechanics

Abstract

Additive manufacturing has quickly found widespread applications in various industries. It allows for manufacturing of complex geometries, weight reduction, material waste minimization, and improved component quality. This has especially gained attention in the aerospace industry due to its ability to repair complex and expensive parts instead of replacing them.^[1] While there are many benefits that come with using additive manufacturing, there are also many challenges. One of the challenges is understanding the thermal residual stress generated during the formation of the part.^[2] The aim of this work is to model the laser powder bed fusion process to provide an effective way to understand the thermal stress undergone by the part during the build process. This process was modeled in Abaqus with a user defined Fortran subroutine to simulate the laser with a moving heat flux. Layers were built using element activation and deactivation. It is found that there is an increase in max temperature and melt pool size with decreasing layer thickness.

Project Objectives

The scope of this project is to develop a finite element model to gain a deeper understanding of thermally induced residual stress in the laser powder bed fusion (LPBF) process as layers are added to the build. The model will then be used to compare to the experimental data from the printing of a cubic sample in a EOS M290. In LPBF, metallic powders are uniformly spread on the building platform by a rake instead of being blown out from nozzles as in directed energy deposition (DED) method. A focused laser beam scans the surface according to the prescribed path and selectively melts the powders in this layer, after which a new layer of powders is spread after lowering the building platform to the distance of the layer thickness. The layer height of LPBF is in the scale of tens of microns, which is much thinner than that of DED and electron beam melting (EBM) products.^[2] High residual stress created when using this technique can lead to cracking, fatigue-failure, distortion and the need for support structures. This modeling strategy can predict temperature distribution and melting pool size which serves as a beginning step towards a full residual stress analysis.^[3]

Methodology Used

The LPBF process was modeled using Abaqus with a user defined Fortran subroutine to simulate the laser with a moving heat flux. The thermal analysis was done with stainless steel 316L. The thermo-physical material properties required are specific heat (0.5 kJ/kg/K), density (7.99 g/cm³) and thermal conductivity (0.201 W/m·K).^[4]

A rectangular domain of 0.3m x .02mm x 0.3m was used with 8 node hexahedral elements and an initial temperature of 20°C. A laser path was defined across the top surface of the rectangular domain with the laser parameters listed in Table 1. These parameters match those of the EOS M290 printer. The heat flux was defined by the following equation.

$$q(x,y) = \frac{\alpha_R P}{\pi r_0^2} \exp\left\{-\frac{r^2}{r_0^2}\right\}$$

Table 1. The Process parameters used to define heat source

Laser Power (W)	20	Radius of Laser Beam (mm)	.01
Scan Speed (mm/s)	104.3	Absorption Efficiency (%)	40

Results Obtained

The figure below shows the temperature distribution as the laser moves across the rectangular domain. The laser increased the temperature of the powder to exceed its melting point, turning the powder into liquid and creating a melt pool. The size and shape of the melt pool can also be seen in the figure below. The melt pool has a radius of 30mm compared to the laser diameter of .01mm. Once the laser passes, the temperature returns below its melting point where it then cools and hardens to form a segment of the first layer. Figure 2 shows the temperature of node 457 throughout the simulation. The node is at the center of the first melt pool.

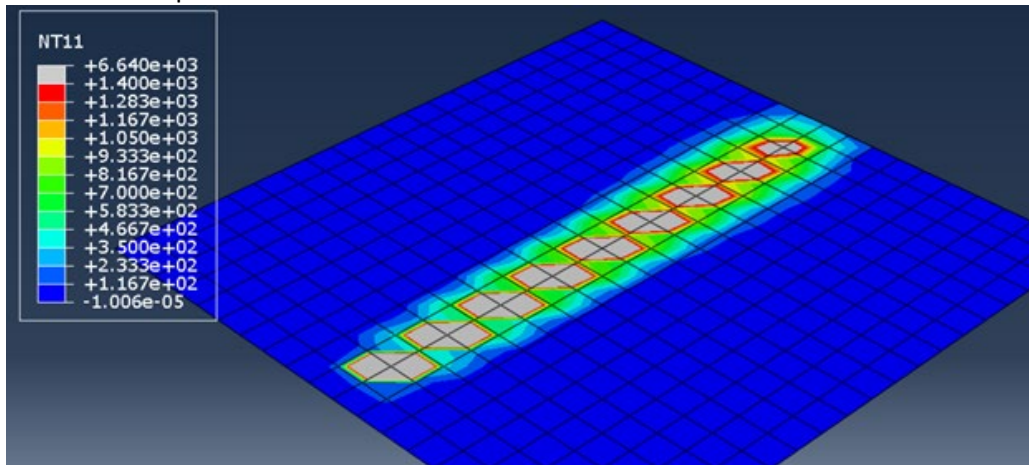


Figure 1a): Thermal distribution and geometry of melt pool

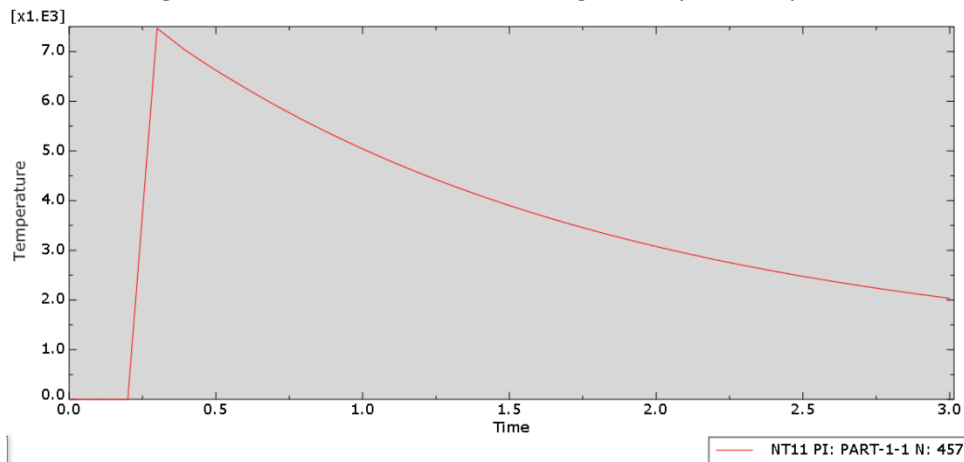


Figure 1b) Temperature evolution at a node

To understand the full thermal residual stress that occurs during a LPBF build, layers were simulated with a model change in ABAQUS. But first, analysis was done on how layer thickness affects the size of the melt pool. Three layer thicknesses were analyzed using the same laser parameters listed in table 1. The results are shown below in table 2.

Table 2. Melt pool size for given powder layer thicknesses

Layer Thickness (mm)	Melt Pool Diameter (mm)
0.02	30
.1	7.5
.2	Does not reach melting point

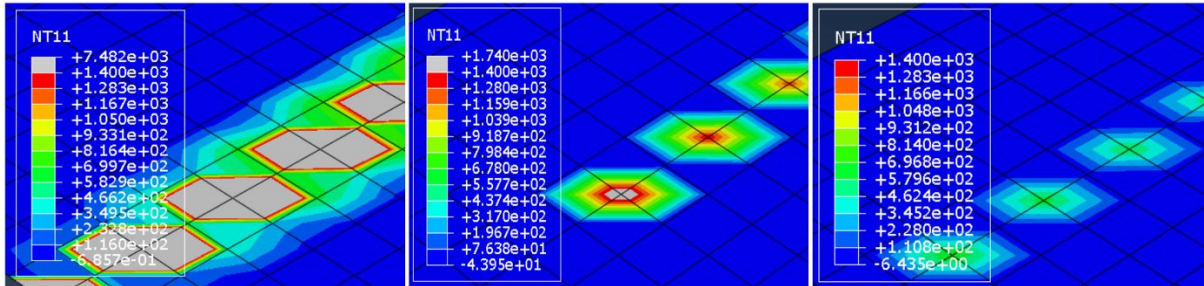


Figure 2) Melt pool dimension for given powder layer thickness (0.02mm, 0.1mm, 0.2mm respectively)

Due to the node restrictions in the ABAQUS student version, during the layer simulation, parameters for the build and the laser were changed. The new build size is 34mm x 7.3mm x 40mm with a layer thickness of 7.3mm. The changes to the laser parameters are shown in the table below.

Table 3. Laser parameters for layer simulation

Laser Power (W)	20	Radius of Laser Beam (mm)	2
Scan Speed (mm/s)	10.4	Absorption Efficiency (%)	40

The results of layer build up are shown below in figure 3.

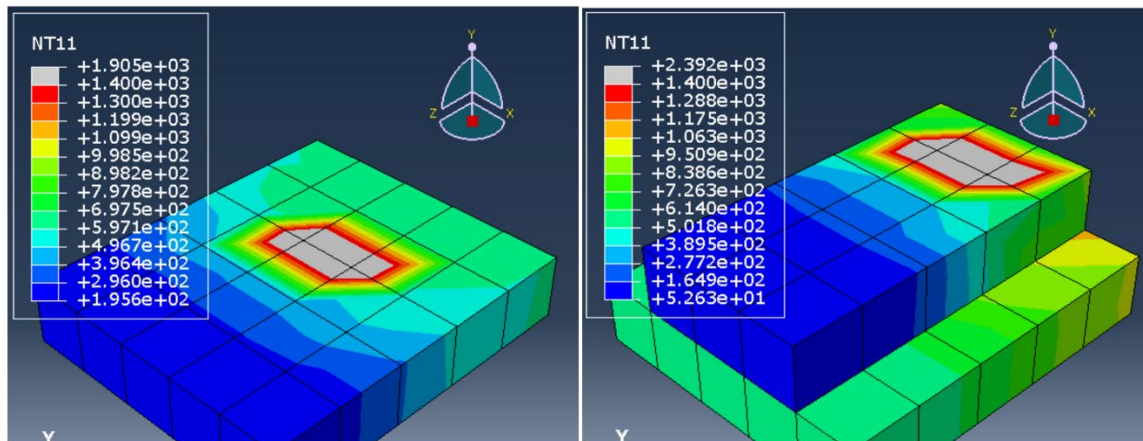


Figure 3) Layers 1 and 2 of LPBF build up in ABAQUS

Conclusion and Future Work

Using finite element modeling it was found that as the thickness of the layer of powder increases there is a decrease in the size of the melt pool and max temperature. To further investigate the LPBF process, a full thermal residual stress analysis should be completed. This should be done using a non-student version of ABAQUS to avoid the node limitation. This would give greater insight to the true shape of the melt pool as well as the heat distribution across the build. This updated model would include simulating the building

of layers within a sequentially coupled thermo-mechanical microstructural finite element model and multiphase field model that can be compared to the experimental data. [5]

References

1. Direct Metal Deposition Fabrication Process for Metal 3D Prints. (n.d.). Retrieved March 31, 2020, from <https://www.sculpteo.com/en/glossary/dmd-definition/>
2. Gouge, M., Michaleris, P., (2018) "An Introduction to Additive Manufacturing Process and Their Modeling Challenges: Laser Powder Bed Fusion Systems" in Thermo-Mechanical Modeling of Additive Manufacturing
3. Parry L., Ashcroft I., Bracket D., Wildman R. D., Kolacinski R. (2014) "Investigation of Residual Stresses in Selective Laser Melting", In Key Engineering Materials Vol. 627, pp. 129-132
4. Türkyılmaz, M. "A Designers' Handbook Series No 9004: High-Temperature Characteristics of Stainless Steels"
5. Li, Q., Gnanasekaran B., Fu Y., Liu G.R., "Prediction of Thermal Residual Stress and Microstructure of Additive Manufacturing Processes of Direct Laser Metal Deposition via a Coupled Finite Element and Multiphase Field Framework"

Development Of An Optimization Method For An Offset Jet Engine Inlet Utilizing Non-Linear Optimization Methods

Student Researcher: Noah A. Broski

Advisor: Dr. Jen-Ping Chen

The Ohio State University

Department of Mechanical and Aerospace Engineering

Abstract

Inlets whose centerlines are offset of the aircraft's engine have been utilized in many applications across both the civilian and military aircraft. Some advantages of an offset inlet include but are not limited to: being able to place the engine along the centerline of the aircraft allowing for better propulsion integration, reducing heat signatures by having the engine insulated in the body of the aircraft, reducing radar detection by having a more compact cross-sectional area, and allowing for boundary layer ingestion to reduce overall drag on the aircraft. However, utilizing an offset inlet does not come without complications. Two of the main complications are having a large pressure loss in the inlet and having large flow distortion at the aerodynamic interface plane (AIP). Both of these complications can lead to large decrements in engine performance, in addition to the possible formation of dynamic stall cells, leading to catastrophic failure of compressor blades.

During the course of this research a tool was developed which utilizes non-linear optimization methods in order to optimize the geometry of an offset inlet, resulting in reduced pressure loss and flow distortion. This tool requires the user to input geometric constraints for the desired inlet. Using these constraints, the tool creates an inlet using a MATLAB code which parameterizes the inlet into four curves. With these curves defined, a SOLIDWORKS macro creates an inlet geometry to be sent into Fluent, a computational fluid dynamics software. Utilizing user-defined boundary conditions, the pressure loss and flow distortion at the AIP will be computed. These results are then used as the objective function for a non-linear optimization algorithm, which outputs new control points for the inlet's new four Bezier curves. This then iterates until the inlet is optimized and the termination criteria is met.

Project Objectives

The purpose of this project is to develop a tool to optimize S-Duct inlets using non-linear optimization. The objective function for the optimization is to minimize the total pressure loss across the inlet.

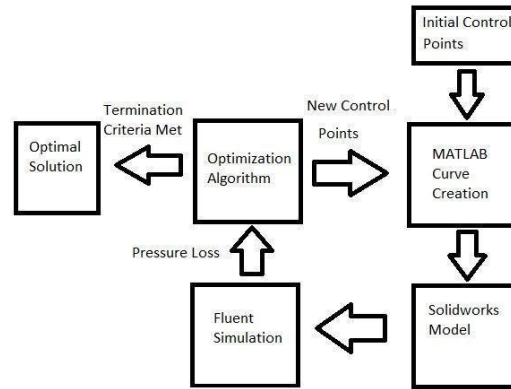
Methodology

The inlets are modeled in SolidWorks and Fluent simulations are then completed to model the flow through the inlet and compute the total pressure differential across the inlet. Additionally, MATLAB is used to generate curves to define the inlet designs along with computing the iterative optimization process.

Many variables and constraints directly affect the performance of an offset inlet duct, as measured by total pressure recovery. In this particular case, the constraints considered are the length to offset ratio and the cross-sectional geometry of the duct, as defined by control points on the Bezier curves. The inlet geometry is defined by four, fifth order, curves, and the position of the four curves are at 90-degree intervals around the inlet. These curves are then connected using four conic curves with a conic parameter ρ set to 0.4142. After creating the conics, the resulting cross sections are combined into a single inlet using surface lofts.

CFD simulations are then used to evaluate the changing designs to determine the effects of inlet geometry on total pressure recovery. The creation, simulation, and optimization of the inlet is being completed automatically via an executable completing the process displayed in Figure 1.

Figure 1. Block diagram of the optimization algorithm

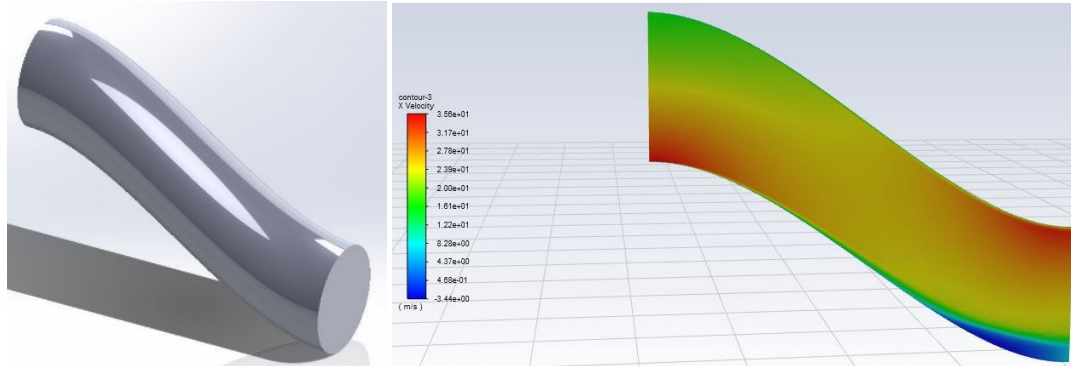


The non-linear optimization algorithm chosen was the Newton Method due to its ability to arrive at local minimum quickly and allowing for a pure step size. The gradients and Hessians being used are computed using finite difference methods to approximate the partial derivatives based on the results from the CFD simulations.

Expected Results

Unfortunately, due to longer than expected times required to script and combine the macros to completely automate the non-linear optimization process the code was unable to be run in its entirety. The code will be run in the upcoming weeks and is expected to minimize the total pressure loss across the inlet by addressing areas of high total pressure loss in the inlet and making changes to the appropriate control point positions. Below is an example of a single inlet that was created and simulated automatically by the scripts. This is a baseline inlet and it can be seen in Figure 2 that there is separation and recirculation of flow in the inlet which causes large total pressure losses. This effect is expected to be reduced or completely through the optimization script.

Figure 2. Solidworks model of the general 12” inlet (left), x-velocity along centerline (right)



Significance of Expected Results

If proven to be a valid and efficient way to optimize offset inlet geometry this tool could be used to greatly reduce the time required to design and implement these inlets for use on aircraft possibly replacing labor intensive trade studies.

Acknowledgements

I would like to thank the Ohio Space Grant Consortium along with my advisor Dr. Chen for allowing me to pursue this research and helping to provide guidance throughout the process.

The Role of *cyp1b1* in the Development of Primary Congenital Glaucoma in *Danio rerio*

Student Researcher: Elizabeth M. Bryson

Advisors: Morris, Jaquelin Ph.D. Munroe, Karen Ph.D.

Baldwin Wallace University
Biology and Geology

Abstract

Primary congenital glaucoma (PCG) is an autosomal recessive disorder of the eye due to a neural crest defect that results in increased ocular pressure (Ko et. al 2015, Lewis et. al 2017). PCG is the most common neonatal and infantile glaucoma, affecting 1/10,000 babies in The United States (Lewis et. al 2017). Retinoic acid (RA), a vitamin A metabolite necessary for the development of the optic nerve and ventral retina is metabolized by *cyp1b1* (Williams et. al 2015). A mutation in the *cyp1b1* gene creates the inability for neural crest cell migration, leading to trabecular meshwork malformation and elevated intraocular pressure (Lewis et. al 2017 Bohnsack and Chawla 2014). This study aimed to use the CRISPR/Cas9 system to create a null deletion of *cyp1b1* to determine whether this method of knockdown is capable of producing PCG in *Danio rerio* as it would occur naturally. Four *Danio rerio* specific oligonucleotides were designed to target the *cyp1b1* gene located on exon 1 of chromosome 13; each sequence is located in the first exon of the chromosome. The oligonucleotides were PCR amplified and purified before undergoing in vitro transcription. Completed gene transcripts were confirmed via electrophoresis. *Danio rerio* one cell stage embryos were then injected with Cas9 protein and the four *cyp1b1* specific gRNAs. DNA isolated from injected embryos was used to confirm mutagenesis.

CRISPR, or Clustered Regularly Interspaced Short Palindromic Repeats targets specific sequences within a gene using guide RNAs designed to bind to the selected sequences, and in this case with the help of Cas9 cut the targeted sequences so a mutation occurs when the DNA is repaired. To do this, gRNA is injected into embryos and binds to the sequence or sequences of interest. After the gRNA binds to the target sequence(s), the Cas9 enzyme binds to the gRNA and begins cutting both strands of the DNA. Once cut, the DNA repairs itself and a mutation in the gene occurs (Medline Plus Genetics 2020).

Methodology

The four target sequences used to design the oligonucleotides and gRNAs were chosen based on an analysis done in the CHOPCHOP program under the metrics that they have high efficacy and no off-target sites that would interfere with the CRISPR. The decision to use four target sites rather than two was made to increase the chances of a successful knockdown in case one or two of the gRNAs were ineffective. Once the oligonucleotides were designed, they were PCR amplified using two gRNA primers and a guide constant oligonucleotide in order to create the template strands. Once the PCR was complete, the DNA was run on a 2% electrophoresis gel, extracted, and purified using the Illustra GFX PCR DNA and Gel Band Purification Kit.

After purification hours the embryos were removed from their chorions and lysed to retrieve DNA. DNA from injected and un-injected embryos were again amplified via Touchdown PCR using a forward and reverse primer designed to determine mutagenesis. Due to complications that are continued to be worked out, mutagenesis has yet to be determined. The DNA went through in vitro transcription and Lithium Chloride precipitation to retrieve the gRNA that would be used for injections. 200 pg of gRNA

and 400 µg of Cas9 protein were put into an injection mixture along with Potassium Chloride, Phenol Red, and water. The mixture was injected into one cell stage embryos to ensure that the Cas9 and gRNA was inserted into the blastula to be incorporated into the genome of the fish. The embryos were placed in a 37° C incubator. After 48

Next Steps

This study is ongoing, and therefore the results have not yet been optimized. Once mutagenesis is confirmed, injected embryos will be raised and bred to establish an F₁ generation. Future plans for this study include studying the heritability of the *cyp1b1* mutation as well as to determine whether the male or female fish containing the mutation makes a difference in heritability.

Figures

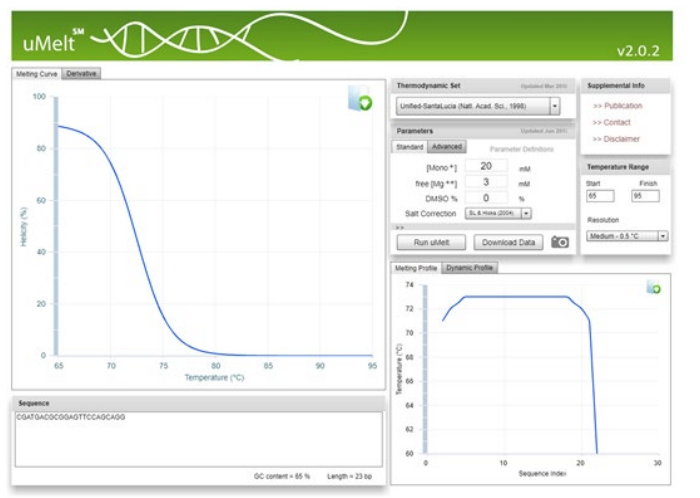


Figure 1. Umelt graph of target sequence 11, depicting a normal melting curve.

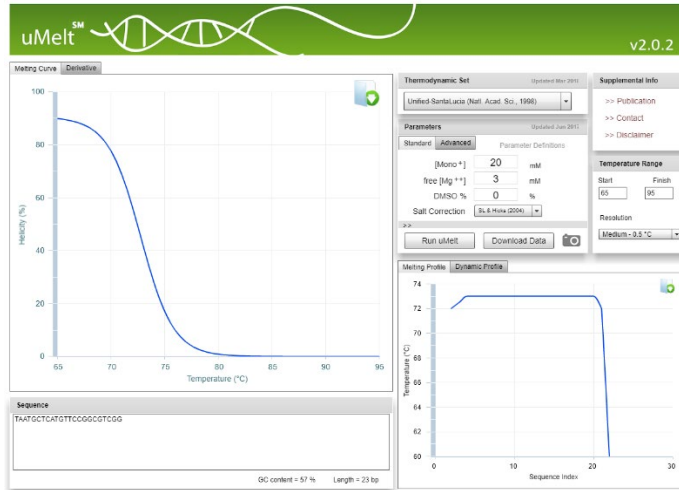


Figure 2. Umelt graph of target sequence 13, depicting a normal melting curve.

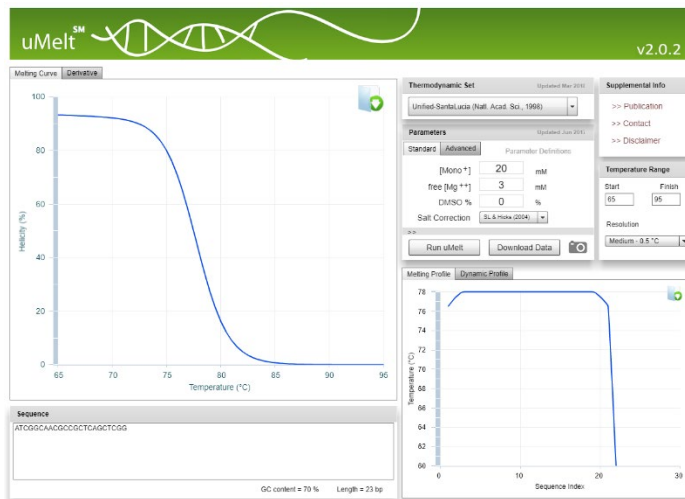


Figure 3. Umelt graph of target sequence 14, depicting a normal melting curve

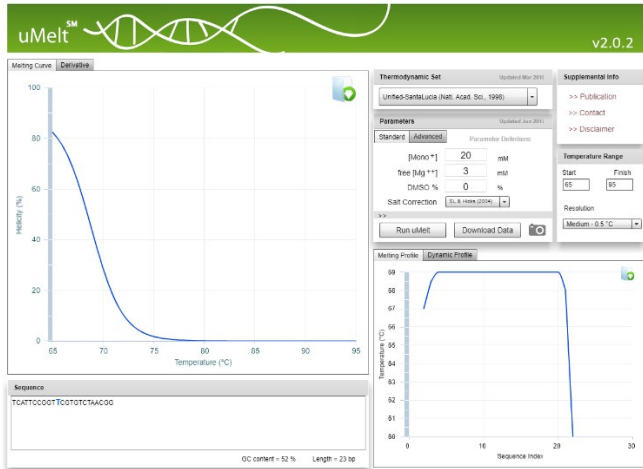


Figure 4. Umelt graph of target sequence 21, depicting a normal melting curve

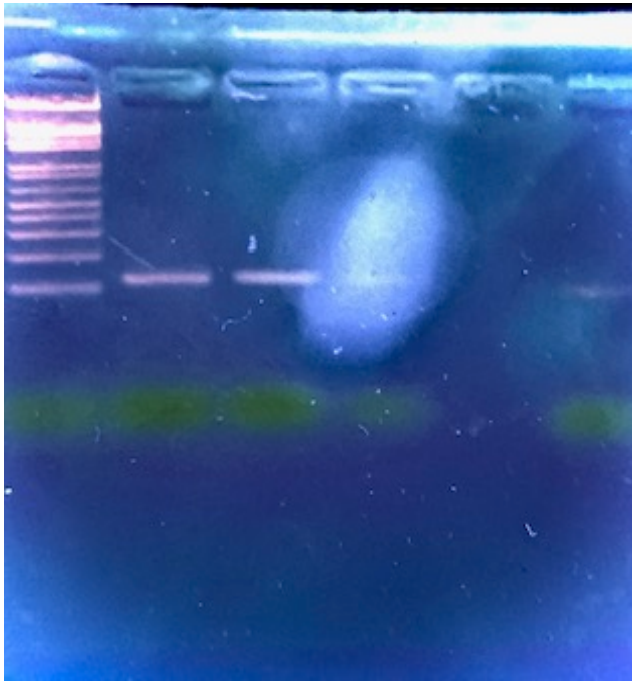


Figure 5. Gel electrophoresis confirmation of PCR product.

References

- Bohnsack, B. L., & Chawla, B. (2014, April 30). Cyp1b1 regulates ocular fissure closure and subsequent neural crest migration. Retrieved March 19, 2021, from <https://iovs.arvojournals.org/article.aspx?articleid=2270122>
- Ko, F., Papadopoulos, M., & Khaw, P. T. (2015, September 09). Primary congenital glaucoma. Retrieved March 19, 2021, from <https://www.sciencedirect.com/science/article/pii/S0079612315000965>
- Lewis, C. J., Hedberg-Buenz, A., DeLuca, A. P., Stone, E. M., Alward, W. L., & Fingert, J. H. (2017, May 26). Primary congenital and developmental glaucomas. Retrieved March 19, 2021, from <https://academic.oup.com/hmg/article/26/R1/R28/3855251?login=true>
- What are genome editing AND Crispr-cas9?: MedlinePlus Genetics. (2020, September 18). Retrieved March 19, 2021, from <https://medlineplus.gov/genetics/understanding/genomicresearch/genomeediting/>
- Williams, A. L., Chawla, B., & Bohnsack, B. L. (2015, June 11). Cyp1b1 regulates retinal and ocular neural crest development through retinoic acid-dependent and ra-independent pathways. Retrieved March 19, 2021, from <https://iovs.arvojournals.org/article.aspx?articleid=2331187>

Characterization of a New Open-Jet Wind Tunnel

Student Researcher: Joe C. Castma

Advisor: Dr. Kevin J. Disotell

Youngstown State University
Rayen School of Engineering

Abstract

A boundary-layer wind tunnel has been converted to an open-jet facility at Youngstown State University. The open-jet facility is capable of achieving velocities of up to 35 m/s. This research consisted of assembling and installing a two-axis system in the open-jet test cell and utilized a Pitot-static tube, hot-wire anemometer, and a 3-D sonic anemometer, to measure the modified test cell flow quality in support of future air mobility systems testing.

Project Objectives



Figure 1. 3-D sonic anemometer.

This project's objective was to deploy a two-axis traverse system in a new open-Jet wind tunnel and acquire initial measurements. The assembly and installation of the two-axis traverse system allowed a probe instrument can be automatically positioned at any desired point in a plane, using a custom MATLAB code. Secondly, an inherited 3-D sonic anemometer (Figure 1) was to be deployed in the open-test cell, including designing a mounting bracket and preparing homemade cables for signal transmission, allowing measurement of large-scale velocity fluctuations.

Methodology

The two-axis traverse system was mounted to the top of the test section, allowing motion across the width and height of the jet in a single plane. Adapters were designed to enable mounting of three different probes, as follows. A Pitot-static tube measures the dynamic pressure to calculate velocity from the Bernoulli equation. A hot-wire anemometer uses the relationship between the temperature-dependent wire resistance and the flow speed to determine the airflow velocity as the air flowing past the wire cools it. The commercial 3-D sonic anemometer measures the wind speed in terms of its three orthogonal components, as well as the speed of sound c [1]. The design incorporated a flat steel plate bolted to the traverse carriage with a 3-D printed adapter component to attach each probe. After the design was tested, further improvements were needed. In order to null the encoders on the two-axis traverse according to the established coordinate system so that the position of

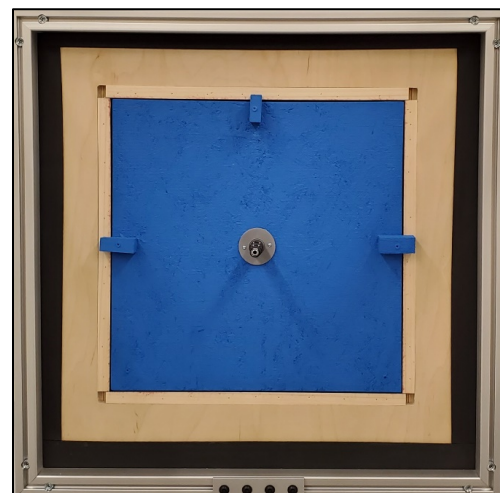


Figure 2. Telescoping probe centering tool installed at jet exit plane.

the probes could be reliably located, the centering tool shown in Figure 2 was designed and built. The design incorporates a telescoping tube at the center of a board installed on the jet exit plane. Lastly, to set up the 3-D sonic anemometer shown in Figure 1, a different mounting design was created, and all the necessary parts were purchased and assembled to ensure data collection.

Results and Recommendations

The Pitot-static tube and hot-wire probe mounts enabled datasets presented in a conference paper at the SAE AeroTech Forum in March 2021 [2]. Recent data acquired with the 3-D sonic anemometer were obtained at a sample rate of 60 Hz for several jet exit speeds in Figure 3, for only the dominant streamwise component (defined as the x-direction) due to space limitations. The mean y- and z-components were less than 3% of the mean streamwise velocity for each operating condition.

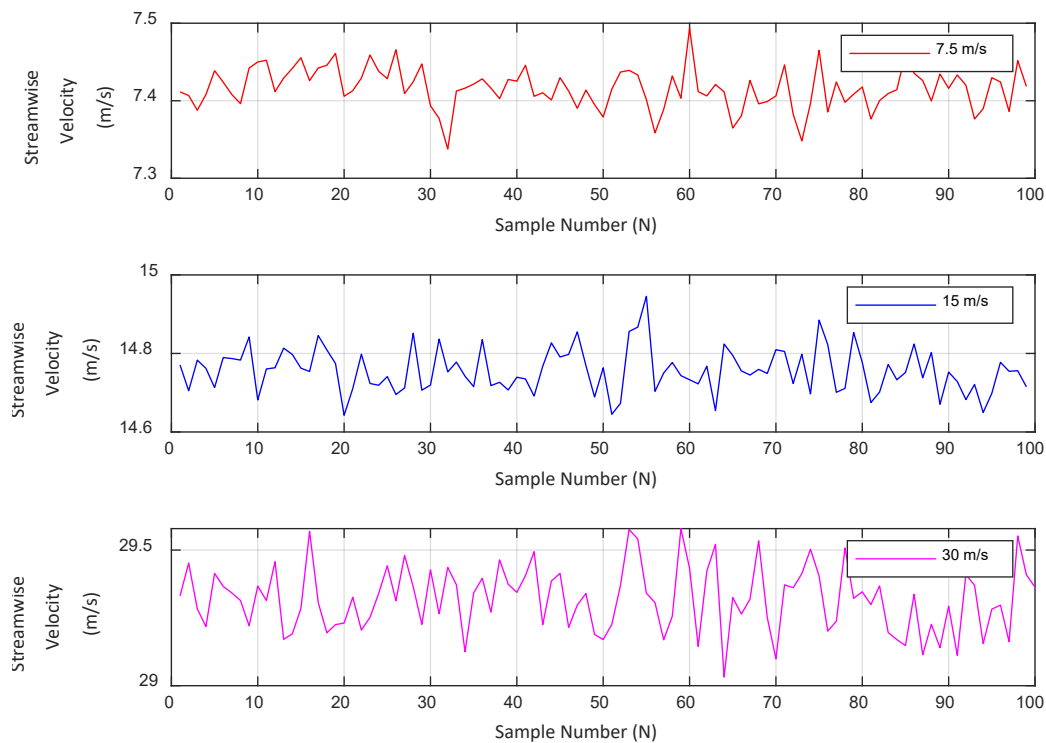


Figure 3: Streamwise velocity signals acquired from sonic anemometer at several test speeds.

In Figure 3, the velocities were plotted against sample number instead of time due to a discrepancy with timestamp encoding in the data files from the packaged software program. Further investigation is needed to interpret the timestamp data in order to give confidence to time history data; however, the working operation of the inherited device was proven.

References

- [1] Campbell Scientific, Inc., 2017, "CSAT3 Three Dimensional Sonic Anemometer Instruction Manual."
- [2] Disotell, K.J., Chamberlain, T.J., and Castma, J.C., 2021, "Multi-Modal Conversion of a Boundary-Layer Wind Tunnel to Open-Jet Test Cell," SAE Technical Paper 2021-01-0018, doi:[10.4271/2021-01-0018](https://doi.org/10.4271/2021-01-0018).

Cyber Security For Distributed Energy Resource

Student Researcher: Zackry D. Cephas

Advisor: Dr. Deok H. Nam

Wilberforce University

Department of Computer Engineering

Abstract:

The proposed project explores the current industry's best practices related to DER cybersecurity and studies the possible recommended functionalities for improving the cybersecurity posture of DERs. In addition, for improving the cybersecurity posture of DERs, possible attack prevention, detection, and response measures specifically designed for DER integration across the cyber, physical device, and utility layers of the future smart grid are examined.

Project Objectives:

This survey study examines the cybersecurity resources that can help how people use energy resources to expanded networks inside energy frameworks and their parts and expanding the attack surface that a dangerous entertainer can target.

Methodology Used:

The recent trends in modern distribution systems of power electric grids increase Information and Communication Technology (ICT), cyber-physical interdependency, and new vulnerabilities. Hence, the modern distribution system of power electric grids normally needs to prepare for bidirectional power flow, unpredictable load pattern, increasing energy storage capacity, high penetration of DERs and renewable energy, a large number of smart devices, and more monitoring and control, while the traditional distribution system of power electric grids used to be unidirectional power flow, very predictable load pattern, insignificant energy storage capacity, low penetration of DERs and renewable energy, and a relatively small number of smart devices. Even though the electric grid is getting improved and bigger, its function remains to provide safe, secure, and reliable electricity to consumers.

From the security point of view for DER, malware, and cybersecurity threats are continuously and rapidly growing even though DERs such as solar, storage, fuel cells, flexible load, and combined heat and power, are getting more extended and increased. Due to the described DERs, we are getting less reliant on central station power plants. Simultaneously, greenhouse gas emissions are more reduced and the need for new transmission & distribution (T&D) infrastructure construction is getting deferred. Increased reliance on DERs is beneficial for society even though some DERs like wind, lessen reliance on traditional power stations and provide resilient power backup alternatives. Moreover, DERs can provide new opportunities and benefits to strengthen cybersecurity by mitigating the impact of cyberattacks on the electric power grid even though there are also new potential risks that must be carefully considered.

To avoid wreaking various types of cyberattacks by intruders on the distribution system and its operation, considering potential physical impacts on the distribution systems resulting from a data-integrity attack targeting DERs is important to prepare for the possibilities of cyberattacks by the control over targeted DERs and the number and size of the hacked DERs in a given attack to limit the impact of the consequences from such cyberattacks [1]. Physical impacts on the distribution system can be frequency deviation, higher or lower voltage, reduced grid efficiency, grid assets overload, disconnection of DERs, loss of load, and damage to electric devices corresponding to DER operation modes [2].

The effective and efficient methods of securing DERs for practical cybersecurity connected to the distribution grid are as follows: 1) use most updated software and operating systems along with security services and software from the control center to DERs and communication systems and scan the whole communication network of the smart distribution system and identify the firmware and software status of all DERs, 2) make DER be an effective roll-back firmware in place with updating the firmware to restrict any possible cyber-attacks or its impact on the electric power grid, 3) verify the user's identity on acquired information for accessing various privileged system services based upon the authentication, 4) use the passwords to restrict invalid accesses to protect the distribution grid from cyber-attacks and privilege violations, 5) manage the security protocol of transport layer security (TLS) cryptography between two hosts and protect the DER against MITM, eavesdropping, replay, and spoofing cyberattacks, 6) use the security management for the public key infrastructure and verification of user's certificate status to protect DERs from least privilege violation, MITM, eavesdropping, replay, and spoofing attacks, 7) use the expiration of DER certificate to protect DERs from least privilege violation, MITM, eavesdropping, replay, and spoofing attacks, 8) deploy TLS protocol to renegotiate the TLS session identification resumption to protect DERs from MITM, eavesdropping, and spoofing attacks, and 9) examine the entire supply chain to verify the valid vendors and organizations for manufacturing DERs to protect DERs from eavesdropping and least privilege violation [3, 4].

Significance Results:

The proposed project examines the cybersecurity resources that can help how people use energy resources about commonly known cyberattacks targeting DERs and restricted recommendation for DERs to protect the vulnerabilities of DER cybersecurity functionalities based upon related utilities, vendors, manufacturers, and researchers through the communication protocols at the transmission level.

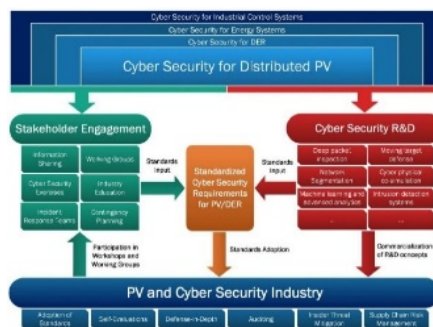


Figure 1. Process for achieving cyber security of PV systems. Image Sandia Roadmap for Photovoltaic Cyber Security [5]

Acknowledgments:

The author is grateful to the supervisor Dr. Deok H. Nam at Wilberforce University for his invaluable support, encouragement, and guidance. The author also thanks Ohio Space Grant Consortium (OSGC) for the academic scholarship program. Special thanks to Dr. Andrew L. Gyekenyesi and Mr. Timothy M. Hale of OAI for the OSGC Program.

References:

- [1] D. Saleem, A. Sundararajan, A. Sanghvi, J. Rivera, A. Sarwat, and B. Kroposki, "A Multidimensional Holistic Framework for the Security of Distributed Energy and Control Systems," in IEEE Systems Journal, Vol. 14, Issue 1, March 2020, pp. 17-27
- [2] IEEE, "1547-2018 - IEEE Standard for Interconnection and Interoperability of Distributed Energy Resources with Associated Electric Power Systems Interfaces," April 6, 2018.

- [3] A. Sundararajan, A. Chavan, D. Saleem, and A. I. Sarwat, "A Survey of Protocol-Level Challenges and Solutions for Distributed Energy Resource Cyber-Physical Security," *Energies*, vol. 11, 2018, pp. 1996–1073.
- [4] Sunspec Alliance, and Sandia National Laboratories, "SunSpec/Sandia Distributed Energy Resource Cybersecurity Workgroup" [Online]. Available: <https://sunspec.org/sunspec-cybersecurity-workgroup/> [Accessed Jun. 19, 2019].
- [5] Sandia National Laboratory, "Cybersecurity for Distributed Energy Resources." <https://www.labpartnering.org/success-story/cf0bc562-024d-434c-ab43-e74c3b1cd81a>

Water Purification and the Efficiency and Viability within the Mid-Ohio Valley

Student Researcher: Victoria L. Clarchick

Advisor: Ben Ebenhack, Chris Jacobs

Marietta College
Petroleum Engineering

Abstract

The purpose of this experiment is to determine if a water purification plant could be implemented into the Mid-Ohio Valley to improve the quality of the surrounding environment. To arrive at a proposal research within the area, process of removal, and previous implementations were considered. The final proposal is to implement a dual treatment plant that draws water from the Buckhannon River to treat the Acid Mine Drainage as well as a water disposal location on site for produced water from local oil and gas pad locations. The process and complete proposal is detailed within the following report. There are references to Figure 1, a map of the Buckhannon River, and Table 4.2, a table with the chemicals that are commonly used in AMD and produced water treatment. References listed.

Background

Water is a vital part of human life, therefore as a collective, people need to contribute to the effort to recycle and clean water. All water that is distributed from a community water treatment facility forgoes a process of purification to provide safe drinking water. This water may come from a natural water source or it may be recycled. Water that is distributed to the public to drink is treated and purified for the safety of people. Organizations like the Center for Disease Control (CDC) and the Environmental Protection Agency (EPA) work together to determine the process and regulation for treating water that is to be distributed to the public. Roughly 286 million people consume water that was treated at a community water treatment facility, therefore the care and consideration for treating water is not a light subject². Acid Mine Drainage (AMD) formation occurs when specific sulfide minerals are exposed to oxidizing conditions³. Produced water from oil and gas wells is often disposed of in disposal wells, wells that are currently not producing. The decision to dispose produced water in disposal wells is driven by the cost factor of trucking the produced water. Most often it is more cost efficient to truck produced water to these disposal wells because the locations are much closer than a produced water treatment facility.

Problem

In the county of Upshur West Virginia, the city of Buckhannon is known for Acid Mine Drainage from the mines that surround the area draining into the Buckhannon River. The Buckhannon River is a tributary of the Tygart Valley River and Monongahela River, reference Figure 1 in Appendix A, flowing with an average discharge rate of $600 \text{ ft}^3/\text{s}$ ⁵. Currently the Buckhannon River is under a passive AMD treatment project conducted by the National Mine Land Reclamation Center (NMLRC)⁶. Along with the Acid Mine Drainage issues, Upshur, WV and the surrounding counties over 180 operators have a total of 14.3 thousand wells that were producing in the year 2019¹. All of the activity in this area is affecting the environment, wildlife, and community people. Since the water from the Buckhannon River is contaminated from AMD the people and wildlife cannot use the river as a viable water source unless the water is actively treated because a passive treatment process is unable to produce the amount of clean water needed to reach demands. To reclaim the waterways taken over by AMD an active treatment in

partner with a produced water treatment plan would benefit the environment, community, and oil and gas industry.

Process

There are four components in the process for treating water that is produced from wells or contaminated by AMD, coagulation and flocculation, sedimentation, filtration, and disinfection. Coagulation is the addition of chemicals, rapidly mixed into the water, that help to break down and neutralize components within the water. Production water and AMD Treatment chemicals added during coagulation similarly include coagulants, neutralizers, and oxidants, all included in table 4.2 (Appendix B). Flocculation, Mechanical Surface Aeration, is the process where components within the water oxidize forming into bigger particles during a continuous mixing process, either performed through paddle flocculators, vertical mixers, or dissolve air flotation (DAF). Directly after the water is transported into a sedimentation basin. In this process the water is rested to allow for gravity separation. The larger particles, sludge, will fall to the bottom of the basin and the sludge is then vacuumed and disposed of at a waste management plant³. The next step is to undergo filtration. There are two popular methods, media filtration and microfiltration membranes. Media filtration and microfiltration membranes are similar to the process of a sieve. Some downfalls for both systems include: media filtration system often needs to be serviced every 48-72 hours and often does not filter out Cryptosporidium, and microfiltration membranes are better operational at warmer temperatures (around 18°C) and therefore need to cycle the water through the membranes twice⁴. The final step in the process is disinfection. Conventional disinfection adds chlorine to the water but in more recent years UV disinfection has become more popular due to the lack of Cryptosporidium removal in media filtration.

Proposal

Based on the research conducted I would like to propose the following plan. I think that Buckhannon West Virginia would be a good location for this treatment plant. Based on the process for implementing a water treatment plant in Beckenridge, CO, I propose that the plant process around 5 Million Gallons/Day (MGD)⁴. The layout for the plant will have two separate inlet streams, one from the Buckhannon River and the other will be a designated place on location where production water can be unloaded. The water from the Buckhannon River will flow directly into the coagulation basin whereas the produced water will go through a three phase glycol separator to remove any residual oil and gas within the produced water then it will join with the AMD water in the coagulation basin. During the coagulation process the chemicals included within Appendix B will be and the water will undergo rapid mixing. Based on the recommendation paddle flocculators will be implemented. The sedimentation will follow a conventional sedimentation with plates design. The filtration process will use a Microfiltration membranes system with a separate sludge filtration tank that will recycle through the beginning of the process. Finally, through the disinfection process chlorine will be added and I suggest that a UV light also be implemented for safety factors.

Appendix A

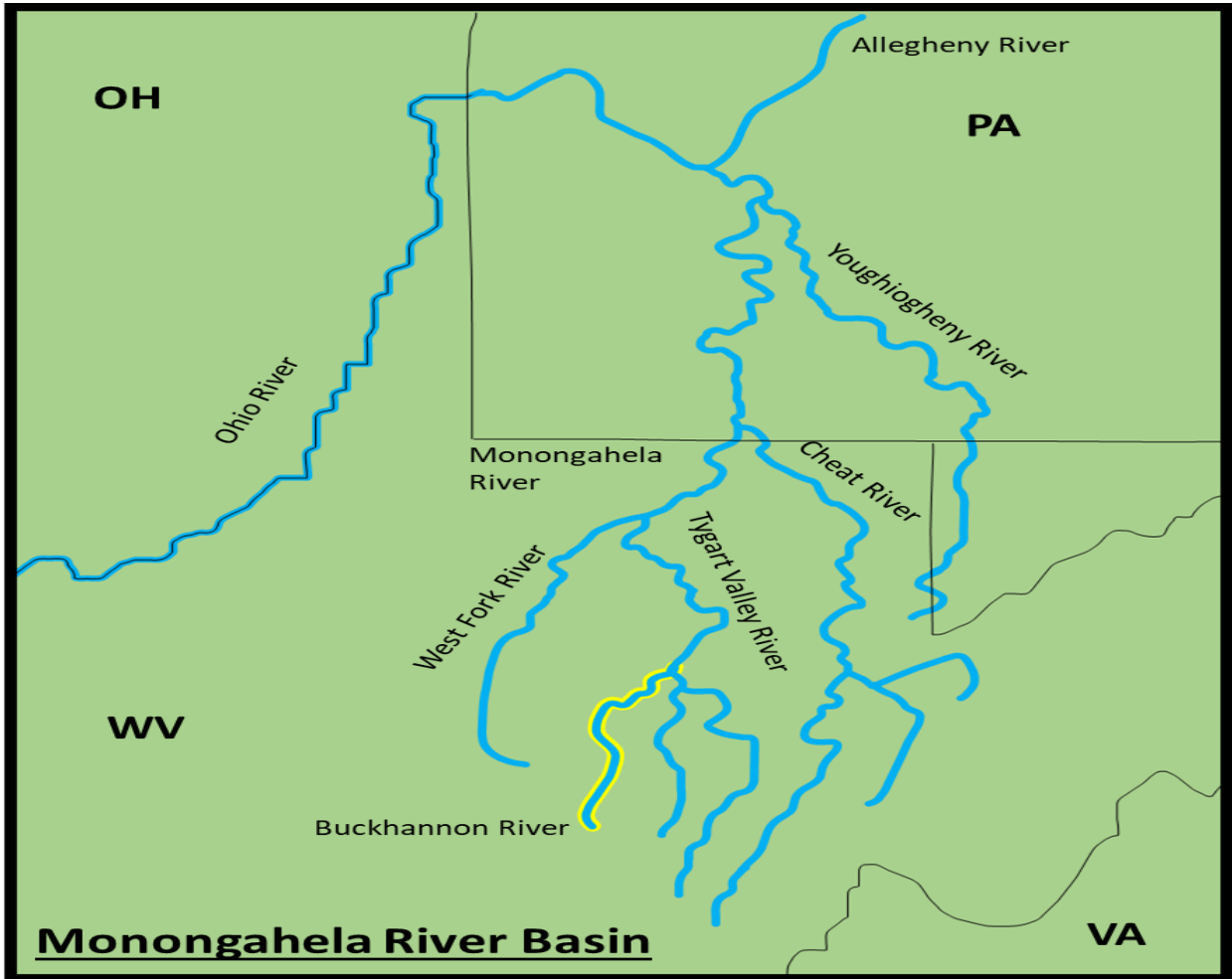


Figure 1

Appendix B

Table 4.2. Chemicals for acid neutralization, coagulation/flocculation, and oxidation

NAME	CHEMICAL FORMULA	COMMENTS
Acid Neutralization		
Limestone	CaCO ₃	Used in anoxic limestone drains and open limestone channels.
Hydrated Lime	Ca(OH) ₂	Cost effective reagent, but requires mixing.
Pebble Quick Lime	CaO	Very reactive, needs metering equipment.
Soda Ash Briquettes	Na ₂ CO ₃	System for remote locations, but expensive.
Caustic Soda	NaOH	Very soluble, comes as a solid in drums, beads, or flakes, or as a 20% or 50% liquid. Cheaper in the liquid form.
Ammonia	NH ₃ or NH ₄ OH	Very reactive and soluble; also purchased as aqua ammonia.
Potassium Hydroxide	KOH	Similar to caustic.
Magnesium Hydroxide	Mg(OH) ₂	Similar to hydrated lime.
Magna Lime	MgO	Similar to pebble quicklime.
Calcium Peroxide	CaO ₂	Used as a neutralizer and oxidant; either powder or briquettes.
Kiln Dust	CaO, Ca(OH) ₂	Waste product of limestone industry. Active ingredient is CaO with various amounts of other constituents.
Fly Ash	CaCO ₃ , Ca(OH) ₂	Neutralization value varies with each product.
Coagulants/Flocculants		
Alum (aluminum sulfate)	Al ₂ (SO ₄) ₃	Acidic material, forms Al(OH) ₃ .
Copperas (ferrous sulfate)	FeSO ₄	Acidic material, usually slower reacting than alum.
Ferric Sulfate	Fe ₂ (SO ₄) ₃	Ferric products react faster than ferrous.
Sodium Aluminate	NaAlO ₂	Alkaline coagulant.
Anionic Flocculants		Negatively-charged surface.
Cationic Flocculants		Positively-charged surface.
Polyampholytes		Both positive and negative charges on surface based on pH.
Oxidants		
Calcium Hypochlorite	Ca(ClO) ₂	Strong oxidant.
Sodium Hypochlorite	NaClO	Also a strong oxidant.
Calcium Peroxide	CaO ₂	Trapzene, an acid neutralizer.
Hydrogen Peroxide	H ₂ O ₂	Strong oxidant.
Potassium Permanganate	KMnO ₄	Very effective, commonly used.

References

1. Database information. (n.d.). Retrieved March 31, 2021, from <https://dep.wv.gov/oil-and-gas/databaseinfo/pages/default.aspx>
2. EAP. (2021, March 18). Statistics and facts. Retrieved April 01, 2021, from <https://www.epa.gov/watersense/statistics-and-facts>
3. Skousen, J. G. (1998). *Handbook of technologies for avoidance and remediation of acid mine drainage*. Morgantown, W. Va.: National Mine Land Reclamation Center, West Virginia University.
4. Town of Beckenridge. (n.d.). NORTH WATER TREATMENT PLANT. Retrieved April 01, 2021, from <https://www.townofbreckenridge.com/live/public-utilities/water/second-water-plant>
5. USGS. (n.d.). USGS current conditions for Usgs 03053500 Buckhannon River AT Hall, wv. Retrieved April 02, 2021, from <https://waterdata.usgs.gov/usa/nwis/uv?03053500>
6. West Virginia water research Institute. (n.d.). National Mine land Reclamation Center. Retrieved April 01, 2021, from <https://wwri.wvu.edu/programs/energy/reclaim>

Paraoxonase Regulation of Vascular Dementia

Student Researcher: Jacob A. Connolly

Advisor: Dr. David Kennedy

University of Toledo
Department of Medicine

Abstract

Chronic Kidney Disease (CKD) has shown to be a possible risk factor for dementia and cognitive impairment¹. These cognitive changes often occur early in the progression of CKD and the rate of decline varies¹. Furthermore, CKD is considered to be a model of accelerated aging due to increased vascular calcification, oxidative stress, and vascular dysfunction². Around 45 percent of adults above the age of 70 are affected by CKD and that number is only expected to rise due to the increasing prevalence of hypertension and diabetes in an aging US population³. My research is conducted on the Dahl-S strain of rats, a model that exhibits premature vascular remodeling and cognitive decline⁴. Even when placed on a low salt diet, Dahl-S rats show the development of fibrosis in cardiac and renal tissue along with the development of CKD. Furthermore, genes implicated in the development of Alzheimer's disease are overexpressed in the hippocampus of these animals⁴. The family of enzymes known as the paraoxonase enzymes were originally discovered because they have the ability to hydrolyze paraoxon⁵. There are three known members of the paraoxonase family: paraoxonase-1 (PON-1), paraoxonase-2 (PON-2) and paraoxonase-3 (PON-3). Previous studies on this family of enzymes have shown that they also possess lactonase and esterase activity⁵. Furthermore, PON-1 is believed to be a major protein that is responsible for the antioxidant properties of high-density lipoprotein (HDL)⁶. Studying dementia on the background of CKD can provide insights into the mechanism of the disease and how we can discover better treatments.

Project Objectives

The goal of this project was to test the cognitive ability of our novel Paraoxonase knockout animal models to determine if paraoxonase has an influence on cognitive function.

Methodology Used

In order to test the cognitive ability of our animal models, the Barnes Maze and Open Field Maze tests were performed. The Barnes Maze is a hippocampus dependent task where the animal learns the relationship between cues in the surrounding environment and the location of an escape box. The Barnes Maze I constructed is a circular table 4 feet in diameter with 20 holes evenly spaced around the perimeter (**Figure 1**). An escape box is placed underneath one of the holes while the other 19 are left open. Bright lights and open spaces are used as motivating factors for the animal to find the escape box as quickly as possible. The testing proceeded over a two-day period. On the first day, a habituation trial occurs. The habituation trial consisted of a 3-minute trial, and if the animal was unable to find the escape box within that interval it was gently guided to it. The animal then remained in the escape box for 2 minutes before returning to its home cage. 24 hours later, the testing phase consisting of 4 trials began. Each testing trial was 5 minutes in length and if the animal was unable to find the escape box in the allotted time, it was given a latency value of 300 seconds and was gently guided to the box. The animal remained in the escape box for 1 minute before it was returned to its home cage. The animal would then wait in their home cage for at least 15 minutes before the next trial. The amount of time it took for the animal to reach the escape box was recorded as latency time. Primary latency time was defined as the length of time it took for the animal to correctly identify the escape hole.

The animals were then tested using the Open Field maze (**Figure 2**). The Open Field maze consists of a square box 72 by 72 cm that is split into a grid of squares. The animal was then allowed to explore the maze for 10 minutes. During their run, tracking software was used to track their movements. Rodents show an aversion to open and brightly lit spaces and will avoid the center of the box. The anxiety level of the animal can be determined by the amount of time spent in the inner vs outer regions. Motor ability can also be assessed through values such as total ambulatory distance and average speed.

After completing both tests, the animals were euthanized, and their brains were examined for evidence of inflammation, oxidative stress, and vascular fibrosis using unbiased proteomic, genetic, and histologic techniques.

Results Obtained

The Barnes Maze test has been performed on animals aged 6 and 9-months old along with the Open Filed Maze performed on animals 9 and 12-months-old. The Results from the Barnes Maze test on the 6-month-old animals can be seen below in **Figures 3A** and **3B**. The results from the Barnes Maze performed on 9-month-old animals can be seen below in **Figures 4A** and **4B**. The Open field maze data from the 9 and 12-month-old animals is currently being analyzed.

Significance and Interpretation of Results

The results in **Figure 3B** show that there is an increase in the area under the curve for latency time of the PON-3 Knockout Dahl-S animals versus the Wild Type Dahl-S animals. This indicates that the PON-3 Knockout animals have greater cognitive impairment than their age matched counterparts. The data also suggests that PON-3 Knockout males have greater cognitive impairment than PON-3 Knockout females, indicating the present of PON dependent sex differences in cognitive ability.

The results from **Figure 4A** and **4B** show that Wild Type Dahl-S male animals have significantly worse cognitive ability than the Wild Type Dahl-S females and the PON-1 Knockout animals at 9 months of age. **Figures 4A** and **5A** show that as the trials progress, the animals are locating the escape box faster, indicating the presence of learning. However, the speed at which each group of animals learns is different.

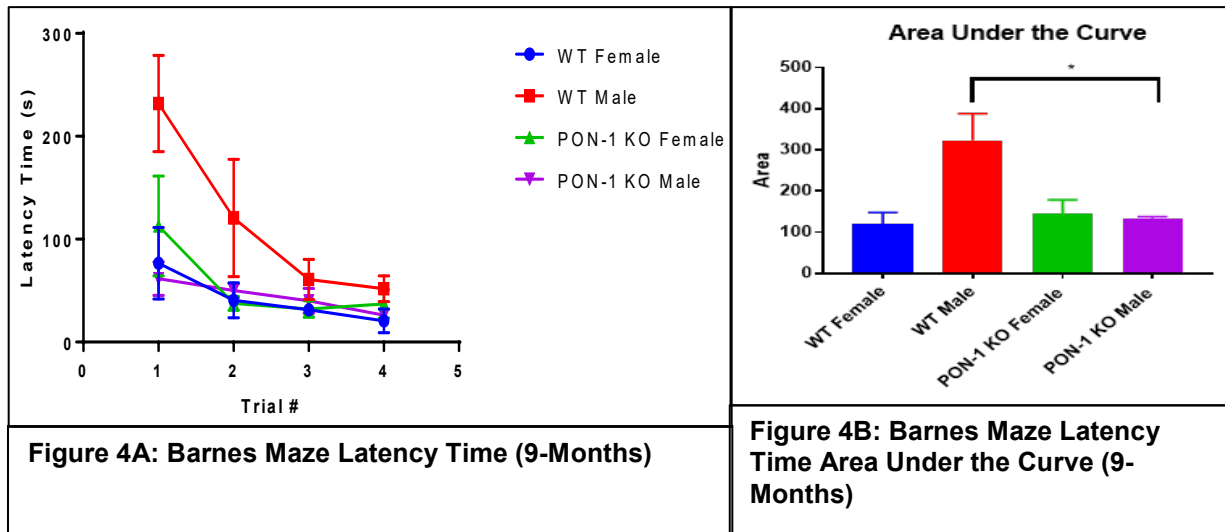
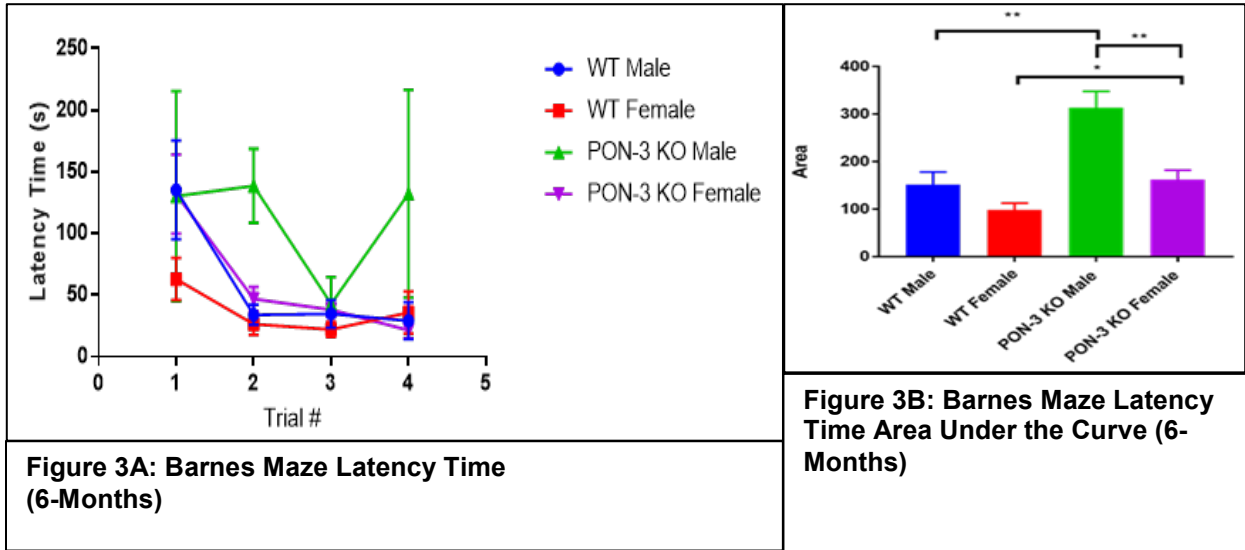
Figures/Charts



Figure 1: Barnes Maze



Figure 2: Open Field Maze



Acknowledgements

The author of this paper would like to thank Dr. David Kennedy and Dr. Steven Haller for their continued guidance and all the members of the Kennedy/Haller lab for their assistance and support in this research project. The author would also like to thank the Ohio Space Grant Consortium for their support.

References

1. Etgen T, Chonchol M, Forstl H, Sander D. Chronic kidney disease and cognitive impairment: a systematic review and meta-analysis. *Am J Nephrol.* 2012;35(5):474-482.
2. Bronas UG, Puzantian H, Hannan M. Cognitive Impairment in Chronic Kidney Disease: Vascular Milieu and the Potential Therapeutic Role of Exercise. *Biomed Res Int.* 2017;2017:2726369.
3. Coresh J, Selvin E, Stevens LA, et al. Prevalence of chronic kidney disease in the United States. *Jama.* 2007;298(17):2038-2047.
4. Fedorova OV, Lakatta EG, Bagrov AY. Endogenous Na,K pump ligands are differentially regulated during acute NaCl loading of Dahl rats. *Circulation.* 2000;102(24):3009-3014.
5. Draganov DI, Teiber JF, Speelman A, Osawa Y, Sunahara R, La Du BN. Human paraoxonases (PON1, PON2, and PON3) are lactonases with overlapping and distinct substrate specificities. *J Lipid Res.* 2005;46(6):1239-1247.
6. Mackness MI, Arrol S, Durrington PN. Paraoxonase prevents accumulation of lipoperoxides in low-density lipoprotein. *FEBS Lett.* 1991;286(1-2):152-154.

Evaluation of the Adhesive Properties of Glycoproteins in Snail Mucin

Student Researcher: Kayla Covington

Advisor: Dr. Bi-min Zhang Newby

The University of Akron

Department of Chemical and Biomolecular Engineering

Abstract

A biopolymer, such as snail mucin, could be pivotal in the development of strong adhesives for wet conditions. Determining the adhesive properties of the viscoelastic glycoprotein complexes within snail mucin is the first step before enhancing the adhesive strength through increased cross-linking. In previous studies, the JKR method has been used to quantify adhesion between elastomers with a sphere-plane geometry. The same method was applied to *Cornu aspersum* mucin. Due to the high water content (>99.9%) of the mucin, modifications to the JKR measurements, such as extended contact time, or utilizing the probe tack test or peel test may be necessary to obtain accurate adhesion properties.

Project Objectives

Strong adhesives in wet conditions could be highly beneficial for underwater and medical applications. Snail mucin is known to have excellent adhesion properties, and its main constituent is a mucin-like viscoelastic glycoprotein complex that is biocompatible, biodegradable and antimicrobial.¹ Certain ions, both anions and cations, can lead to changes in protein solubility and crosslinking, resulting in mechanical property alterations.² In the proposed project, the adhesive properties of snail mucin will be evaluated to allow for further studies into the effects of some of these ions (e.g., sodium, calcium, thiocyanate, sulfate) on the extent of cross-linking, hence the viscoelastic properties and consequently the adhesion strength of the modified snail mucin. The optimal goal is to provide some needed insights in generating strong snail mucin-based adhesives for various underwater applications.

Methodology Used

Garden snails, *Cornu aspersum*, with an average weight of 6 g and shell diameter of 27 mm, were purchased commercially. They were housed in a mason jar containing a layer of soil under a mixture of green sphagnum moss and pillow moss. Ventilation holes were placed in the lid and distilled water was added to rehydrate the soil and the moss. Snails were placed on top of the moss and fed a diet of kale and iceberg lettuce every 3 days. Misting with distilled water was performed weekly to maintain humidity within the jar. To collect snail mucin, snails were placed on a petri dish and allowed to roam for 15-30 minutes. Distilled water was occasionally dripped onto the snails to maintain their hydration and encourage mucin production. The mucin was collected from the dish with a pipette and placed into Eppendorf tubes. Snail mucin collection ranged from 150 – 300 μL per snail.

The adhesion measurements were carried out using a set up for contact mechanics, in which the modulus of the system, work of adhesion, and adhesion strength can be measured. The set up consisted of a data logging analytical scale for recording the contact force (or load), a digital microscope for monitoring the contact area, a stand for suspending the sample above the microscope, and a x-y-z stage for attaching a probe and manipulating the probe movements (Figure 1). The probe was prepared by melting a glass capillary tube to form a bulb tip and then bending at a 90° angle 1-2 cm from the tip. The tip was then modified with a hydrophobic agent, octadecyltrichlorosilane (OTS), as described by Taokaew et al.³ Samples consisted of a layer of mucin (~150 μL) on top of a thin layer of 10% gelatin (700

μL per 35 mm petri dish) to prevent the sample from drying out too quickly. Partially dehydrated samples were also prepared by allowing the mucin to dry until the surface was no longer wet (~ 1.5 hrs.). The control consisted of a thin 10% gelatin layer with 150 μL of 15% gelatin applied on top. During each test, the contact area and contact load were recorded every second, and the probe was moved downward until contact with the sample was made and held at that position for 10-15 seconds before moving the z stage downward by ~ 10 microns. After 5-10 downward movements (i.e., loading), the z stage was moved upward (i.e., unloading) with 10-15 second pauses until the probe detached from the sample. The adhesive properties of the samples were determined with the Johnson, Kendall, and Roberts (JKR) method,⁴⁻⁵

$$\frac{a^{3/2}}{R} = \frac{1}{K} \left(\frac{P}{a^{3/2}} \right) + \left(\frac{6\pi W_A}{K} \right)^{1/2} \quad (1)$$

where a represents the radius of the contact area, R is the radius of curvature of the probe, P is the applied load, K is the effective modulus of the system, W_A is the work of adhesion between the probe and the sample. During the unloading measurement, W_A is replaced by G , which is the adhesion strength between the probe and the sample. For a stronger adhesion, the value of G is expected to be larger.

Results Obtained

The as collected mucin had a very low solid content of about 0.1 wt. %. Figure 2 is a representation of a set of data gathered and presented based on the JKR model for the control (C), as collected (hydrated) mucin (H), and partially dehydrated mucin (PD) samples. The W_A values for samples C, H, and PD were 88, 5, and 144 mJ/m^2 , respectively, with G values of 125, 18, and 193 mJ/m^2 , respectively. As compared to control, the PD mucin resulted in a 30 – 40% increase in both W_A and G .

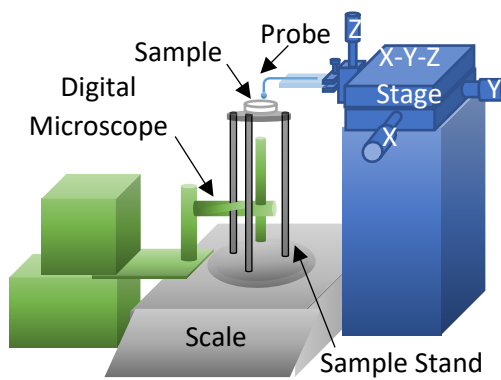


Figure 1. The adhesion test apparatus setup used for the experiments consisted of a data logging scale, sample stand, digital microscope, x-y-z stage, and a probe attached to a glass slide clamped to the stage.

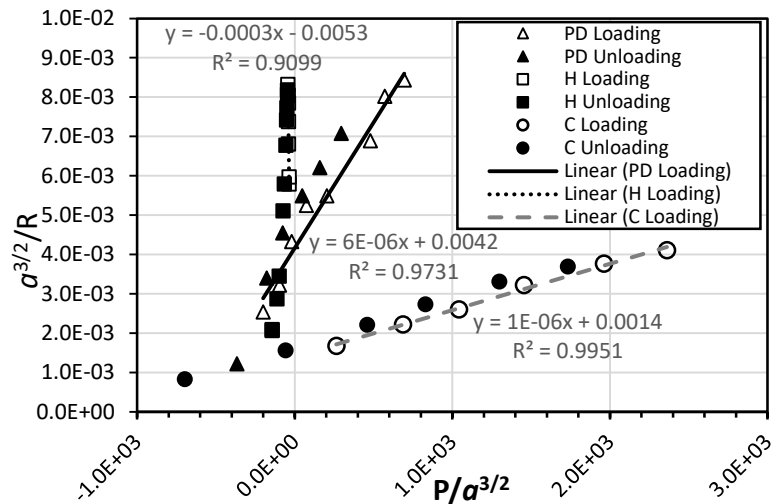


Figure 2. The relationship between displacement and force for control (C), hydrated mucin (H), and partially dehydrated mucin (PD).

Significance and Interpretation of Results

The solid content (~ 0.1 wt.%) was much lower than the reported value of 2 – 8 wt.%,⁷ it could be the result of water needed to stimulate snails to release their mucin or due to the snails being stressed during mucin collection. The W_A for the control matched the expected results.⁶ However, the negative slope and low work of adhesion from the hydrated snail mucin indicates that the current setup, which was designed for determining the properties of elastic or highly viscoelastic materials might not be

suitable for determining the adhesion properties of an extremely low viscosity liquid that contains primary water (> 99.9%). The JKR method is not generally applicable for the deformation of a low viscosity liquid drop. When the same procedure was applied to a 150 μ L drop of deionized water, negative slope also resulted. The PD sample might represent the actual mucin better. Other methods might be able to obtain more reasonable adhesion behaviors of the snail mucin, unfortunately, those experiments were not attempted due to the lack of time and the limited amount of snail mucin we could collect. These potential methods are: (1) hold the probe in contact with snail mucin until it gels, then follow with unloading measurements to obtain the adhesion strength, (2) apply the probe tack test or peel test using a thin layer of snail mucin.

Acknowledgements

The author would like to thank her advisor, Dr. Bi-min Zhang Newby, as well as the Ohio Space Grant Consortium for the opportunity to conduct this research.

References

1. Gabriel, U. I., Mirela, S., & Ionel, J. (2011). Quantification of mucoproteins (glycoproteins) from snails mucus, *Helix aspersa* and *Helix Pomatia*. *Journal of Agroalimentary Processes and Technologies*, *17*, 410-413.
2. He, Q., Huang, Y., & Wang, S. (2018). Hofmeister Effect-Assisted One Step Fabrication of Ductile and Strong Hydrogels. *Advanced Functional Materials*, *28*, 1705069.
3. Taokaew, S., Phisalaphong, M., & Newby, B.-m. Z. (2015). Modification of bacterial cellulose with organosilanes to improve attachment and spreading of human fibroblasts. *Cellulose*, *22*, 2311-2324.
4. Flanigan, C. M., & Shull, K. R. (1999). Adhesive and Elastic Properties of Thin Gel Layers. *Langmuir*, *15*, 4966-4974.
5. Shull, K. R. (2002). Contact mechanics and the adhesion of soft solids. *Material Science and Engineering Reports*, *36*, 1-45.
6. Thakre, A. A., & Singh, A. K. (2019). Specimen Thickness Dependency of Energy Release Rate of a Gelatin Hydrogel and Glass Substrate Interface. *Journal of Tribology*, *141*, 021801.
7. Machin, J. (1964). The Evaporation of water from *Helix aspersa*. *Journal of Experimental Biology*, *41*, 759-769.

Detection of Hazardous Gases Using 3D Printed Platforms

Student Researcher: Alexis C. Cresanto

Advisor: Dr. Pedro Cortes

Co-Advisor: Dr. Eric McDonald

Youngstown State University

Chemical Engineering

Abstract

Society is threatened daily by potentially harmful chemical substances that may not be detectable by human sensing. It is essential that these chemicals can be detected accurately and immediately before lives are threatened. To accomplish this, carbon nanotubes are being used as the main detection material in sensor creation because of their electrochemical properties. These properties allow them to detect changes in conductivity in the presence of a foreign substance. The carbon nanotubes must be functionalized specifically for the chemical in testing so that the sensors will not detect incorrectly to similar substances. The production of small and integrated sensors is a beneficial feature for commodity on wearable structures. The answer to this requirement is the incorporation of additive manufacturing on the production of bio-chemical sensing platforms.

Project Objectives

The goal of this research work is to produce 3D printed structures assisted with Multi-Wall Carbon Nanotubes (MWCNTs) to detect hazardous gases. The gases being detected in this study were ammonia (NH_3) and Nitrogen dioxide (NO_2). The MWCNTs were physically functionalized with different polymers that were selective to each gas.² Figure 1 below shows the scanning electron microscope view of the MWCNTs.

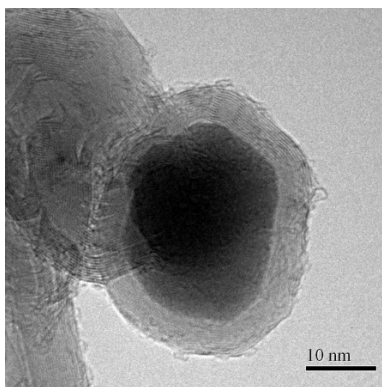


Figure 1. SEM image of a Multi-walled Carbon Nanotube

Methodology Used

Carbon nanotubes have electrochemical properties that allow them to detect changes in conductivity in the presence of a foreign substance. The functionalized MWCNTs were selective towards the different gases based on which polymer was used. To gather this data, different polymers were tested with each

gas and resistance was recorded. Ammonia was best detected when polyether glycol (PEG) was used to functionalize the MWCNTs, while nitrogen dioxide was best detected with polyaniline (PAN) as the polymer.² A ratio of 1:1 v/v of the MWCNTs in water and the polymer in water were combined. This mixture was layered on an electrode. The electrodes voltage was subsequently tracked using a DAQ system while it was in an enclosed chamber with one of the gases present. Ammonia was created by combining 1 gram of ammonium chloride and 20 microliters of a sodium hydroxide and water mixture.² Nitrogen Dioxide was created by placing 20 microliters of nitric acid on a copper sheet.²

Results Obtained

Ammonia was detected as seen in figure 2, showing that the resistance increased with the presence of NH_3 .

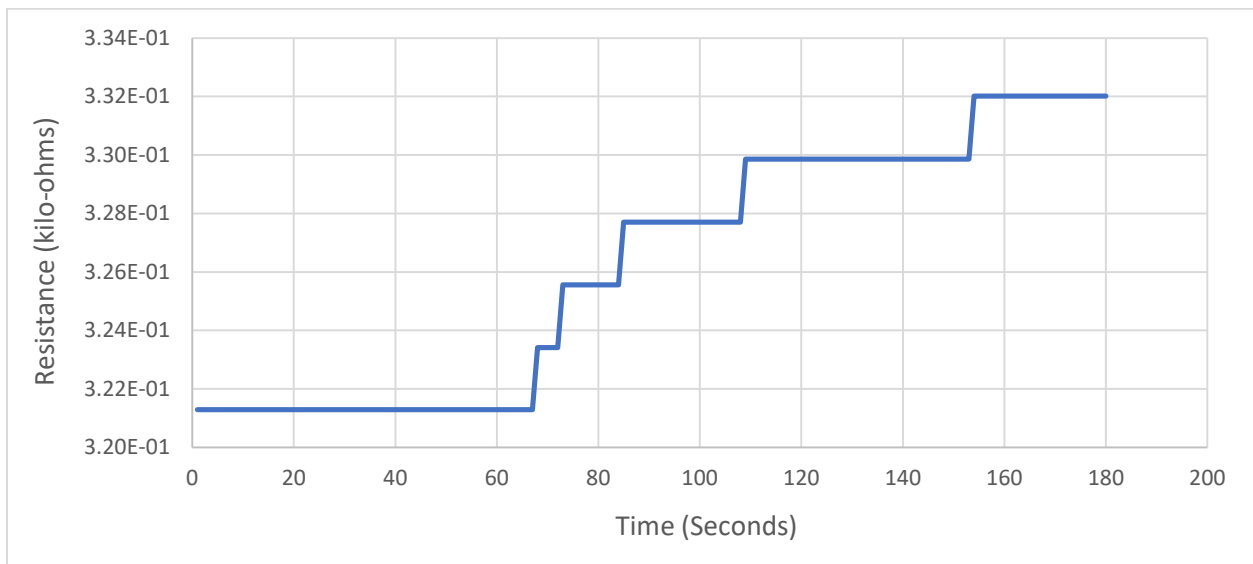


Figure 2. Graph showing detection of NH_3 gas on MWCNTs

Nitrogen dioxide was detected as seen in figure 3, showing that the resistance decreased with the presence of NO_2 .

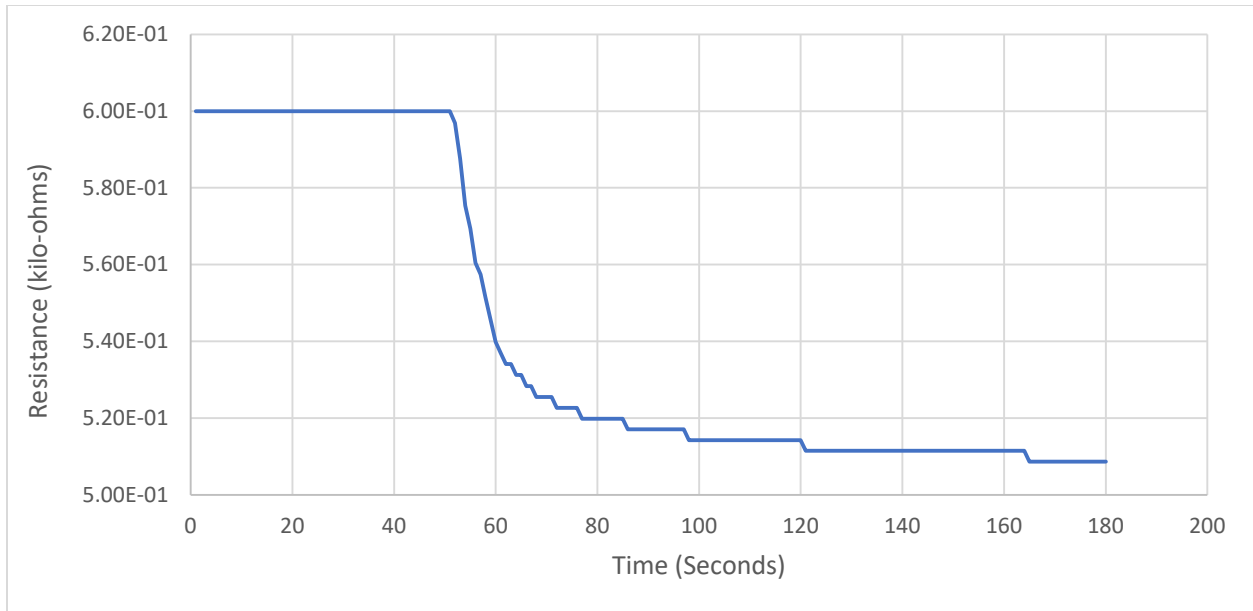


Figure 3. Graph showing detection of NO₂

Current Work

Following the detection on commercial electrodes, the MWCNTs combined with polymers were incorporated onto 3D printed sensors, as seen in figure 4. Here, when the gas was detected, the light started flashing.

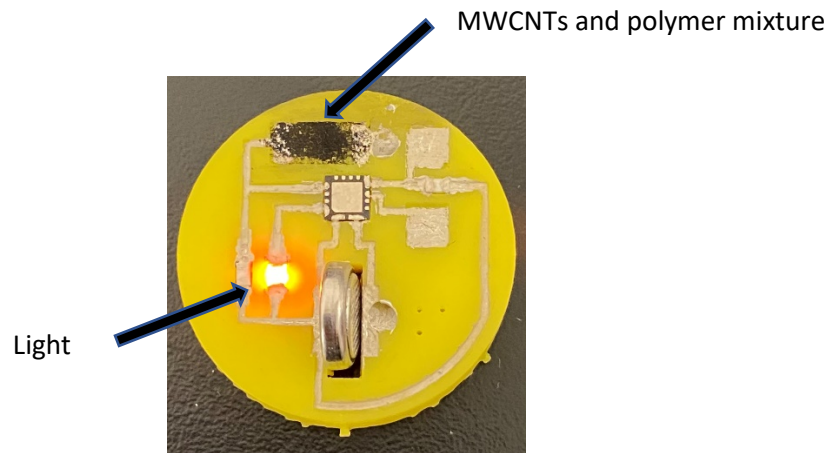


Figure 4. 3-D printed sensor based on a voltage divider workflow

The 3D printed sensor in figure 4 was produced to detect NH₃. PAN has been used with the MWCNTs to create a sensor that detects NO₂ as well. Future efforts will concentrate on detecting other gases like carbon monoxide.

References

1. Anderson, M. (2015, March 19). Multi-walled carbon nanotube. Retrieved March 11, 2021, from <https://www.fei.com/image-gallery/multi-walled-carbon-nanotube/#gsc.tab=0>
2. Olszewski, M. Lara-Romero, J. Cortes, P. (2012). "The Detection Properties of Bulky Wrapped MWCNTs Towards Hazardous Gases". *NSTI-Nanotech*, 1, 256-259.

In-Situ Process Monitoring of Additive Manufacturing

Student Researcher: Sabrina D'Alesandro

Advisors: Kelly Davis, Alexander Groeger, Joy Gockel, Tanvi Banerjee, Joe Walker, Jon Middendorf

Wright State University
Engineering and Computer Science

Introduction

Additive manufacturing (AM) is known as the layer-by-layer style of manufacturing products and parts. This is completed by depositing a layer of material on a build plate in the shape of the part and repeating the process iteratively until the completion of the build. AM has numerous benefits that make it an attractive manufacturing method; however, defects continue to be a problem scientist need to mitigate against. The most challenging defect are pores, which are holes or voids in the material. Pores present a challenge in AM parts due to the rapid change in geometry which creates crack propagation leading to the premature failure of parts. A specific type of AM process which struggles with porosity is laser powder bed fusion (LPBF). LPBF is a metal AM process which builds parts with melted metal powder. The operator then excavates the part in the remaining pool of powder. To observe the LPBF process and mitigate against possible defects, in-situ monitoring is used. In-situ monitoring is the real time observation of the AM process using numerous sensors within the machines to gather data about the efficiency while the machine is in use. These sensors include tomography, spatter, long wavelength infrared (LWIR), and more. This project will focus on the image processing of the LWIR in-situ data. Infrared data is particularly useful at analyzing differences in temperature for a given area on a material. Due to this application of the sensor data, it will be used to analyze the melt pool data. LWIR data gives information about significant thermal relationships for the thermoelectric material and its melt pool. After the sensors have collected the data from the printing process, it outputs raw form data. The data comes in many different types but is typically a photograph format such as a .tiff, .jpeg, or .bin. The raw data must then be processed using image processing techniques. These techniques are crucial when using in-situ monitoring data because it formats the images allowing for quantification of the data. The subsequent sections of this paper will discuss the experiment, image processing techniques and results from this project.

Experiment and Results

The goal of the project is to develop a machine learning model to accelerate additive manufacturing of thermoelectric materials. The steps of this project are to first complete single bead experiments. Then a process map will be made using potential parameters for the LBBF machine. This will explore the varying laser speeds and power that will directly impact the melt pool size. Next, 4 coupons with varying parameters will have the material deposited on it. The parameters that will be used will be the parameters chosen from the process map. Then training data will be made, which includes 50 samples. This will gain the team practice of the sample preparation. Meanwhile the image processing will be completed so the machine learning model can be constructed. In subsequent sections of this paper, the experiment will be explained and analyzed. Figure 1 shows the completed process map using bismuth telluride parameters that will be used for the experiment and the table below outlines the parameters.

Figure 1

Coupon Line	1	2	3	4	5	6	7	8
Laser Speed (mm/s)	400	700	1000	1300	700	1100	1500	1900
Laser Power (W)	30	30	30	30	50	50	50	50
Coupon Line	9	10	11	12	13	14	15	16
Laser Speed (mm/s)	900	1400	1900	2400	1100	1600	2100	2400
Laser Power (W)	70	70	70	70	90	90	90	90

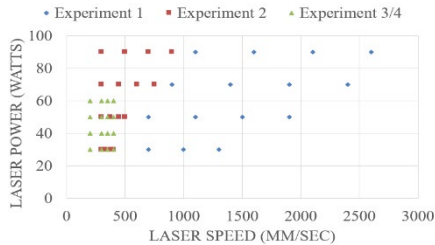


Figure 1 shows the experiment process map. Source: Author.

It is shown from Figure 1 that as the laser speed is increased, it will be expected that the melt pool will decrease. This phenomenon expected to be observed because as the laser speed is increased, there will be less time that the thermal energy will be focused on the material. As the power is increased the melt pool should decrease. Unlike the laser speed, as power is increased more thermal energy will be focused on the material, increasing the overall melt pool width. After the process map is completed the next stage of the experiment can be conducted. In this stage, 4 coupons will have bismuth telluride deposited on it with varying laser speeds and laser powers. On each of the 4 coupons there will be 16 lines. Figure 2 shows the coupon images after the experiment was conducted.

Figure 2

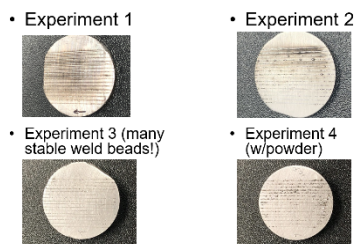


Figure 2: Experiment 1 images. Source: Author.

Looking at the coupon visually, there are distinct differences. It can be seen by the eye that experiment 2 has rounder beads than experiment 1. Finally, experiment 3 is seen to have the most stable beads of all the experiments. Experiment 4 was conducted with also laying down a layer of powder to test how the material would melt. It shows more beads but provides knowledge of which parameters are optimal. This is important to the quality of full build with Bismuth Telluride. Next, optical microscope images were taken of the melt pools of the experiments at 5x magnification. The first goal of this experiment was to have few gaps in the melted line length. Figure 3 shows a closer image of the experiment 1 melt pools.

Figure 3

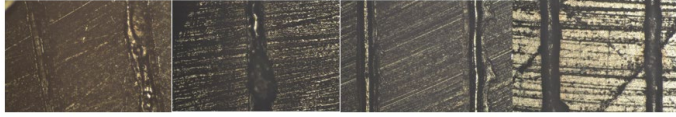


Figure 3: Melt pool from 4 experiments. Top left: Experiment 1, top right: experiment 2, bottom left: experiment 3, bottom right experiment 4.

Observing figure 3, important takeaways can be noted. Experiment 1 shows a consistent weld of the material. However, experiment 2 has more large beads on the surface. Experiment 3 shows the most consistent, and optimal melt pool. There are few round beads on the surface, and the weld is consistent. Finally, experiment 4 also involved powder and showed many round beads on the surface. Once the experiments are conducted the machine learning model can be created. Machine learning is a set of algorithms that is given data to predict and complete tasks [1]. In this experiment the machine learning model is fed the in-situ monitoring data, so it can learn which parameters create defects. This model will then be able to predict defect creation from given parameters. However, the in-situ data must first be processed using image processing techniques to give the model an accurate view of the material during the printing.

Image processing is the method of manipulating a set of images to visualize meaningful data from the sensors. Image processing is an integral step in the experimentation process so meaningful relationships can be extracted from the raw data. The steps for image processing usually follow the following: sensor, output image, programming, created output image, and analysis. Once the sensor has gathered the data it outputs the raw data in image format. After the output image has been collected, programming is required to change the image in a meaningful way to extract the material relationships. After the sensors initially collected the data, the raw data comes in a series of binary images for each layer. These binary images can be visualized using FIJI, but it will not show the entire layer. To see the whole layer, with all the thermal data the code must be used. The code first opens the directory with the binary files. Next because the resolution is a 4:3 ratio, a matrix is made of zeros that is (480 by 640). Next all the images are iterated through the code. We are then interested in the max value of each pixel to interpret the images, so the axis is specified so it takes the max value across all the layers for each pixel in the layers. This will output a grayscale image of width 640 and height 480. Figure 8 shows an example of one of the LWIR images after the code is ran.

Figure 4

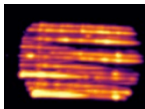


Figure 4: LWIR Image. Source: Author.

Using images like Figure 4, thermal data can be analyzed. Melt pool data is easily extracted with LWIR data due to the varying temperatures on the material. To get data about the melt pool first the width of the lines is analyzed. Using FIJI image software, the widths of all 16 lines were measured. Figure 5 shows the widths for the lines on experiment 1.

Figure 5

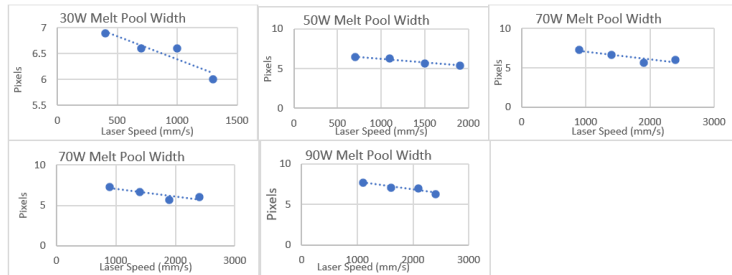


Figure 5 shows the melt pool width for the varying laser power.

The melt pool width results show negative trends lines for each of the various laser speeds. This is too be expected since as the laser speed increases the width should decrease due to less thermal energy concentrated in the material. Now that the experiment has obtained these expected results from experiment 1, in future work the workflow can be applied to the next 3 experiments.

Conclusion

AM is a style of manufacturing that saw a rise in popularity due to its ability for rapid prototyping, wide material choice, and low cost. However, despite these benefits many types of AM processes including LPBF struggle with defects including porosity. In order to mitigate against porosity in-situ monitoring, the real-time collection of data, has begun to be used to monitor the LPBF process. In this experiment in-situ monitoring was done of the LPBF process as it printed the thermoelectric material Bismuth Telluride. Modeling of the parameters was done in order to accurately predict the expected relationships between laser power and speed. It was expected that faster power would have smaller melt pools and higher power would have larger melt pools. Next, the in-situ monitoring data was processed using image processing techniques. The image processing of the in-situ monitoring data was an integral step in this experiment so that meaningful relationships could be extracted from the data. The image processing techniques allowed for the visualization of the data and the graphical analysis of the data. One of the sensors, which was the primary focus of this paper was LWIR data. This was a type of in-situ monitoring data that showed the thermal comparisons of various areas on the printed coupon. This gave valuable relationships about the melt pool data that could be used to aid in the machine learning model. In the future, more data will be processed to continue to improve upon.

References

[1] <https://www.nber.org/system/files/chapters/c14009/c14009.pdf>

Optimization of Lunar Rover Suspension

Student Researcher: Mark A. DeAngelis

Advisor: Dr. Jason M. Walker

Youngstown State University

Rayen School of Engineering, Mechanical Engineering Program

Abstract

The Youngstown State University (YSU) Robotics Team will be competing in the 2020 NASA Lunabotics Competition with the task of designing, building, and programming a rover that must traverse a simulated lunar surface as autonomously as possible to mine icy regolith (gravel) at a secondary ground layer 30 cm below the surface. This rover must meet specified volume, mass, and design constraints, as well as be capable of handling various obstacles. As such, a small, lightweight suspension system capable of meeting these requirements was designed to potentially increase the performance of the team's rover. A broad range of suspension systems have been utilized and proposed for planetary rovers, but a novel solution had to be implemented for this rover which is substantially smaller in size. Specifically, an active, four-wheeled suspension system was designed to increase the mobility of the rover as it crosses slopes craters and boulders.

Project Objectives

In accordance with the NASA Lunabotics competition, the overall rover was required to fit within an initial volume of 1 m long, 0.5 m wide, and 0.5 m tall, and have a maximum mass of 60 kg. The rover must also be capable of avoiding or crossing boulders and craters. Additionally, since the designed suspension system was created for the YSU Robotics Team rover – shown in Figure 1 – it had to remain contained to the sides of the rover to ensure enough space at the center of the rover for the digging system to pivot and operate. Thus, the overall objective of this suspension system was to be lightweight, compact, and be compatible with the YSU rover.

Methodology

A wide variety of suspension systems have been utilized and proposed for planetary rovers – including the six-wheeled, rocker-bogie system on all of NASA's Martian rovers called the Mars Exploration Rovers (MER) [1]. While there are a number of categorizations for suspension systems, two specific areas that were noted during a comprehensive literature review were the number of wheels on the rover, and whether the system was active (actuated using a powered device) or passive (moves from external forces). A four wheel system was desired to better mirror the design utilized for the YSU rover as shown in Figure 1, and either a passive system or active system with minimal motors was necessary to minimize the amount of added mass. Through the research of previously designed systems, a novel design was developed to suit the NASA Lunabotics Competition's requirements.

Many of the suspension systems for planetary rovers have consisted of six wheels and utilize kinematic mechanisms to actuate the positions of those wheels. This allows for a greater range of motion, as well as the ability to almost always ensure that a minimum of four wheels are on level ground when crossing over large obstacles. Thuerer and Siegwart [1] discuss three such passive designs – called MER, RCL-E, and CRAB – and analyzed their kinematic performance and wheel slippage. However, other researchers have proposed an active rocker-bogie system similar to MER that utilizes a "wheel-step" to reduce slippage [2]. One set of wheels is braked, and then an adjacent set of wheels is driven while the suspension system

raises or lowers to allow the rover to reduce slippage and better navigate “a looser sand trap and climb a steeper slope”; this process is shown in Figure 2 [2].

Several four wheeled designs have also been devised with varying strengths and weaknesses. For example, the four-wheel-rhombus-arranged (FWRA) design created by Wen et al. [3] mimics the wheel locations of a six-wheel design but has stability issues from placing two of the four wheels in the front and back of the rover, and the other two on the sides. Also, the wheel-walking design by Malenkov and Volov [4] has a highly complex drive system with wheels placed at the end of independently controlled legs, thus having higher mobility. However, the Scarab design shown in Figure 3 by Bartlett, Wettergreen, and Whittaker [5] appears to be a viable four wheeled option for the NASA Lunabotics competition, having significant changes in ground clearance and good stability, but its “body averaging” mechanism would take up too much space on the inside of the rover for the large, actuated digging system the YSU rover plans on using.

Results

The final suspension design created as shown in Figure 4 (which excludes the rest of the rover for clarity) was inspired from the active rocker-bogie and Scarab suspension designs. This design utilizes a five-bar kinematic mechanism (shown in blue) on each wheel that is extended with a linear actuator (grey), which is similar to the concept used in the Scarab. As shown in Figure 5, this allows for an additional 5.5 cm of ground clearance with only 1 inch (2.54 cm) of extension from an actuator capable of outputting 400 lbf. In conjunction with the wheel-step driving process, this type of mechanism should assist the rover with traversing through the sandy arena, slopes, and obstacles faced in the NASA Lunabotics Competition. Additionally, the overall suspension system would add a total of 5.80 kg to the entire rover (2.90 kg per side) and fits within 13 cm on either side of the rover. This was done through the use of 6061 aluminum rectangular tubing and plates (shown in yellow in Figure 4), and 0.25 inch thick 7075 aluminum plates for the kinematic mechanism.

Significance and Interpretation of Results

Given that payload mass and volume on rockets to space is scarce, it is important to design planetary rovers that are lightweight and compact. The created design is a possible solution that interfaces with the already-built wheels and frame of the YSU rover that meets the competition’s constraints and project objectives. This design was based largely on the material composition and structure of the YSU rover as it is currently designed. With the use of readily available supplies such as 8020 extruded members (shown in orange in Figure 4), and manufacturing techniques that have been proven to work – such as carbon fiber reinforced 3D printed brackets (shown in black in Figure 4) as frame structural members – the design could be produced by the YSU team. However, its benefit for traversing the competition arena will have to be weighed against the points lost in the competition due to increasing the rover’s mass by 13.5%. Should future teams attempt to construct this design, it would be recommended to optimize the mass of the kinematic mechanism, which held most of the added mass besides the linear actuator. Also, by altering the internal structure of the rover such that additional depth could be added to the suspension system, more support members could be added to prevent deflection of the kinematic mechanism.

Figures/Charts

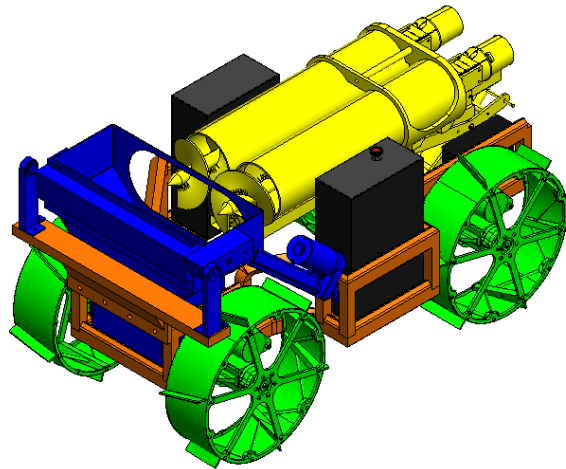


Figure 1. The Youngstown State University NASA Lunabotics Competition rover design.

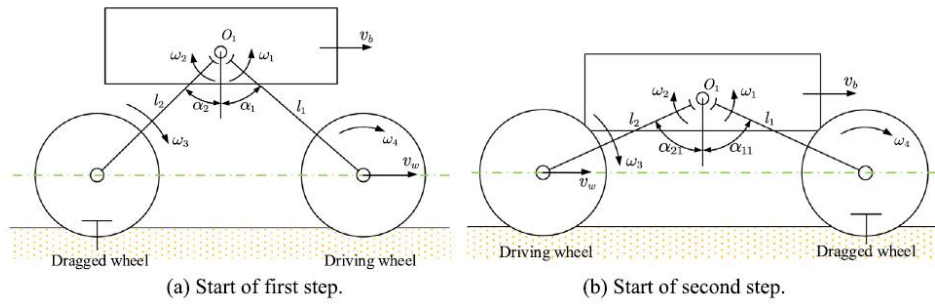


Figure 2. Diagram of the wheel-step driving process. Image sources: Reference [2].



Figure 3. Varying ground clearances of the Scarab suspension design. Image sources: Reference [5].

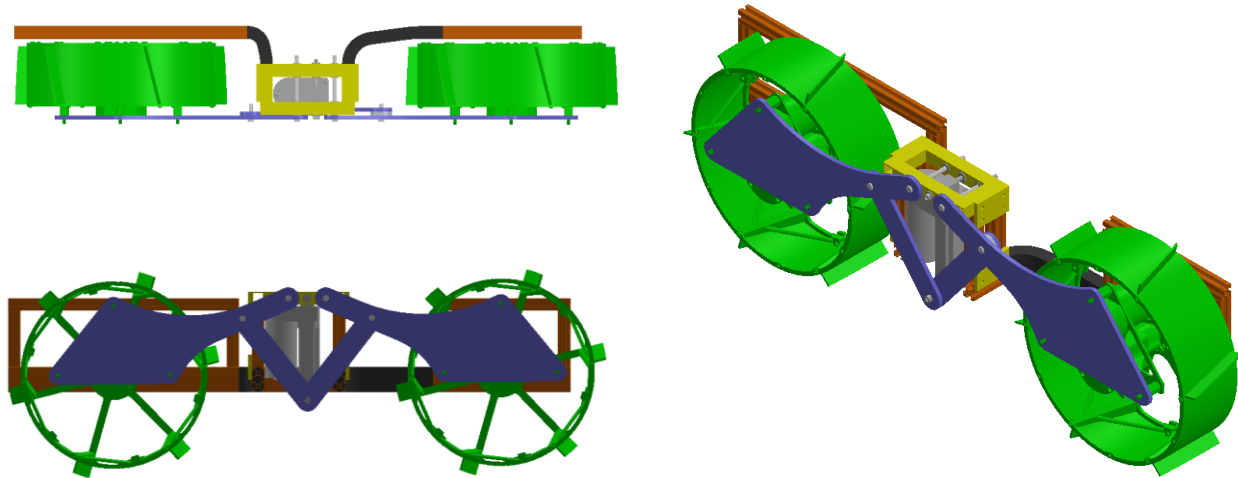


Figure 4. Top, front, and isometric views of the suspension system for the YSU NASA Lunabotics rover.

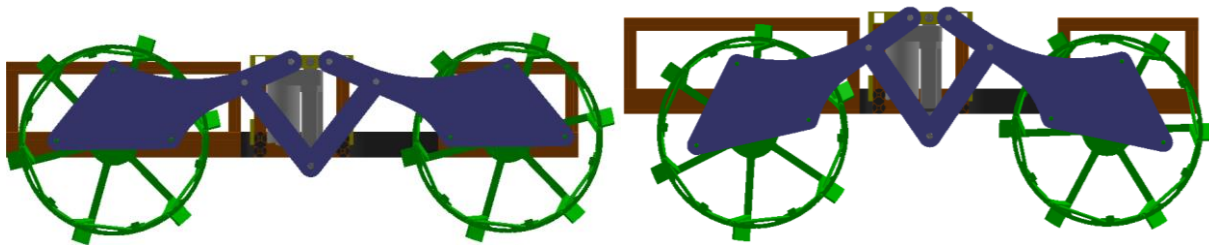


Figure 5. Novel suspension system design at its extreme positions.

Acknowledgments

The author would like to thank the Ohio Space Grant Consortium for this opportunity and their sponsorship. Also, the author would like to express their gratitude to the faculty who encouraged and supported this research, including Dr. Jason Walker, Dr. Kevin Disotell, and Dr. Hazel Marie.

References

- [1] Thueer, T., and Siegwart, R. "Characterization and Comparison of Rover Locomotion Performance Based on Kinematic Aspects." *Field and Service Robotics*. C. Laugier, and R. Siegwart, eds. Springer Berlin Heidelberg, Berlin, Heidelberg (2008): pp. 189–198. DOI 10.1007/978-3-540-75404-6_18.
- [2] Zheng, J., Gao, H., Yuan, B., Liu, Z., Yu, H., Ding, L., and Deng, Z. "Design and Terramechanics Analysis of a Mars Rover Utilizing Active Suspension." *Mechanism and Machine Theory* Volume 128 (2018): pp. 125–149. DOI 10.1016/j.mechmachtheory.2018.05.002.
- [3] Wen, G., Ma, C., Cheng, D., Jin, Q., Chen, Z., Yang, X., Yin, H., and Zhou, J. "A Four-Wheel-Rhombus-Arranged Mobility System for a New Lunar Robotic Rover." *International Journal of Advanced Robotic Systems* Volume 10 No. 10 (2013): p. 370. DOI 10.5772/56917.
- [4] Malenkov, M. I., and Volov, V. A. "Wheel-Walking Propulsion Unit of a Planetary Rover with Active Suspension." *Russian Engineering Research* Volume 37 No. 12 (2017): pp. 1033–1040. DOI 10.3103/S1068798X17120127.
- [5] Bartlett, P., Wettergreen, D., and Whittaker, W. "Design of the Scarab Rover for Mobility & Drilling in the Lunar Cold Traps." (2008). <https://lens.org/037-544-311-450-980>.

Water Purification with a LED UV-C Reactor

Student Researcher: Kevin Decato

Advisor: Dr. Glenn Lipscomb

University of Toledo

Chemical Engineering Department

Abstract

Access to clean drinking water is one of the world's largest problems of our generation. As global populations tick upwards, an estimated 663 million lack access to an improved source of drinking water [2]. While of course there are a variety of water treatment methods that exist the today, the struggle has always been finding a method that consistently works in developing parts of the world, which often lack access to the requirements of these alternative methods, as well as the capital to purchase and maintain them. A UV-C photoreactor to inactivate bacteria and viruses constructed using LED bulbs addresses many of these issues.

A traditional UV-C reactor utilizes a fluorescent bulb that emits a wavelength of UV-C radiation at 254 nm. This wavelength of UV-C light inactivates the bacteria and viruses by catalyzing a reaction between amino acids that fuses their DNA together, preventing reproduction and thus preventing illness [4]. The optimal range for this process to occur is between 250-280 nm and varies between microorganisms. While the fluorescent bulb has worked to date, there are many improvements to be made around the design, especially with the development of LED lights that mimic the same UV-C output as fluorescent bulbs. LED chips offer a more robust 40-50% power efficiency compared to the 20-30% of the fluorescent tube [3]. In areas where the power supply is lacking or given at a variable rate, the highest efficiency possible would be desired. LED chips also last 10 years compared to the 1 year of a fluorescent bulb, along with removing the complication of disposing fluorescent bulbs and the mercury within them [3]. Due to COVID-19 and a variety of factors, increased research into sanitization using UV-C light should have a positive effect on the price as demand and supply increase. The increased efficiency, longevity, and lack of maintenance makes the LED bulbs the superior choice for a UV-C reactor.

Personal Objective

The objective is to develop an alternative UV-C reactor using LED instead of fluorescent bulbs. This would allow the reactor to be more durable, environmentally friendly, require less maintenance and become more efficient.

Method

Although the LED bulbs are the future, it's not as simple as just switching them out with the fluorescent bulbs. Water flowing through the reactor needs to be exposed to a minimum cumulative fluence dose to achieve inactivation of the bacteria and viruses. While the required dose is fixed at 40 mJ/cm^2 , light intensity varies with distance (normal and angular) from the bulb surface and is dependent on bulb and water flow channel design [1]. Currently, we are evaluating alternative flow channel designs that give sufficient fluid residence time to achieve the target dose. One of the biggest challenges is measuring intensity as a function of distance and angle for use in design calculations. Currently all intensity information and measurements are provided by the LED supplier but we are evaluating options for making measurements locally. For example, the bulb intensity at $\frac{1}{2}$ inch distance is 1.821 mW/cm^2 and 1 inch is $.582 \text{ mW/cm}^2$, indicating a significant decrease over $\frac{1}{2}$ inch distance [3]. Also, the light is confined

to a 120 degree angle conical volume, meaning that if we had a 1 inch depth in our channel, the water in the bottom right corner would be exposed to a much lesser intensity than water flowing directly in front of the bulb due to the intensity fall off from distance and angle. Switching from a fluorescent tube as the light source to a light bar containing 5 LED chips means that there isn't a uniform intensity output coming from one bulb across the whole channel. Instead, we have to measure the intensity coming from 5 point sources. Proposed designs include a 1-inch deep channel with light bars along the channel top and bottom. Once the relationship between intensity and distance is known, computational fluid dynamics software will be used to evaluate cumulative fluence for different photoreactor designs (channel shape and bulb placement).

Preliminary Results and Future Work

Given that this is a major improvement on an existing design, we know what fluence dose is required and the general design of the reactor. Since the relationship between intensity and distance is unknown, we cannot evaluate design parameters a priori.

For prototype development, we purchased a light bar with 5 LED chips emitting UV-C light at 276 nm (This wavelength corresponds to the solid red line in Figure 1) which is comparable to the 254 nm light from a mercury fluorescent bulb (This wavelength corresponds to the solid green line in Figure 1)[3]. Water that flows through the channel needs to receive a cumulative fluence dose of 40 mJ/cm². Once we establish the relationship between fluence and distance from the bulb, optimal dimensions for the channel will be determined and the required residence time calculated. The results will establish the maximum water flow rate that can be treated for comparison to experimental measurements.

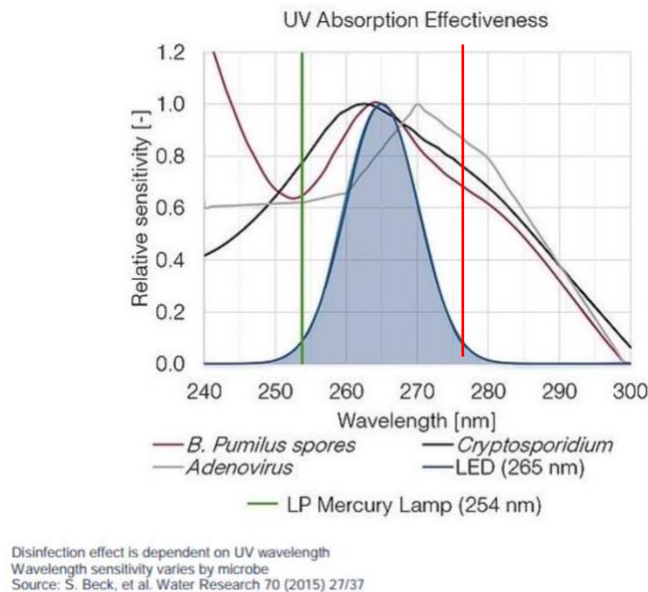


Figure 1. Relative sensitivity of various microorganisms to inactivation as a function of light wavelength.

Conclusion

The LED UV-C reactor offers a more efficient version of its predecessor. Although reactor designs have not been optimized, the designs are expected to be more efficient, environmentally friendly and durable than the current fluorescent bulb reactor. The longevity of the LED bulbs allows the unit to remain in place for 10 years without significant maintenance, which is a massive improvement upon the current design in which the fluorescent bulb has to be replaced annually. As the world shifts in a new direction,

Increased research in UV-C light being used in sanitization should reduce the overall cost of the LED chips as production ramps up and a greater demand develops. With major developments in efficiency and design, more people will be able to reap the benefits of this type of reactor.

Sources

- 1.) "UV-FAQs" IUVA, <https://iuva.org/UV-FAQs>
- 2.) "Drinking-Water." *World Health Organization*, World Health Organization, <https://www.who.int/news-room/fact-sheets/detail/drinking-water>.
- 3.) "UV-C Light Bar" Irtronix, <https://www.irtronix.com/uv-bar-uv1001t>
- 4.) "UV LED Benefit: Wavelength Selection." *Aquisense*, <https://www.aquisense.com/wavelength-selection>.

ONU Wind Tunnel

Student Researcher: William A. Deisler

Advisor: Jed Marquart

Ohio Northern University

Mechanical Engineering Department

Abstract

Wind tunnel testing is used throughout many aspects of engineering, from testing new cars to testing parachutes used to land the next rover on Mars. One of the most important aspects of wind tunnel testing is the calibration. Wind tunnel calibrations allow tunnel operators to ensure the tunnel is operating as expected, provides data which allows for interpretation and correction of test data, and provides a data-base for flow field parameter variability [1]. The wind tunnel at Ohio Northern was recently disassembled and moved to a new location, which could have significant effects on its operation. Performing a full calibration would verify the operating conditions within the tunnel and ensure accurate results obtained from testing.

Project Objectives

A full calibration would require hardware selection, installation and checkout, data acquisition and reduction system implementation, along with several other systems checkouts to ensure the calibration system is functioning properly. The objective of this project was to make recommendations for the calibration hardware to be used in a calibration of Ohio Northern University's open return wind tunnel. Additional research is needed to develop a data acquisition system and system checkout procedures should be established prior to any tunnel calibration.

Facility Overview

Ohio Northern University's wind tunnel is a modified Model 404 from Engineering Laboratory Design, which can be seen in Figure 1. Air is drawn in through the inlet, sent through a honeycomb and screen pack to straighten the flow, pulled through the test section and diffuser, then discharged to the atmosphere [2]. The tunnel is constructed from fiberglass laminate with a PVC foam core. Various tunnel characteristics are shown in Table 1.

Recommendations

The goal of a calibration program is to measure quantities such as total pressure, static pressure, and total temperature to calculate flow conditions such as mach number, Reynolds number, and dynamic pressure. These calculated measurements are then related to tunnel conditions such as motor speed, which allows the tunnel operator to reliably set the airspeed in the test section. Due to its relatively small test section, calibrations performed on the ONU tunnel should follow the point calibration method, which relates measurements taken at a specific point to the flow conditions throughout the

test section. This method requires the least amount of time to perform, provides a high degree of accuracy, and is relatively simple in terms of instrumentation required.

The primary instrumentation used for this calibration would be a pitot tube, to measure static and total pressure, and a thermometer to measure the total temperature. The pitot tube should be located horizontally at the primary model locations and vertically at tunnel centerline. For the ONU tunnel, the total temperature will be taken as the room temperature taken prior to testing. This temperature should be considered constant for any given run, but should be expected to fluctuate day to day. Additional hardware, such as temperature and pressure rakes, could be added to the test section for additional analysis, however this is not required for the calibration procedure.

Conclusions

Due to the small size of the test section, the calibration hardware required for the Ohio Northern University wind tunnel is relatively simple, one pitot static tube to measure static and total pressure and a thermometer to measure the total temperature of the facility which is assumed to be the test section total temperature. Follow up research is required to develop a data analysis system to process the calibration data. Additionally, a detailed list of pre-run checkouts should be developed prior to operating the wind tunnel to ensure both facility and personnel safety.

Figures and Charts

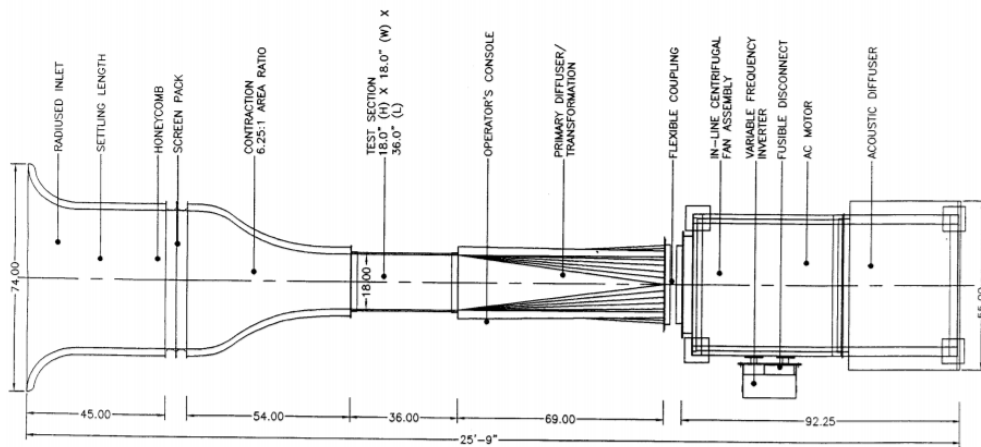


Figure 1: Approximate Ohio Northern University Tunnel Layout

Table 1: Wind Tunnel Performance Characteristics

Test Section Dimensions (in):	36L x 18W x 18H
Airspeed (fps):	10-100 (15hp motor) or 10-150(25hp motor)
Contraction Area Ratio:	6.25:1
Diffuser Expansion (degrees):	6

Acknowledgments and References

- [1] A. Arrington, et al., (2014, Sept. 24). *Recommended Practice: Calibration of Subsonic and Transonic Wind Tunnels* [online]. Available: <https://arc.aiaa.org/doi/10.2514/4.476624.001>
- [2] Engineering Design Laboratory, (1996). *18" Open Circuit Wind Tunnel - Model 404* [online]. Available: https://www.artisan-tg.com/info/ELD_WindTunnel_Full_Specifications.pdf

UAM Acoustics Prediction Model

Student Researcher: Amanda M. Devillier

Advisor: Daniel R. Cuppoletti, Ph.D.

University of Cincinnati

Department of Aerospace Engineering and Engineering Mechanics

Abstract

As cities become more crowded, Urban Air Mobility (UAM) becomes a more viable option for transporting people and goods; however, the noise radiation from UAM remains a major concern. Many of the aircraft proposed to use for UAM are small electric vertical takeoff and landing (eVTOL) vehicles with distributed electric propulsion (DEP). Current acoustics models for these electric vehicles are based off helicopter rotors or propeller aircraft which have very different operational characteristics. This research project ultimately aims to create an Acoustic Analysis Framework that allows users to input a vehicle configuration and flight path and outputs an approximate overall Sound Pressure Level (SPL) and energy distribution based off measured rotor acoustics data. This research will allow companies to better understand the noise impact of their vehicle design in the preliminary development stages rather than build and test a design with no knowledge of the acoustics signature of the vehicle.

Testing on two and three blade rotor configurations was performed in UC's anechoic chamber. The sound pressure level data was then processed through MATLAB to output the Narrowband Spectrum and Third Octave Band Spectrum (TOB). Curve fitting to the TOB was performed in order to try and create a lower order model that can be used to look at the impact of acoustic energy distribution on noise metrics. Work has been started to decouple the tonal and broadband energy in the time domain, in order to determine how each component will affect noise metrics individually.

Project Objectives

The objectives of this research were to capture acoustic trends with a lower order model that can be used to explore how the acoustic energy distribution may impact noise propagation. Ultimately the model will be used to explore acoustic exposure on the ground for a simulated flight.

Methodology Used

The majority of this work was done in MATLAB using rotor data taken in the University of Cincinnati's hemi-anechoic chamber. The chamber has a lower cutoff frequency of 100 Hz and a porous grate floor with acoustic absorbers below to simulate flight at altitude. The rotors used in testing were 18.5" (0.47m) diameter, folding rotors from KDE Direct. A small-scale KDE Direct electric motor was operated up to 3,500 RPM. The motor was supplied a constant 16 VDC from a Magna-Power 6kW power supply. The motor was controlled via a KDE Direct ESC that received a pulse-width modulation signal from LabVIEW. The motor was mounted on the test stand with the rotors positioned 72" (1.83m) above the ground. An array of 8 Brüel & Kjær microphones were sampled at 204.8 kHz per second during each 15 second trial. The 8 microphones were 105.25" (2.67m) from the center of the rotor and were placed at heights of 12, 24, 36, 48, 60, 72, 82 and 92 inches. The set up can be seen in Figure 1.

Results Obtained

Sound pressure level data from the microphones was processed through MATLAB and plotted in both the Narrowband (NB) Spectrum and Third Octave Band (TOB) Spectrum. The TOB data was curve fit at

varying rotor speeds and microphone heights to obtain a lower order model that can be used to assess how the acoustic energy distribution will affect noise metrics. Work has been begun to decouple the broadband and tonal energy in the time domain. The sound pressure level data from the microphones was put through a low-pass filter to smooth it and then subtracted from the raw data. The resultant was put through a Fast-Fourier Transform and plotted.

Figures/Charts

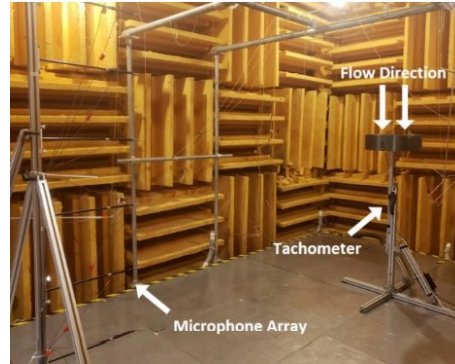


Figure 1. Lab Set-up

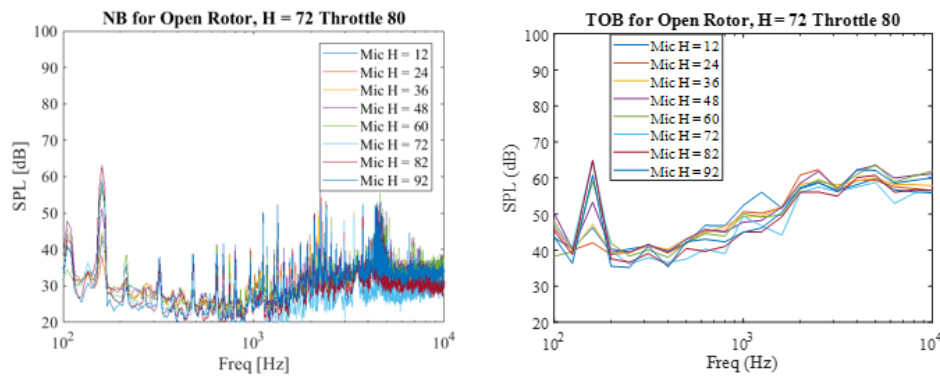


Figure 2. Narrowband & Third Octave Band Spectrum

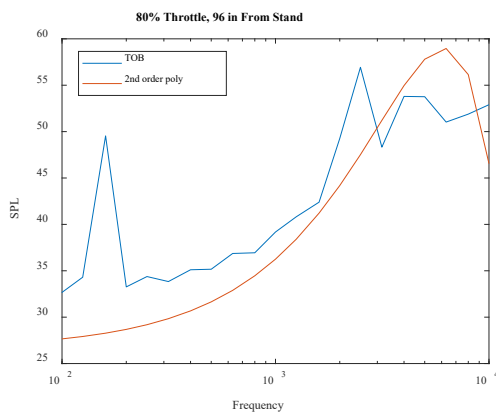


Figure 3. Curve Fitting the Broadband Shape

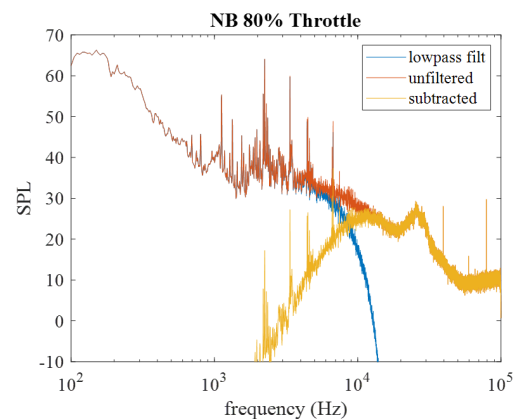


Figure 4. Beginning to Decouple Broadband & Tonal

Acknowledgments

Special thanks to Dr. Cuppoletti for the support and guidance on this project.

Stress Ball Modification to Assist in Pediatric Stroke Rehabilitation Process

Student Researcher: Brooke, E. DeVriendt

Advisors: Jed E. Marquart, Ph.D., P.E. and Hui Shen, Ph.D.

Ohio Northern University
Mechanical Engineering

Abstract

Often times brain injuries can be fatal without the performance of an immediate high-risk surgery. The recent improvements in biomedical engineering have allowed for these processes to be less dependent on the surgeon and more focused on precision-oriented robots. In addition to the surgery itself, the post-operation patient recovery varies greatly. There are also devices in developmental stages that help to measure and track the recovery process. This research is intended to analyze new ways to go about surgeries and recovery processes.

Project Objectives

The objectives of this project included getting a better understanding of what devices are out there to measure brain surgery recovery and how these processes are being implemented. In addition to this research, ideas on how to improve these concepts to make them more accurate or practical are included. This project was completed with research and analysis of tools and materials involved in pediatric strokes. The physical model of the theoretical rehabilitation design solution imposed was not able to be done due to the limitations of equipment. Instead, the equipment and materials that would be used and how they would be used will be discussed.

Methodology Used

The best way to measure the recovery process of a patient's strength may be evaluated using a special glove, as shown in Figure 1. The issue that this glove is trying to help fix is the ability to quantify the strength in a patient's hand, rather than using the traditional touch and feel evaluation that is typically performed by the doctor. The glove currently has over 300 pressure sensors, just on the palm of the glove alone (Nelson). Other solutions discovered were found to be more involved in the process of fixing the stroke, rather than focusing on the rehabilitation process. One of these concepts was a robot to perform brain surgery, rather than risking human error by having an actual surgeon to do this (Abrams). While this idea may be essential in the future to removing blood clots which cause strokes, the glove was a more viable option to start with and improve upon for the rehabilitation process.

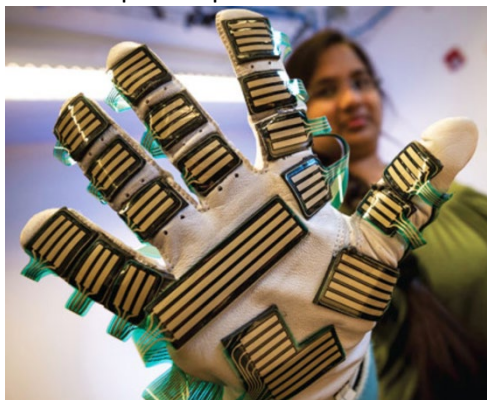


Figure 1. The pressure sensing glove currently in development (Nelson).

While this glove currently only has pressure sensors in the palm of the hand, it would be beneficial to have sensors on each individual finger to evaluate strength as well. The concept behind this thought process could be having a foam and rubber ball, similar to the makeup of a stress ball, that is able to analyze the force and pressures on the ball. The significance of this is that physical therapy is already an integral part of patient recovery and typical includes squeezing a stress ball in either hand in order to strengthen the hand. Aside from observing how much the ball compresses when it is squeezed, there is currently no way to measure how and track the process of how their strength is recovering.

The main goal of modifying the use of the glove, or rather enhancing the abilities of a stress ball would consist of trying to make the recovery process as normal as possible. A stroke patient will often times be in the hospital for weeks after the cause of the stroke is eliminated. This is a very rigorous process already, including intense physical therapy multiple times a day. If the child sees what they are doing as physical therapy, they may get upset or frustrated with the progress they are making. The modified stress ball would allow for the patient to be completing physical therapy without having to think about it too much. In order to do so, several thin-film pressure sensors could be imbedded in the ball (Tekscan). The concept behind using a pressure sensor, such as the one in Figure 2, would be that it is thin enough to hopefully be masked by the material of the stress ball. There ideally would be an output reader that could calculate the different stresses and forces on the ball and store the memory. The other alternative to storing the memory would be displaying the data directly to an LED screen on the ball. The issue with this alternative would be that the child would see these numbers and know that some sort of “test” is being done. In order to get an accurate reading of how they are improving in their normal life, rather than when they are simply being pushed to their limits in therapy, the ability to download and track this data on a computer would be ideal. This also provides the ability to save and track data with the creation of charts and graphs, to truly track and quantify how the child is improving after their surgery.

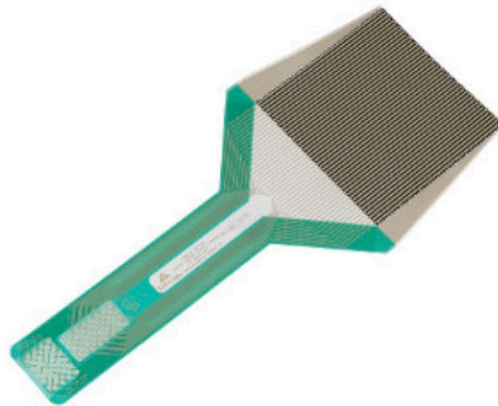


Figure 2. Example of a thin-film pressure sensor (Tekscan).

Overall, this project was designed to enhance the knowledge of the complex process that go into the rehabilitation processes of pediatric strokes, or more generally speaking, brain injuries as a whole. While the proposed solution to one aspect of this process may be able to be implemented, there is still so much work to be done in the area of pediatric strokes. The most important thing is knowing that they exist and can happen to anyone. The project idea came from my nephew suffering from a pediatric stroke and watching his physical therapy process. Tracking this process is not easy and any way to quantify the progress gives the ability for doctors and patients families to be better prepared for steps in the future when considering life post-pediatric-stroke.

References:

Abrams, Michael. "Musa Is a Robot Allowing Surgeons to Perform at the Highest Levels of Precision Ever Achieved in the Operating Room." ASME, 16 June 2020, www.asme.org/topics-resources/content/a-robot-for-the-tiniest-surgeries.

Nelson, Meredith. "A Glove With an Objective Touch." ASME, Mechanical Engineering Magazine, 23 Aug, 2017, www.asme.org/topics-resources/content/glove-with-an-objective-touch. "Thin-Film Pressure Sensors." Tekscan, 10 Mar. 2021, www.tekscan.com/thin-film-pressure-sensors?utm_source=google.

Investigating Impact Tolerance of Sea Urchin for Aerospace Applications

Student Researcher: Kristel H. Doong

Advisor: K.T. Tan

College of Engineering and Polymer Science/The University of Akron
Mechanical Engineering Department

Abstract

Biomimicry takes inspiration from nature to create more resilient and innovative sustainable solutions to complex human problems. The structure of sea urchins can be used as a biological model to create lightweight, impact-resistant material that can be adapted to develop more structurally sound architecture in infrastructure. This report focuses on *Echinocyamus pusillus* since it primarily relies on its skeletal construction because it lacks collagen fibers within its sutures [1]. Since these bioinspired structures can be used to tolerate harsh environments where impact protection is essential, they can be utilized for many applications like high pressure structures in deep sea exploration and landing gears for space exploration purposes. The purpose of this project is to examine the unique shell structure of the sea urchin through experimental testing and Finite Element Analysis.

Project Objectives

This study focuses on two specific characteristics: the overall dome shape and its internal supports (the radial buttress system and the longitudinal ribs) (**Figure 1**). The objectives are to investigate the impact tolerance of the shell of a sea urchin by studying the effect of different thickness (2 mm or 3 mm), different numbers of buttress (0, 4, or 8), and different spacing of buttresses (even or uneven spacing) through experimental testing and Finite Element Analysis (FEA) using Abaqus.

Methodology Used

The specimens are 3D modeled using SolidWorks and then 3D printed using the Stratasys Objet260 Connex3. The material used is TangoPlus FLX930 because a sea urchin is not completely rigid, but slightly flexible. It has a tensile strength of 0.8-1.5 MPa and elongation at break of 170-220%. It is hard to 3D print a part that is hollow inside, so the part is cut in half in the horizontal direction, so two individual parts are printed where the two parts are inserted into each other to form the elliptical shape. Instron CEAST 9350 drop tower is used to impact the specimens at room temperature (**Figure 2a**). The impactor is a cylindrical in shape with a diameter of 16 mm. The specimens are tested at various impact energy levels of 5 J, 10 J, 20 J, and 40 J. Instron 5582 Universal Testing Machine with a load cell of 10kN is used for compression tests (**Figure 2b**) with a load sensitivity of 50% and a displacement rate of 5 mm/min. The specimens are placed between two parallel load platens, representing a fixed-fixed end condition. Furthermore, Abaqus FEA software is used to simulate a simple compression of 40 mm. For the material property, Mooney-Rivlin is used to model the hyperelastic material [2]. Experimental data from uniaxial and biaxial testing are used for the C10 and C01 values [2].

Results Obtained

Impact and compression graphs are analyzed to understand the effect of different thicknesses, number of buttresses, and buttress spacing. Stiffness against number of buttresses graph are presented in **Figure 3**. The stiffness are obtained through experimental compression testing and a simple compression simulation using Abaqus FEA. Representative energy against time curves for all the ten specimens impacted with 40 J of impact energy at room temperature are presented in **Figure 4**.

Significance and Interpretation of Results

The experimental and FEA data are both in agreement that adding buttresses increases the stiffness. FEA data shows that uneven spacing has a higher stiffness for the 8 buttresses, but even spacing has a higher stiffness for the 4 buttresses. For the 40 J impact test, the 4 and 8 buttresses have no rebound, which indicate that the structure absorbs all the energy during impact.

Figures/Charts

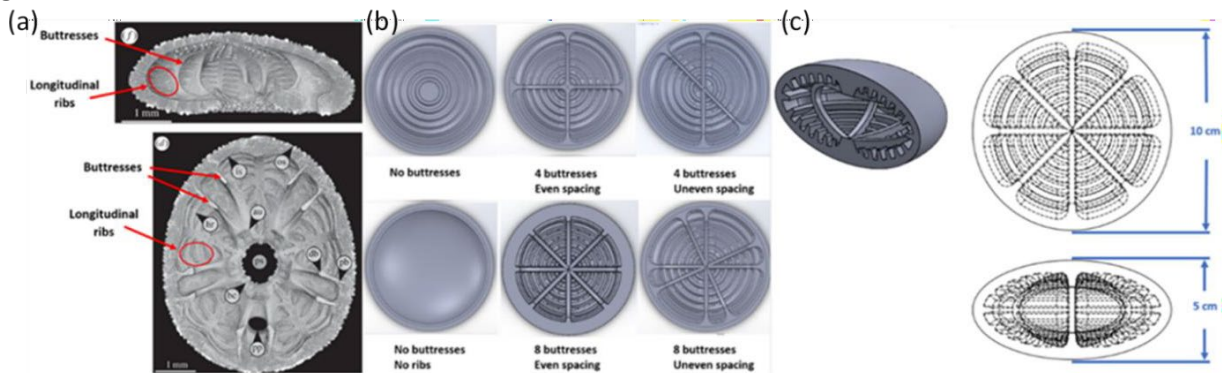


Figure 1. Design: (a) internal support [1]; (b) cross-section cut; (c) overall dimensions

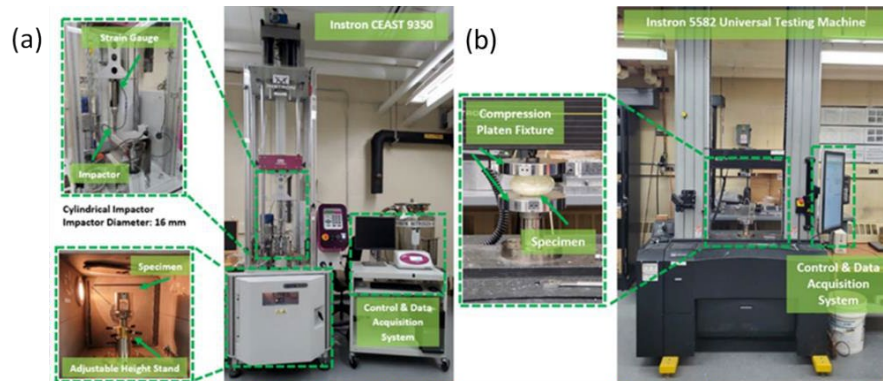


Figure 2. Experimental setup: (a) impact test; (b) static compression test

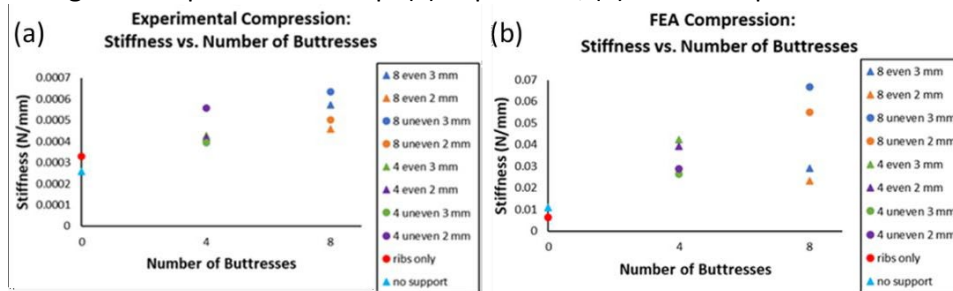


Figure 3. Compression Test: (a) experimental; (b) Finite Element Analysis

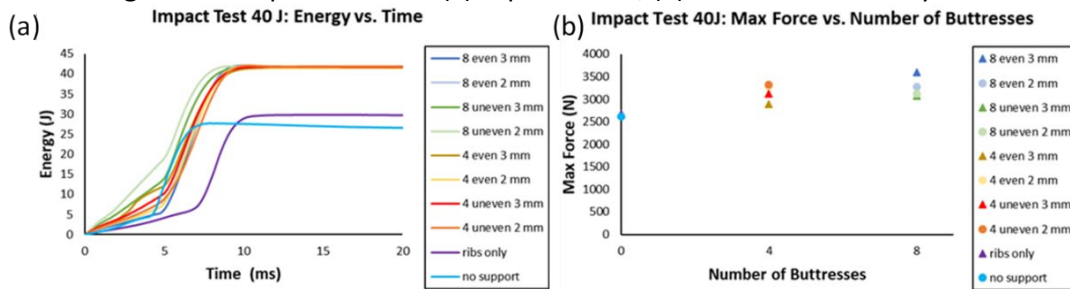


Figure 4. Impact Test of 40 J: (a) Energy vs. Time; (b) Max Force vs. Number of Buttresses

Acknowledgments and References

We are thankful for the support of the Ohio Space Grant Consortium Undergraduate STEM Scholarship.

[1] Grun TB, Nebelsick JH. Structural design of the minute clypeasteroid echinoid *Echinocyamus pusillus*. Royal Society Open Science. Year 2018, Volume 5, Issue 5, Page 171323.

[2] Morris K et al. Uniaxial and biaxial testing of 3D printed hyperelastic photopolymers. Journal of Applied Polymer Science. Year 2020, Volume 137, Issue 8, Page 48400.

Effects of Soy-Based Nutrients on the Properties of Self-Healing Concrete

Student Researcher: Hiba EL Rassi

Advisor: Dr. Anil Patnaik

The University of Akron
Civil Engineering

Abstract

Concrete consists of three basic components: water, aggregate and cement. It is considered a focal construction material in any infrastructure project and the second most used material on earth (after water). While concrete provides wide range of benefits, it has some drawbacks. A major downside of concrete is the crack formation affecting the structure aesthetics and most importantly its degradation over time reducing its lifespan. Cracks initiate in a form of microcracks and eventually propagate to form an easy path for moisture to penetrate into the concrete causing corrosion of the embedded steel reinforcement and degrade the strength. Worldwide research is being conducted to enhance concrete durability. Recent research focus has been directed towards the use of biological agents containing bacteria that would seal concrete cracks as they form. This type of concrete is commonly known as self-healing concrete. Nutrients are an essential constituent for biological agents as they enable spores to remain potent (alive) and act as food source for germination during crack sealing. Using data obtained and other material trials [1]–[4], this paper demonstrates the effects of the nutrients on the mechanical properties of the concrete.

Project objectives

The primary goal of this research was to determine the effects of soy-based nutrients that will be used to encapsulate biological agents. Using ASTM standards, this study investigated and characterized various concrete properties such as compressive strength, setting time, heat of hydration, and unit weight of self-healing concrete when soy-based nutrients (Soy Flour, Soy Molasses and Soy Hull), are added during wet mixing of concrete.

Methodology used

The process of microbial healing begins when water percolates into a crack formed in the concrete. Many cracks start off as microscopic openings, and this is all the bacteria needs for activation. The bacteria are originally embedded into concrete matrix as 'spores' during the mixing process of the concrete. Those spores can be encapsulated (filled/coated) with nutrients which serves as a food source for the bacteria when they are activated. As crack initiates and propagates, the embedded bacteria capsules will rupture and chemically react with water to form calcium carbonate crystals and infiltrate into the existing cracks. The bacteria can survive in the concrete matrix for over 200 years, and they can be reactivated multiple times if the healed area were to crack again [5]. A major concern when using bacterial self-healing concrete is whether the bacteria will negatively affect the mechanical properties of the concrete during the 28-day period. This was verified experimentally in this study. Concrete specimens for the setting time, compressive strength testing, and density determination were all prepared from the same batch of mortar for a given set of tests. Six specimens were preserved for compressive strength testing at 3 ages (7 days, 14 days and 28 days). For setting time, penetration was conducted at a certain duration until samples were hardened to a resistance capacity of 4,000 psi (pounds per square inch). For the density testing, wet samples were measured immediately after mixing and dry density was measured after six days from mixing. For heat of hydration, samples were tested with variation of time for 120 hours.

Results and interpretation

After data analysis, it was observed that the setting time of concrete with Soy Flour and Soy Molasses approximately doubled with the addition of the nutrients compared to the control sample (Figures 1-2). While Soy Hull showed a decrease in the setting time (Figure 3). The compressive strength tests showed similar results compared to the setting time (Figures 4-6). Soy flour and Soy molasses showed a dramatic decrease in compressive strength during the 28-day duration compared to control sample. Soy Hull showed a slight decrease which can be adjusted using admixtures. The trends observed for the density as well as heat of hydration for those mortars (Figures 7 – 12) were similar to the ones for setting time. It is worth noting, all results have been normalized as this research falls under a proprietary category.

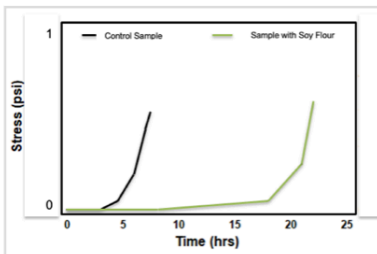


Figure 1. Setting time for Soy Flour.

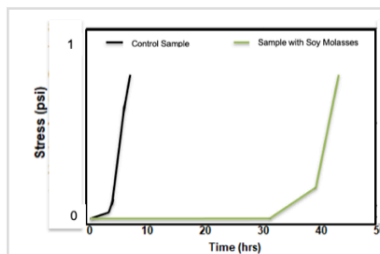


Figure 2. Setting time for Soy Molasses

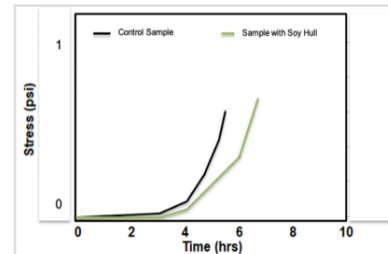


Figure 3. Setting time for Soy Hull

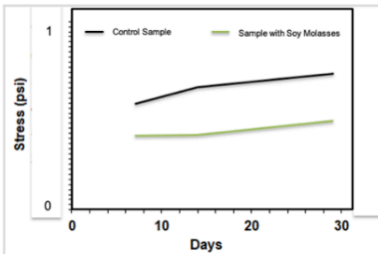


Figure 4. Compressive Strength for Soy Molasses

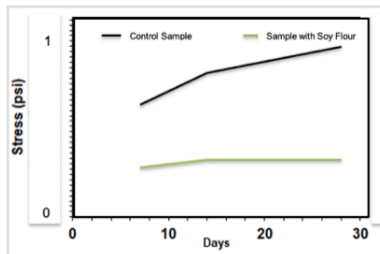


Figure 5. Compressive Strength for Soy Flour

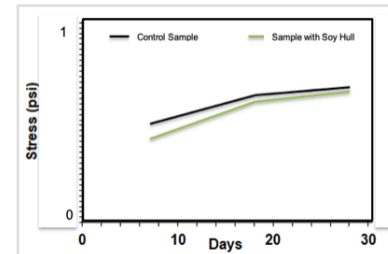


Figure 6. Compressive Strength for Soy Hull

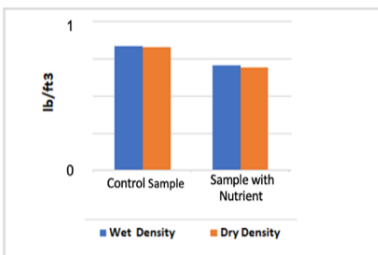


Figure 7. Density for Soy Flour

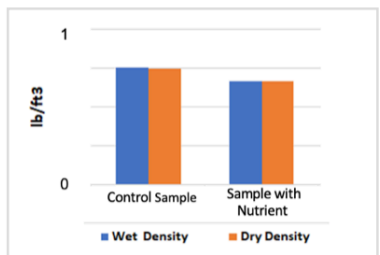


Figure 8. Density for Soy Molasses

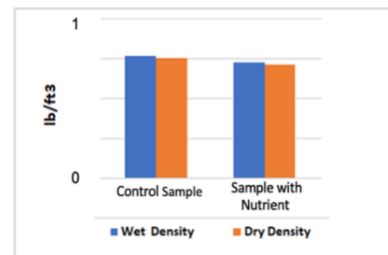


Figure 9. Density for Soy Hull

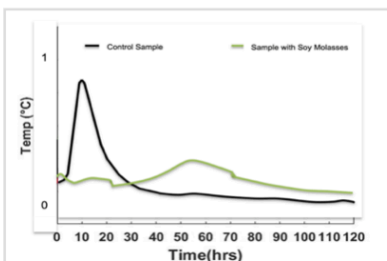


Figure 10. Heat of Hydration for Soy Molasses

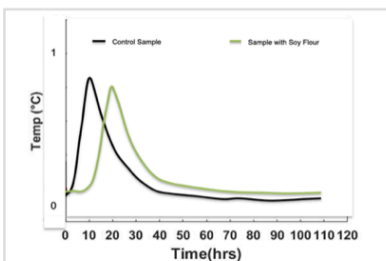


Figure 11. Heat of Hydration for Soy Flour

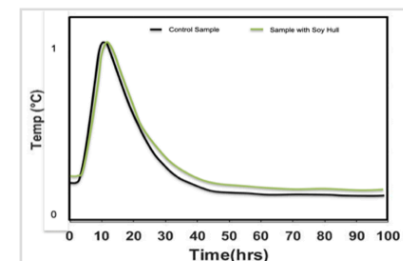


Figure 12. Heat of Hydration for Soy Hull

Acknowledgment

I would like to express my deepest appreciation to the Ohio Space Grant Consortium who provided me the possibility to complete this research. A special gratitude to my advisor, Dr. Anil Patnaik, whose contribution in stimulating advice, support, suggestions and encouragement, helped me to throughout this research. Moreover, I would like to thank Puskar Dahal for his help and guidance throughout the research. Last but not least, I would like to thank The University of Akron for allowing me to use their testing facility.

References

- [1] R. Singh Rathore, S. Khan, S. Arya, and T. Sharma, "A Review on Self Healing Concrete."
- [2] N. Chahal, R. Siddique, and A. Rajor, "Influence of bacteria on the compressive strength, water absorption and rapid chloride permeability of concrete incorporating silica fume," *Constr. Build. Mater.*, vol. 37, pp. 645–651, 2012.
- [3] K. Van Tittelboom, N. De Belie, W. De Muynck, and W. Verstraete, "Use of bacteria to repair cracks in concrete," *Cem. Concr. Res.*, vol. 40, no. 1, pp. 157–166, 2010.
- [4] S. Luhar, G. Suthar, and S. Gourav, "A review paper on self healing concrete Self healing of concrete by using bacteria View project Urban water management, water scarcity and water market View project A Review Paper on Self Healing Concrete," *J. Civ. Eng. Res.*, vol. 2015, no. 3, pp. 53–58, 2015.
- [5] E. Tziviloglou, Z. Pan, H. Jonkers, and E. Schlangen, "Bio-based Self-healing Mortar: An Experimental and Numerical Study," *J. Adv. Concr. Technol.*, vol. 15, pp. 536–543, Sep. 2017.

Initiation of Super-Detonations Following a Porous Medium Using a Global 4-Step Combustion Model

Student Researcher: Grace N. Floring

Advisor: Dr. Brian Maxwell

Case Western Reserve University
Mechanical and Aerospace Engineering

Abstract

The main topic being studied in this project is the deflagration-to-detonation transition (DDT). This is a phenomenon not well understood in the field of fluid mechanics. A detonation wave is a supersonic combustion wave consisting of a shock wave tightly coupled to a short reaction zone. A choked flame is supersonic relative to the observer, and defined when the flame speed equals the speed of sound in the product gases. The run-up distance, or the distance the flame travels before becoming choked, is a necessary critical value for DDT because that is when detonation can be triggered in sensitive mixtures [1]. Overall, the ability to predict run-up distance leads to knowing when a flame will become choked, and therefore understanding when DDT could occur. For this project, the specific scenario being studied is a detonation wave encountering a bank of cylinders. The phenomenon was modeled numerically, first with a 1-step Euler model and in the future with a 4-step model. The 4-step model saves chemical data for four species (two reactants and two products) and allows the properties of the flow to change with temperature. With improved chemical kinetics and turbulence models, the goal is to have this simulation accurately model “super-detonations” in the flow after encountering a bank of cylinders. The scenario was successfully modeled using the 1-step Euler model with a stoichiometric methane-oxygen fuel mixture, and there are plans in place to continue this project using a 4-step model.

Project Objectives

The overall objective of this research is to accurately model the deflagration-to-detonation transition (DDT) numerically. The first step in achieving that goal is this project, which looks at a specific scenario involving detonation re-initiation following a porous medium. When encountering an obstacle, detonations can become quenched and then re-initiate. This is observed when encountering a bank of cylinders, as studied by Radulescu and Maxwell in 2010 [2]. This scenario can be applicable to detonation arrestors, which is a device connected to an opening to allow flow but stop supersonic flame propagation. As observed in experiments, after detonations encounter a bank of cylinders, a transverse detonation wave propagates into the shocked yet unreacted gas, which is visibly seen as bright bands (Fig. 1) [2]. These bright bands are denoted as super-detonations, and have not been captured numerically in past work.

The main objective of this project is to apply a 4-step model to this scenario to successfully model those super-detonations, a model originally proposed by Zhu et al [3]. The 4-step model provides a significant advantage over past models, as it only requires storage of four species, as opposed to hundreds. It does this while still performing better than the 1-step model. This project is still in progress, and the preliminary methodology and results are highlighted below.

Methodology Used

The first step in this research was to model the scenario in a 1-step Euler model for a 2D detonation, to set up the boundaries and initial conditions. This project used a stoichiometric methane-oxygen fuel mixture at temperature 300 K and pressure 12 kPa, which differs from the 2010 study that used an acetylene-oxygen mixture, due to the fact that the latter is fuel-rich and would not be compatible with

the 4-step model. This mixture was chosen also because a similar study was conducted in 2012 with this mixture, and the results are deemed to be repeatable [4].

For the parameters, gamma (the ratio of specific heats) was set to 1.17, the half-reaction length was 2.24 mm and the detonation Mach number was 6.44. Lengths were normalized to the half-reaction length (the distance from the shock to where half of the heat is released), with a cylinder radius of 152 mm (68 units), and a channel height of 203 mm (90 units).

For this project, it is important to note how symmetry is being applied. In experimental data it was observed that the field becomes symmetric around a cylinder, therefore it is most efficient to apply the symmetry condition along the top and bottom boundary, and model the scenario with a half cylinder. The channel length was set to 500 units, with the x boundary set to -100 to 400, and the half cylinder centered between 0 and 200. This was done so that backwards propagation of the shock waves could develop and be observable.

Results Obtained

The preliminary results using a 1-step Euler model are highlighted in Fig. 2. These are compared side by side with the work done by Bhattacharjee, who also modeled the same scenario with methane-oxygen. Overall, these results are satisfactory because there is an observable, clear separation of the shock and reaction zone. The resolution that was deemed adequate was 32 grids per half reaction length. With the problem successfully replicated from the original study in the 1-step model, the next step in this ongoing project is to move on to modeling it in the 4-step model.

The 4-step model is currently being constructed, mainly by PhD student Mohnish Peswani. For this project, the ZND Detonation model will be used [5]. This is a one-dimensional model that describes the reaction zone behind a shock wave, and uses chemical reactions coupled with steady-state gas dynamics. Initial results indicate that the model responds as it should when compared to detailed chemistry. It improves upon simpler models, such as the 1-step model, as it captures a correct final equilibrium temperature and correct stiffness. For the reaction zone, the model almost exactly captures correct temperature and spatial scales, as can be seen in Fig. 3. Once the setup of this model is complete, the scenario for this project can be simulated using the 4-step model.

Significance and Interpretation of Results

These results are only the first part of this project, and the research will continue into the summer term. However, the preliminary modeling of the phenomenon in a 1-step Euler model was successful. The problem has been set up with satisfactory results, and demonstrated that the results from the original experiment are repeatable. In the preliminary results, an unburned "tongue" of reacted gas is visible, as seen in Fig. 2b. In physical experiments this is consumed by the super-detonation. As expected, the super-detonation was not observed in this model. This is due to some drawbacks of the Euler model, which includes ignoring diffusion mathematically and not addressing turbulent mixing. The 4-step model will address these errors in the next phase of research. The goal for the next part of the project is that by including turbulence statistics and better chemistry into the numerical model that the super-detonation will be observed.

Figures

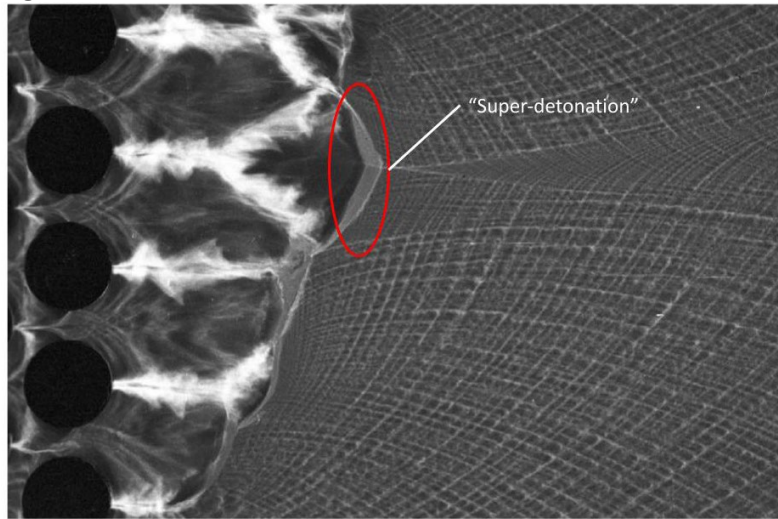


Figure 1. An open shutter photograph of the flow field where the bright bands, or "super-detonations," were observed [2].

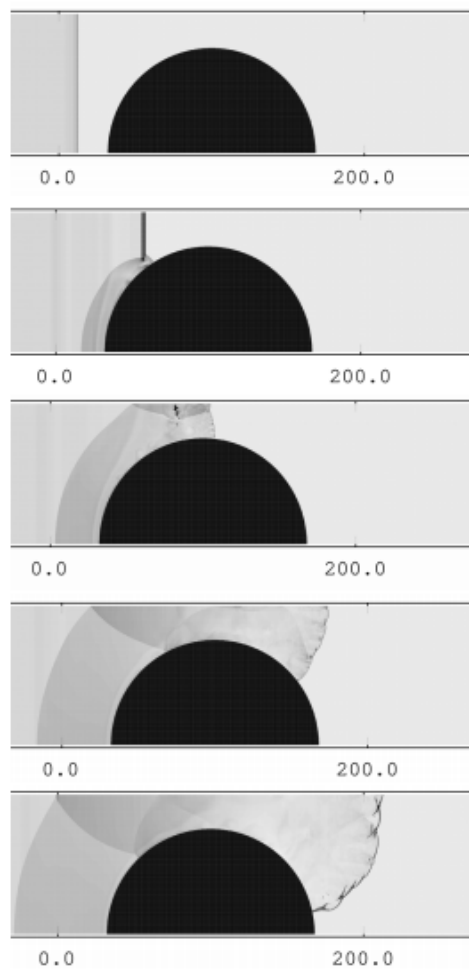


Figure 2a. Density field evolution for the detonation transmission, preliminary results obtained with 1-step Euler model.

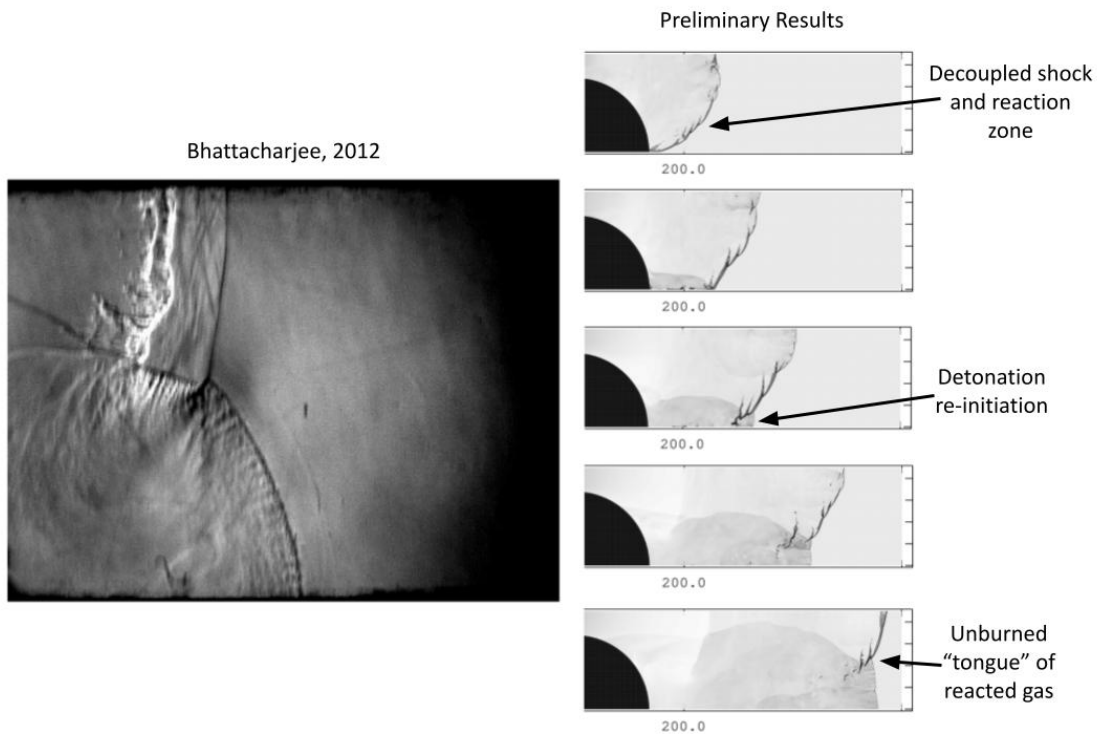


Figure 2b. Density field evolution compared to previous work. (Left) Experimental results from Bhattacharjee, which studied the same scenario [3]. (Right) Preliminary results using 1-step Euler model for this project.

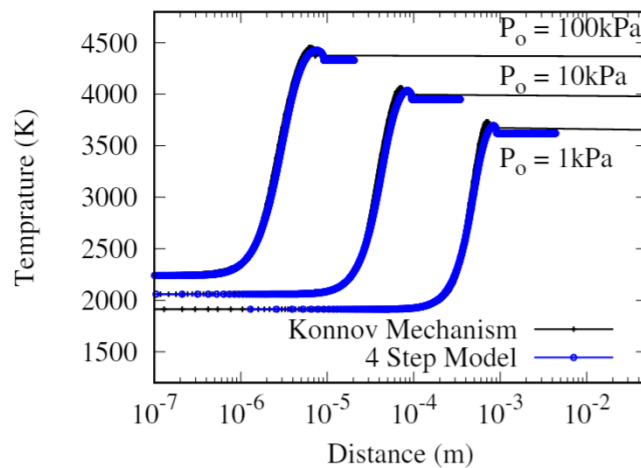


Figure 3. Initial results from 4-step model using ZND Detonation model for a stoichiometric acetylene-oxygen mixture, compared to Konnov mechanism [6].

Acknowledgments

I would like to thank my advisor Dr. Brian Maxwell for the guidance and insight, who introduced me to this topic and got me interested in fluids and thermal sciences with his fluid mechanics course. I would also like to thank Mohnish Peswani for his work with the 4-step model and his assistance for my project.

References

- [1] Silvestrini, M., Genova, B., Parisi, G., et al., "Flame acceleration and DDT run-up distance for smooth and obstacles filled tubes," *Journal of Loss Prevention in the Process Industries*, vol. 21, no. 5, pp. 555-562, 2008.
- [2] Radulescu, M., Maxwell, B., "The mechanism of detonation attenuation by a porous medium and its subsequent re-initiation," *Journal of fluid mechanics*, vol. 667, pp. 96-134, 2011.
- [3] Zhu Y., Yang J., and Sun M., "A thermochemically derived global reaction mechanism for detonation application" *Shock Waves*, vol. 22, pp. 363–379, 2012.
- [4] Bhattacharjee, R. R., Lau-Chapdelaine, S. S. M., Maines, G., Maley, L., & Radulescu, M. I., "Detonation re-initiation mechanism following the Mach reflection of a quenched detonation," *Proceedings of the Combustion Institute*, vol 34, no. 2, pp 1893-1901, 2013.
- [5] Fickett W., Davis W., "Detonation: Theory and Experiment," *Dover books on physics*, Dover Publications, 2000.
- [6] Peswani M., Gerace C., Maxwell B., "Combustion properties of a simple and efficient 4-step combustion model," *Manuscript submitted to Combustion Theory and Modelling*, 2021.

Integrating Unmanned Aerial Vehicle and Unmanned Ground Vehicle Collaborative Systems

Student Researcher: Rebecca N. Gilligan

Advisors: Dr. Kelly Cohen, Bryan Kowalczyk, Justin Ouwerkerk, Austin Wessels

University of Cincinnati
Mechanical Engineering

Abstract

With a growing need for more efficient and autonomous tasks, one area which requires further investigation is collaborative air-ground systems. Whether it's a worldwide pandemic requiring contactless services, interplanetary missions with communications delays too long for manual control, or the need to traverse large, multi-terrain areas efficiently, autonomous collaborative systems are gaining attention. This research is focused on creating a collaborative Unmanned Aerial Vehicle (UAV)/Unmanned Ground Vehicle (UGV) pair, dividing assigned tasks to complete a complex mission. The UGV will serve as a dynamic takeoff/landing platform for the UAV, with both systems using and communicating via a series of nodes in Robot Operating System (ROS) 2. The system will utilize FlyMASTER, a UAV software system created by the University of Cincinnati's UAV MASTER Lab.

Project Objectives

The ultimate goal of this project is to develop an aerial/ground vehicle pair that can be utilized in various applications and together provide greater capabilities than either vehicle alone, particularly in complex environments.

Methodology

This project is divided into several phases. The first phase of this project involved designing the UAV and UGV systems, and creating the logic to be implemented in ROS. Phase two involves building both platforms with basic testing, phase three begins collaborative testing, complete with several takeoff and landing scenarios.

Results

The UAV, Figure 1, is a 690mm hexacopter, equipped with a Pixhawk 2.1 Cube autopilot, a Raspberry Pi 4B, and Raspberry Pi HQ Camera, among other standard hardware. The ground vehicle, Figures 2 and 3, is in a skid steer configuration with four belt driven wheels powered by two brushless motors. Similar to the UAV, it will use a Pixhawk 2.1 Cube autopilot and Raspberry Pi 4B for command and control. The Raspberry Pi serves as an on-board computer (OBC), which will handle computer vision on the UAV, and calculations for the levelling platform on the UGV. Both vehicles utilize a Here GPS receiver and RFD 900x telemetry modem for navigation and communication, with the UGV having two GPS receivers to prevent signal loss when the UAV is above the vehicle. The vehicles will communicate GPS location and telemetry through a common ground station. Built into the UGV is a two degree of freedom levelling landing platform, driven by four linear servos. The top of the landing platform is covered by large nested ArUco marker to be used in autonomous landing. An ArUco marker is a square code that has a black border surrounding a matrix of binary squares. These squares create the markers identifier, which is useful when using multiple markers.

Figures and Charts



Figure 1. Six rotor Unmanned Aerial Vehicle design

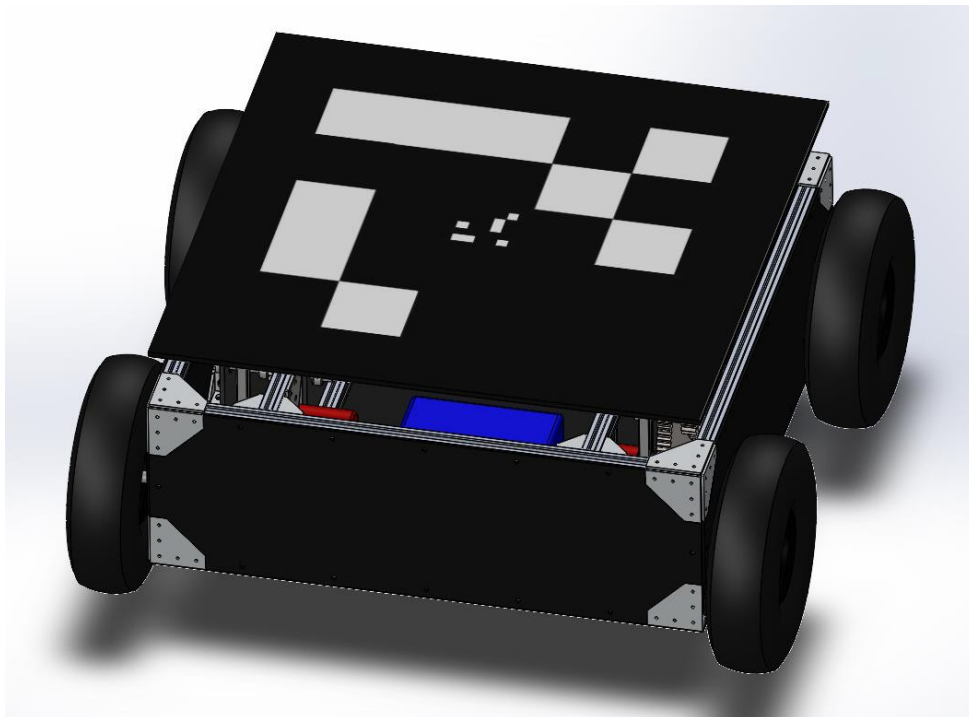


Figure 2. Unmanned Ground Vehicle design with nested ArUco markers on landing platform

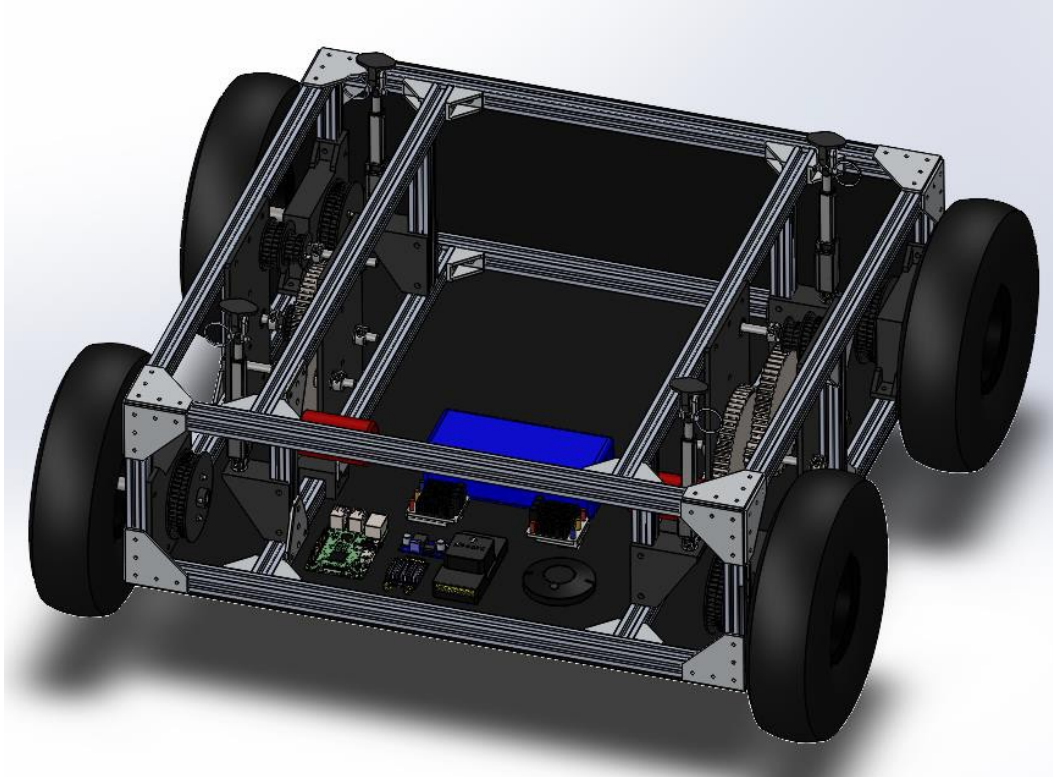


Figure 3. Unmanned Ground Vehicle design, cover plates removed

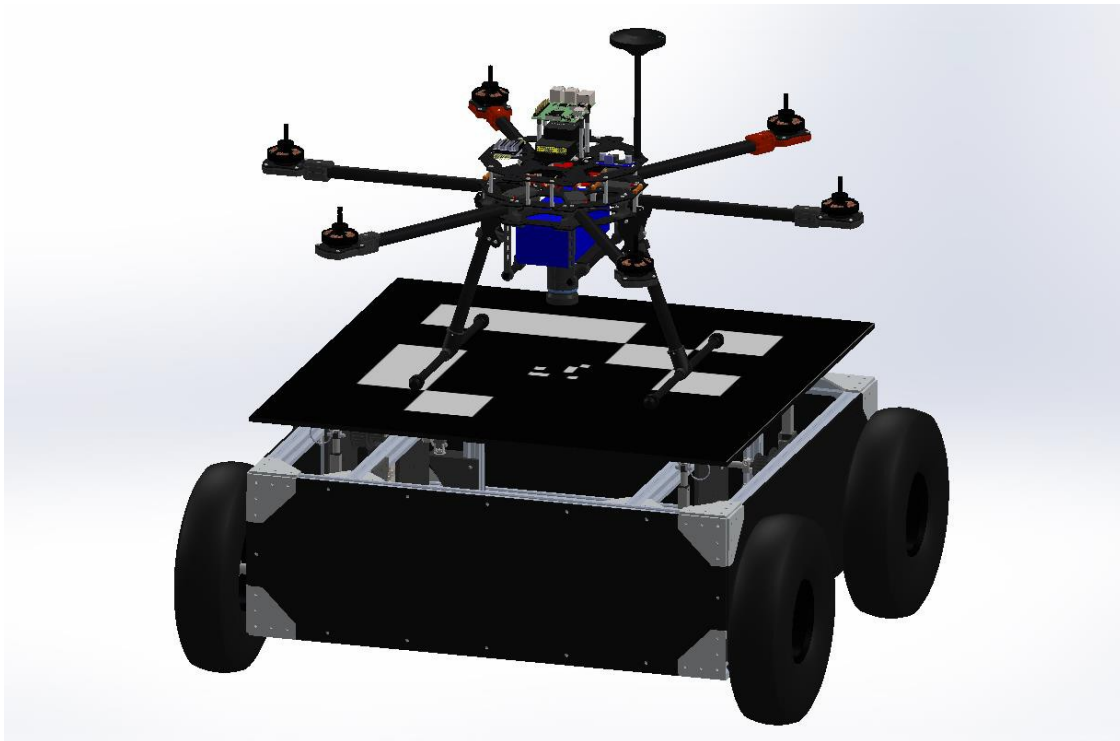


Figure 4. UAV/UGV combined assembly

Additional sensors such as LIDAR, other types of cameras, and more can be added for increased functionality such as obstacle avoidance. The UGV was also designed with enough internal space to carry a payload such as a solar charging array in possible upgrades to the project.

The UGV's frame is 600mm*600mm*200mm. The 250mm diameter pneumatic wheels give it good ground clearance to clear obstacles up to 65mm in height and can traverse grass, gravel, and uneven surfaces. Quick pins allow easy removal of the landing platform to access electronics or change the size of the platform during testing. Choosing 2020 aluminum extrusions for the frame and 3D printable brackets allow the UGV to be adaptable and modular, making it easy to mount and adjust additional hardware on the vehicle.

The levelling landing platform on the UGV will allow for autonomous landing of the UAV while the UGV traverses uneven terrain. This is an important feature because, especially when both vehicles are in motion, an uneven or unstable landing platform could cause the UAV to crash, potentially damaging both vehicles. The linear servos will be driven by data from the Pixhawk's inertial measurement unit (IMU) and a secondary IMU attached to the landing platform to continuously maintain a level surface with respect to the earth while in the UAV is in landing mode. This servo configuration was designed to accommodate up to a 30-degree angular difference from the chassis. This will ensure that when the UAV lands, it will be relatively level, preventing the vehicle from crashing or falling off.

ArUco was chosen as a landing aid as it can define a relative coordinate system and can be used to calculate the relative position of the vehicles, facilitating a smooth landing. Additionally, since FlyMASTER runs on ROS, and there are existing Python libraries and documentation for ArUco [2] (ROS utilizes Python scripts), it will be relatively simple to implement. A relative coordinate system is defined between the vehicles to simplify the task of aligning them, creating a stable landing. This vehicle-to-vehicle alignment will become more critical in possible future upgrades such as adding charging capabilities. Existing research [3] has utilized ArUco markers for UAV landing before, however these ground targets were stationary and did not account for the UAV's changing field of view as its altitude changes. Creating a mobile landing platform adds another level of capability to the system, and the nested markers make the landing procedure even more reliable. Last, since ArUco is detected with computer vision, it does not require the assistance of other sensors or data, meaning it can achieve a precision landing even in a GPS denied environment.

The following describes the ground system functionality to be implemented into FlyMASTER as services to communicate and compare vehicle states. When the UAV is ready to land, it uses the GPS location and heading of the UGV, passed through the ground station, to fly toward the UGV and match its velocity until the outer ArUco marker is within the frame of the camera. Marker detection analyzes the image and extracts ArUco markers. The extracted image is then divided into the grid and each square is determined to be black or white by the majority of pixels in the grid cell [1]. As a result, it is possible to nest ArUco markers inside a larger marker given that the center cell of the larger marker is black. With the smaller ArUco marker having a black border, it is easy to create a center cell with a clear majority of black pixels. Once the identifier is detected, the camera pose can be estimated from the markers four corners. This produces a 3d transformation relative to the camera coordinate system [1]. Knowing the position of the camera on the UAV, this can be translated and the relative position of the marker can be

used to orient the vehicle to the marker's coordinate system, set the heading, and begin descent of the UAV. While the UAV is descending, it continues to use computer vision to stay centered within a sufficiently small radius to keep the ArUco marker in the camera's field of view. Once the smaller nested ArUco marker is clearly visible in the camera frame, the UAV uses the smaller marker to begin final descent. During this stage, the UGV speed will be limited and the UAV will use PID control to stay centered and land.

To reduce power consumption and hence maximize both vehicles endurance, the computer vision will only be used when the UAV is in a landing state and the levelling servos will only be used when the UAV is in a takeoff or landing state.

Conclusion and Future Work

Revisions to the design include verifying that the current gear ratio provides sufficient torque to drive the UGV while carrying the UAV on a 20-degree incline. Another improvement would be adding a mechanism to grasp the landing gear on the UAV when it is positioned on the UGV and the UGV is in motion. Space inside the UGV could be optimized further by replacing the large 3D printable gears with planetary gearboxes and adding a shelf for the electronics.

Future work includes completing phases two and three, as mentioned above. Phase two, and possibly phase three will be implemented this summer. Beyond that, future work can include implementing additional features such as solar charging dock to the UGV and exploring payload and swarming capabilities. This research can then be applied to larger collaborative autonomous systems such as land/air swarms that could open new opportunities in search and rescue, product delivery, exploration, and defense.

Acknowledgements

I would like to thank my advisors Dr. Kelly Cohen, Bryan Kowalczyk, Justin Ouwerkerk, and Austin Wessels for their guidance and support. I look forward to continuing the project!

References

1. "Detection of ArUco Markers." Open Source Computer Vision (OpenCV) https://docs.opencv.org/master/d5/dae/tutorial_aruco_detection.html
2. S.Garrido-Jurado, R. Munoz-Salinas, D.J. Madrid-Cuevas, and M.J. Marin-Jimenez. "Automatic generation and detection of highly reliable fiducial markers under occlusion." *Pattern Recognition* 47, 6, June 2014. DOI=10.1016/j.patcog.2014.01.005
3. Wubben, J.; Fabra, F.; Calafate, C.T.; Krzeszowski, T.; Marquez-Barja, J.M.; Cano, J.-C.; Manzoni, P. Accurate landing of unmanned aerial vehicles using ground pattern recognition. *Electronics* 2019.

Chemical Signature of Fracture in Thermosetting Polymers

Student Researcher: Jason T. Godawski

Advisor: Dr. James Moller

Miami University

Department of Mechanical Engineering

Abstract

Epoxy resins are thermoset plastics that are widely used in many different applications that require surfaces to be bonded together. An epoxy is cured when a resin and a hardener are mixed together. The resin and hardener molecules react to form a cross-linked molecular network. The result is a substance that is hard and sticks to the pores of whatever selected materials are being bonded together. This bond created from epoxies are very durable and hard to disrupt, but chemical bond failure due to mechanical fracture in cured epoxy resins has not been thoroughly explored.

The goal of this research is to identify chemical end groups on fracture surfaces of cured epoxy. If these end groups can be identified, the covalent bond scission that occurs during the fracture of the epoxy will be able to be understood more. When a polymer chain is broken or opened, it is chemically reactive with the surrounding environment. By mechanically pulverizing cured epoxy samples in specific gas environments to prompt differing chemical reactions, these groups can be determined by diffuse reflectance infrared spectroscopy. Creating a method that provides insight into the weaknesses of epoxies will allow for safe and secure bonds to be created for any situations in which epoxy resins are utilized in the future.

Project Objectives

The principal objectives of this project stem from the work already completed in past semesters for this area of study. Selecting and obtaining the proper gas environment for fracture to occur in will be vital to collecting accurate data from the pulverized epoxy resin samples. An apparatus needs to be created so that the vacuum lines, gas supply, vacuum chamber, and blender power can all be mounted together so that testing of the sample can be done smoothly. Utilizing temperature controllers, epoxy resins will be blended and cured using the molds designed last year. Once these samples have been fully and properly cured, they need to be pulverized in the vacuum chamber and stored properly. Lastly, diffuse reflectance infrared spectroscopy needs to be utilized in order to determine the end groups formed on the fracture surfaces of the epoxy resin after pulverization. The goal of this research is to create a repeatable experiment that can be used by other scientists and researchers to conduct analyses on specific epoxy resins.

Methodology Used

To begin with this experiment, cured epoxy resin samples will need to be created in a controlled environment to ensure proper formation of the resin. Utilizing a vacuum oven in the lab, these epoxy samples will be melted and left in for a period of time to allow for any outgassing from the samples. These cured epoxy samples will then be poured into four separate aluminum molds that can hold 6 samples a piece. Prior to the pouring of the epoxy, mold release wax and a PVA release lacquer will be applied to all surfaces of the molds to ensure the epoxies do not bond to the metal [1]. These four aluminum molds are attached to a set of temperature controllers that will maintain different

temperature schedules for each group of samples. The goal of the temperature controllers is to keep the curing epoxy samples as close to their target temperatures as possible. Once cured, these samples will be moved to the gas chamber connected to the vacuum line and a nitrogen gas supply to be pulverized by a coffee grinder inside of the vacuum chamber. Once inside the chamber, all air will be removed and then filled with nitrogen gas. Once pulverized, the chamber will return to atmospheric pressure and the samples will be removed for observations and testing. Diffuse reflectance infrared spectroscopy will be used to determine the end groups formed and insights into the covalent bond scission in epoxies will be able to be formed.

Results Obtained

Although no testing has been completed at this time in the lab due to limited lab availability and the pandemic, much research has been done to ensure proper selections of materials and helpful insights into the research at hand. Preliminary choices for a gas environment were vacuum, nitrogen, oxygen, and carbon monoxide. Research conducted to find the proper gases to be used inside the chamber led to the selection between nitrogen and oxygen. A dry nitrogen atmosphere is ideal because oxygen exposure results in development of peroxy signals and rapid decay of free radical concentration [2]. Pure oxygen gas poses the potential of surface oxidation which is too severe. We want to observe the consequences of the presence of free radicals so comparison among the results in dry nitrogen versus dry air environments is planned. With the use of oxygen, there might be a decrease in the thermal stability of polymers [3]. With the use of a nitrogen environment, oxidation is not expected when the epoxy is pulverized [4].

An apparatus was also created in order to hold the vacuum chamber and create connections between the vacuum chamber, vacuum, and gas supply. This assembly can be seen in figure 1.

Significance and Interpretation of Results

It has been found by other researchers that the surface concentration of the side groups changes after exposure to an ionizing environment with nitrogen present [4]. This is shown in Figure 2. None of the oxidation should be anticipated from the discharge of nitrogen, so the discharge behavior will be much different in a dry air environment. Given our review of previous research conducted, it was determined that nitrogen gas should be used inside of the chamber during pulverization of the epoxy samples so no reactions with the outside surface of the epoxies will be present.

Now that the apparatus for testing is ready for use, developing a curing schedule and readying temperature controllers, testing the gas system for leaks, and creating the epoxy resin samples is all that is left to continue on with this research.

Figures/Charts



Figure 1. Test stand and gas handling system

731

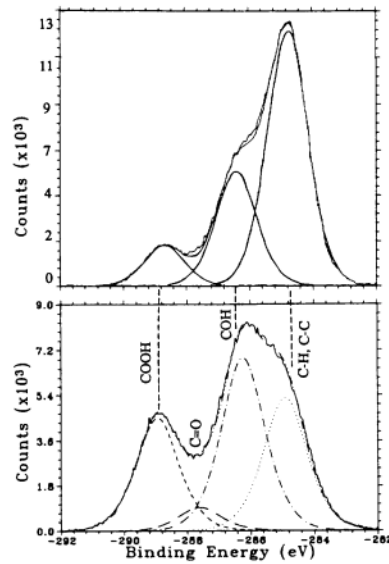


Figure 4: ESCA surface analysis of virgin epoxy (upper) and degraded epoxy (lower) surfaces after 830 hours of PD activity in a nitrogen atmosphere.

Figure 2. Surface analysis of virgin epoxy and degraded epoxy after 830 hours in a nitrogen atmosphere [4].

Acknowledgements

Special thanks go to the Ohio Space Grant Consortium for providing the opportunity to conduct research and learn. Also, a very special thanks goes to Dr. Moller for his guidance and expertise over the course of this research project.

References

[1] "Mold Release Guide - The best Epoxy Release Agent," *Your Epoxy Resin and Finishing Guide*, Jul. 20, 2020. <https://resin-expert.com/en/guide/mold-release> (accessed Apr. 01, 2021).

[2] D. K. Backman and K. L. Devries, "Formation of Free Radicals during Machining and Fracture of Polymers," *Journal of Polymer Science Part A-1*, vol. 7, no. 8, pp. 2125–2134, 1969.

[3] K. S. Chen, R. Z. Yeh, and C. H. Wu, "Kinetics Of Thermal Decomposition of Epoxy Resin In Nitrogen-Oxygen Atmosphere," *Journal of Environmental Engineering*, pp. 1041–1046, Oct. 1997.

[4] C. Hudon and R. Bartnikas, "Surface And Gas Phase Reactions Arising With Epoxy Exposed To Partial Discharges," pp. 725–734.

Investigating Technology Leading to the Design of a High Altitude Ballooning Platform

Student Researcher: Devin R. Grant

Advisor: Augustus Morris, Jr., Ph.D., P.E.

Central State University
Manufacturing Engineering

Abstract:

Exploration of the upper atmosphere and near space became has become increasingly affordable for students at all levels over the last 20 years. Thanks to modern technology, instrumentation and communications needed to support scientific ballooning missions have become miniaturized, reliable, and affordable. Dubbed by some as the poor man's space program, it is now possible to conduct real science at near space altitudes for less than \$1000. Central State University is revisiting high altitude ballooning as a means to attract students toward, and choose careers in, the STEM fields. Working toward this goal, understanding the basic instrumentation necessary to measure key atmospheric variables is required if custom payloads are designed with such instrumentation. Knowing the range of environmental conditions encountered during a flight at altitudes up to 100,000 feet is necessary in order to protect the instrumentation on such missions.

Project Objectives:

There are several objectives to accomplish for this project:

1. Understanding of the variation of the Earth's atmosphere from sea level to an altitude of 100,000 feet.
2. A listing of key atmospheric variables to be monitored during a balloon flight.
3. Development of appropriate sensors and supporting electronics needed to build instrumentation with the capacity to measure the full range of variation of atmospheric variables during the flight.

Methodology Used:

A search through appropriate literature and references has provided a good foundation on the changes that occur in temperature and pressure in the troposphere and stratosphere of the Earth. Near space is defined at altitudes in the stratosphere beginning around 30 km.

Key variables used in weather monitoring and other atmospheric research include temperature and air pressure. These are the chosen variables to be monitored on balloon missions at Central State University.

A number of sensors are available capable of measuring temperature and pressure. However, these sensors require supporting electronics to ensure its measurements are calibrated and spans the range of the desired variables.

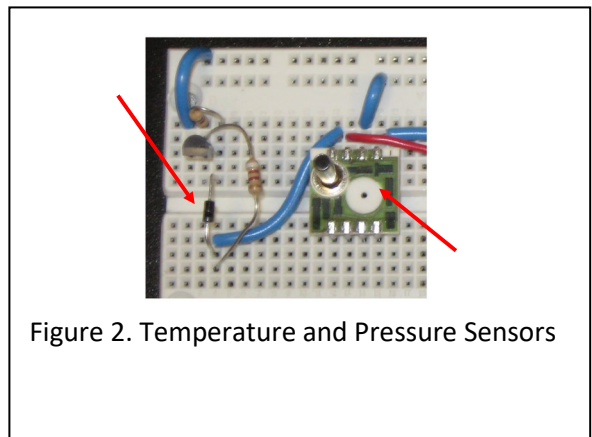
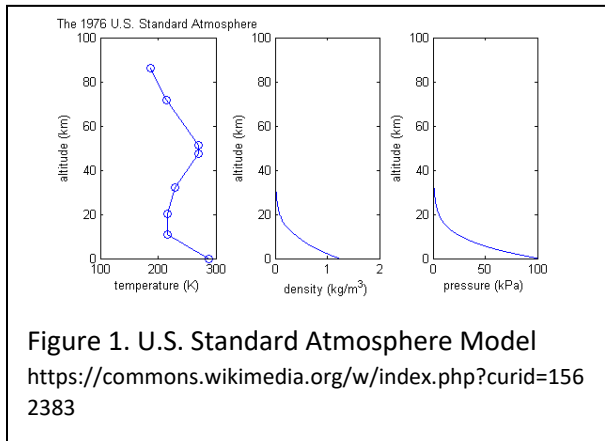
Results Obtained:

Figure 1 shows how temperature, pressure, and density changes as the altitude increases from sea level. Air density decreases with altitude. Air pressure ranges from around 1000 mbars at sea level to nearly 0 mbars at near space altitudes. In contrast, the temperature decreases with altitude near the Earth's surface, but then temperature begins to increase in the stratosphere. Of particular note, the temperature during a journey to near space can reach lows of -40C. Figure 2 shows a temperature and pressure sensor along with supporting circuitry and instrumentation.

Significance and Interpretation of Results:

The next phase of this effort will focus on designing payload structures to enclose and protect the instrumentation from the extremes in atmospheric conditions. An embedded system will be considered to coordinate the instrumentation and provide storage of the data collected. When an appropriate communication and tracking system is decided on, the critical instrumentation is in place to plan and execute a high altitude balloon mission.

Figures/Charts:



Acknowledgments:

This work would not be possible without the support of the Ohio Space Grant Consortium, the Manufacturing Engineering Department at Central State University, and my advisor, Dr. Augustus Morris.

References:

Larson S.L., Armstrong J.C. and W. A. Hiscock. The First Frontier: High Altitude Ballooning as a Platform for Student Research Experiences in Science and Engineering, American Journal of Physics 77(489) June 2009.

Modeling Liquid Hydrogen Spills Through Analysis Of Pool Temperature, Mass Accumulation, And Evaporation Rate

Student Researcher: Amy R. Gravenstein

Advisor: Dr. Edward Evans, Dr. Chelsea Monty-Bromer

The University of Akron

Chemical and Biomolecular Engineering

Abstract

The potential of using hydrogen for propulsion is often undermined due to its wide flammability range when mixed with air (4.0-75.0% hydrogen) and low ignition energy (0.019 mJ).⁶ Liquid hydrogen offers more energy dense storage but adds to this high risk as a cryogenic fluid that is to be maintained below -22 K.⁶ In response to the high safety risk associated with hydrogen propulsion, a liquid hydrogen model has been created in MATLAB that can model various leak/spill scenarios from cryogenic liquid hydrogen containers. This model takes into consideration the spill rate, spill temperature, ambient air temperature, duration of spill, and air flow conditions to calculate the mass accumulation, pool temperature, pool radius, pool height, and evaporation rate as a function of time. It can also predict a safe distance radius for users to abide by if a spill/leak is occurring.

Project Objectives

The objective of this project focuses on achieving accurate predictions of the variables indicated previously. By modeling these variables and relating them to spill conditions, a baseline can be created for different safety scenarios. In the long term, operators of liquid hydrogen systems can identify high hazard components and use this model to predict worst case scenarios.

Methodology Used

The model utilizes mass and energy balances that programs such as PVAP in Phast (Process Hazard Analysis Software Tool) use to model cryogenic liquid spills on various surfaces.^{1,2,5} These analytical functions are used to calculate the changes in pool mass, radius, temperature, and evaporation rate over the course of a theoretical spill. Along with these variables, pool height was determined to be function of mass accumulation for a cylindrical shape. The conditional logic of the model follows the pathway given in Figure 1. This figure displays the key mass and energy equations used to predict each spill scenario. The model has been compared to values found in literature and adapted for the modeling of liquid nitrogen and liquid methane, which are much safer to conduct experiments in comparison to liquid hydrogen. The results from modeling a liquid methane spill are show in Figure 2. The results for evaporation rate, pool temperature, and mass accumulation are consistent with verified models for liquid methane.¹ These models use a constant pool height and radius; however, the MATLAB model uses a varying pool height and radius. Because of this difference, pool radius and height must be verified through experimentation.

Significance and Future Work

Currently, experimental testing is underway in which a liquid nitrogen spill test on a cement surface is performed. Figure 3 displays the test apparatus for this experiment. The general design uses funnels

with varying spout diameters to provide specific spill rates of liquid nitrogen onto a cement surface.⁷ Temperature probes are placed in strategically distanced pockets within the cement spill surface to monitor pool temperature and radius. Using this test method, various spills will be performed, and results will be compared to other model values.^{1,2,5} Figure 3 displays the test apparatus. With the additional experimental liquid nitrogen values, pool height and radius values can be verified within the MATLAB model. Thus far, the model can accurately predict pool temperature, pool mass, and pool evaporation rate over time. This model shows great potential to enhance the safety of liquid hydrogen system designs which will in turn help advance the use of hydrogen for propulsion.

Figures and Charts

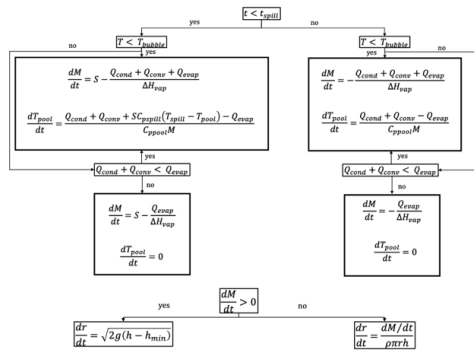


Figure 1: Displays the logic pathway of the MATLAB code modeling cryogenic liquid spills and leaks. Key terms include time (t), spill time (t_{spill}), mass (M), conduction heat transfer (Q_{cond}), convection heat transfer (Q_{conv}), evaporation heat transfer (Q_{evap}), spill rate (S), specific heat of cryogenic pool (C_{ppool}), temperature of spill (T_{spill}), temperature of pool (T_{pool}), bubble point temperature (T_{bubble}), enthalpy of vaporization (H_{vap}), density of pool (ρ), height of pool (h), minimum height of pool (h_{min}), and gravity (g).

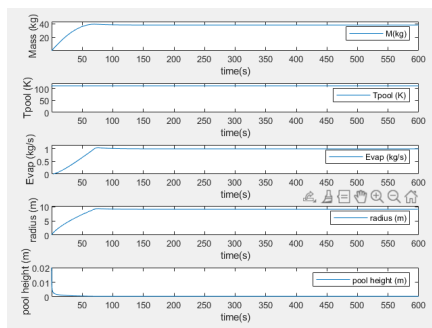


Figure 2: MATLAB results for the following test conditions: S (1 kg/s), T_{spill} (110K), t_{spill} (600s), t_{max} (600s), wind speed (5m /s). The mass rate of accumulation, pool temperature, evaporation rate, and pool height reflect those seen in literature. Pool radius is larger than values observed in literature.

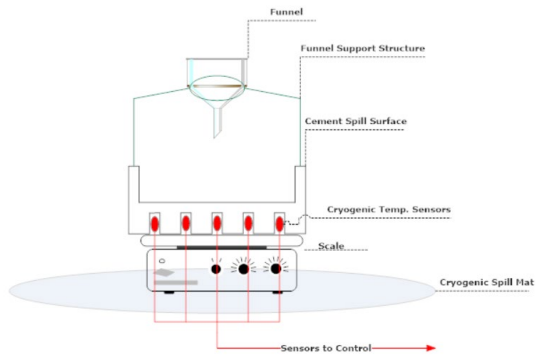


Figure 3: Technical drawing of test design for liquid nitrogen spill. The apparatus consists of the funnel, concrete spill surface, cryogenic temperature sensors, control board for monitoring sensors, support structure for the funnel, cryogenic spill mat. Each component is labeled within the diagram.

Work Cited

¹Fernandez, Maria. 2013. *Modelling spreading, vaporisation and dissolution of multi-component pools*. [Doctoral Dissertation, University College London].

²Fernandez, M. et al. 2012. "An integral model for pool spreading, vaporisation and dissolution of hydrocarbon mixtures". Institution of Chemical Engineers Symposium Series. pp 466-472.

³Holborn, P.G. et al. "Modelling hazardous distances for large-scale liquid hydrogen pool releases". International Journal of Hydrogen Energy. Volume 45(43). pp 23851-23871.
<https://doi.org/10.1016/j.ijhydene.2020.06.131>.

⁴Liu, Yuanliang, et al. 2021. "Evaluation and prediction of the safe distance in liquid hydrogen spill accident". *Process Safety and Environmental Protection*, Volume 146, pp 1-8.
<https://doi.org/10.1016/j.psep.2020.08.037>.

⁵Nawaz, Waqas. 2014. *Modeling of the Cryogenic Liquid Pool Evaporation and the Effect of the Convective Heat Transfer from Atmosphere*. [Master of Science, Texas A&M University].

⁶Newsholme, G, et al. 2006. "Hydrogen: Too dangerous to base our future upon?". Institution of Chemical Engineers Symposium Series. Volume 151. pp 1-19.

⁷Nguyen, Le-Duy, et al. 2017. "An experimental investigation of the evaporation of cryogenic-liquid-pool spreading on concrete ground". *Applied Thermal Engineering*. Volume 123. pp 196-204.
<https://doi.org/10.1016/j.applthermaleng.2017.05.094>.

The Neuroscience of Gender – Exploring the Link between Prenatal Hormone Exposure and Sex-Specific Neuroanatomy in a Rat Model

Student Researcher: Delenn R. Hartswick

Advisor: Clare Mathes

Baldwin Wallace University
Neuroscience Department

Abstract

Sexual differentiation of the brain may follow a different pattern in transgender individuals than in cisgender individuals, and this may be due to different prenatal hormone environments. Some brain areas that are sexually dimorphic, such as the bed nucleus of stria terminalis (BNST), present in transgender humans at a volume intermediate to that of cisgender male and female individuals ([4]). This can be causally recapitulated in a rat model by using testosterone exposure – when female pups are exposed in utero and upon birth to testosterone, their BNST at 12 days of age display a volume in between that of male and female pups exposed to only vehicle ([1]). We seek to replicate and extend these findings by: 1) limiting testosterone exposure to prenatal only, 2) using a lower dose, and 3) examining effects at multiple time points. We planned to inject impregnated rats with testosterone propionate (TP) or with vehicle to prenatally expose their pups; however, only two rats produced litters, giving us one litter of TP-exposed pups and one litter of vehicle-exposed pups. Thus, the brains of 1 male and 1 female pup in each condition (TP and vehicle) were harvested at 3 time points. Once perfused, the rats' brains were sliced, stained, and the volume of the BNST qualitatively ranked. While our small sample sizes precluded statistical analysis, we found that the BNST of male pups were larger than the BNST of female pups at postnatal day 11 (analysis of other time points was prevented due to constraints imposed by the pandemic). This supports the known sexual dimorphism of BNST size. However, when comparing within-sex, the BNST of vehicle-exposed rats were surprisingly larger than that of the TP-exposed rats. This suggests that testosterone-exposure in early postnatal times (as done in [1]) may be more influential than prenatal testosterone exposure on brain sexual dimorphism, at least of the BNST.

Project Objectives

The overarching goal of this project is to examine the neural and hormonal components that contribute to gender and gender differences, and it is based on the hypothesis that gender identity is influenced by the developing brain's exposure to sex hormones at certain critical periods (e.g., [3]). According to this hypothesis, the brain will develop in response to the hormones it is exposed to later in prenatal development rather than the hormones it was exposed to earlier, which were regulated by chromosomal arrangement and contribute to the masculinization or feminization of the gonads and genitals of the fetus. Therefore, when the brain of a XX fetus is exposed to masculinizing or defeminizing hormones, the brain will develop differently than that of a XX fetus not exposed to those types of hormones. This often results in differing sexually dimorphic neuroanatomy and behavior in both animal models (e.g., [1, 2]) and in humans (e.g., [4]) and, potentially, in cognitive experiences including expression of gender identity. The present study sought to replicate and extend past research but by using methods that focus on prenatal exposure.

Methodology

Across two phases, 8 female rats were mated one-on-one with 8 male rats overnight to allow for accurate gestational day (GD) tracking. On GD 17, the dams were treated with either a 0.1 ml subcutaneous injection of TP (2 mg; n=1) or its vehicle (0.1 ml of 50/50 sesame oil + DMSO; n=1). However, only one

rat in the first phase, and two rats (one vehicle-exposed and one TP-exposed) in the second phase had litters, thus only those in the second phase could be used. Immediately after birth, each litter was culled to 6 males and 6 females. Pups were then cross-fostered, such that each dam has 3 of each sex of TP-exposed pups and 3 of each sex of vehicle-exposed pups. One pup of each sex and each treatment was randomly selected and removed from the vehicle-injected dam (since TP injection may alter maternal behavior) at PND 11, PND 25, and PND 46 to be perfused for the collection of brain tissue. Brain tissue was sliced, mounted, and Nissl stained with cresyl violet, and then BNST volume at PND 11 qualitatively ranked (the pandemic reduced our ability to process tissue at the later time points).

Results

The BNST was identified, and one slice that encompassed the most rostral portion per brain was selected (as per [5]). The nucleus was then outlined on by a researcher blind to the sex and treatment condition of the rat, and the outlines rank-ordered from largest to smallest. We found that the BNST of male pups were larger than the BNST of female pups at postnatal day. This supports the known sexual dimorphism of BNST size. However, when comparing within-sex, the BNST of vehicle-exposed rats were surprisingly larger than that of the TP-exposed rats. This suggests that testosterone-exposure in early postnatal times (as done in [1]) may be more influential than prenatal testosterone exposure on brain sexual dimorphism, at least at the level of the BNST.

Significance and Interpretation of Results

This study sought to explore the hypothesis that prenatal sexual differentiation of the brain may follow a different pattern in transgender individuals than it does in cisgender individuals. The results of this study suggest that perinatal and prenatal testosterone surges may play different roles in the development of sexual differentiation. Further exploration could facilitate better understanding of differing development.

Acknowledgments

Research funding and support provided in part by the Edith Robinson Fund, the Joyce Evans Schanz Summer Scholars Endowment, and the Ohio Space Grant Consortium. This research proposal was presented at the September 2019 Midwest and Great Lakes Undergraduate Research Symposium, Wooster, OH, and the October 2019 Faculty for Undergraduate Neuroscience poster session, Chicago, IL, travel for which was supported in part by the Baldwin Wallace Office of Undergraduate Research and Creative Studies and Interdisciplinary Neuroscience Society.

References

1. Chung, W. C., Swaab, D. F., De Vries, G. J. (1999). Apoptosis during sexual differentiation of the bed nucleus of the stria terminalis in the rat brain. *J. Neurobiol.*, 43: 234-243.
2. Goldman, A. S., Bongiovanni A.M., Yakovac, W.C. (1966). Production of congenital adrenal cortical hyperplasia, hypospadias, and clitoral hypertrophy (adrenogenital syndrome) in rats by inactivation of 3-beta-hydroxysteroid dehydrogenase. *Proc. Soc. Exp. Biol. Med.*, 121: 757-766.
3. Savic I. (2010). Sex differences in the human brain, their underpinnings and implications. *Prog. Brain Res.*, 186: 7-9.
4. Zhou, J., Hofman, M.A., Gooren, L.J.G., Swaab, D.F. (1995). A sex difference in the human brain and its relation to transsexuality. *Nature*, 378: 68-70.
5. Paxinos, G., Törk, I., Tecott, L. H., Valentino, K. L. (1991). *Atlas of the Developing Rat Brain*. San Diego: Academic Press Inc

Fuzzy Logic Attitude Controller of Quadcopter

Student Researcher: Daniel R. Heitmeyer

Advisor: Dr. Kelly Cohen

University of Cincinnati
Aerospace Engineering

Abstract

With the ever-increasing usage of Unmanned Aerial Vehicles (UAVs) in civil and military applications, a higher level of control and mobility of these UAVs is desired to increase stability and controllability. Fuzzy Logic has been chosen for this problem due to its proficiency with highly nonlinear systems in addition to offering explainable results through its rule base [1]. Previous work has shown the effectiveness of fuzzy logic for quadcopter usage [2]. However, this work is not compatible with the code generation used to flash the software onto a quadcopter's autopilot for real world testing.

Project Objectives

The objective of this project was to build a fuzzy logic controller to replace the PID loops typically found in a Pixhawk running PX4 flight control software. PID controllers are the most widespread used controllers for typical flight control software due to their simple structure and performance when tuned properly. These systems, however, tend to worsen when the complexity of the system is increased and could benefit when replaced with a fuzzy logic controller. This controller was aimed to exhibit faster rise times and quicker settling times when compared to the typical PID controllers. A custom fuzzy logic "toolbox" was created for this project to maintain compatibility with MATLAB's Embedded Coder and Simulink Coder so that the fuzzy logic controller can be flashed onto a Pixhawk.

Methodology Used

The benefits of fuzzy, in this project and many others, is the explainability of its results and the proficiency with highly nonlinear systems. Fuzzy logic takes a crisp input value and determines the inputs membership with one of its membership functions. Then the rule base defines a set of if then rules which determine which output group is associated with some combination of input groups. The rule base is where expert knowledge can be input as easily understood linguistic rules that determine the input to output relationship such as the two rules below.

IF 'error' is positive big AND 'error_dot' is negative small THEN 'PWM' is negative big

IF 'error' is negative small AND 'error_dot' is zero THEN 'PWM' is positive small

...

The rule base was developed for all 25 possible input combinations of the error and error dot. After all rules are calculated for the set of inputs, the system defuzzifies the result to obtain a crisp value which can be commanded to the motors. Defuzzification is done in many methods, but in general is a weighted average of all the results produced by the rule base when a set of inputs is introduced. The defuzzification method chosen for this was the mean of maximum (MeOM) as a simple yet effective method for computations. The fuzzy logic toolbox was used to visualize the system but serves no functionality in the actual computations and system structure.

The UAV Toolbox in MATLAB was used for providing a model for the flight controller to be flashed onto the Pixhawk, as well as providing integration with the code generators used in this project [3]. The

model used in this problem accepts joystick data as an input and outputs the PWM values to the actuators.

Results Obtained

To encourage the fuzzy system to output PWM commands near the saturation limit, the membership functions of the inputs were clustered near the center and wide trapezoidal membership functions were put at the ends as seen in Figure 1. Both inputs share the same membership function shapes. This was aimed to produce output values near the saturation limit to fester quicker rise times in the controller when compared to a typical PID controller. The output membership functions chosen are simple triangles as seen in Figure 2.

Combining the rule base with these input and output membership functions, a surface plot shown in Figure 3. is created which shows the overall response of the system for a set of inputs. Notably the surface plot is symmetric so the same response, but opposite is provided for the same input set of opposite sign.

Deployment and testing of this fuzzy system requires the use of MATLAB's embedded coder. The other packages required by the UAV Toolbox have been purchased and installed, but the embedded coder requires a MathWorks representative to approve a trial. I have yet to receive responses to my request and for that reason the fuzzy system has not been deployed onto simulation or a quadcopter yet.

Significance and Interpretation of Results

A fuzzy logic based attitude controller was developed and is ready for deployment into simulation and then real flight testing. Once simulated, the rule base can be further tuned if desired to improve markers such as rise time and settling time. Future work includes adding a fuzzy logic position controller, testing under scenarios where typical pilots and autopilots would fail such as slung payloads, and the actual test flights to determine its worth in real world applications.

Figures/Charts

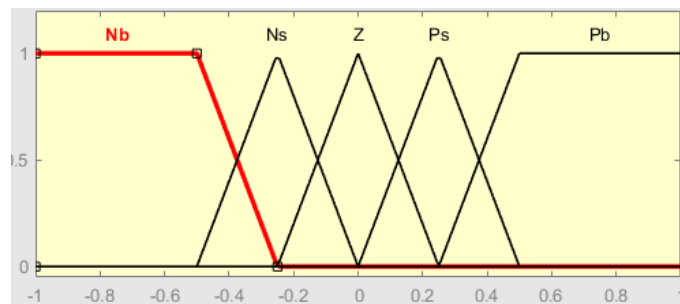


Figure 1. Generic Input Membership Functions

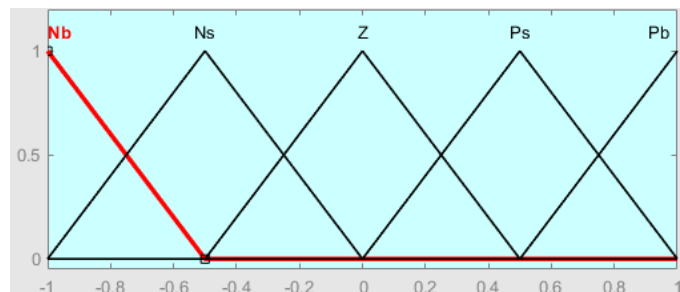


Figure 2. PWM Output Membership Functions

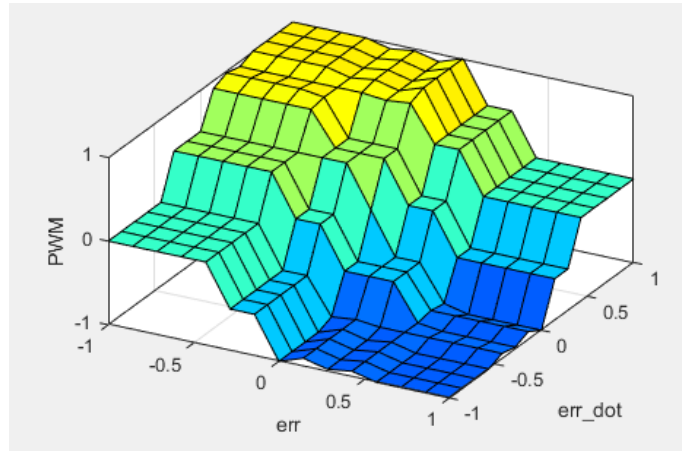


Figure 3. Surface Plot

Acknowledgments

My thanks go to Dr. Kelly Cohen for his help and guidance and to the Ohio Space Grant Consortium who made this possible.

References

1. Vandana, A. and Kathyaini, C., "Controlling of Nonlinear System by using Fuzzy Logic Controller," *International Research Journal of Engineering and Technology*, Vol. 2, No. 7, Oct. 2015.
2. Sureshkumar, V. "Autonomous Control of A Quadrotor UAV Using Fuzzy Logic." Electronic Thesis or Dissertation. University of Cincinnati, 2015. *OhioLINK Electronic Theses and Dissertations Center*.
3. MathWorks. (2021). *Attitude Control for X-Configuration Quadcopter Using External Input* (r2021a). Retrieved March 10, 2021 from <https://www.mathworks.com/help/supportpkg/px4/ref/attitude-control-px4-external-input.html>

Creating Fluorescent Quantum Defects in Chirality-Pure Carbon Nanotubes Using Small Molecules

Student Researcher: Brandon J. Heppe

Advisor: Geyou Ao, Ph.D.

Cleveland State University

Department of Chemical and Biomedical Engineering

Abstract

Pure-chirality single-wall carbon nanotubes (SWCNTs) possess well-defined optical and electronic properties that can be functionalized covalently with molecular precision to develop applications, such as biochemical sensing and imaging and single photon sources via exciton trapping. Pure-chirality SWCNTs are isolated utilizing recognition DNA sequences in a polymer aqueous two-phase system. DNA coatings can further be displaced by surfactants, such as sodium dodecyl sulfate (SDS), due to their stronger binding affinities toward the surface of nanotubes compared to that of DNA in water. This provides an avenue to modulate the coating structures on the SWCNT sidewalls as needed for photochemical reactions of nanotubes. Diazonium salts will be utilized to create fluorescent quantum defects on pure-chirality (6,5) SWCNTs with UV irradiation. Optical properties of the functionalized SWCNTs will be compared to determine the efficiency of photochemical reactions of nanotubes with different molecules. Nanotube chemistry offers vast potential for creating carbon-based fluorescent probes with tunable photoluminescence in the near-infrared (NIR) region for developing novel applications. [1], [2]

Project Objectives

The ultimate goal for this project is to better understand the structure-property relationships of chirality-pure SWCNTs functionalized by small molecules of various functional groups, and developing applications of SWCNTs with specific optical functionality. To achieve this goal I have focused on using diazonium salts to react with pure-chirality (6,5) SWCNT species and to compare the resulting optical properties, and to determine the efficiency of photochemical functionalization of nanotubes. This will also involve investigating the effects of coating materials (i.e., surfactants and DNA) adsorbed on the surface of nanotube on the photochemical reaction of nanotubes.

Methodology Used

DNA-wrapped SWCNT solution was created using CoMoCAT SWCNT powder (SG65i-L39, CHASM Advanced Materials) in a recognition DNA sequence solution TTA TAT TAT ATT (Integrated DNA Technologies) with a NaCl concentration of 0.1 mol/L and probe tip sonication (model VCX 130, Sonics and Materials, Inc.) for 2 hours at a power level of 8 W. Supernatant was collected after centrifugation of aqueous dispersions of DNA-wrapped SWCNTs. (6,5) was separated using a polymer aqueous two-phase (ATP) system containing polyethylene glycol (6 kDa) 5.5 mass%/ dextran (70 kDa) 7.5 mass% (PEG/DX). (6,5) SWCNT was isolated in the PEG rich top phase with the addition of polyvinyl pyrrolidone (PVP), which modulates the distribution of SWCNTs in the ATP system. Samples were incubated at 4 °C and centrifuged for 30 minutes at 17,000g. Supernatant was discarded and (6,5) pellet was washed with deionized water (DI). (6,5) pellet was resuspended in DI with additional free DNA concentration of 100 µg/ml for improved stability of SWCNTs.[3] DNA coatings on the surface of (6,5) SWCNTs were replaced with surfactant coatings of sodium dodecyl sulfate (SDS) *via* DNA/exchange reaction.. SWCNT sample was then diluted to obtain an optical density of 0.1 ± 0.02 at the E_{11} absorption peak of (6,5) near 995 nm.[4] Synthesis of diazonium salt was carried out by combining aqueous 4-aminobenzoic with excess HCl and aqueous solution of NaNO_2 to result in the formation of a diazonium ion.[5] Then, SDS-coated (6,5) SWCNT was combined with diazonium solution at various concentrations. SWCNT sample was irradiated by ultraviolet

(UV) light (3UV Lamp, cat# 95034, Thermo Scientific) for photochemical reaction. Sample was protected from ambient light after addition of diazonium salt and during irradiation. SWCNT sample absorption spectra and fluorescence spectra were measured using NS3 Nanospectralyzer (Applied NanoFluorescence, LLC) prior to and post reaction.

Results Obtained

In Figure 1a. there is an apparent blueshift of 8 nm after completing the surfactant exchange procedure using SDS. Surfactants are known to have stronger binding affinities towards the surface of nanotubes than DNA in water. In Figure 1b. the presence of diazonium salt and irradiation causes the creation of a new, red-shifted emission peak (E_{11}^-) of 1144 nm. With the formation of the E_{11}^- peak, intensity of the original emission peak (E_{11}) diminished at the 995 nm location is seen as a result. Using aliquots of the 0.02 mg/ml diazonium solution showed the largest formation of E_{11}^- peak. With the addition of a larger concentration of diazonium of 0.03 mg/ml, E_{11}^- peak formation was found to be less significant.

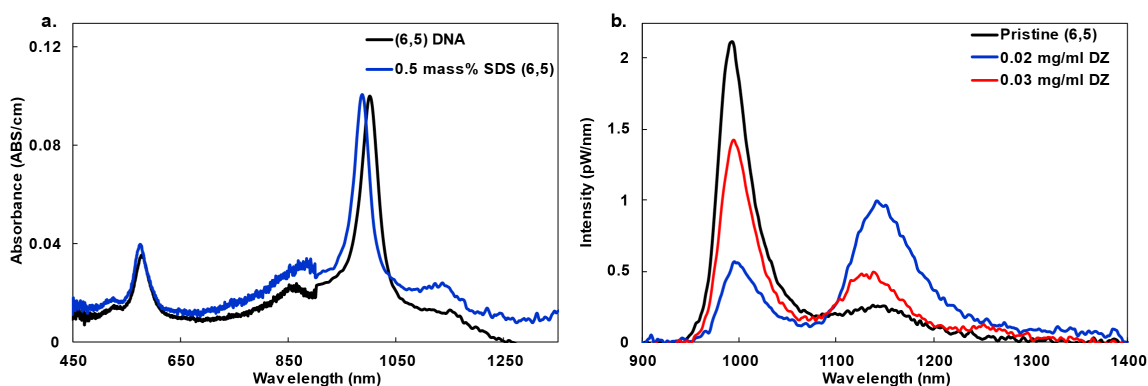


Figure 1. (a) Absorbance spectra of DNA-SWCNTs and SDS-SWCNTs after displacing DNA coatings on nanotubes. (b) Fluorescence spectra of SDS-coated (6,5) SWCNTs before and after diazonium (DZ) reaction at various concentrations of DZ salt with UV light irradiation.

Significance and Interpretation of Results

From results gathered we can conclude that irradiation of the (6,5) 0.5 mass% SDS and diazonium solution has caused the formation of a fluorescent quantum defect on the surface of the SWCNT. From previous literature, optimal diazonium doping occurs at a reactant molar ratio of [Diazonium]:[SWCNT Carbon] of 2.5×10^{-3} (400:1) indicating that synthesis of diazonium under discussed procedure is low.[6] With assuming that optimal diazonium doping occurs using the 0.02 mg/ml diazonium solution, calculated yield of diazonium synthesis is found to be approximately 3%. Further research is underway to analyze the exact yield of diazonium synthesis, how to improve on current diazonium synthesis procedure, and to verify fluorescent quantum defect reaction being caused by diazonium and to rule out potential O_2 doping through oxygen removal from the sample. Continuation of this project will include: use of various surfactants to coat SWCNTs, locating optimal irradiation time, and the effects of under doping and over doping of SWCNTs.

Acknowledgments and References

B.J.H acknowledges the NASA OSGC Scholarship and NSF REU support. We also acknowledge Dr. Xue-Long Sun and Ka Keung Chan for useful discussion.

- [1] M. E. Sykes *et al.*, "Ultrafast Exciton Trapping at sp^3 Quantum Defects in Carbon Nanotubes," *ACS Nano*, vol. 13, no. 11, 2019, doi: 10.1021/acsnano.9b06279.

- [2] L. R. Powell, Y. Piao, and Y. Wang, "Optical Excitation of Carbon Nanotubes Drives Localized Diazonium Reactions," *Journal of Physical Chemistry Letters*, vol. 7, no. 18, 2016, doi: 10.1021/acs.jpcllett.6b01771.
- [3] G. Ao, C. Y. Khripin, and M. Zheng, "DNA-controlled partition of carbon nanotubes in polymer aqueous two-phase systems," *Journal of the American Chemical Society*, vol. 136, no. 29, pp. 10383–10392, 2014, doi: 10.1021/ja504078b.
- [4] F. Xhyliu and G. Ao, "Chirality-pure carbon nanotubes show distinct complexation with recognition DNA sequences," *Carbon*, vol. 167, 2020, doi: 10.1016/j.carbon.2020.06.040.
- [5] D. R. Grimes, C. Robbins, and N. J. O'Hare, "Dose modeling in ultraviolet phototherapy," *Medical Physics*, vol. 37, no. 10, pp. 5251–5257, 2010, doi: 10.1118/1.3484093.
- [6] Y. Piao *et al.*, "Brightening of carbon nanotube photoluminescence through the incorporation of sp³ defects," *Nature Chemistry*, vol. 5, no. 10, 2013, doi: 10.1038/nchem.1711.

Advanced Polymeric Materials for Aerospace Applications

Student Researcher: Sarah C. Herbruck

Advisor: Mark A. Sidebottom

Miami University

Department of Mechanical and Manufacturing Engineering

Abstract

Solid Polymer bearing materials are useful for use in aerospace situations. Graphite-filled polyimide is one such material with useful characteristics. With the use of a flat-on-flat tribometer, the tribological performance (friction and wear) of graphite-filled polyimide is evaluated. Wear rates improved as pressure increased. Initial wear rates are higher when graphite-filled polyimide is tested with rough surfaces, as opposed to mirror polished surfaces.

Project Objectives

Solid Polymer bearing materials are used in turbofan engines where the extreme conditions (high thermal and mechanical loads) would cause traditional liquid lubricants to fail. An example of a solid polymer bearing material is graphite-filled polyimide, which combines heat resistance, lubricity, dimensional stability, and chemical and creep resistance. This material is often used for bearings, thrust washers, and dynamic seals. By testing the friction and wear properties of graphite-filled polyimide under different conditions (contact pressure and surface finish), this study aims to allow for better machine and material design choices. These improvements may lead to longer maintenance intervals, higher engine temperature (higher performance), and improve combustion output in turbofan engines.

Methodology Used

Before testing began, the dimensions of each sample were taken using a caliper with resolution of 0.01mm. The initial mass of each sample was recorded using a 10 μ g resolution scale (Mettler Toledo XS205). Using these two values, the density for each sample was calculated. After the initial measurements, a flat-on-flat tribometer was used to evaluate the friction coefficient and wear rate between graphite-filled polyimide against 304 stainless steel. The tests conditions and details are included in Figure 1a. During the tests, the normal force, frictional force, volume lost, and distance traveled were all recorded to calculate the friction coefficient (Eq. 1) and wear rates (Eq. 2) of each sample.

Results Obtained

Two tests were run for each combination of pressure and surface finish. Each test's results were reviewed for possible outliers and variation within the experiment. For each set of test conditions, the test with the least number of outliers and smallest deviation was chosen to represent the representative behavior of graphite-filled polyimide at those conditions. The average friction and wear rates for each testing condition are presented in Figure 1b.

Significance and Interpretation of Results

Through observation of the data provided on the graphs, a few trends in the wear and friction performance of graphite-filled polyimide can be observed. In Figure 1b, it can be observed that graphite-filled polyimide performs better under higher pressures. More mass was lost in every test under 280N, ranging from 9.27 mg to 4.09 mg, as compared to the 28 N tests, which lost mass ranging between 3.2

mg and 1.29 mg. Despite these results, it is observed that the total wear rates of samples tested at 280N vary between $4.4 \times 10^{-7} \text{ mm}^3/\text{Nm}$ and $9.7 \times 10^{-7} \text{ mm}^3/\text{Nm}$, while the total wear rates for cycles run with an applied force of 28N were as high as $1.4 \times 10^{-5} \text{ mm}^3/\text{Nm}$, with minimum wear rates of $2.1 \times 10^{-6} \text{ mm}^3/\text{Nm}$. From this data, it can be concluded that the ratio between volume lost and force applied improves as force increases.

There is small evidence of correlation between surface roughness and initial wear rates. At each pressure, the samples tested against the rough surface experienced a much higher initial wear rate, compared to the samples tested against the mirror surface. For the test simulating a contact pressure of 6.9 MPa, the lowest initial wear rate for samples tested on a rough counter surface is $2.6 \times 10^{-5} \text{ mm}^3/\text{Nm}$, while the highest initial wear rate for samples tested on a mirror surface is $8.6 \times 10^{-6} \text{ mm}^3/\text{Nm}$. In the case of 0.69 MPa, maximum initial wear rates for samples against mirror surfaces is $6.0 \times 10^{-5} \text{ mm}^3/\text{Nm}$, while minimum wear rates for the rough surface is $7.2 \times 10^{-5} \text{ mm}^3/\text{Nm}$. In both cases, initial wear rates are consistently higher when samples are tested with rough countersurfaces. No apparent correlations can be drawn between the friction coefficients and the force applied or surface finish.

Figures/Charts

$$\mu = \frac{F_f}{F_n} \quad (1)$$

$$\kappa = \frac{V_{Lost}}{F_n * d} \quad (2)$$

$$V_{Lost} = \frac{m}{\rho} \quad (3)$$

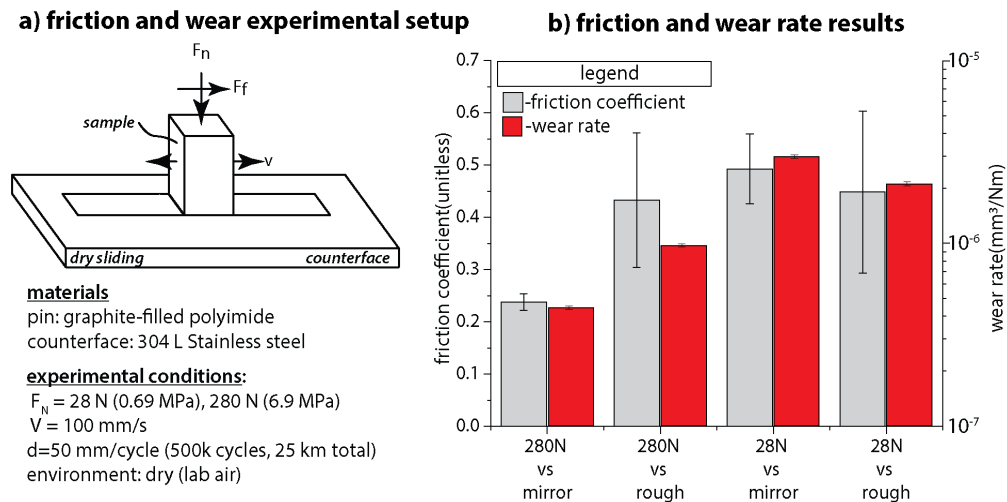


Figure 1. Experimental Setup and Results

Acknowledgments and References

I would like to express my gratitude towards Miami University graduate students Sifat Ullah and Faysal Haque for their guidance and assistance in running tribometer tests. Thanks are extended to Brad Martin for facilitation in machining the graphite-filled polyimide samples. I would like to express my special gratitude and thanks to DuPont for supplying the graphite-filled polyimide samples for testing.

Fractionation and Purification of Lettuce Cell Sub-compartments

Student Researcher: Catherine E. Howell

Advisors: Ajay Mahajan and Catherine Konopka

Akron University
Biomedical Engineering

Abstract

Currently, there are three methods used to produce vaccines: egg-based, cell-based, and investigational manufacturing systems. Investigational manufacturing systems refers to the use of biological systems such as plants, insect cells, or bacterial culture to manufacture vaccines. Recently, plant-based vaccines have been suggested as an alternative to egg-based and cell-based vaccines. A gene delivery system can be used to transform the genome of a biological cell. This approach allows an antigenic protein to be produced in plants. We apply reported methods used for isolating organelles from Arabidopsis, to isolate organelles from lettuce leaves. Specifically, we use cell fractionation and differential centrifugation with various gradients, such as Percoll and sucrose. Sub-cellular and sub-organelle fractions are assessed for purity using immunoblotting.

Project Objectives

The overall objective of this project is to produce transgenic lettuce lines that produce bioactive proteins. One of the sub-objectives to help fulfil this goal is to develop a method that can successfully purify subcellular compartments from lettuce cells. This will allow for the eventual purification of an antigenic protein from plant cells once they have undergone genomic transformation. By showing that lettuce cell sub compartments can be purified using previously published methods, this project lays the foundation for the future purification of an antigenic protein from plant cells.

Methodology Used

Methods were adopted from research by Bouchnak et al. (2018). This protocol was originally used on Arabidopsis leaves but was adapted for use on lettuce in this project. Buffers and solutions used throughout the procedure were made to match those of Bouchnak et al. (2018). Throughout the procedure, samples were taken to be run through gel electrophoresis.

Growth and Harvesting of Lettuce Leaves

Two types of lettuce plants were used for this project, simpson elite and rosanita. Simpson elite seeds were obtained from Reimer Seeds, while rosanita seeds were obtained from USDA ARS Grin. 250 g of leaf material was harvested for purification. Once weighed, this material was kept on ice throughout the procedure. Leaves were homogenized with 1L of grinding buffer (with added BSA) using a Waring blender. After this the homogenate was filtered using four layers of muslin and one layer of nylon blutex. Any remaining tissue that did not pass through this filtering step was recollected and placed into the blender for a second extraction carried out by repeating the previous process.

Purification of Crude Chloroplasts

The crude cell extract from homogenization of the lettuce leaves was equally distributed into six 500 mL bottles that were placed on ice. These were centrifuged for 2 minutes once maximum speed was reached (2,070 x g) using maximum acceleration and brake, at a temperature of 4 degrees Celsius. The supernatant

was discarded, and the pellet was resuspended using a minimal amount of washing medium. This resuspended mixture was collected into one tube that was inverted to obtain a homogenous mixture.

Purification of Chloroplasts Using a Continuous Percoll Gradient

Chloroplast suspension was equally divided and placed on top of six Percoll gradients. Gradients were centrifuged for 10 minutes at 13,300 g and 4 degrees Celsius using a swinging-bucket rotor, slow acceleration and no brake were used. The upper phase of the gradients was aspirated, and intact chloroplasts present in the lower phase were retrieved using a micropipette (Figure 1). Intact chloroplast suspension was diluted 3-4-fold using washing buffer. This was centrifuged for 2 minutes once maximum speed was reached (2,070 x g) using maximum acceleration and brake, at a temperature of 4 degrees Celsius. The supernatant was discarded and the pellet containing intact chloroplasts was kept on ice.

Lysis of Intact Chloroplasts

Intact chloroplasts were lysed by resuspending the pellet in hypotonic medium. 3mL of lysed chloroplasts were loaded onto preformed sucrose gradients. Gradients were centrifuged for 1 hour at 70,000 x g at 4 degrees Celsius. The yellow band containing the envelope was recovered from these gradients, as well as the thylakoid pellet at the bottom of the gradient (Figure 2). Due to collapse of the tubes from centrifugation, the stromal layer, which would normally be at the top of the gradient was unable to be obtained. During a 2nd trial it was also unclear whether the stromal layer was obtained.

Results

The protocol detailed above was performed two times. During the first trial, test tubes collapsed during centrifugation of the sucrose gradients once they were loaded with lysed chloroplasts (Figure 2). Due to this the stromal layer could not be collected. Additionally, this contributed to mixing of the fractions that were trying to be separated. Gel electrophoresis of intact chloroplasts and sub-compartment samples showed that, some fractions were mixed and not successfully separated. Abundant proteins, such as RUBISCO, the major carbon-fixing enzyme, are evident in aliquots taken throughout the procedure. Although present throughout the procedure, partial separation of RUBISCO can be seen as indicated by Figure 3. During trial two, modifications were made to prevent the test tubes from collapsing during centrifugation. Modifications involved doubling the volume of each layer in the sucrose gradient to prevent collapse of the tubes. Although this prevented collapse of the tubes, it made obtaining the layers containing the sub-compartments much more difficult because these proteins were diluted throughout a larger volume. Due to this, it was unclear whether proper samples were obtained for the stromal and envelope layers. Gel electrophoresis for this trial also indicates mixing of some fractions but shows the successful separation of proteins such as RUBISCO. Additionally, this gel indicates successful fractionation of the thylakoid compartment as indicated by Figure 4.

Significance and Interpretation of Results

Complete fractionation and purification of lettuce cell sub compartments wasn't successful in these trials, but the protocol itself shows potential to be successful with proper modification. Pattern repeats on the gels show that there was mixing of sub-fractions during the protocol. Purification of larger proteins, such as RUBISCO, as well as the separation of the thylakoid compartment show that this protocol has the potential to be successful with additional trials. Using more plant starting material will lead to better results, since there will be more material to obtain protein from. Additionally, using tools such as a gradient maker and water pump may allow for better obtainment of sub-compartments using the Percoll

and sucrose gradients. Overall, this protocol shows potential for the successful fractionation and purification of lettuce cell sub-compartments.

Figures/Charts



Figure 1- Shows the Percoll gradient after centrifugation with the crude chloroplasts extract. The thick band towards the top is broken chloroplasts, while the thick band near the bottom is intact chloroplasts.

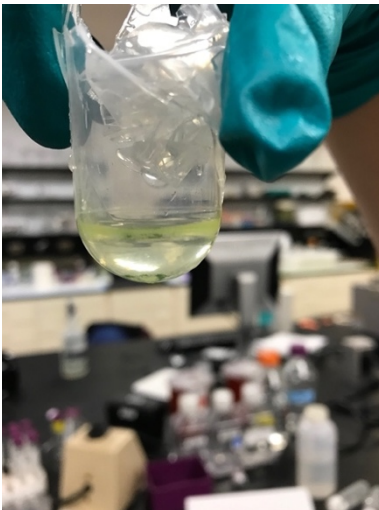


Figure 2- Shows the sucrose gradient after centrifugation with the intact chloroplast extract. It can be seen that the tube collapsed inward during centrifugation, causing the stromal layer that would normally be at the top to get destroyed. The faint yellow green band shown at the top of the gradient in this picture is the envelope, while the small green material at the bottom is thylakoid.

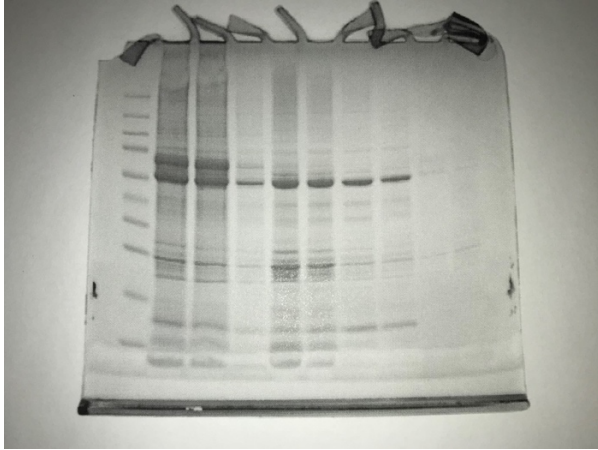


Figure 3- Gel electrophoresis for trial 1. Lanes are as follows (from left to right): Plus pre-stained protein ladder, crude chloroplast extract, spin 1, upper layer, lower layer, broken chloroplasts, intact chloroplasts, lysed chloroplasts, chloroplast envelope, chloroplast thylakoid. Spin 1 refers to supernatant collected from centrifugation performed during purification of crude chloroplasts. Upper layer and lower layer refer to samples taken of the in between layers from the Percoll gradient. Upper layer is the layer above the broken chloroplasts, while lower layer is the layer above the intact chloroplasts.

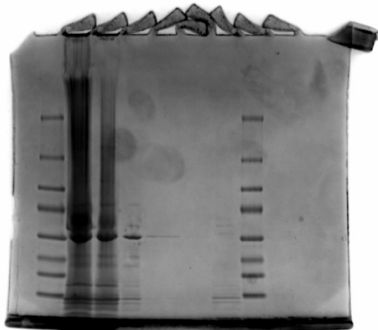


Figure 4- Gel electrophoresis for trial 2. Lanes are as follows (from left to right): Plus pre-stained protein ladder, crude chloroplast extract, lysed chloroplasts, stroma, thylakoid, second ladder. During trial 2, a sample was not taken of supernatant from spin 1. Additionally, samples of the layers in between layers of interest were not taken from the Percoll gradient.

Acknowledgements and References

This work was performed at the University of Akron. I would like to acknowledge the University of Akron for supporting this project and for allowing use of their on-campus lab resources. I also would like to acknowledge the Ohio Space Grant Consortium for their financial contribution to my education, which allowed me to have the time to dedicate to this research.

Reference

Bouchnak, I., Moyet, L., Salvi, D., Kuntz, M., & Rolland, N. (2018). Preparation of Chloroplast Sub-compartments from Arabidopsis for the Analysis of Protein Localization by Immunoblotting or Proteomics. *Journal of visualized experiments: JoVE*, (140), 58581. <https://doi.org/10.3791/58581>

Sixth Generation(6G) Technology for Future Cognitive Satellite Communication

Student Researcher: Allayah C. Hughes

Advisor: Dr. Deok H. Nam

Wilberforce University

Department of Computer Engineering

Abstract: The proposed project presents the investigation of the basic issues and key expected highlights of the sixth generation (6G) interchanges including vision and key highlights of the 6G satellite communication. Besides, difficulties and possible arrangements of the 6G satellite communication, and the 6G satellite communication research exercises in terms of the connection to the inspiration of their different sub-spaces to accomplish an exact, concrete, and compact end are presented.

Project Objectives: The objectives of the proposed project are understanding the foundational background on the 6G satellite communication with its vision and key highlights of the 6G satellite communication, the technical restriction of the 6G satellite communication along with its possible arrangements, and 6G satellite communication research to improve the current satellite communication technologies.

Methodology Used: A remote cell correspondence age arises around like clockwork since 1980, including the original simple FM cell frameworks in 1981, the second era in 1992, the third era (3G) in 2001, and the fourth era (4G) (regularly alluded to as the drawn-out development [LTE]) in 2011. Figure 1 [4] presents a summation of the developing remote advancements. Due to the data speed of fifth generation (5G) [1] by the rapid increase of massive and extended data-oriented applications, 6G wireless communication network is getting more focused to satisfy the demand of proliferated wireless services including 6G satellite communication. The normalization exercises of the 5G satellite communication are completed and an arrangement has been initiated all around the world. To support the serious edge of remote satellite communication, the mechanically and scholarly world collaboration have started to conceptualize the up-and-coming age of remote correspondence frameworks such as the 6G satellite communication. To satisfy the necessities of different upcoming applications, the future 6G versatile satellite communication will be relied upon to be a naturally smart, exceptionally unique, ultra-dense heterogeneous communication network that interconnects everything with low-idleness and quick information transmission. Hence, man-made reasoning like Artificial Intelligence (AI) will be the most creative strategy that can accomplish smart mechanized organization tasks, the board, and upkeep in future complex 6G satellite communication. Driven by AI methods, satellite communication with localized node-to-node correspondence will be one of the bits of the 6G satellite communication structure. To develop the advanced 6G satellite communication research to improve the current satellite communication technologies, the present circumstance must be considered, which presents troublesome difficulties on a zone or spatial ghastly productivity and the required recurrence range groups for the network. Subsequently, a more extensive radio recurrence range data transfer capacity has become a need and must be found at the sub-terahertz (THz) and THz groups [2]. Additionally, the new upsurge of expanded portable applications, particularly those upheld by Artificial Intelligence (AI) innovation [3], is prodding warmed conversations on the future development of remote correspondences. These difficulties have propelled industry and the scholarly world to begin conceptualizing the up-and-coming age of remote correspondence frameworks (6G) pointed toward giving correspondence administrations to the future requests of the 2030s and keeping up the maintainability and intensity of remote

correspondence frameworks. Consequently, the 6G correspondence frameworks are required to give an enormous inclusion that permits supporters to speak with each other wherever with a high information rate speed because of the flighty advances that will be received by 6G correspondence frameworks, like an incredibly huge data transfer capacity (THz waves) and high AI that incorporate the operational and ecological perspectives just as the administrations of the organizations.

Results: Through this study, the foundational background on the 6G satellite communication with its vision and key highlights of the 6G satellite communication has been presented along with the technical restriction of the 6G satellite communication along with its possible arrangements to develop the advanced 6G satellite communication research to improve the current satellite communication technologies.

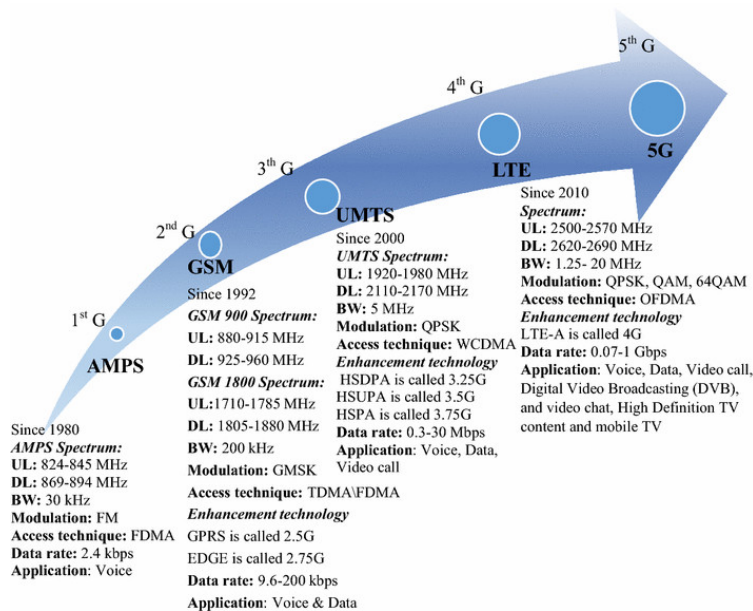


Figure 1. Major milestones for different generations of communications (1–6G) [4].

Acknowledgments: The author is grateful to the supervisor Dr. Deok H. Nam at Wilberforce University for his invaluable support, encouragement, and guidance. The author also thanks Ohio Space Grant Consortium (OSGC) for the academic scholarship program. Special thanks to Dr. Andrew L. Gyekenyesi and Mr. Timothy M. Hale of OAI for the OSGC Program.

References:

- [1] M. Alsharif and R. Nordin, "Evolution towards fifth-generation (5G) wireless networks: Current trends and challenges in the deployment of millimeter-wave, massive MIMO, and small cells," *Telecommunication System*, 2017, 64, 617–637.
- [2] M. Albreem, M. Alsharif, and S. Kim, "A Robust Hybrid Iterative Linear Detector for Massive MIMO Uplink Systems," *Symmetry* 2020, Vol. 12, pp. 306-317.
- [3] H. Yang, A. Alphones, Z. Xiong, D. Niyato, J. Zhao, and K. Wu, "Artificial Intelligence-Enabled Intelligent 6G Networks," *IEEE Network*, Volume: 34, Issue: 6, November / December 2020, pp. 272 - 280.
- [4] S. Mohammed, A. Kelechi, M. Albreem, S. Chaudhry, M. Zia, and S. Kim, "Sixth Generation (6G) Wireless Networks: Vision, Research Activities, Challenges, and Potential Solution," *Symmetry* 2020, 12(4), pp. 676-696.

Quadrotor Arm Dihedral and Motor Twist Angle Impact on Maneuvering Stability

Student Researcher: Sebastian J. Lemieux

Advisor: Dr. Kelly Cohen

University of Cincinnati
Aerospace Engineering

Abstract

Many commercially available multirotor Unmanned Aerial Vehicles (UAVs) incorporate some amount of dihedral or anhedral angle to improve stability while filming and carrying payloads. To improve yaw authority and stability, this research seeks to make discrete changes in the twist of a multirotor's motors by changing each motor's angle relative to vertical on each arm. This gives each motor a degree of horizontal thrust to control yaw rather than conventionally relying on changing the total torque of the system through motor rpm. The small UAV used in this research will utilize a custom arm mount design that allows for increasing changes to the angle of the platform's tube arms accompanied with motors that may rotate to any desired twist angle. The effects of these factors on flight will be analyzed by reviewing the flight logs created by the ardupilot flight control software to determine the attitude tracking error and waypoint tracking error of the platform in each configuration.

Project Objectives

The goal of this project is to evaluate the effects that arm angle and motor twist have on the flight stability of a multirotor. As the evaluation of flight characteristics will require repeated iterations in each arm angle and motor twist configuration, this project aims to create a testing platform that can reliably change the arm angle and motor twist of a sub-55-pound platform and complete autotune flights and waypoint missions in a scope of standard UAV operating weather conditions. This requires sufficient flight time of at least 8-9 minutes to complete autotuning flights. This custom platform named "Archimedes" seen in Figure 1 allows for these discrete changes when utilized with the modified arm mounts visible in Figure 2 and Figure 3. These arm mounts are machined aluminum and allow for 1 degree increments from 14° dihedral to -12° anhedral.

This project also sought to establish a well-constructed data collection methodology for the flight log attitude data from each flight. This was done by creating a MATLAB script that parses data from the .bin file ardupilot provides and uses APIs to create a Google Sheets spreadsheet where the data can be displayed for all team members.

Methodology Used

The effects of these factors on flight will be analyzed by first using ardupilot's autotune in varying configurations of arm angle and motor twist to obtain optimal PIDs. Next an evaluation flight is flown autonomously where a flight log is made. Gyro data, accelerometer data, and desired versus actual rates are then compared from each flight log and used to quantify both the stability of the small UAV as well as the level of controllability. The evaluation flights will follow a square and horizontal waypoint mission as visible in Figure 4 and Figure 5. This allows the UAV to enter a larger variant of flight attitudes, positions, and wind directions and provides a substantial sample of error data to be evaluated.

A multivariate analysis of variance is to be completed after each test flight at varying arm angle and motor twist configurations as a canonical regression method used to determine if there is an interaction

between the arm angle and motor twist and resulting attitude and waypoint tracking error. These changing configurations are done in a non-sequential order specified by the pilot in command to ensure varying weather conditions throughout the day have minimal effect on the variance shown in results from each configuration. Within the MATLAB script for parsing the flight log data, the waypoint tracking error along with attitude tracking error are calculated and a mean absolute deviation, as shown below, of each error is gathered as a metric of controllability and stability of the platform.

$$\frac{1}{n} \sum_{i=1}^n |x_i - m(X)|.$$

Results Obtained

Shown in Figure 6, the initial mean absolute deviations of the roll and pitch directions were within the scope of 1.0 to 1.50 degrees of average deviation, which has been deemed acceptable by previous studies [1]. The yaw direction, however, needs further tuning to be considered viable for this study, especially considering the impact of motor twist on yaw stability.

The platform failed to complete ardupilot's autotune in the yaw direction during initial testing due to insufficient battery flight times. This issue was solved after research into improved battery technologies, and the platform Archimedes can now complete accurate autotune flights and remain airborne for at least 8 minutes. The autotunes resulted in a maximum mean absolute deviation in yaw of 1.319. Further testing is required to validate the platform's airworthiness and repeatability of control with its current system of motors and ESCs. This will allow for waypoint tracking error to be analyzed as the platform could not reliably complete waypoint missions under proper tuning during initial testing. Alterations to the initial design increasing overall motor size, ESC capability, and arm length are underway to improve the range of operations of Archimedes and allow for an appropriate range of testing conditions.

Significance and Interpretation of Results

The initial results of this project show that the platform Archimedes is a viable platform to continue this research and test the effects of arm angle and motor twist on multirotor UAV systems. Further tuning is needed to consider this platform ready for strenuous testing of varying flight configurations. A change in the power system and change of the arm design mounting hardware will allow for longer flight times, larger propellers, and improve the range of operations and consistency in performance of the platform. The test methodology and data collection method of this research will remain unchanged as they prove proficient in providing representation of controllability and stability in multiple flights of Archimedes.

The results of this research may hopefully be implement on future UAV platforms to create improved multirotor arm designs that provide better stability and controllability during flights for various operations.

Figures/Charts



Figure 1. Archimedes Platform

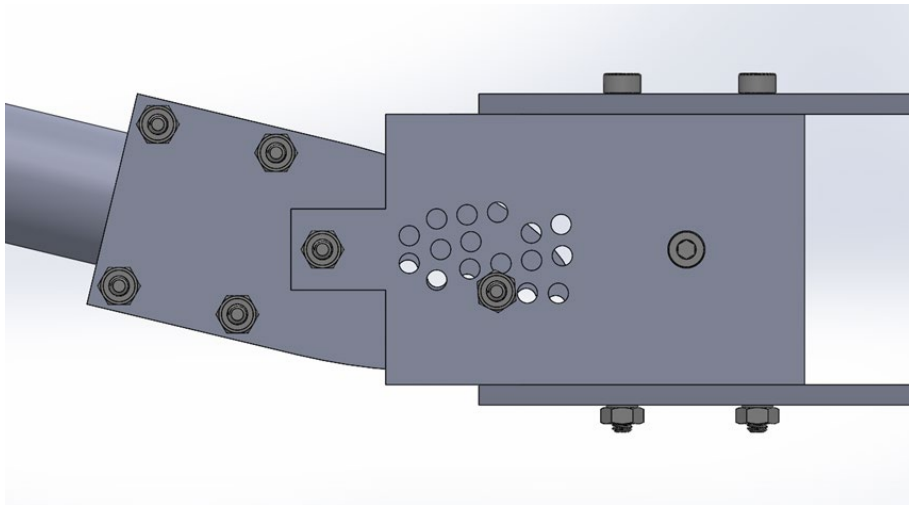


Figure 2. Custom Arm Mounting Bracket

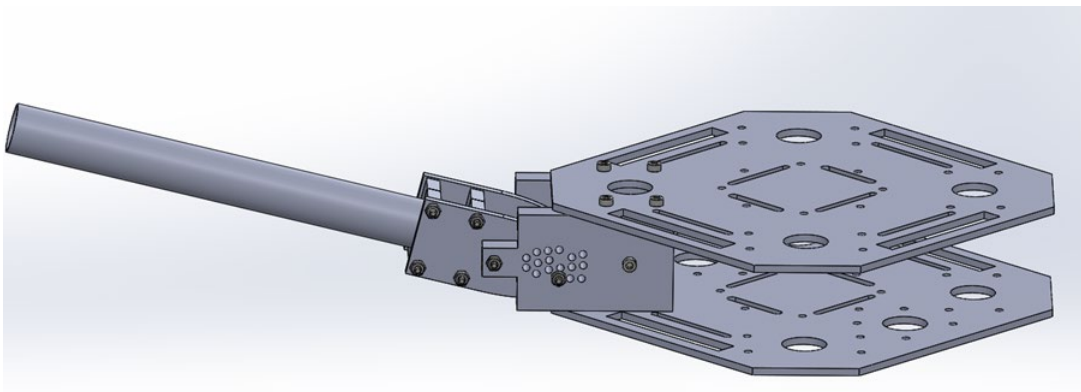


Figure 3. Arm Bracket on Archimedes Plates



Figure 4. Square Waypoint Mission

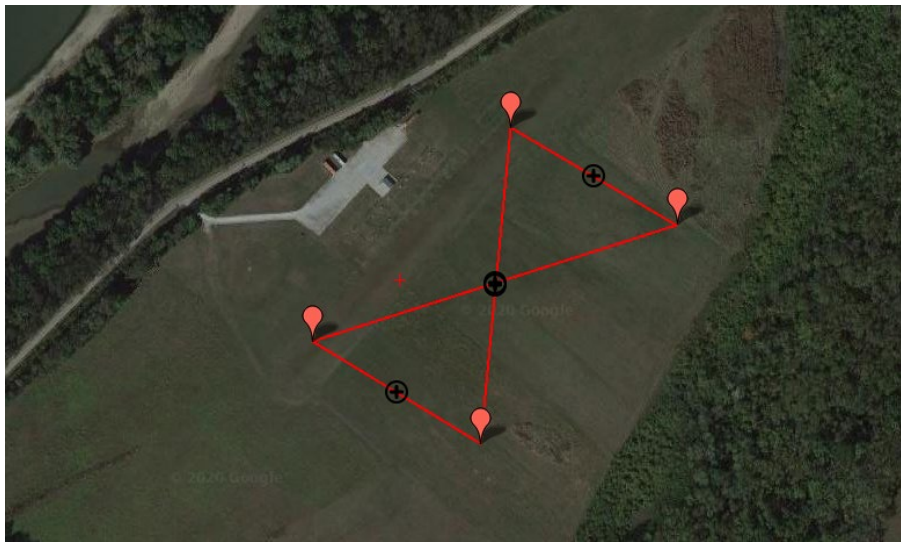


Figure 5. Hourglass Waypoint Mission

	Flight				
Mean Absolute Deviation	1	2	3	4	5
Command Roll Vs Actual Roll	0.7605442442	0.6607687537	0.5912619411	0.580201614	0.3160057419
Command Pitch vs Actual Pitch	1.109487847	0.5747793461	2.633200525	3.043792276	0.40637696
Command Yaw vs Actual Yaw	5.629751621	3.353592107	2.688473317	2.621853592	7.17442149

Figure 6. Stock Archimedes Deviation Results

Acknowledgments

My thanks go to Dr. Kelly Cohen for his help and guidance, Heath Palmer for his thesis research work that directs and guides this project, and to the Ohio Space Grant Consortium who made this possible.

References

1. Mardan, Maziar, et al. "Attitude and Position Controller Design and Implementation for a Quadrotor." *International Journal of Advanced Robotic Systems*, vol. 14, no. 3, 18 Nov. 2016, pp. 1–11., doi:10.1177/1729881417709242.

Space Food Trials on Fruit Flies

Student Researcher: Naja T. Long

Advisor: Mark Nielsen

University of Dayton
Biology

Abstract

When it comes to fruit flies, they are seen as unwanted pests within the kitchen hovering over unwanted foods. Little do we know fruit flies can be the change of something greater dealing with the evolution of space. As fruit flies do seem to have a reflection of the human body set up, it is easy to experiment how fruit flies can test whether they are capable of withstanding food being in space. The purpose of this experiment is to test how fruit flies are able to survive during space conditions while being fed the necessary nutrients.

Research Problem

Astronauts perform very difficult and dangerous jobs and need to be in top physical and mental condition. Nutrition is key to maintaining good health and alertness, a hungry astronaut can cost lives. Astronauts work in zero gravity, which makes food storage, preparation, and eating difficult. For example, much of their food needs to be rehydrated before use, salt and pepper come in liquid form. These limitations and the need for astronauts to be at peak performance has resulted in a great amount of research into space food. Space food was first used in 1962 when John Glenn brought a tube of pureed beef and vegetables into space. Since then, improvements to taste and nutrition have been made. In 1968 turkey with gravy and cranberry sauce were thermostabilized for use in space and today freeze dried foods have become the most important staple in the astronaut diet. Nutritional studies have been performed to insure healthy space food. But one thing that has not been studied is long-term, generational effects on health and reproduction. This could be important if we are to travel to new planets, is the food sufficiently nutritious for long flights in space that may involve multiple generations?

Here we propose to test the generational quality of space food in a fruit fly model to see if it supports healthy children, grandchildren, and great-grandchildren. Fruit flies have been developed as an important model for human health, over 70% of human diseases can be modeled in a fruit fly. Given their short generation time fruit flies serve as a good model to study the generational effect of space food.

Methods/Experimental Design

Twenty-flies (10 of each sex) will be started on one of three diets: 1) rehydrated space food 2) rehydrated space food using only 80% of recommended water (to model a mistake or malfunction in space) and 3) a control of normal fly food (Bloomington Stock Center Recipe, Bloomington, IN). Three tests on the health of flies under different treatments will be made.

- 1) Number of progeny. The number of progeny will be recorded each generation to determine if space food has any impact on reproduction. Each new generation is started with 20 flies selected at random from the previous generation.

- 2) CO₂ challenge. The time it takes for flies to awaken from 1 minute of CO₂ exposure (used to knock out the flies in order to work with them) will be assessed, as a test of overall robustness.
- 3) Mass. The mass of flies will be recorded each generation, as a measure of overall health.

Because the impact of diet can vary with natural genetic variation, each test will be performed on two different natural populations of fruit flies, one from Kuala Lumpur, Malaysia and a second from Bogata, Columbia.

Results Obtained

It is known that fruit flies can survive in space, but only for a few days. When placed in space conditions with the necessary nutrients they are able to survive for weeks on end.

When it comes to feeding fruit flies space food, it only benefited them when it was equipped to their nutritional needs.

Significance and Interpretation of Results

1) Dehydrated space food: The fruit flies did not respond well to the dehydrated food due to the lack of nutrients and water.

2) Rehydrated space food using only 80% of recommended water (to model a mistake or malfunction in space): The fruit flies did respond semi well to the food being rehydrated, but due to the food being re-hydrated with water.

3) A control of normal fly food: with the control group the fruit flies were still introduced to food being hydrated because they are attracted to the smell and humid foods.

The three test:

- Number of progeny. The number of progeny will be recorded each generation to determine if space food has any impact on reproduction. Each new generation is started with 20 flies selected at random from the previous generation.
 - Did a total of two generations to keep the experiment simple.
 - In a total of each generation study did show fruit flies did not make it past a couple days. This is due to the fact that each generation experienced different environmental impacts to test survival skills.
 - More women were left alive than men.
- CO₂ challenge. The time it takes for flies to awaken from 1 minute of CO₂ exposure (used to knock out the flies in order to work with them) will be assessed, as a test of overall robustness.
 - The fruit flies did not respond well to the impact of carbon dioxide because it does slow down their mobility.
- Mass. The mass of flies will be recorded each generation, as a measure of overall health.
 - The mass of the fruit flies was not impacted.

Acknowledgments and References

I would like to acknowledge my advisor, Mark Nielsen, for taking the time to help me with the experiment as a whole. As an advisor he provided his expert intellect on the fruit flies mechanism. With further research, I was able to complete the proceedings of finding out how fruit flies react to a space environment, what type of foods is good for them, and they're reproductive system. Once again, thanks to my advisor for the amazing help.

Spatial Modification of Microstructure and Properties through Additive Manufacturing

Student Researcher: Elizabeth C. Malek

Advisor: Dr. Joy Gockel

Wright State University

Engineering and Computer Science

Introduction

Additive manufacturing (AM) has become a widely used tool in materials research. It provides an opportunity to change aspects of a sample at different regions within the component. The ability to change properties of the sample is important when creating functionally graded materials. The most popular AM process for metallic processes is laser powder bed fusion (LPBF) also known as selective laser melting (SLM) [1] which is a process where thermal energy selectively melts metal powders in correspondence with an associated 2D slice of a 3D computer-aided design (CAD) model. As it cools, the metal powder forms a strong metallurgical bond layer by layer as it sets into the finished part. This process is often performed in an argon-filled atmosphere. LPBF creates a 3D physical model of almost any CAD model that fits within the machine's parameters [2]. In the present work, the sample that is to be investigated has six different composition regions varying from 100% titanium (Ti) to 100% tantalum (Ta). The manufacturing processing parameters within each region are changed to account for differences in the thermal properties of the composition mixture. Results of Vickers hardness testing within the six regions is incredibly important to investigate because it displays how the microstructure and composition within each region will affect the properties. Understanding the changes in hardness can aid in selecting the suitable parameters to fabricate the composition that exhibits specific desirable hardness properties. This paper aims to further investigate the material properties, specifically Vickers Hardness, of a functionally graded Titanium-Tantalum alloy using LPBF AM at different composition sections throughout the sample.

Discussion/Experimental Procedure

For this experiment, the specimen was made with novel GAP machine technology. It works very similarly to the traditional LPBF procedure but can deposit multiple different materials at specific locations. This allows the composition of a 3-dimensional part to be tailored based on location for optimized composition. Using this process, the sample was produced to consist of six different compositions starting at 100 wt % Ti to 100 wt % Ta. Each of the six regions are 10 x 5 mm and the height of the sample is about 1.5mm. The uncut and unpolished raw sample is shown in Figure 1. To investigate changes across the different sections of the sample, Vickers Hardness was performed, and the results were recorded. Vickers hardness was measured using a Buehler Micromet Micro Hardness Tester. Traditional Micro-Vickers Hardness standards were followed which uses a square-based pyramid diamond indenter. The measurement produced by the machine is a combination of the loading and the actual surface area of the indent [3]. The machine measures the distance from one corner of the diamond shaped indent to the opposite corner. Average applied loads for standard Vickers Hardness vary from 1-120 kgf, for times between 10-15 seconds, while the only difference with Micro-Vickers Hardness is a smaller load normally less than or equal to 1 kgf. The Ti-Ta specimen was evaluated with at a load of 300g and a dwell time of 13s.

However, similar results were displayed in an experiment by Chao Wei et.al. where they tested functionally graded 316L/Cu10Sn [6]. Their results show a similar curve to the one found in this study, where the graph shows a distinct dip and then following peak. This supports the results found in this study as the behaviors could be mirrored through the same processes, regardless of material. Ultimately, the results of the hardness tests were somewhat unexpected, but supported by a few other performed research studies.

Conclusion

A functionally graded Ti-Ta sample with distinct compositional sections was successfully created using LPBF AM techniques. The process utilizes specified compositions of Titanium and Tantalum to create six equally sized sections each with unique compositions. Vickers Hardness data collected horizontally across the sample displayed a wave like pattern with two relatively distinct peaks around 250 HV at approximately 1250 μ m and 2250 μ m from the furthest 100% Titanium side of the sample. The results of the graphs show a pattern that is not a traditionally familiar one, but seen in a few other studies, suggesting an area of interest for further study of this hardness phenomenon.

References

- [1] C. Guo, Z. Xu, Y. Zhou, S. Shi, G. Li, H. Lu, Q. Zhu, and R. M. Ward, "Single-track investigation of IN738LC superalloy fabricated by laser powder bed fusion: Track morphology, bead characteristics and part quality", *Journal of Materials Processing Technology*, vol. 290, p. 117000, 2021.
- [2] Valérie Gunenthiram, Patrice Peyre, Matthieu Schneider, Morgan Dal, Frédéric Coste, et al.. Analysis of laser–melt pool–powder bed interaction during the selective laser melting of a stainless steel. *Journal of Laser Applications*, 2017, 29 (2), pp.Article number 022303. 10.2351/1.4983259. hal-01664637
- [3] Broitman, Esteban. "Indentation Hardness Measurements at Macro-, Micro-, and Nanoscale: A Critical Overview." *Springer*, Springerlink.com, 2016.
- [4] S.S.D. Rocha, G.L. Adabo, G.E.P. Henriques and M.A.D.A. Nóbilo, "Vickers hardness of cast commercially pure titanium and Ti-6Al-4V alloy submitted to heat treatments", *Brazilian Dental Journal*, 17 [2] 126–129 (2006).
- [5] "Tantalum - Properties - Price - Applications - Production." *Material Properties*, 1 Feb. 2021, material-properties.org/tantalum-properties-applications-price-production/#Mechanical_Properties_of_Tantalum, 2021.
- [6] C. Wei, Z. Sun, Q. Chen, Z. Liu, L. Li, "Additive Manufacturing of Horizontal and 3D Functionally Graded 316L/Cu10Sn Components via Multiple Material Selective Laser Melting", *University of Manchester*, 2019.

Active Flow Control for Manipulation of Flow Aerodynamics in Jets

Student Researcher: David Marshall

Advisors: Prof. Mo Samimy and Dr. Nathan Webb

The Ohio State University
Mechanical and Aerospace Department

Abstract

Thrust vectoring (the ability to modify the angle of thrust generated by the exhaust nozzle on an aircraft) is of great interest to the military as it could be used in fixed wing unmanned aerial vehicles (UAVs) to increase hyper-maneuverability and short or vertical take-off/landing capabilities. Therefore, proposed experiments are to be conducted using localized arc-filament plasma actuators (LAFPAs) coupled with a Coanda-based thrust vectoring (CTV) inspired reaction surface to deflect the primary jet of a subsonic, axisymmetric jet engine. The LAFPA's are believed to be a more efficient way of deflecting a jet over other previously tested methods such as CTV since CTV requires a significant amount of bleed air (up to 15 % of the primary jet) [1] whereas LAFPA's exploit natural instabilities in shear flows to control the mixing and entrainment characteristics of the flow [2]. Thus, LAFPA's are more efficient active flow control concept (AFCC) since it requires less power and zero mass flow. The proposed experiments involve documenting experimental sweeps of excitation frequencies and other excitation parameters of the LAFPAs using schlieren and pressure measurements for the purpose of determining the ability of the AFCC to deflect the jet. The focus of the past year's research efforts have been on researching CTV and using results of previous CTV experiments to inform the design and implementation of similar experiments instead using the proposed LAFPA's as the AFCC. Based upon the findings of this literature review a nozzle made of boron-nitride (a ceramic capable of withstanding the high-temperature, high-voltage LAFPAs) has been designed for use in the proposed experiments.

Project Objectives

The overall projects objectives are to obtain preliminary evidence documenting the localized arc-filament plasma actuator's ability to vector the thrust from a subsonic, axisymmetric jet. The project objective from the past year of research was to gather an understanding of Coanda-based thrust vectoring and how the results from previous research can aid the proposed experiments and the design of the nozzle for the proposed experiments.

Methodology

The methodology used in the research was reading technical papers involving experiments where thrust vectoring was investigated and using results from these papers to aid in the design considerations of the nozzle and subsequent experiments. A considerable amount of effort went into figuring out what results from CTV research experiments were relevant considerations for the proposed nozzle design and experiments. Additionally, papers studying the effects of LAFPAs on the flow of a primary jet from a subsonic, axisymmetric nozzle were also read to gather additional information to best aid in the design of the nozzle so that all design choices best use the LAFPA's to generate as much deflection of the primary jet and control over that deflection as possible. After sufficient knowledge had been gained the nozzle was designed in Solidworks so that it could be manufactured for use in the future experiments.

Results Obtained

The most significant result of the research was the design of the nozzle, which can be seen as a Solidworks model in Figure 1. Additionally, important information was found from the technical papers on Coanda-based thrust vectoring. It was found that there were tradeoffs in different parameters for the design of the nozzle [3]. One parameter that was considered was the reaction surface radius. It was found that thrust vectoring efficiency increases as the reaction surface radius increases (see Figure 2). However, if the reaction surface radius is sufficiently large the flow can enter a bi-stable region which is unwanted for consistent control. Additionally, important information was found from the technical papers on research conducted using LAFPA's to manipulate flow. It was found that when the LAFPA's are activated they create vorticity within the flow [2]. The structures created as a result of this vorticity in the flow differ in size, spacing and persistence based on the excitation frequency of the LAFPA's. It was found that for low excitation frequencies the structures are larger, spaced further apart and are more coherent. It was also found that for higher excitation frequencies the structures are smaller, more closely spaced and dissipate more quickly (see Figure 3 for examples). Another significant outcome was from the professional development gained from both using the work of others to aid in the research process and from the CAD skills developed in designing the nozzle. Conducting research requires building on the work of others who have conducted experiments that utilize relevant concepts or provide relevant results to the research and then interpreting those findings to best aid in the design considerations and experimental procedure of the research. Thus, many valuable skills for interpreting and utilizing technical papers in research were developed. Designing the nozzle in Solidworks helped to develop CAD modelling skills since the nozzle design had bores and a reaction surface which required many new and unfamiliar modelling techniques which can now be incorporated into future CAD projects.

Significance and Interpretation of Results

From these results the design considerations of the nozzle and the future experimental procedure were made. It was determined that the reaction surface radius required for the experiment needed a 15° angle with the primary jet because, as can be seen from Figure 2, with increasing reaction surface radius there was increased thrust vectoring efficiency, so the reaction surface radius needed to be large enough to maximize efficiency while also being small enough to not enter the bi-stable region (a 15° angle with the primary jet would satisfy this requirement). It will be of great use to know that the structures caused by the LAFPAs creating vorticity in the flow were of different sizes, spacing and structural integrities since varying these parameters by varying the excitation frequency of the LAFPAs is the method by which various control effects could be obtained. It is believed that low frequencies will deflect the primary jet more than high frequencies, so flow control can be achieved by modifying the LAFPA's excitation frequencies.

Figures

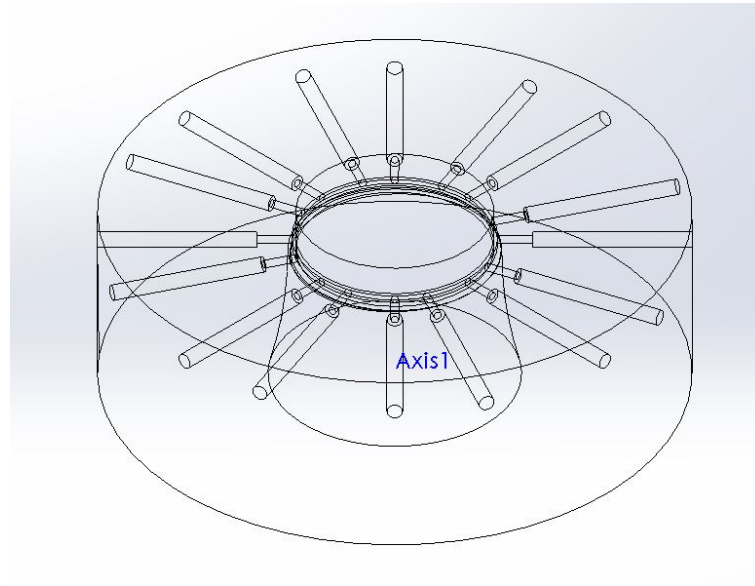


Figure 1. Nozzle Design

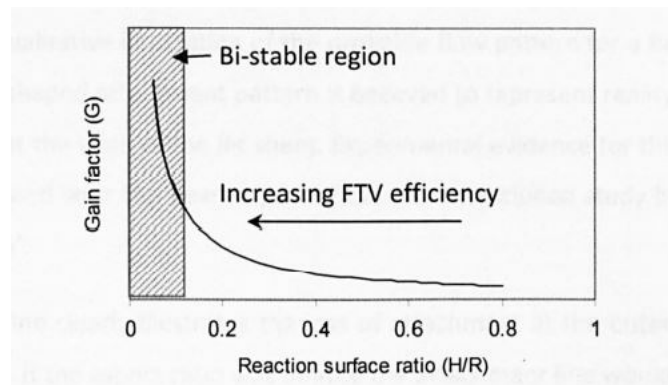
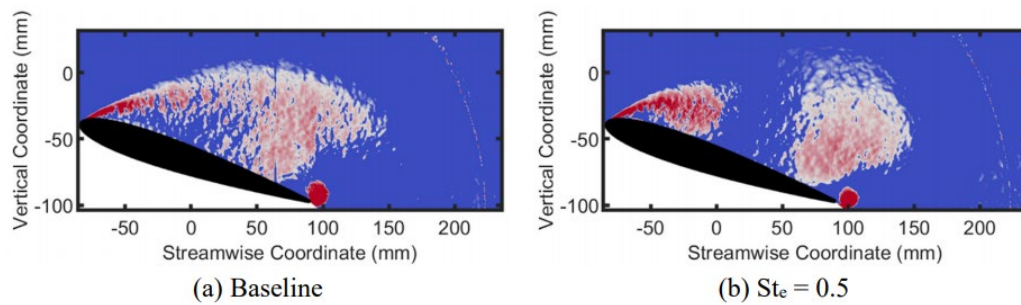


Figure 2. Effect of Reaction Surface Ratio (Nozzle Diameter/ Reaction Surface Radius) on Fluidic Control Efficiency



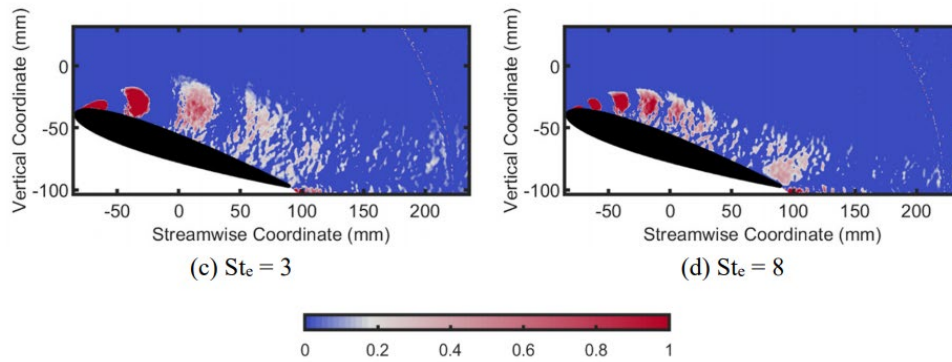


Figure 3. Effect of Excitation Frequency on Flow Structures (Maps of Swirling Strength, a Vortex Identification Method)

Acknowledgments

The author would like to thank Dr. Nathan Webb and Prof. Mo Samimy. Their guidance and work was instrumental in completing this research. The author would also like to thank the Ohio Space Grant Consortium (OSGC) and The Ohio State University for providing both the opportunity and funding that made this research possible.

References

1. Warsop, C., Crowther, W., "Fluidic Flow Control Effectors for Flight Control," AIAA Journal Vol. 56, No. 10, 2018.
2. Webb, N., Samimy, M., Castaneda, D., "Active Control for Targeted Objectives of Flow over an Oscillating Airfoil," AIAA SciTech Forum, 2021-1832, 2021.
3. Gill, K., "The Development of Coflow Fluidic Thrust Vectoring Systems," Ph. D. Thesis University of Manchester, 2008.

Dissecting The Interaction Between PCDH19 And NCAD And Its Relationship To Neural Development

Student Researcher: Kristina G. Mills

Advisor: Dr. Sharon Cooper

Cedarville University

Department of Science and Mathematics

Abstract

Adhesion proteins are a group of proteins that play a role in connecting neurons during brain development. One group of adhesion proteins, the cadherin family, and specifically protocadherin 19 (PCDH19) and neural cadherin (NCAD) play an important role in this development. Mutations in PCDH19 have been shown to cause a specific form of epilepsy. Children with this epilepsy syndrome begin experiencing seizures around six months of age. Sometimes the seizures will subside around puberty, whereas others continue experiencing seizures throughout adulthood; even when seizures end in childhood, cognitive impairment still exists. In some of the PCDH19 mutations, it is clear how protein function is disrupted, but the mechanisms for others are unclear. Structural studies suggest that a cluster of mutations in extracellular domain 6 (EC6) of PCDH19 may disrupt interactions with other proteins. In this study, we test whether mutations D618N, R625G, and P567L in this cluster impact the interaction of PCDH19 and NCAD. Wild-type or mutant versions of PCDH19 were expressed in HeLa cells along with wild-type NCAD. Co-immunoprecipitations (CoIP) with these proteins indicated the D618N, R625G, and P567L mutations disrupt the interaction between PCDH19 and NCAD. This disruption could be the molecular mechanism of epilepsy in patients with these specific mutations.

Project Objectives

The objective was to test D618N, R625G, and P567L mutations in the EC6 cluster of PCDH19 to determine whether these mutations impact PCDH19 and NCAD interaction. This will provide insight into neurodevelopment and hopefully result in better treatment for these patients in the future.

Methodology Used

Previously created DNA constructs were transformed into bacteria for replication to generate additional DNA. This DNA was purified and then transfected into HeLa cells to produce protein, specifically PCDH19 and NCAD. The protein generated was used in CoIPs followed by western blots to evaluate their interaction. This was performed with both wild-type and mutant versions of PCDH19 along with wild-type NCAD to determine whether the mutations altered the ability of PCDH19 to interact with NCAD.

Results Obtained

Wild-type and mutants were successfully generated, shown by western blots of the sample input, which is a reserved portion of generated protein prior to CoIP in Figure 1A and Figure 1C. In lanes 4, 5, and 6 of Figure 1A and Figure 1C mutants are shown to have successfully produced protein. We see a band for NCAD indicating wild-type PCDH19 pulled down NCAD in Figure 1D lane 2, but lanes 4, 5, 6 do not show a band for NCAD indicating NCAD was not pulled down by the mutant versions. The negative control in Figure 1D lane 3, unexpectedly had a band for NCAD. Based on these results, the mutations of PCDH19 disrupted the interaction between PCDH19 and NCAD, but this should be further confirmed by replicating the experiment.

Significance and Interpretation of Results

This research project provided insight into the interaction between PCDH19 and NCAD as well as a potential molecular cause for epilepsy in patients with D618N, R625G, and P567L mutations. Further research could build on these discoveries to understand how neurons get connected during neurodevelopment and ultimately to provide better treatments for epilepsy patients.

Figures/Charts

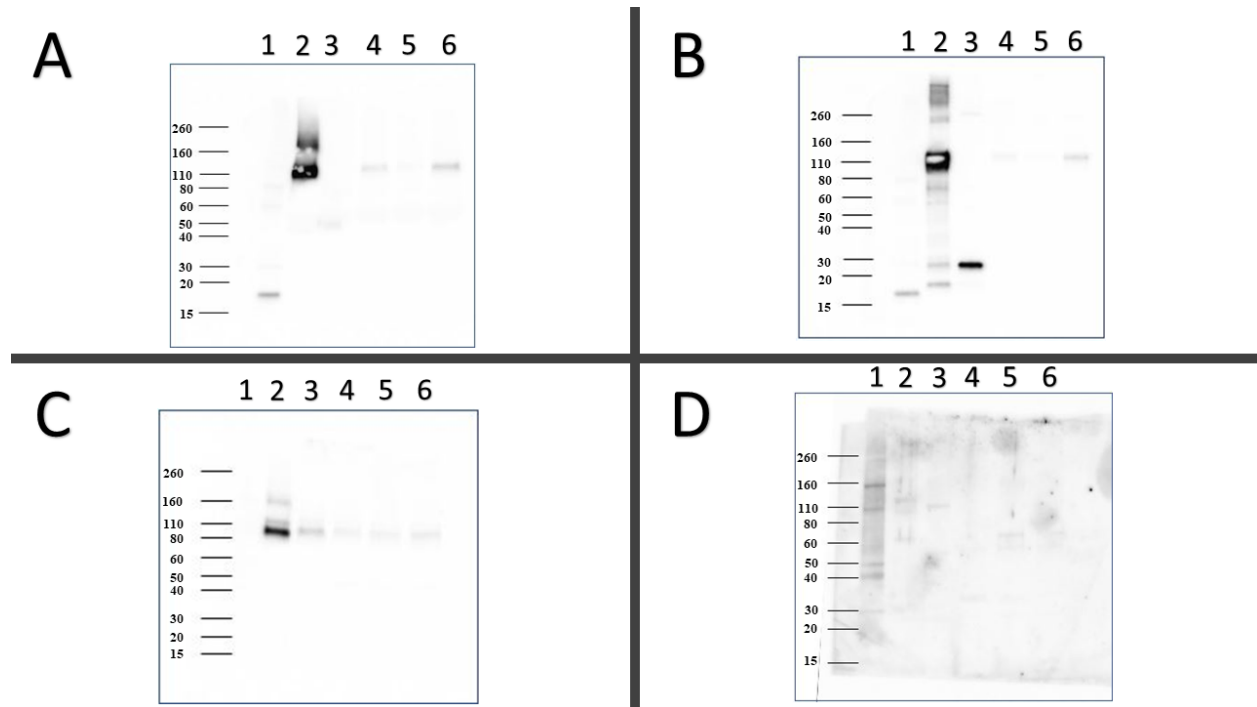


Figure 1. Western blots of protein samples.

In each western blot, (A-D), lanes from left to right are Novex sharp pre-stained protein standard, PCDH19-GFP + NCAD-Strep positive control, NCAD-strep + GFP negative control, PCDH19 P567L- GFP + NCAD-Strep, PCDH19 R625G- GFP + NCAD-Strep, PCDH19 D618N- GFP + NCAD-Strep. A portion of the protein produced was set aside and was run on an SDS-PAGE gel (A, C). The remainder of the sample was used in a CoIP and the elution was loaded in an SDS-PAGE gel (B, D). Western blots were performed on both gels using antibodies for GFP (A, B) and Strep (C, D).

Acknowledgments and References

The author of this paper would like to thank Dr. Sharon Cooper and Dr. Kaleb Pauley for their continued guidance and input in the project. The author would also like to thank the Ohio Space Grant Consortium for its support.

Preparation and Description of a Sauropod Femur from the Morrison Formation at Skull Creek, CO

Student Researcher: Sara A. Mitchell

Advisor: John H. Whitmore

Cedarville University

Department of Science and Mathematics

Abstract

The purpose of this research was to prepare and describe a sauropod femur that is approximately 1.5 meters in length. The sample studied was collected from the Morrison Formation in northwest Colorado from the Skull Creek area. The fossil was poorly preserved in a loosely consolidated sandy conglomerate matrix. It was prepared by removing the debris, and restoration was begun by gluing the broken fragments together. The research also focused on understanding the depositional environment of the fossil, as well as investigating the viability of fossil remains for academic study in similar states of preservation. The study could also have potential implications for the dinosaur fossils of the Morrison Formation and how this site compares to other localities. Additionally, a concise lithological study was done to investigate depositional processes and the ramifications for the stratigraphic site. This project concluded that the most likely candidate for the identification of the femur is of the genus *Diplodocus*.

Project Objectives

The purpose of this research was to prepare and describe a sauropod femur that is approximately 1.5 meters in length. The research also focused on understanding the depositional environment of the fossil, as well as investigating the viability of fossil remains for academic study in similar states of preservation. The study could also have potential implications for the dinosaur fossils of the Morrison Formation and how this site compares to other localities.

Methodology Used

The plaster jacket protecting the bone was removed using a variety of saw tools. The surrounding rock and debris were removed to expose the fossil. Using various thicknesses of cyanoacrylates (superglues), the bone fragments were glued together. A morphological graphical analysis was performed to attempt to determine the genus of the specimen. Data was collected from literature review to compare against four abundant genera of sauropods in the Morrison Formation: *Apatosaurus*, *Camarasaurus*, *Diplodocus*, *Haplochanthosaurus*, and *Barosaurus*. Additionally, a lithological study was conducted to learn more about the potential depositional processes of the location and its implications for the site.

Results Obtained

While full restoration could not be accomplished in the timeframe established for this project, the process was begun and the procedure learned. The full extent of the exposed specimen can be seen in Figure 1. Additionally, the artistic speculation of the bone can be seen in the same figure. A brief lithological study determined that the femur was deposited in sandstone interbedded with thin, polymictic conglomerate layers. The bone was reported to be isolated and unarticulated, while higher stratigraphically a well-articulated *Allosaurus fragilis* was found. Preliminary results based on ratio measurements from anatomical markers on the femur are displayed in Figure 2. The graph indicates that the sample lands close to the *Diplodocus* trendline.

Significance and Interpretation of Results

The morphological graphical analysis on the femur suggested that this specimen belongs to a Diplodocid (Figure 2). Because the location is stratigraphically uncertain, utilizing biostratigraphy yields more

possible genera to which the specimen could belong. Morrison diplodocids that are likely candidates are *Diplodocus*, *Barosaurus*, *Galeomopus*, or *Kaatedocus*. The latter two are too small to match this specimen. So, the bone most likely belongs to either *Barosaurus* or *Diplodocus*. The limited data acquired from femurs of the former genus, though, makes it difficult to do a comparison of the two statistically/graphically. However, on average the *Barosaurus* is smaller than the *Diplodocus*, and measurements from the specimen indicate that it would have been a large individual for even a *Diplodocus*. The author has concluded, therefore, that this specimen most likely belongs to *Diplodocus* sp. The site might still yield more bones still, and is certainly worthy of further investigation. Based on the lithological study, the specimen was likely in a flow regime deposit of some kind. However, due to the unsure exact stratigraphic location and limited field data, a more conclusive explanation for the depositional environment cannot be determined at this time. Studies of the Morrison Formation in general indicate that the strata is likely a part of a depositional basin. Ultimately, due to the poor nature of preservation of the studied specimen, further identification would necessitate more preparation and study that were beyond the scope of this project.

Figures/Charts



Figure 1. Full femur & artistic reconstruction.

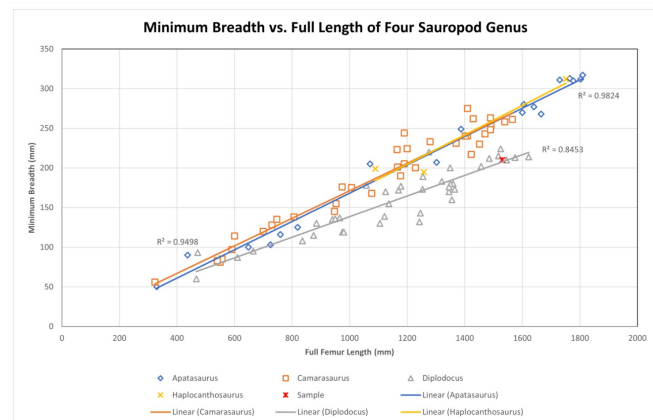


Figure 2. Graphical analysis of four Morrison sauropod genera compared to the studied femur.

Acknowledgements and References

I would like to thank my advisors Dr. John Whitmore for his invaluable counsel and direction as well as Jordan Oldham for his helpful assistance. Additionally, I would like to thank both OSGC and CU for the support of this project.

Bonnan, Matthew F. (2004). Morphometric analysis of humerus and femur shape in Morrison sauropods: implications for functional morphology and paleobiology. *Paleobiology*, 30(3), 444-470. doi: 10.1666/0094-8373(2004)030<0444:maohaf>2.0.co;2

Carpenter, Kenneth. (2013). History, Sedimentology, and Taphonomy of the Carnegie Quarry, Dinosaur National Monument, Utah. *Annals Of Carnegie Museum*, 81(3), 153-232. doi: 10.2992/007.081.0301

Whitlock, John A. (2011). A phylogenetic analysis of Diplodocoidea (Saurischia: Sauropoda). *Zoological Journal Of The Linnean Society*, 161(4), 872-915. doi: 10.1111/j.1096-3642.2010.00665.x

Wilhite, Ray. (2003). Biomechanical reconstruction of the appendicular skeleton in three North American Jurassic sauropods. *LSU Doctoral Dissertations*. 2677. https://digitalcommons.lsu.edu/gradschool_dissertations/2677

Active Flow Control in an Aggressively Offset Inlet

Student Researcher: William A. Mullin

Advisors: Dr. Mo Samimy and Dr. Nathan Webb

The Ohio State University

Department of Mechanical and Aerospace Engineering

Abstract

Aggressively offset inlet systems are becoming increasingly important in the field of aerospace engineering, with many potential military and flight applications. Prospective advantages of improving the integration of the propulsion and aerodynamic systems include reducing the radar cross-section of an aircraft and improving overall performance [1]. However, due to the curved S-shape of the duct, an adverse pressure gradient forms around the inside of the turns in the inlet. This adverse pressure gradient causes flow separation and the formation of streamwise vortices which result in significant flow distortion and pressure loss at the aerodynamic interface plane (AIP) [2]. These flow characteristics are very undesirable; they can cause decreased aircraft performance and the resultant high-cycle fatigue reduces the structural life cycle of the engine components [3]. To counteract the unsteady flow, plasma actuators may be used to excite the flow and reduce the effect of the streamwise vortices throughout the duct. Many different types of plasma-based actuators have been proposed to excite the flow: localized arc-filament plasma actuators (LAFPA), pulsed DC plasma actuators, and plasma synthetic jets have been considered. The goals of this project are to investigate the effect of the active flow control on the aerodynamic performance throughout the duct and to gain a better understanding of the flow physics and dominant instability features of flow through an aggressively offset inlet.

Project Objectives

An aggressively offset inlet causes multiple aerodynamic problems, including separation, flow distortion, pressure loss, and strong crossflows propagating after the second turn of the duct. There have been many previous efforts to control the unsteady flow characteristics in such an inlet geometry. Passive flow control devices such as vanes or vortex generators work well, however, these devices are optimized to work only at one specific design condition [4]. On the other hand, active flow control devices are flexible and remain effective at many different flow conditions. Traditional active flow control devices, such as microjet or sweeping jet actuators, require the bleeding of airflow from the main propulsion system, which can be undesirable [4].

This project aims to investigate the capability of plasma-based actuation, a more recent form of active flow control. Plasma flow control is advantageous because it does not require the bleeding of flow from the engine; instead, the flow control is provided by a circuit which uses electrical power to inject thermal perturbation or momentum into the flow [5]. Different types of plasma-based actuators have been considered, including localized arc-filament plasma actuators (LAFPA), pulsed DC plasma actuators, and plasma synthetic jets. Previous efforts in this research group have attempted to investigate the efficacy of the previously mentioned plasma-based flow control devices. The LAFPA were inserted into the wind tunnel geometry and, while improving the flow separation region, did not provide any meaningful improvement from the baseline flow. The pulsed DC actuators were tested in a benchtop experiment which replicated the procedure of McGowan et al. [6], but no measurable thrust was detected. It was determined that the plasma synthetic jets would not be able to provide enough thrust to achieve at minimum a 20% reduction in distortion, based on calculations related to the work of Burrows et al. [7].

With previous research efforts in plasma-based control having not proven successful, it was determined that more insight was needed regarding the time-resolved content of the flow at the AIP. Time-resolved data was not able to be collected at the current facility, so data was provided by Boeing, from an experiment on a nearly identical geometry, for analysis. Using this data, this research aims to investigate the spectral content of the flow at the AIP to gain a greater understanding of the dominant flow instability characteristics and frequency content.

Methodology

The offset diffuser facility at the Aerospace Research Center (ARC) at The Ohio State University is shown in Figure 1. This diffuser is attached to a high mass flow blowdown-type subsonic wind tunnel. The geometry for the diffuser was provided by Boeing, and 3D printed for use at the ARC. The inlet throat is D-shaped, with a throat area of 100.15 cm^2 , transitioning to a circular AIP with an area of 126.62 cm^2 and a diameter of 12.7 cm [8]. The same inlet geometry was used in the research of Burrows et al. [9], which serves as a good source for comparison.

The data used for the time-resolved analysis was provided by collaborative experiments between Dr. Ari Glezer at the Georgia Institute of Technology and Dr. Mori Mani at Boeing. The data provided was the total pressure at the AIP, normalized by the upstream total pressure, or in other words, the local pressure recovery at the AIP. Data was provided from 40 stagnation pressure probes at the AIP, consisting of eight equally spaced rakes of 5 radial pressure probes. Each probe recorded data at a rate of 25 kHz for 5 seconds, resulting in 125,000 total pressure recovery data points for each probe.

Analysis of Results

The total pressure recovery data was first averaged over the 125,000 data points for each probe to determine the mean steady-state pressure recovery at the AIP, shown in Figure 2. The top of this image correlates to the top wall of the duct after the second turn of the offset inlet. This region demonstrates a highly concentrated region of pressure loss and distortion due to the high-intensity crossflows which propagate through the flow after the second turn. The streamwise vortices generated by the crossflow are illustrated with arrows in the figure to show the flow turning in upon itself. The region of the AIP closer to the bottom duct wall also shows some pressure loss, although less extreme, due to the more diffuse vortices propagating from the first turn of the duct.

The time-resolved pressure recovery spectra and frequencies were obtained for each of the 40 probes using a power spectral density function in MATLAB along with a Fourier Transform. This resulted in a power spectral density plot for each probe, shown in Figure 3. For this analysis, the spectral attribute of most interest was the prominence of the peaks of the spectra. The MATLAB function “findpeaks” was used to determine the most prominent spectral peak for each probe, and each of these peaks was circled on the diagram in Figure 3. Some of the probes did not exhibit any meaningfully prominent peaks, so peaks below a specified prominence of 5.25 were not circled on the plot. Figure 3 shows that the most prominent spectral peaks occurred in the second and third probe rings from the center, with the most prominent peaks among all the rings being approximately 500 or 1000 Hz.

The amplitude and frequency of each of the spectral peaks was then represented on a plot of the AIP, shown in Figures 4 and 5, respectively. The data is somewhat “choppy” due to discontinuities in the low number of peaks being plotted, and a large white space is present near the bottom wall since no prominent spectral peaks were found in this region of the flow. Figure 4 shows that the main frequency of interest is 1000 Hz, with a highly concentrated red area in the top-middle of the duct, and additional 1000 Hz frequencies present at the adjacent top-diagonal corners. A frequency of approximately 500 Hz is present at the locations in-between the 1000 Hz peaks, shown by a pale green color in Figure 4.

Significance and Interpretation of Results

The spectral content of the flow shown in Figures 3 through 5 can lead to further understanding of the flow physics and instability. Figures 4 and 5 show that the region of the AIP at the very middle-top of the duct has no prominent spectral peaks, shown by the blank white space at the top of the diagrams. However, Figure 2 indicates that this is where the crossflows have the greatest effect, causing the greatest amount of total pressure loss. This implies that the pressure probes in this region of the AIP are nearly constantly engulfed by the high-loss region of the flow.

On the contrary, the probes surrounding this region move in and out of the high loss region, demonstrating unsteadiness and spectral peaks. Figure 4 shows three concentrated areas of 1 kHz frequency surrounding the high-loss region: one area just below the high-loss region and two areas at both top corners of the duct. This indicates that the 1 kHz frequency is highly related to the crossflows and flow unsteadiness in this region. The area of highest loss generated by the crossflow is concentrated at the top-middle of the duct, and the edges of this high-loss region tend to move about the upper area of the AIP with a frequency of 1 kHz, shown by the red areas in Figure 4. This explains the other dominant flow instability frequency of 500 Hz. As the high-loss region moves between the 1 kHz peaks (red contours in Figure 5), it intermittently occupies the region between those peaks. Since this occurs at either side of the center of the duct, the instability frequency related to this event should be half of the main instability frequency. This in-between state of instability explains the 500 Hz peaks present in Figure 3.

These findings agree with recently published works regarding proper orthogonal decomposition modes for the same inlet geometry. One mode investigated demonstrated a strong back-and-forth shape between the two upper diagonal corners of the duct, similar to the intermittent 500 Hz modes discussed previously [9]. Additionally, Burrows found that frequencies of 475 Hz and 1000 Hz are strongly related to the instability along the upper surface of the duct [9]. Overall, this research has reinforced the idea that the intense crossflow, not flow separation, is the dominant instability feature in this flow. The dominant instability frequencies of 1 kHz and 500 Hz point to the contribution of the vortices in increasing distortion and decreasing pressure recovery at the AIP.

Figures

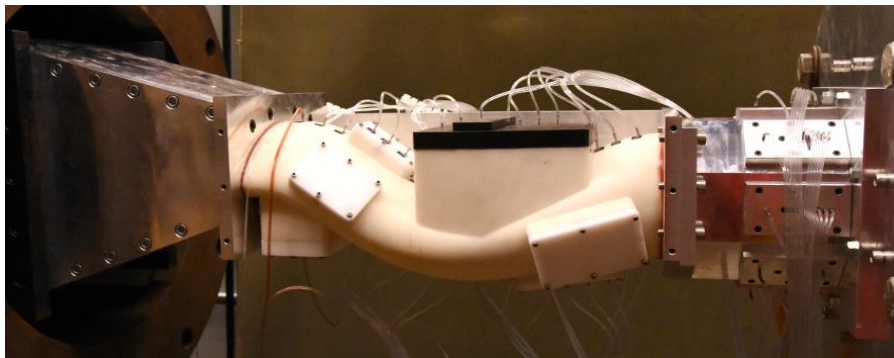


Figure 1. Offset Diffuser in Wind Tunnel at the Aerospace Research Center.

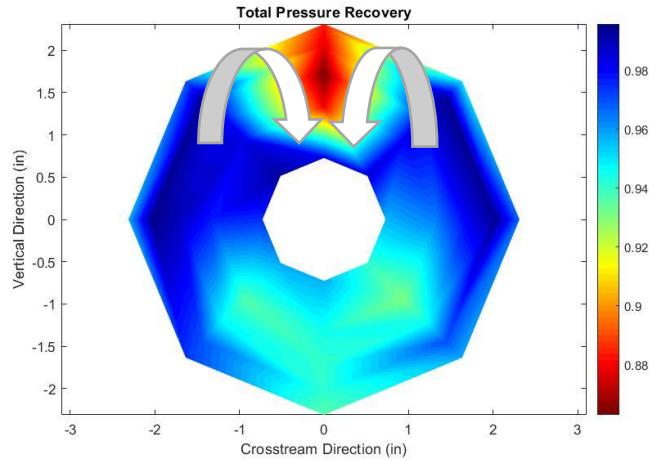


Figure 2. Time-Averaged Total Pressure Recovery at AIP

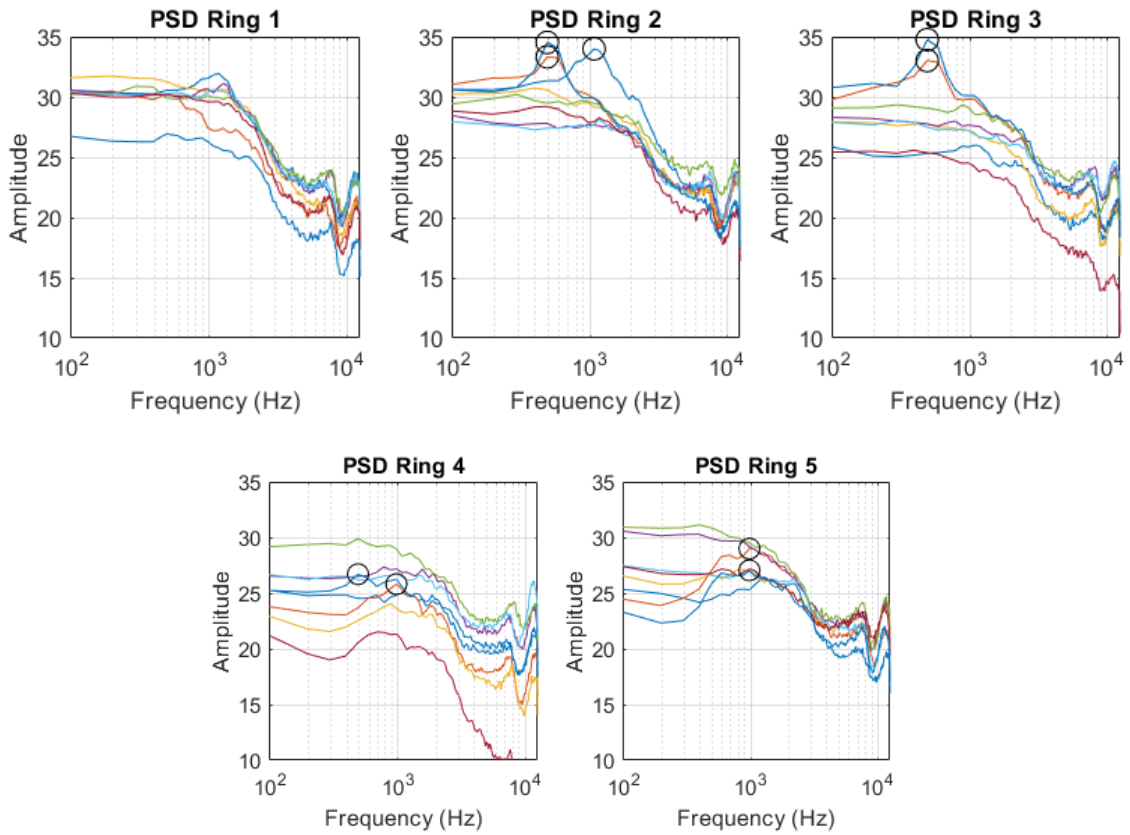


Figure 3. Total Pressure Recovery Power Spectral Density for Each Probe.

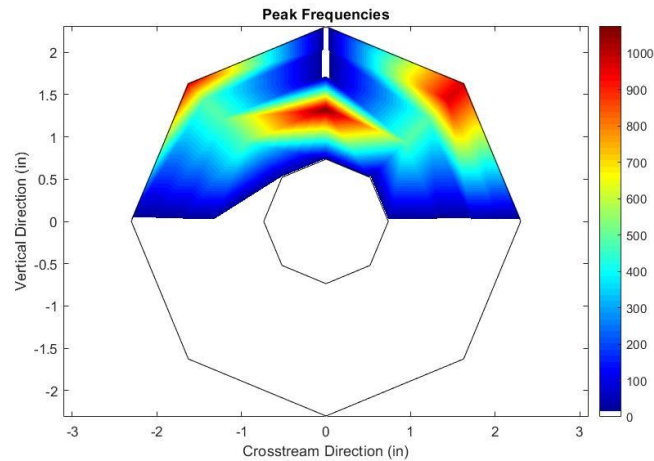


Figure 4. Frequency of Spectral Peaks at AIP.

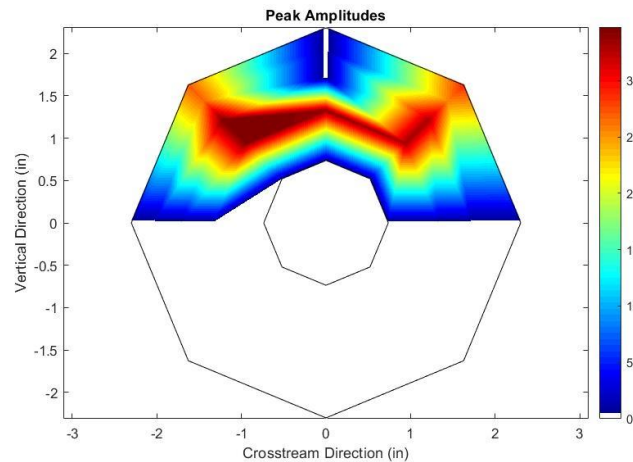


Figure 5. Amplitude of Spectral Peaks at AIP.

Acknowledgements

The author would like to thank the Ohio Space Grant Consortium and Office of Naval Research (ONR) for providing the funding to make this research possible. Additionally, the author would like to thank Dr. Nathan Webb and Dr. Mo Samimy for their advice and oversight in completing this research project.

References

1. Rabe, A. C., "Effectiveness of a Serpentine Inlet Duct Flow Control Scheme at Design and Off-Design Simulated Flight Conditions," Ph.D. Thesis Virginia Polytechnic Institute and State University, 2003.
2. Wojewodka, M. M., White, C., Shahpar, S., and Kontis, K., "A Review of Flow Control Techniques and Optimization in S-Shaped Ducts," *International Journal of Heat and Fluid Flow*, Volume 74, 2018. <https://doi.org/10.1016/j.ijheatfluidflow.2018.06.016>.
3. Chen, Z.J., Wang, J.J. "Numerical Investigation on Synthetic Jet Flow Control Inside an S-Inlet Duct," *Sci. China Technol. Sci.* 55, 2578-2584, 2012. <https://doi.org/10.1007/s11431-012-4970-y>.

4. Gissen, A. N., Vukasinovic, B., McMillan, M. L., and Glezer, A., "Distortion Management in a Boundary Layer Ingestion Inlet Diffuser Using Hybrid Flow Control," *Journal of Propulsion and Power*, Vol. 30, No. 3, May-June, 2014. <https://doi.org/10.2514/1.B34981>.
5. Cybyk, B.Z., Land, H. B., Simon, D.H., Chen, J., and Katz, J., "Experimental Characterization of a Supersonic Flow Control Actuator," AIAA 2006-478. *44th AIAA Aerospace Sciences Meeting and Exhibit*. January 2006. <https://doi.org/10.2514/6.2006-478>.
6. McGowan, R., Corke, T.C., and Matlis, E., "Pulsed-DC Plasma Actuator Characteristics and Application in Compressor Stall Control," AIAA 2016-0394. *54th AIAA Aerospace Sciences Meeting*. January 2016. <https://doi.org/10.2514/6.2016-0394>.
7. Burrows, T. J., Vukasinovic, B., and Glezer, A., "Fluidic Control of an Aggressive Offset Diffuser for a Supersonic Inlet," AIAA 2017-4304. *47th AIAA Fluid Dynamics Conference*. June 2017. <https://doi.org/10.2514/6.2017-4304>.
8. Webb, N. J., O'Neill, C., and Samimy, M., "Aggressively-Offset Inlet Flow Facility Design and Characterization," AIAA 2020-1614. *AIAA Scitech 2020 Forum*. January 2020. <https://doi.org/10.2514/6.2020-1614>.
9. Burrows, T. J., Vukasinovic, B., and Glezer, A., "Flow Dynamics Effected by Active Flow Control in an Offset Diffuser," AIAA 2018-4024. *2018 Flow Control Conference*. June 2018. <https://doi.org/10.2514/6.2018-4024>.

CFD Analysis of Effects of Inlet Velocity on Outlet Frequency for a Fluid Oscillator

Student Researcher: Zane Myers

Advisor: Dr. Jed E. Marquart

Ohio Northern University
Department of Mechanical Engineering

Abstract

Fluid Oscillators are mechanical devices capable of redirecting linear fluid flow into steady oscillating flow. The basis of operation is the Coanda effect, which is a fluid's tendency to attach to a wall. This is what allows flow to be directed into the feedback channel and for oscillation to begin. Applications of fluid oscillators include turbine vane cooling, microbubble aeration, airfoil boundary layer control, and many others [1,2]. Some of the attractions of fluid oscillators over other oscillation control methods include; maintenance-free - no moving parts, simple design, rugged - applicable to harsh environments, and scalable - from micro to macro scale [3]. This analysis explores the effects of inlet velocity on outlet frequency for a fluid oscillator. The fluid oscillator geometry used in this analysis is a two-feedback channel fluidic oscillator [4]. This type of oscillator consists of an inlet power nozzle, a mixing chamber, two feedback channels and an exit nozzle [1]. Ansys Fluent was used as the meshing, solving, and post processing software.

Project Objectives

The goal of this analysis is to collect computational data to help explain the relationship between inlet fluid velocity and outlet frequency for a fluid oscillator.

Methodology Used

Building from the methodology used by *Let's Do Dynamic Simulations*, the working fluid water was simulated in the provided fluid oscillator geometry [5]. The independent control variable in this analysis is the inlet velocity of the oscillator. This is controlled by changing the inlet velocity boundary condition in four separate simulations. The remaining boundaries were set to wall with the exception of the rectangular cross section in the far-field set to outlet. The outlet frequency was measured by analyzing the velocity gradient post processed images at separate 0.1s timesteps and recording at what time difference one steady state oscillation occurred. The cycle time was then converted to Hertz and recorded. Steady state frequency was ensured by running the simulation for extended timesteps, totaling up to ten seconds.

Results Obtained

The results of the four simulations are shown in Figure 1. The data is encouraging that a relationship does exist between inlet velocity (m/s) vs. oscillator frequency (Hz). This is in accordance with the multi parameter relationship to oscillator frequency pointed out by Ghanami [4]. It is unclear whether the data indicates a linear or quadratic relation between inlet velocity and oscillator frequency. The behavior of the oscillation can be better understood from Figure 2 which shows the time stepped simulation. From Figure 3, the flipping process is further understood first by looking at the low-pressure region that develops in the lower feedback loop, and then noticing how a portion of the velocity streamlines rush in to fill the pressure low.

Significance and Interpretation of Results

As suspected, the results indicate correlation between the inlet velocity and the outlet frequency of the fluid oscillator. To establish a mathematical relationship between the parameters, further simulations need to be run in order to expand the dataset. In the future, it would be interesting to build a test rig in order to collect empirical data and validate the simulations.

Figures/Charts

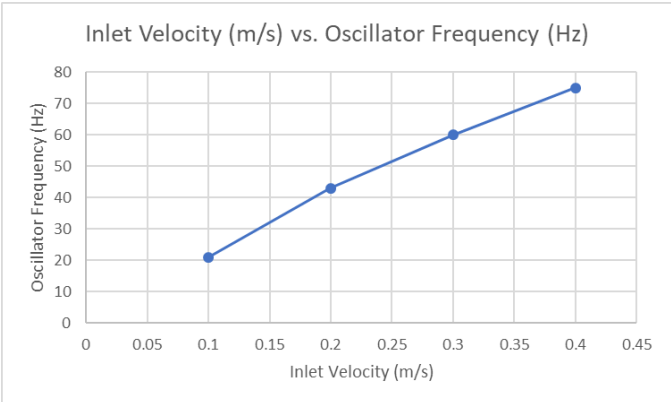


Figure 1: Inlet Velocity (m/s) vs. Oscillator Frequency (Hz)

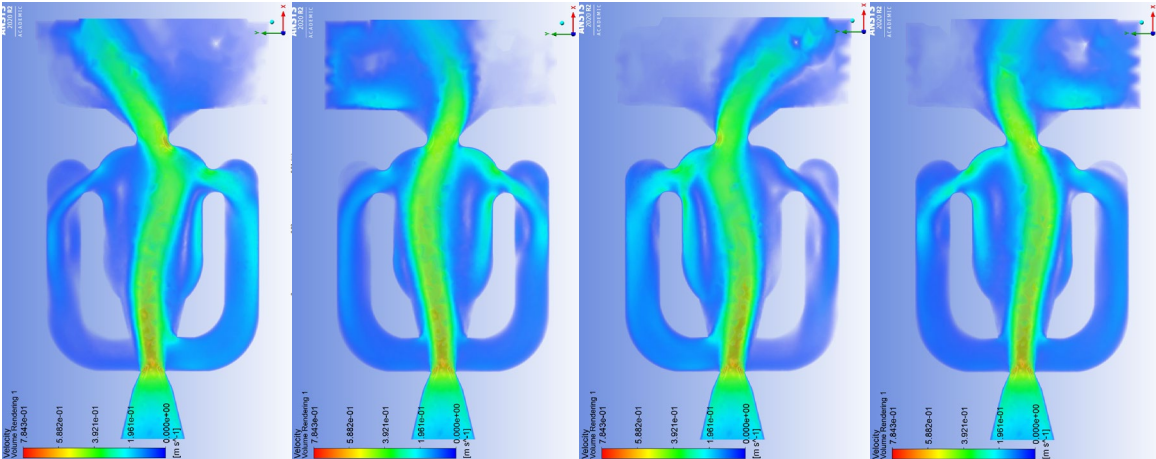


Figure 2: Velocity Gradient at Multiple Timesteps for Fluid Oscillator Simulation (2 m/s)

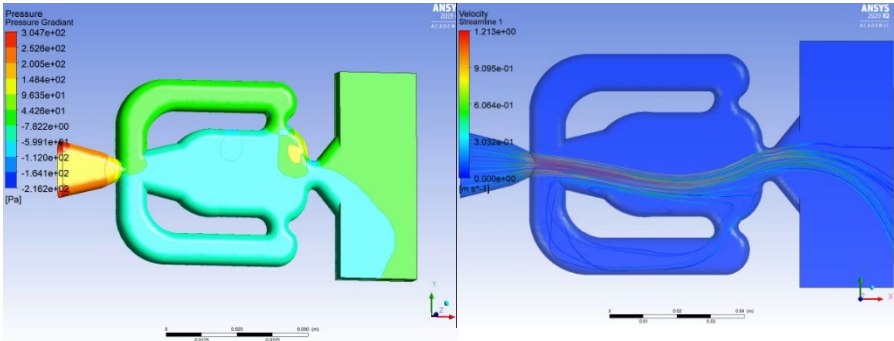


Figure 3: Pressure Gradient (Left) and Velocity Streamlines (Right) for Fluid Oscillator Simulation (3m/s)

Acknowledgements and References

[1] Hossain, Mohammad Arif. "Sweeping Jet Film Cooling." Electronic Thesis or Dissertation. Ohio State University, 2020. OhioLINK Electronic Theses and Dissertations Center. 01 Apr 2021.

[2] Rizaldi, Muhammad & Rahman, Arif & Aan, Deendarlianto & Prihantini, Nining & Nasruddin, Nasruddin. (2019). Generation of Microbubbles through Single Loop and Double Loop Fluid Oscillator for Photobioreactor Aeration. *International Journal of Technology*. 10. 1446. 10.14716/ijtech.v10i7.3691.

[3] NASA, Technology Transfer Program, "Patent Details." Mechanical and Fluid Systems, ref LAR-TOPS-36, pat num 9,333,517 9,339,825; 9,802,209; 9,789,496. Access: technology.nasa.gov/patent/LAR-TOPS-36.

[4] Ghanami, Soheil, et al. "Fluid Oscillators' Applications, Structures and Mechanisms- A review" Babol Noshirvani University of Technology, vol. 7, ResearchGate, doi 10.22111/tpnms.2018.25051.1153

[5] *Let's Do Dynamic Simulations*, director. Fluidic Oscillator: Ansys Fluent Tutorial: Transient, Turbulent (CFD Simulation). YouTube, YouTube, 9 Mar. 2020, www.youtube.com/watch?v=uUIwy6Y-OZY.

Design of the Trunk and Torso of a Lower Body Exoskeleton

Student Researcher: Maja Paar

Advisor: Roger Quinn

Case Western Reserve University

Department of Mechanical and Aerospace Engineering

Abstract

Lower-limb exoskeletons are used attached to a person's lower body, extending from the back to the feet. The motorized hip, knee, and ankle joints allow paraplegic patients to simulate able-bodied walking. Many exoskeletons on the market and in development are not being chosen over wheelchairs because they lack comfort, require a lot of energy to use, and need to be custom manufactured. Due to these limitations, I am working on making changes to the trunk and torso portions of the exoskeleton. This includes adding extra degrees of freedom to the hip joints so it more realistically mimics walking and therefore makes movement easier. Currently, the hips only move forward and backward, leaving the abduction and adduction joint at zero degrees. In addition to the existing forward and backward motion of the hip joints, there is now the ability to adjust the angle of abduction and adduction. There is added adjustability to the torso so that it can be worn by a wider range of people and does not have to be custom-manufactured for each user. Simple adjustments can be made in a matter of minutes to expand or contract for different users. The hip joints can also be moved forward and backward so that the center of rotation of the device lines up with the user's hip's center of rotation, which is crucial to a realistic, comfortable gait. These improvements should aid in making the device more comfortable and less strenuous to use as well as easing the testing process.

Project Objectives

The following goals were set for this project:

1. Add an extra degree of freedom to the hip joint with abduction and adduction
2. Allow the exoskeleton to be worn by a range of people of different sizes without custom manufacturing
3. Ability to adjust the size within a few minutes and while the device is being worn
4. Manufacture and integrate the design changes with the existing device
5. Test on at least one person
6. Ensure comfort and safety of users of the exoskeleton

Methodology

All of the design was created in Solidworks. The 3D model comprises torso or corset pieces, a trunk with movable abduction and adduction joints, and an attachment to the existing hip joints. In order to test the strength of the parts, finite element analysis was performed under a load that is expected while

someone is wearing the exoskeleton. Manufacturing is going to start soon, so the 3D model can be physically made and tested.

Results

The size adjustment of the torso and trunk and the abduction and adduction joints show promise for more comfort and easier use of the exoskeleton. Once manufacturing has been completed, the device will be tested for size and the metabolic rate will be measured during walking to see if the design has made any changes to energy output.

Significance

Adding an extra degree of freedom to the hip should improve ease of gait and balance. Currently, a lot of energy is used to maintain stability, and having an abduction and adduction joint should help reduce the energy output. Having size adjustment will allow the exoskeleton to be worn by people of most sizes and can expedite testing by eliminating custom manufacturing for each test subject.

Figures/Charts

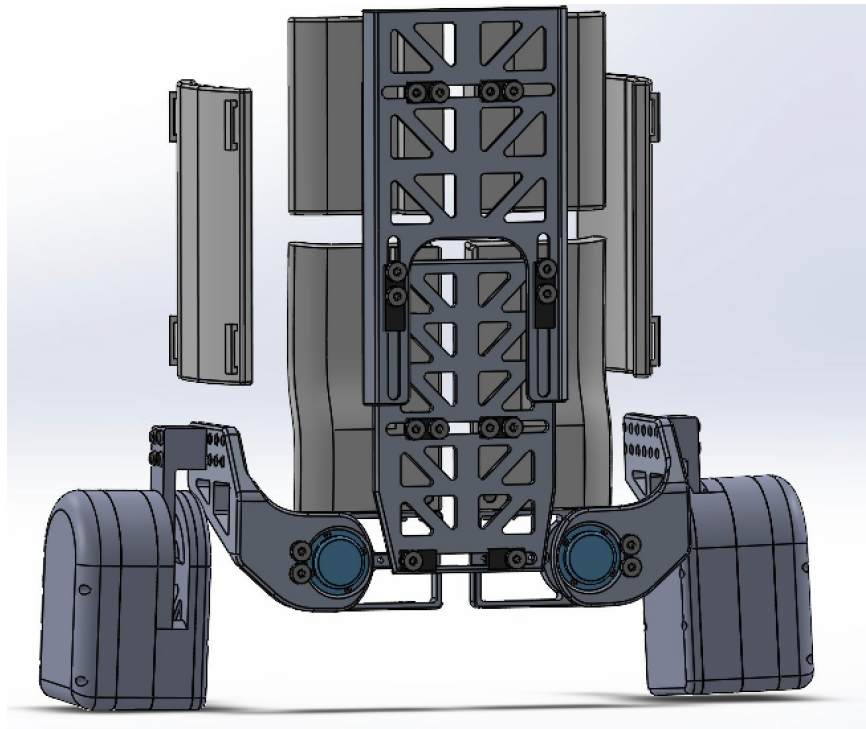


Figure 1: CAD Model of Trunk and Torso of Lower-Body Exoskeleton

Acknowledgments

I would like to thank the Ohio Space Grant for helping to fund my tuition. I would also like to thank Roger Quinn, Mark Nandor, and Marshaun Fitzpatrick for their help in designing.

Wetting Transition of 3D-printed Featured Surface

Student Researcher: Hannah J. Pineault

Advisor: Dr. Bi-min Zhang Newby

The University of Akron

Department of Chemical, Biomolecular, and Corrosion Engineering

Abstract

The primary objective of this research project was to gain a better understanding of surface characteristics to produce a hydrophobic or hydrophilic surface. In other words, when will a droplet of water remain on top of a featured surface and when does the transition occur to water filling the grooves of the surface? This research focused on how to best fabricate porous structures that would stay completely dry at all times by preventing the liquid from penetrating. In particular, we followed the behaviors of water droplets placed on top of 3-D printed featured surfaces with various geometries and surface treatments. Cylindrical pillars in a hexagonal array were 3-D printed with varying pillar diameter and height as well as the spacing ratio (S/D). The as printed models, models oxidized using air plasma, and models treated with hydrophobic octadecyl trichlorosilane (OTS) were tested. Both the as printed and plasma treated models didn't retain water on top of the features due to their surfaces being hydrophilic, while the hydrophobic OTS treated models were able to prevent water droplets from penetrating down to the surface. The features inversed from the 3-D printed models using hydrophobic silicone elastomer also showed complete prevention of water drops from penetrating the features. Varying the geometry of the pillars had a significant effect in most cases across the various surface treatments on the transition, while it only affected the contact angle on the model as printed.

Project Objectives

The first goal of this project was to gain experience on how to fabricate 3D-printed featured surfaces with different geometries and modify them to achieve various surface wettability. The second goal was to examine the wetting transition on these featured surfaces and determine the surface characteristics that would completely prevent the porous features from being wet by a liquid. Insights gained from this project can potentially be applied to develop technology that can mitigate or even eliminate corrosion or can be used to trap water even in extreme conditions. Other useful applications would include self-cleaning surfaces, effective oil and water separation, water harvesting, anti-fogging and anti-fouling.

Methodology Used

Cylindrical pillars in a hexagonal array were 3D printed using the Stratasys VeroCyan ink with a Stratasys Objet260 Connex3 printer. The printer has a layer resolution of 16 μm and an accuracy of 200 μm . The pillar diameter and pillar height were varied from 300-500 μm and 1000-2000 μm respectively. All of the models had a hexagonal array rather than a square array to increase the likeliness of the surface to be in the Cassie-Baxter state ^[1]. Tests were run on four variations of the 3D surface; as printed, oxidized, OTS deposition, and inversed features in silicone polydimethylsiloxane (PDMS). The models were oxidized for 10 minutes at medium power in a Harrick Plasma Cleaner PDC-32G. When treated with OTS, the models were soaked in 40mL of HPLC grade hexane ($\geq 98.5\%$) with $\sim 2\text{mL}$ of 95% OTS for 30 minutes. The model's features were molded in the Syl-gard[®] 184 silicone elastomer kit with a 10:1 weight ratio of the elastomer base to the curing agent. Water drops sitting on these surfaces was monitored via cameras, and images were captured at 0.5 s interval to determine whether and/or how fast the transition from the non-wetting state (i.e., Cassie-Baxter's state, when air fills the grooves/cavities) to the wetting state

(i.e., Wenzel's state, when liquid penetrates the grooves) occurred. A standard droplet size of 10 μ L was used, which was released using a VWR 2-20 μ L pipette. Food coloring was added to water to visually distinguish the drop. The cross-sectional area of the droplet measured from the pictures taken, along with the known volume of the droplet was used to calculate the droplet's contact angle. At least three runs were conducted for each model with each treatment.

Results Obtained

Figure 1 shows water droplets in each of the wetting states as well as pictures for reference. The as printed model was hydrophilic due to the resin used being somewhat polar, which caused the droplets to easily wet the surface. As shown in Figure 2, when the diameter of the pillars decreased on the as printed model, the time to wet increased and the apparent contact angle increased (Table 1). The height increase did not make a significant impact on the time to wet (blue vs. yellow bar), even though the apparent contact angle increased (Table 1).

When the models were oxidized the surface became extremely hydrophilic as expected. The contact angle on the flat surface dropped to a value of $33.7 \pm 8.6^\circ$, and the droplets wet the surface and penetrated into the features almost instantaneously.

The OTS treatment prolonged water droplets from penetrating into the features. When changing the diameter from 0.5mm to 0.3mm, some penetration of water droplets into the features was observed, which suggests the limit for a hydrophobic surface. The drop evaporated from the surface of the remaining models, and the height increase decreased the evaporation time (Figure 1). Unlike the OTS treatment, all of the inversed features PDMS models resulted in the droplet evaporating and never wetting the cavities. The apparent water contact angle varied insignificantly between the different 3D models for the hydrophobic surface treatments (Table 1).

Significance and Interpretation of Results

The geometry parameters, in the sub-millimeter to millimeter range we studied, for the inverse features in PDMS had little effect on the time for the droplet to evaporate and had no effect on the apparent water contact angle. Thus, for the hydrophobic models, the surface wettability was more significant to water penetration into the porous features than the geometry, especially the inversed PDMS features (Table 1).

The 3D printer had size limitations, and to obtain the desired small features, the spacing was not varied and the height could only be varied slightly. In the future with a more capable 3D printer, it would be desirable to study surfaces with smaller pillar diameter, spacing, and varying heights, which would likely obtain more insightful results on the effects of features on liquid penetration. The 3D printer had additional printing limitations that resulted in the pillars having rounded tops (see Figure 1 a-b) instead of the desired flat tops. That downward angle contributed to the droplet more easily wetting the surface. This is ideal for a hydrophilic surface, but a flat or concave top would create a more liquid repelling surface ^[1].

Steps for further research would include investigating additional geometry dimensions and arrays as well as other liquids. The research covered in this report builds upon previous studies involving droplet behavior on superhydrophobic surfaces. Murakami et al. studied the Cassie-Baxter to the Wenzel state transition with ionic liquids and the effect of the energy barrier, primarily the Laplace pressure ^[2]. This also includes Lee et al.'s work on the wetting transition on featured PMDS with respect to the spacing ratio as well as oil/water separation utilizing a biomimicry inspired 3-D printed surface by Yang et al ^[3,4].

Figures/Charts

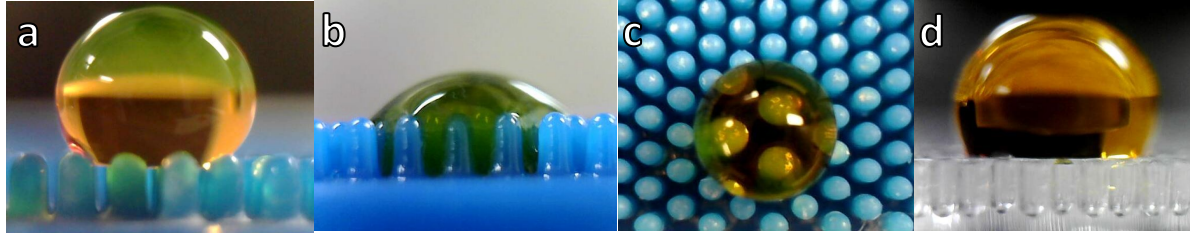


Figure 1. a. Droplet in the Cassie-Baxter’s state. b. Droplet in the Wenzel state. c. Example aerial image used to calculate contact angle. d. Droplet on the molded PDMS with inverse features.

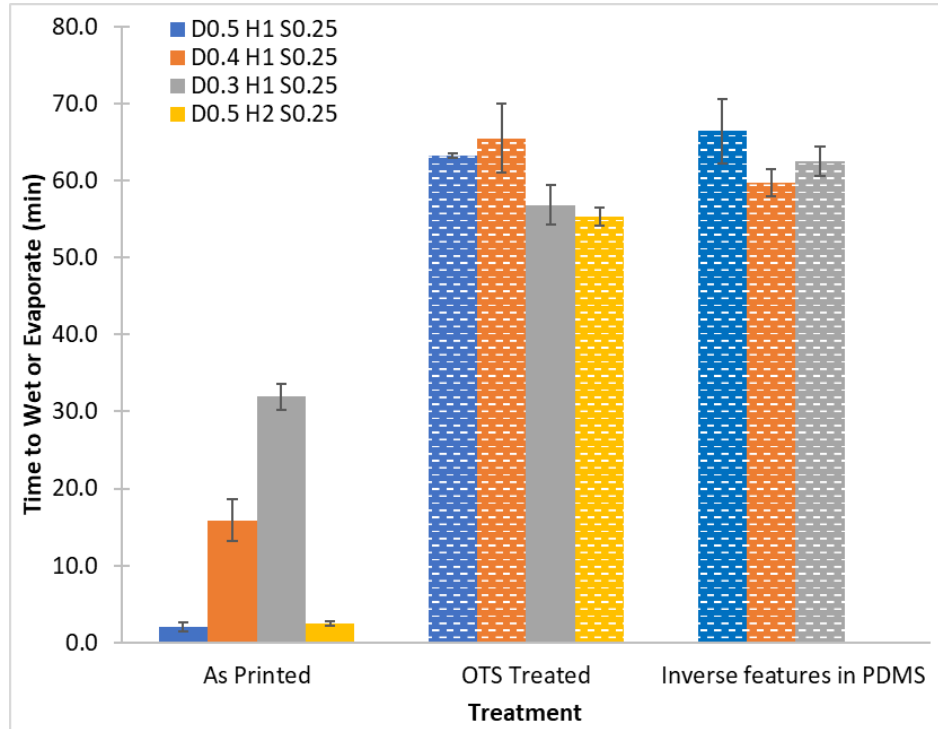


Figure 2. The time for water droplets to penetrate into the features for various models (for as printed models), or completely evaporate before observing water penetration into the features (dashed bars, for the OTS treated models and PDMS models with inversed features). The solid bar for the D0.3 H1 S0.25 OTS treated indicated partial penetration of the water drop into the feature. D, H, and S represent the pillar diameter, pillar height, and spacing between the bases of the pillars, respectively. The number immediately following D, H or S is the dimension in mm.

Table 1. Apparent water contact angles on the flat surfaces (of the polymer used for 3-D printing) and models of various features summarized for the four treatments.

	Flat	D0.5 H1 S0.25	D0.4 H1 S0.25	D0.3 H1 S0.25	D0.5 H2 S0.25
As Printed	76.1±5.8	111.0±4.4	117.3±7.1	124.4±5.7	180±0
Air Plasma Treated	33.7±8.6	~0. The droplets penetrated into the features instantaneously.			
OTS Treated	118.8±5.1	115.0±1.5	116.7±4.7	127.1±8.1	124.2±6.7
Inverse features in PDMS	99.4±8.9	102.3±6.2	103.2±6.7	101.7±4.5	-

(Note: D, H, and S represent the pillar diameter, height, and spacing, respectively. The number immediately following each letter is its dimension in mm. There is no statistically significant difference between the water contact angles on models with OTS treated and features inversed in PDMS.)

Acknowledgements and References

The author would like to thank OSGC/NASA and The University of Akron College of Engineering and Polymer Science for the funding of this project. The author would also like to thank Dr. Bi-min Zhang Newby for guidance and direction throughout the project's life.

1. Jung, K., Lee, D. "Fundamental Studies on Cassie equation and Cassie-Baxter to Wenzel Transition." *Graduate School of UNIST*. 2019.
2. Murakami, D., et al. "Wetting Transition from the Cassie–Baxter State to the Wenzel State on Textured Polymer Surfaces." *Langmuir*, vol. 30, no. 8, 2014, pp. 2061–2067.
3. Lee, J., Gwon, H., Lee, S., & Cho, M. "Wetting Transition Characteristics on Micro structured Hydrophobic Surfaces." *Materials Transactions*, vol. 51 no. 9, 2010, pp 1709-1711. Doi: 10.2320/matertrans.M2010118.
4. Yang, Y., Li, X., Zheng, X., Chen, Z., Zhou, Q., & Chen, Y. "3D-Printed Biomimetic Super-Hydrophobic Structure for Microdroplet Manipulation and Oil/Water Separation." *Advanced Materials*, vol. 30, 2018, pp. 1-11., doi:10.1002/adma.201704912.

Low Temperature Catalytic Gasification of Household Recyclables

Student Researcher: Nicholas W. Plentovich

Advisor: Dr. Jorge E. Gatica

Cleveland State University

Department of Chemical Engineering

Abstract

As landfills approach capacity and take up valuable land space, metropolitan areas have realized the need for waste disposal alternatives. Thus, there has been a widespread use of waste incinerators. Although modern incineration technology has improved efficiency, there is an increasing need in formulating “greener” alternatives to incinerators.

Gasification converts organic and carbonaceous materials into a combination of gaseous products known as “syngas,” or synthetic gas. This process greatly reduces hazardous emissions. The syngas produced by gasifiers has a wide range of uses, including their conversion into diesel, ethanol, methane, methanol and other synthetic fuels.

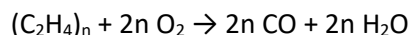
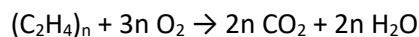
A low temperature gasification has been investigated in our laboratory. Wet Thermal Catalytic Oxidation of long-chain polymers. WTCO has shown great potential to gasify different model polymers. Low-temperature gasification promoted by Ru and Pt-Based catalysts has been characterized. Our group is now focusing on gasification studies of high-fidelity simulants and scale-up for continuous processing.

In this research we examine a conceptual design of Low-Temperature Wet Thermal Catalytic Oxidation (WTCO) promoted by Ru-based and Pt-based catalysts as a gasification technology to process household recyclables.

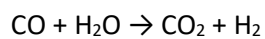
Project Objectives

Waste management poses an urgent problem to society. Landfills take up large areas of land and render that area useless for development for years to come. Incineration creates hazardous byproducts and takes large quantities of energy.

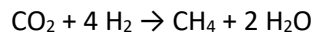
At NASA’s GRC a process was developed that seeks to take this waste and convert it to energy while using less energy than incineration and without creating the same harmful byproducts. This process is a wet thermal catalytic oxidation (WTCO) characterized by the reactions:



Complimented by the water gas shift (WGS) reaction



And the gas phase methanation of carbon monoxide



This process also has applications in space travel. NASA has interests in In Situ Resource Utilization (ISRU) and WTCO certainly serves this purpose. Waste must effectively be managed on longer term space trips as ejection of waste proves dangerous and returning the waste to Earth proves expensive, so WTCO provides a solution to this. Not only can the waste be successfully disposed of, but it can also return useful energy.

Methodology Used

To characterize the gasification reactions we must begin with reaction kinetics experiments in a small scale batch reactor. Our lab is using a 100 mL stirred pressure reactor. The kinetics experiments were conducted isothermally at 315°C for various amounts of time and the gas was then collected and analyzed using a GC-TCD. This was then analyzed to determine the concentration of each product compound from the gasification reactions. This is then able to give us an idea of the average residence time needed to achieve a decent conversion.

The kinetic experiments began by determining the amount of oxygen that is in the reactor when it is pressurized from a tank of compressed air at room temperature. This was then used to calculate the amount of our substrate to add. A stoichiometric amount of substrate was then added along with an equal weight of catalyst. 20 mL of DI was added to aid in stirring and the reactor was sealed and pressurized with the compressed air. Stirring was started, cooling water was started for the sensors, and the heater was activated. The heater was set to the desired reaction temperature or 315°C and once the reactor reached temperature the reaction time started. Once the desired reaction time had elapsed the reactor was allowed to cool and a gas sample was collected. This sample was then analyzed over several trials in a GC-TCD.

The GC-TCD was calibrated with standard samples that included each of the product compounds. The results of the analysis were then used to determine the conversion and gasification of the solid carbon in the original substrate. This process was repeated for various reaction times and was used to determine the time dependence of the gasification of the substrate.

Results Obtained

Composition data from various reaction times are shown in figures 1-4. These are the result of many gasification experiments on PE. More experiments are being conducted on PET and will be expanded to include Cellulose and HFWS. The combination of these results will then be able to predict the gasification of true household waste and can be scaled.

Significance and Interpretation of Results

As you can see in figure 1, there is little reaction time dependence on the composition of CH₄ in the gas phase. This is echoed in the results of CO, CO₂, and H₂. Further study of this could confirm the reaction kinetics of the gasification reactions and can expand these results to other compounds. Once this process has been generalized for further compounds scale up can begin for larger waste processing.

Figures / Charts

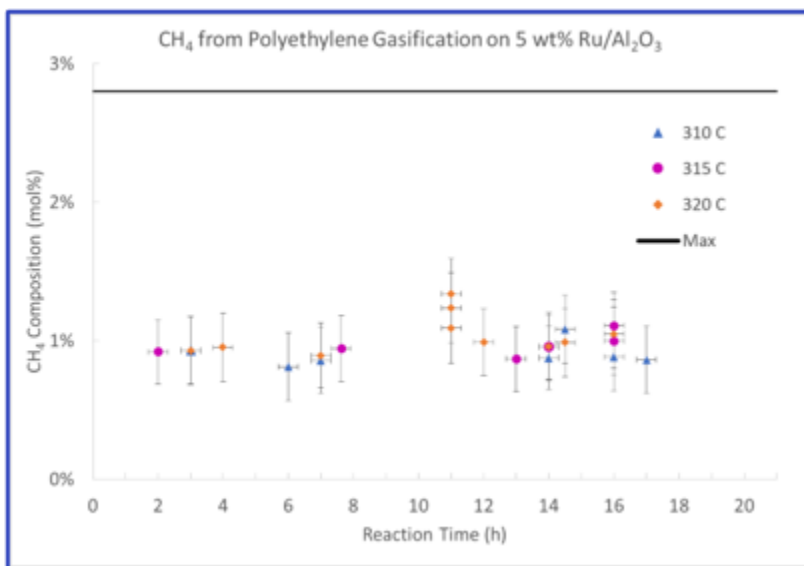


Figure 1. Reaction time and Gas Composition for CH₄

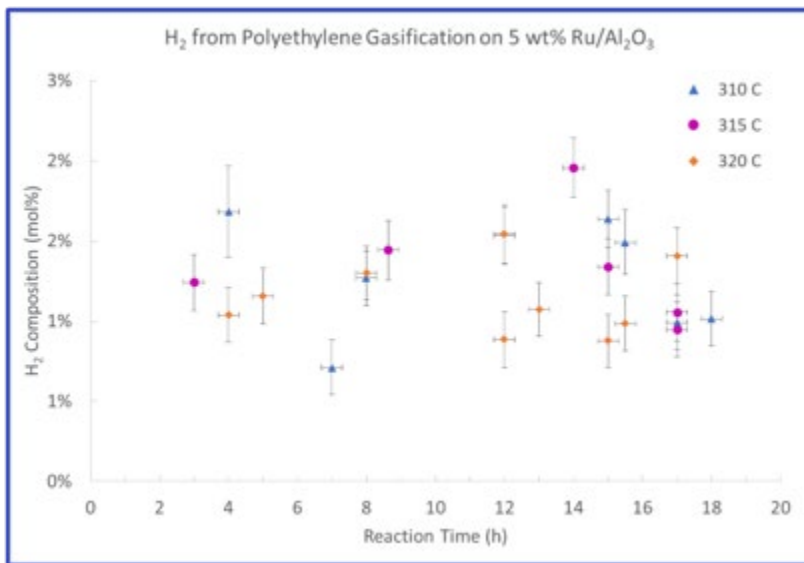


Figure 2. Reaction time and Gas Composition for H₂

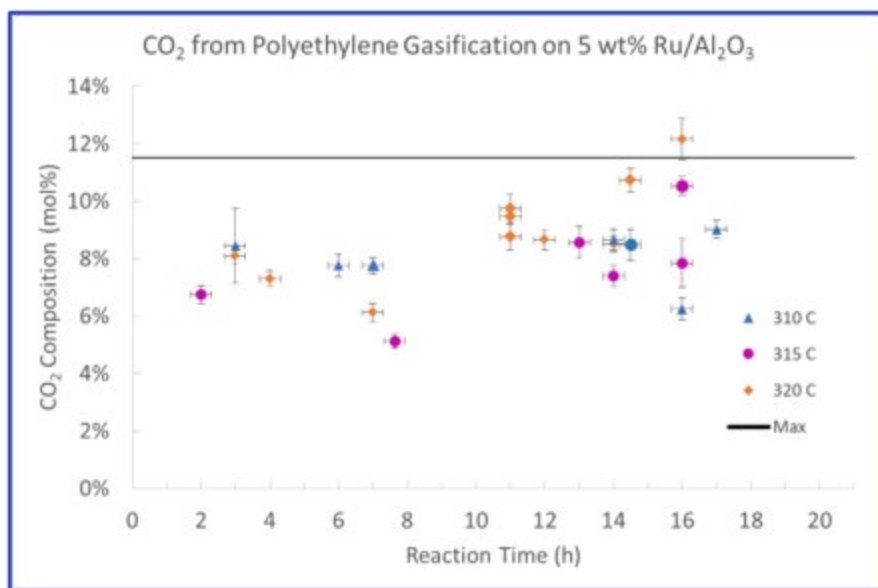


Figure 3. Reaction time and Gas Composition for CO₂

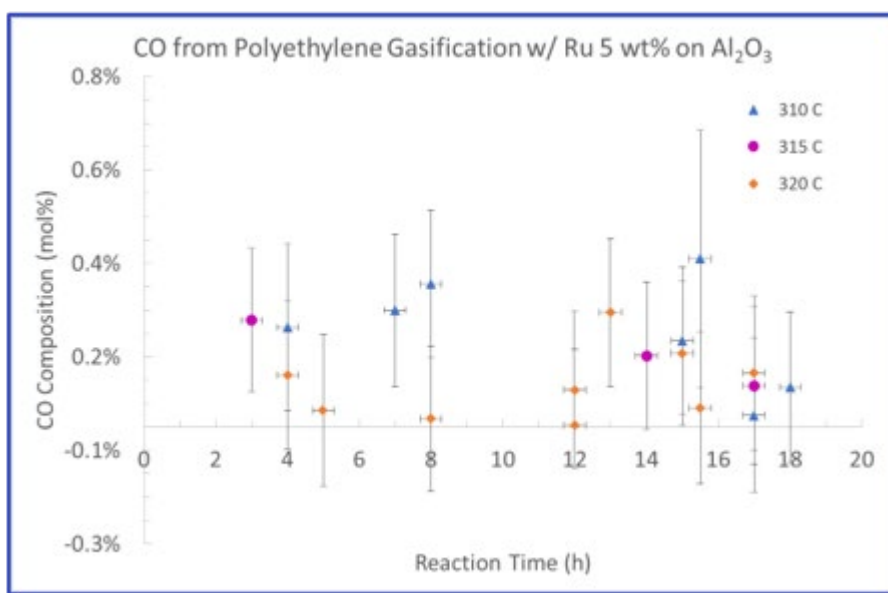


Figure 4. Reaction time and Gas Composition for CO

Acknowledgements and References

I would like to thank Dr. Gatica for mentoring me in this research and the Department of Chemical Engineering at Cleveland State University for giving me this opportunity. Thank you to NASA's GRC for the support on this project and to Kristen Reyes for working alongside me on this project.

Investigating Structure – Properties Relationship and Machinability of 3D Printed Carbon Fiber Reinforced Polymer Composites

Student Researcher: Christina B. Praprost

Advisor: Dr. Muhammad Pervej Jahan

Miami University

Department of Mechanical & Manufacturing Engineering

Abstract

As additive manufacturing practices have emerged as a more widely available solution to challenges, the applications have been expanding as well. 3D Printers are no longer limited to plastics, stepper motors, or brittle products, they can use metals, reinforcements, and servo motors, allowing the structures to be much stronger and widely applicable. This research focuses on optimizing the mechanical properties like tensile, compression, and flexure strength within additive manufactured products and the application of carbon fiber reinforcements in polymer composites. Using current publications, printed samples, and ABAQUS software, samples could be tested, simulated, and improved throughout an iterative process.

Project Objective

The long-term goal of this project is to discover new, reliable methods to improve the overall strength of additive manufactured parts and determine the optimal machinability processes. With higher strength, new applications could include medical, aerospace, automobile, and many others. By only altering preparation methods, internal structures and orientations of fibers, this can be a cheaper, lighter option for many structural applications. The goals of this research project involve:

- Identifying the optimal carbon fiber reinforcement orientations for improvement of mechanical properties
- Research and identify naturally occurring, bio-inspired engineering solutions for internal structures (like honeycomb shape)
- Print, test, and simulate samples using various preparation methods, carbon fiber reinforcement orientations and frequencies, and internal structure patterns

Standards

To properly test the tensile, compression, and flexure strengths of the specimen created, the following ASTM standards were used in modeling:

- ASTM D-3039: Standard Test Method for Tensile Properties of Polymer Matrix Composite Materials
- ASTM D-3410: Standard Test Method for Compressive Properties of Polymer Matrix Composite Materials with Unsupported Gage Section by Shear Loading
- ASTM D-7264: Standard Test Method for Flexural Properties of Polymer Matrix Composite Materials

Background

In order to begin testing possible solutions, some background research had to be done to analyze current solutions and learn from other researchers. Studies on carbon fiber reinforcements showed evidence that laying fiber chains aligned at 90° from the tensile load was optimal. Additionally, it was found that layer thicknesses have minimal effects on mechanical properties. In a similar study, alternating fiber layers were tested and showed that of the 30°/45°/60°, 15°/45°/75°, and 0°/45°/90° combinations, the 0°/45°/90° fiber combination provided the highest tensile strength. Regarding preparation methods, the study by (Yun Kim et al., 2009) showed that using a combination of heat and laser drawing provided samples with high amounts of energy and therefore, better mechanical properties. The process of hot pressing was also studied, showing that using a higher temperature, lower pressure and longer withholding times on 0°/45°/90° samples resulted in the best mechanical properties. With this information, experimental solutions could now be created and tested.

Results

Many of the samples were modeled in Inventor before uploading them into the 3D printer software, Markforged, where materials, layers, fibers, thicknesses, etc. could be altered in preparation, as illustrated in [Fig. 1]. The simulation software for Finite Element Analysis was ABAQUS, used to show theoretical Von Mises stresses, displacements, strains, and any other desired properties. Data from each ABAQUS simulation had to be confirmed using a convergence plot to show that the property of interest was consistent throughout all mesh sizes. One of these tests is illustrated in [Fig. 2-3].

The printing of new specimen and simulations of those will be modeled and tested using combinations of angles, preparation methods, and some testing with hexagonal internal structures. From these models and prints, machinability and strength improvements will be documented for further use. This project will be passed on upon graduation in May 2021 to a student who will continue this process of testing and simulations to reach new discoveries and applications.

Figures/Charts



Figure 1: Markforged sample, 7-layer CFRP

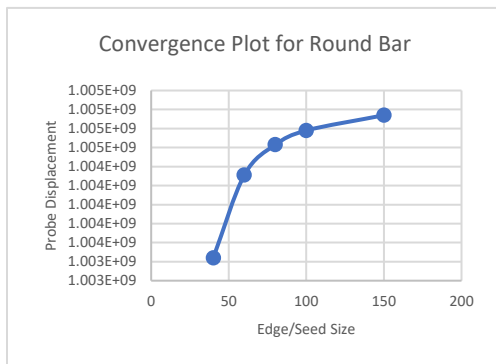


Figure 2 - Convergence Plot for

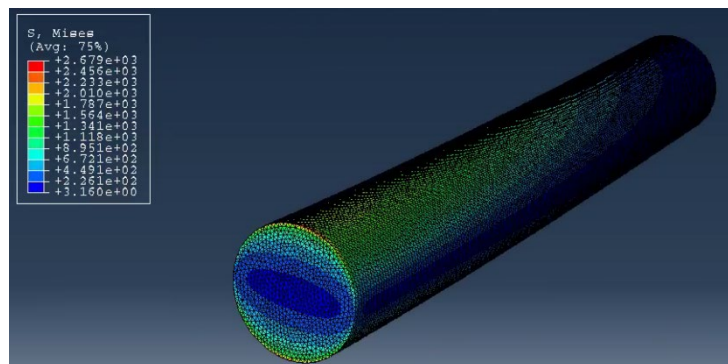


Figure 3: ABAQUS Deformed Sample

References

- 1 E. Baynojr Joyee, L. Lu, and Y. Pan, Elsevier Ltd., Chicago, IL, publication, 2019.
- 2 H. Mei, Z. Ali, Y. Yan, I. Ali, and L. Cheng, Elsevier Ltd., Xi'an Shaanxi, publication, 2019.
- 3 S. Yun Kim, S. Hun Kim, S. Hwan Lee, and J. Ryouun Youn, Elsevier Ltd., Seoul, publication, 2009.

Investigating Technology Leading to the Design of a High Altitude Ballooning Platform

Student Researcher: Markus R. Puckett

Advisor: Augustus Morris, Jr., Ph.D., P.E.

Central State University
Manufacturing Engineering

Abstract:

Exploration of the upper atmosphere and near space has become increasingly affordable for students at all levels over the last 20 years. Thanks to modern technology, instrumentation and communications needed to support scientific ballooning missions have become miniaturized, reliable, and affordable. Dubbed by some as the poor man's space program, it is now possible to conduct real science at near space altitudes for less than \$1000. Central State University is revisiting high altitude ballooning as a means to attract students toward, and choose careers in, the STEM fields. Working toward this goal, understanding the basic instrumentation necessary to measure key atmospheric variables is required if custom payloads are designed with such instrumentation. Knowing the range of environmental conditions encountered during a flight at altitudes up to 100,000 feet is necessary in order to protect the instrumentation on such missions.

Project Objectives:

There are several objectives to accomplish for this project:

1. Understanding of the variation of the Earth's atmosphere from sea level to an altitude of 100,000 feet.
2. A listing of key atmospheric variables to be monitored during a balloon flight.
3. Development of appropriate sensors and supporting electronics needed to build instrumentation with the capacity to measure the full range of variation of atmospheric variables during the flight.

Methodology Used:

A search through appropriate literature and references has provided a good foundation on the changes that occur in temperature and pressure in the troposphere and stratosphere of the Earth. Near space is defined at altitudes in the stratosphere beginning around 30 km.

Key variables used in weather monitoring and other atmospheric research include temperature and air pressure. These are the chosen variables to be monitored on balloon missions at Central State University.

A number of sensors are available capable of measuring temperature and pressure. However, these sensors require supporting electronics to ensure its measurements are calibrated and spans the range of the desired variables.

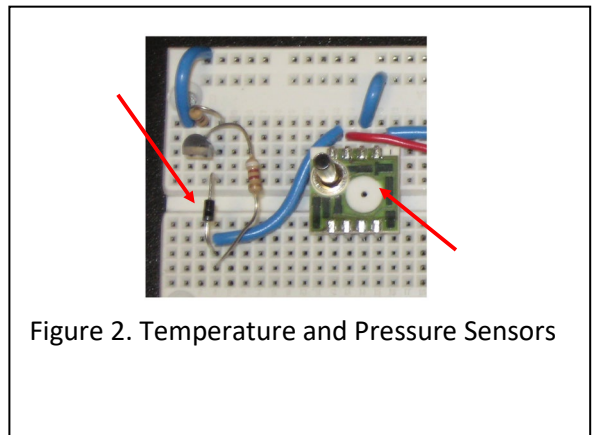
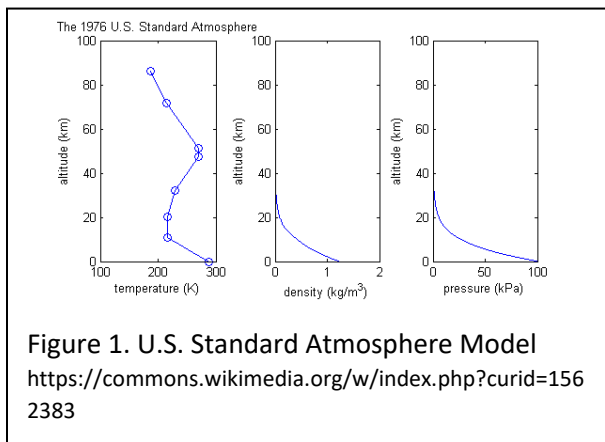
Results Obtained:

Figure 1 shows how temperature, pressure, and density changes as the altitude increases from sea level. Air density decreases with altitude. Air pressure ranges from around 1000 mbars at sea level to nearly 0 mbars at near space altitudes. In contrast, the temperature decreases with altitude near the Earth's surface, but then temperature begins to increase in the stratosphere. Of particular note, the temperature during a journey to near space can reach lows of -40C. Figure 2 shows a temperature and pressure sensor along with supporting circuitry and instrumentation.

Significance and Interpretation of Results:

The next phase of this effort will focus on designing payload structures to enclose and protect the instrumentation from the extremes in atmospheric conditions. An embedded system will be considered to coordinate the instrumentation and provide storage of the data collected. When an appropriate communication and tracking system is decided on, the critical instrumentation is in place to plan and execute a high altitude balloon mission.

Figures/Charts:



Acknowledgments:

This work would not be possible without the support of the Ohio Space Grant Consortium, the Manufacturing Engineering Department at Central State University, and my advisor, Dr. Augustus Morris.

References:

Larson S.L., Armstrong J.C. and W. A. Hiscock. The First Frontier: High Altitude Ballooning as a Platform for Student Research Experiences in Science and Engineering, American Journal of Physics 77(489) June 2009.

Magnus Effect Over Rotating Cylinders

Student Researcher: Joseph Rathkamp

Advisor: Jed Marquart

Ohio Northern University

Mechanical Engineering Department

Abstract

The traditional airplane has become an integral part of societal and economical use. There have been many proposed alternative methods to commercial aircraft, but the one that my summer research focused on was rotating cylinders. In a model form, rotating cylinders can be utilized for small aircraft, however, it becomes difficult to implement on a full size scale. The purpose of this project was to analyze the magnus effect over multiple, in-line, rotating cylinders and their potential use on commercial aircraft. Using various processing and post-processing software, the goal was to first imitate existing research on a single rotating cylinder and afterwards, proceed to add an additional cylinder directly behind it. The distances between the two cylinders were varied in order to observe the amount of lift produced at each distance.

Project Objectives

There were multiple objectives to this project. The first being to replicate an existing study conducted on a single, rotating cylinder [1] in order to validate the method being studied was viable, as well as to ensure it was done correctly. After the study was replicated, the second objective was to place a second cylinder directly behind the first, but leave it stationary. This was done in order to study how the magnus effect of one rotating cylinder would interact at the front end of another in-line cylinder. After this study was conducted, the second cylinder was rotated in both clockwise and counterclockwise directions, at varying distances trailing the first cylinder. This was done in order to examine which case worked best: rotating counterclockwise or clockwise, and which distance worked best (if at all) for both directions.

Recommendations

The goal of this experiment was to introduce an alternative to traditional aircraft that could rival it in years to come. Using the magnus effect on multiple rotating cylinders offers a viable option that deserves to be researched further.

To study this experiment, a scale model needs to be created in order for it to be tested in a wind tunnel. The model created in Pointwise should be replicated for this experiment. In order for this experiment to be justifiable, the original single cylinder Achenbach case should be replicated from the first referenced article [1] in order to ensure accuracy of all tests going beyond that. After a successful replication of this original experiment in the wind tunnel, a model with two in-line cylinders shall be tested. This model needs to have a track that will allow for the trailing cylinder to be moved to varying distances behind the

leading cylinder. Additionally, a motor will be required to rotate the leading cylinder clockwise, while an additional motor for the trailing cylinder to vary between clockwise and counterclockwise.

Conclusions

In conclusion, per the results of the experiment conducted, the best results were generated when the leading cylinder was rotating clockwise and the trailing cylinder was rotating counterclockwise. With this being said, the trailing cylinder generated more lift when it was closer to the leading cylinder as there was little energy loss in between the two rotating cylinders. This in turn generated a substantial amount of lift that could prove to be a viable replacement for standard aircraft, should it be studied further.

Figures and Charts

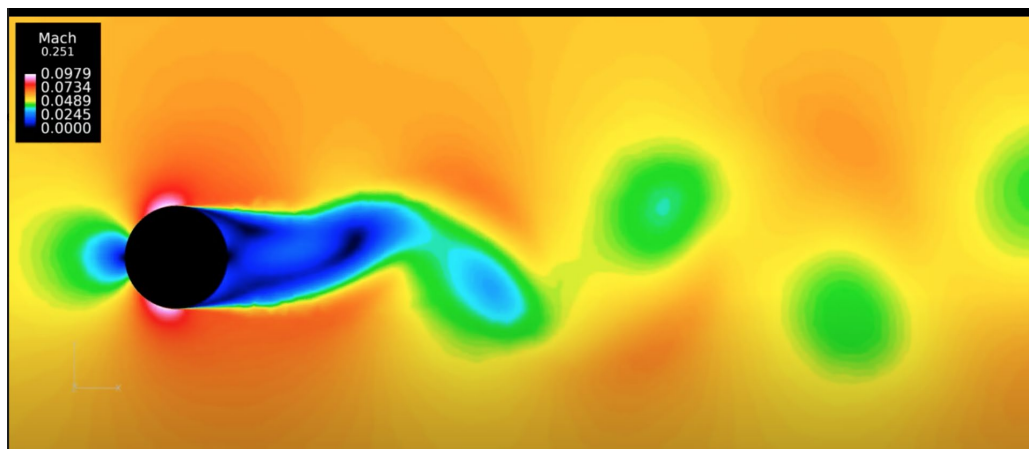


Figure 1: Magnus Effect Over One Rotating Cylinder

References

- [1] E. Achenbach, "Total and local heat transfer from a smooth circular cylinder in cross-flow at high reynolds number", *International Journal of Heat and Mass Transfer*, vol. 18, no. 12, pp. 1387-1396, 1975. Available: 10.1016/0017-9310(75)90252-5.
- [2] W. Sidebottom, A. Ooi and D. Jones, "A Parametric Study of Turbulent Flow Past a Circular Cylinder Using Large Eddy Simulation", *Journal of Fluids Engineering*, vol. 137, no. 9, 2015. Available: 10.1115/1.4030380.

Design of a Test Duct for Thin Film Cooling Research

Student Researcher: William L. Rickman

Advisor: Dr. David E. Munday

Miami University

Department of Mechanical and Manufacturing Engineering

Abstract:

The performance, efficiency, and carbon emissions of a gas turbine are directly related to its operating temperature, with higher temperatures yielding more favorable results. In modern systems, the temperatures at which a turbine can be run have surpassed the temperatures that the blades themselves can physically withstand. Thus, in order to further increase performance and run time, the blades of the turbine must be cooled in some manner. One method of achieving this is through thin film cooling, which integrates rows of small cooling holes along the blade of the turbine. These rows pump coolant to the surface of the blade, producing a thin film of cool gas that acts as a buffer between the blade and the hot flow. This allows for higher operating temperatures, and thus gains in efficiency and performance, as well as a decrease in carbon emissions. While the use of these holes is prevalent, further increasing their effectiveness is highly desirable. This study aims to produce a modular test section to facilitate the further exploration of how cooling hole effectiveness can be improved by altering hole geometry. This test section will include a variety of interchangeable components, eventually allowing for control over the boundary layer conditions, coolant supply, and the pressure gradient over the cooling holes, amongst other parameters. The manufacturing of this new test section has been postponed until recently due to the COVID-19 pandemic preventing access to manufacturing facilities. Since manufacturing wasn't possible, designs were fleshed out and literature reviews were conducted to make the best of the situation.

Project Objectives:

The objectives of this program have changed quite a bit since its initiation. Originally, the goal of the project was to design a duct capable of supporting thin-film cooling research in Miami University's new Engineering Research Annex (ERX). There were also optimistic plans to do some initial testing and data collection over the term. Understandably, as the Covid-19 pandemic began, access to University facilities were cut off, and work was forced to be put into a slight hiatus. Once the world had settled into a more stable state and the research group was able to reconvene, the objectives of the program had to be altered to fit the new circumstances. At the moment Miami University facilities were shut down, preventing any sort of meaningful manufacturing, or testing until the University reopened. Accordingly, all work had to be conducted remotely as students had been ordered to return home.

Since machining couldn't be done as originally planned, with Miami's machine shop shut down, the test duct design was instead fleshed out as fully as possible so that it could be machined once Miami University reopened. Accordingly, since the machining couldn't be done, testing couldn't be completed either, meaning that only about a third of the original goals of the program could be completed. Though instead of burning time until Oxford reopened, the short-term goals of the project were altered to maintain productivity. The primary was to undergo a literature review of existing thin-film cooling hole geometries, allowing a clearer view of what new ground could be broken and provide more direction on the research going forward once the facility was up and running.

Methodology:

The test duct was going to be mounted to a pre-existing flow system and as such had to be designed to fit its specifications. Additionally, there was a distinct desire for modularity and interchangeability within the duct so that experimental parameters such as hole geometry could be changed by exchanging a single part rather than replacing the whole duct. This would also allow for other experiments that use similar setups to those related to thin film cooling, such as internal and backflow cooling, to be explored using the same duct. The hole geometries were intended to be machined into a plate that bolted inside the duct that could be replaced experiment to experiment. The plate's dimensions were chosen such that any of Miami's plates could be used at a similar facility at Wright Patterson Airforce Base, where similar work is being done, only with higher temperature operating conditions. The advisor of this project has worked at this facility in the past and has hopes of eventually developing a partnership with the researchers there, so compatibility was important. The remainder of the design specifications were chosen to promote as much modularity as possible going forward, with space to add bleeds, trips, and other inlet/outlet sections to control the flow over the cooling plate.

The literature review was undergone y starting with several key papers to build a base of knowledge and then narrowing the scope of the search from thin film cooling to only those studies that looked into compound angle and diffuser shaped holes, since a main focus of this research group is compound angle shaped holes. Eventually, a database of cooling hole geometries compiled by another research group looking into similar phenomena [1] supplied plenty of avenues to explore and removed much of the initial legwork of searching for relevant papers. From there a clear map of what geometries had been studied previously was made and a handful of gaps were identified.

Results & Significance

Shown below is the 3D model of the Test Duct Design. As of now the design is fleshed out to the research group's satisfaction and machining is hopefully to start later this month (April 2021). Several of the interchangeable cooling hole plates have already been manufactured with one more on the way from a non-university electrical discharge manufacturing (EDM) vendor. This will facilitate initial testing sometime this upcoming Summer.

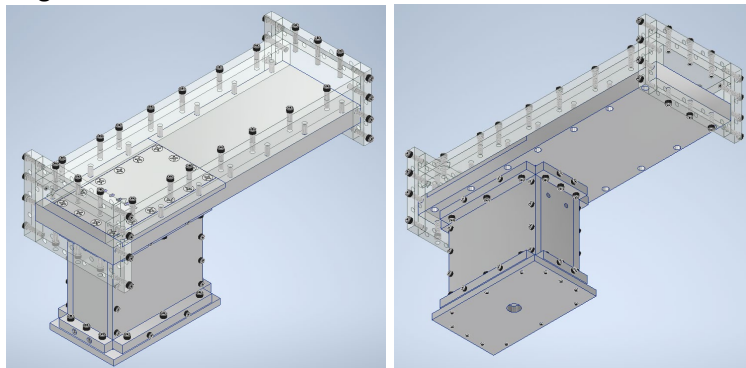


Figure 1: Isometric views of the test duct.

The literature review's fruits are much less concrete than the design work shown above, however the review provided an excellent opportunity to get a real footing on the current state of the science. Particularly, it allowed for the identification of several gaps in current knowledge and for the ability to make a well-educated decision on which geometries should be tested first.

References

Schroeder, Robert. (2015). *Influence of In-Hole Roughness and high Freestream Turbulence on Film Cooling from a Shaped Hole*.

Augmented Reality Overlay System

Student Researcher: Sara J. Roman

Advisor: Irvin Cardenas

Kent State University
Aeronautics and Engineering

Abstract:

The Augmented Reality Overlay System came about during a hackathon hosted at Kent State University. When observing airports across the country there was a noted struggle with constantly fluctuating weather that interferes with landing planes. Nantucket being an example as it had unpredictable heavy fog that grounds flights frequently. Taking advantage of Augmented Reality allowed me to form the concept for a projection of the runway to appear on the windshield (or pair of AR goggles for trial runs) that would aid the pilots in landing even when visibility is low.

The idea is for 'beacons' to be placed in distinct markers along a runway that will communicate to the AR system to help pilots visualize their orientation to land. Future developments being considered is to further develop this into a general guidance to even allow for routes to specified terminals though there are legal restrictions that may inhibit its implementation into commercial airlines.

Research and prototyping have been restricted due to the pandemic though I plan to do what I can from home. Over the last semester I was able to design the concept for the Augmented Reality Overlay System around the guidelines for flight and in this semester, I was able to regain access to the lab and work with the augmented reality system to develop a small working prototype.

Project Objectives:

The objective of the Augmented Reality Overlay System is to create a design concept that can be developed into a more versatile tool for pilots in the future. Its initial objective is and always will be to showcase the capabilities of augmented reality and its potential for aircraft usage. I have gone through the process of laying out my goals into four main categories: concept, research, prototyping and testing.

A. Concept

As described in the abstract the idea for the Augmented Reality Overlay System came about from a hackathon and further developed into a research project. It would allow pilots to 'see' desired landmarks such as runways and other potential aircrafts even when weather inhibits that. It is a safety net rather than a device to rely on in flight.

B. Research

With a design and concept in mind of how I would like the Augmented Reality Overlay System to operate I have to broaden my understanding on how airport systems and communications work and if there are any rules in place that may inhibit any of the original concept.

C. Prototyping

The prototyping phase has taken what I've learned in research with aviation laws and allowed me to understand what needs altered and redesigned withing the original concept. Taking into consideration rules and how communication is handled both domestically and internationally I can take those into account when designing how I want the beacon to operate and how the augmented reality will be displayed.

D. Testing

To date on the AR System, I am still in the prototyping phase and any tests that has been done are related to stress analysis the chassis and short-range tests of the augmented reality's ability to

pick up on the beacon. With future testing I would like to take the project to a bigger scale and see how far the augmented reality can pick up on the beacon.

Methodology:

The method used was a combination of learning and working with skills I already had as well as developing new ones to achieve the objectives of this project. Such skills I had to learn were to work with augmented reality programs such as The Magic Leap which we had in lab to work with from previous projects. My knowledge on coding were limited prior to this project but I was able to learn as I went on and delivered beacons that interacted with The Magic Leap. Additionally, I added chassis for the beacons for both practicality and to showcase CAD design within the project.

Results:

I was able to obtain a tangible interaction between augmented reality and the beacons. From the Magic Leap goggles you can see the beacons even when hidden by means of a red sphere otop of its location. It appears to only work within small distances at the moment though I wish to further experiment and improve upon the design.

During testing we were able to test The Magic Leap's capability to pick up on the beacons both from a distance as well as through barriers such as walls. I was able to learn that the beacons could be picked up from roughly forty feet away and further resulted in glitching of the visible red sphere. Walls and other barriers proved more difficult, and I was unable to get the beacon to pick up through less than a foot of concrete masonry brick wall.

I am able to understand as to why the beacon struggled to penetrate concrete brick though I would like to attempt to find other methods of creating a stronger beacon than the first round. It can be assumed that while a plane shouldn't have to see through a wall, there is potential of cities getting in the way of airport locations and runways close to landing that may interfere with this design. This is however only small-scale testing and I do not predict if it was scaled up to industrial use on planes that this problem would occur.

As for distance testing, I am pleased and still wish to test with different beacon types as well as different weather patterns. I was only able to make a few tests for this distance comparison and would be interested to see if rain, snow and fog have potential to interfere with the beacon. If it does then how severely would the distance be cut or would it simply not show up entirely depending on weather severity.

Acknowledgments:

My Thanks' go out to my advisor Irvin Cardenas and Dr. Kim who have helped me develop my skills every step of the way for this project and others currently being worked on.

References:

Stacey, Dale. *Aeronautical Radio Communication Systems and Networks*. Wiley, 2008.

Mackay, Wendy E., et al. "Reinventing the Familiar." *Proceedings of the SIGCHI Conference on Human Factors in Computing Systems - CHI '98*, 1998, doi:10.1145/274644.274719.

Analysis of Supersonic Jet Control through Spectral Proper Orthogonal Decomposition (SPOD)

Student Researcher: Andrew J. Sais

Advisors: Dr. Mo Samimy and Dr. Nathan Webb

The Ohio State University

Department of Aerospace Engineering and Aerospace Research Center

Abstract

Spectral Proper Orthogonal Decomposition (SPOD) is a mathematical method for the visualization of high energy modes of statistically stationary flows. A supersonic, rectangular, twin-jet exhausting from a military-style nozzle of aspect ratio 2 and design Mach number of 1.5 is used to produce a flow through a range of over-expanded and under-expanded regimes. Plasma actuation is used to modify the flow behavior. SPOD analysis of the modified flow is then used to both reinforce understanding derived from spectral analysis of the flow as well as shed light on characteristics of the flow dynamics.

Project Objectives

The control of supersonic jet flow is an area of research that is of interest to parties that deal with supersonic flight within Earth's atmosphere. In such flow, far field noise is commonly produced by two sources: jet mixing noise and shock associated noise. Within the realm of shock associated noise exists jet screech, a pitch most often of higher amplitude than other far-field jet noise. The ability to control supersonic jet characteristics could yield advances in control of this far-field noise. The objectives of this project are to utilize SPOD techniques to analyze the flow field of a controlled jet in two different flow regimes: an over-expanded regime at $M_j = 1.35$, and an under-expanded flow regime at $M_j = 1.65$. The results from this analysis will then be compared to coherence and phase data derived from near-field microphone array readings. This comparison should substantiate these microphone readings as well as reveal new insights into the flow dynamics.

Methodology

In a supersonic jet, screech is a key component in far-field noise. Any attempt at noise reduction through active jet control will require reducing the jet screech. Screech is produced through an interaction between down-stream convecting structures in the jet shear layer and shock cells contained within the supersonic jet[1]. Kelvin-Helmholtz instabilities within the jet shear layer create vortical structures that travel downstream at a certain frequency and speed. When these structures interact with shock cells, upstream propagating waves are produced at the same frequency as the downstream travelling structures. These upstream travelling waves then reinforce the shear layer instabilities and create a feedback loop and highly coherent structures at this screech frequency, resulting in high amplitude screech. In addition to this feedback mechanism in a single jet, twin supersonic jets can couple with each other, further reinforcing this screech cycle. Any control of a supersonic twin-jet will require a disruption or modification of this feedback loop, as well as the coupling of the jets.

In this project, 16 Local Arc Filament Plasma Actuators (LAFPAs) are placed around a supersonic twin-jet nozzle of aspect ratio of 2 (8 on each jet) and a design Mach number of 1.5. This set-up is shown in Figure 1. For the control experiments, only six of these actuators on each jet were used, the three above

the nozzles and the three below the nozzles. Using very small amounts of energy, the LAFPA's create plasma arcs which induce instabilities into the jet flow to modify the feedback cycle. Additionally, the LAFPA's can be fired in phase or out of phase between the two jets to influence jet coupling.

During control experiments a series of schlieren images are taken of the flow. Schlieren is an imaging technique that allows for the visualization of density gradients in the flow field. This allows for the visualization of flow features such as coherent structures and propagating waves. For this experiment a Z-type schlieren set-up was used, with images taken at a frequency of 40 kHz. These schlieren images were used as the data input to perform SPOD analysis.

Proper Orthogonal Decomposition is a method of finding optimal orthogonal bases vectors for a selected dataset in the spatial domain[2]. This is the solution to an eigenvalue problem, where the resultant eigenvectors being the orthogonal bases. In statistically stationary flow POD can be performed not only across the spatial domain, but the time domain as well, resulting in SPOD. SPOD can be used to find these optimal bases vectors at discrete frequencies in the flow. These optimal eigenvectors are referred to as modes and are ranked by what share of energy (variance of fluctuations) in the flow-field they contain. In practice, SPOD analysis shows the frequencies at which the flow characteristics containing the highest share of energy are occurring along with the coherence of those characteristics. It is expected that the highest energy elements of a supersonic nozzle will be related to the convecting structures reinforced by the screech feedback loop and twin-jet coupling. Therefore, it is expected that the highest energy SPOD mode, mode 1, will show high energy concentration around the screech frequency and its harmonics. The SPOD analysis was performed using a publicly available MATLAB script[3]. Using a set of 1000 images for each data set, the parameters of which were jet Mach number, excitation pattern, excitation frequency and nozzle axis view, the SPOD modes were found for a series of frequencies up to 20 kHz. For the initial round of analysis, the first and second most energetic modes for an over-expanded flow with Mach number of 1.35 and screech frequency of 8.4 kHz, and an under-expanded flow with Mach number of 1.65 and screech frequency of 5 kHz were plotted.

Results Obtained

Figure 2 shows what the SPOD plot displays when there is no high energy coherent modes at a given frequency. This particular image is of baseline flow at a Mach number of 1.35, with the SPOD resolved at a Strouhal number of 0.51. Figure 3 shows the major and minor axis mode 1 SPOD plots for Mach number 1.35 at their respective screech frequency. This is where it is expected to see coherent energy characteristics due to the high energy coherent structures involved in the feedback strengthened screech process. Compared to Figure 2, organized energy patterns of varying intensities can be seen in the SPOD at these frequency. A selection of excited cases are presented here and will be discussed in the proceeding section. Figure 4 shows the SPOD of $M_j = 1.35$, excited at a Strouhal number of 0.41, which approximately relates to the screech frequency of 8.4 kHz. It is being excited with an out-of-phase actuation scheme, shown in Figure 5. Figure 6 shows the SPOD at the excitation Strouhal number of 0.51, approximately 10 kHz, above the screech frequency 8.4 kHz. This excitation was performed using the in-phase actuation pattern 2, shown in Figure 7.

Significance and Interpretation of Results

Using the provided results, the SPOD analysis can be compared with acoustic data to create a fuller understanding of how excitation affects the flow physics. Looking back at figure 3, the baseline jet is at

$M = 1.35$ with a screech frequency of approximately $St = 0.41$. Figure 8 shows time averaged coherence and phase for this operating condition. Coherence represents a correlation between two microphones, one from each jet, and is taken as an indicator of how strongly the jets are coupled. The phase is showing whether the jets, if coupled, are behaving in phase or out of phase, and to what degree. One thing to note about this figure is that, when the phase and coherence were viewed in a time series, not averaged, these two jets at $M = 1.35$ were consistently sliding in and out of phase, so while there is a high average coherence and an average phase of nearly 0 degrees, this was not constant in the flow. However, results were still obtained that fit the expected behavior of highly coupled, in phase jets. It would be expected that exciting the jets out of phase would break the coupling of the jets and indeed Figure 9 shows just that. The high average coherence peak around the screech frequency is greatly reduced when the flow is excited at the screech Strouhal number of 0.41 in an out-of-phase excitation pattern. A reduction of coupling should lead to reduced screech. This shows up in the SPOD shown in Figure 4. When compared to the baseline SPOD in Figure 3. There is a slight increase in energy in the minor axis but a precipitous decrease in energy along the major axis. This could very well be indicative of a loss in energy of the convective structures involved in the screech process. Further confirmation is given by looking at a near-microphone spectrum for one of the jets before and during excitation. In Figure 10 a consistent high amplitude spectrum can be seen at the screech frequency before excitation, but during it has all but vanished. The SPOD seems to confirm screech cycle theory and the acoustic data for this excited flow regime.

Another case of interest is excitation of the $M = 1.35$ flow at a Strouhal number of 0.51. This is approximately a frequency of 10kHz, higher than the screech tone of 8.4 kHz. In this case the flow is excited with an in-phase actuation pattern. Since the baseline flow around this frequency is in-phase, an enhancement or addition to frequencies in the flow is expected. Looking at Figure 6, SPOD reveals that, at this new excitation frequency, coherent energy patterns are present in both the major and minor axis. Compare this to Figure 2, which was previously used as an example of what SPOD analysis looks like when there are no organized high-energy characteristics of the flow. Clearly the control excitation has affected the flow characteristics. Figure 11 shows near-field microphone data for this excited flow case. The black line represents the baseline, with the red representing the excited flow. Every microphone shows a large peak where there previously was none around 10kHz, the excitation frequency.

Similar control results were found for several cases of excitation for the under-expanded regime at Mach 1.65, but have been left out for brevity.

These sample cases are but a small subset of the SPOD data collected for the project so far, but are illustrative of how SPOD can be a useful tool in adding to an understanding of supersonic flow physics and how excitation is affecting the flow behavior. Next steps in the utilization of SPOD in the project are to analyze more, lower energy modes, use more schlieren images for increased frequency resolution, and animate the SPOD results to see if a sense of motion in the images leads to further insights.

Figures

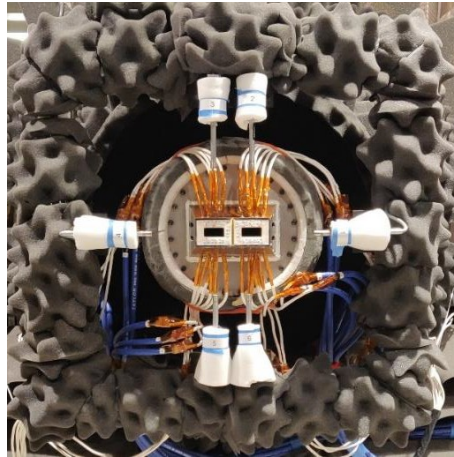


Figure 1: Nozzles with Actuators

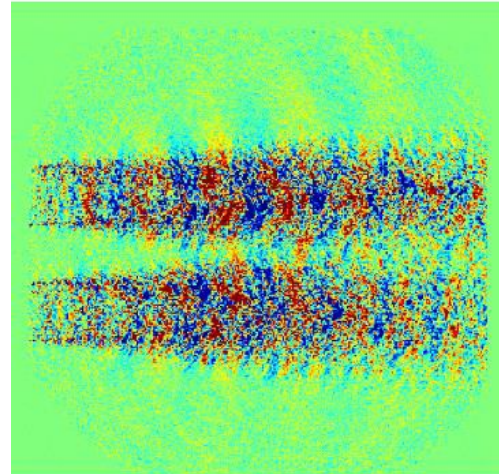
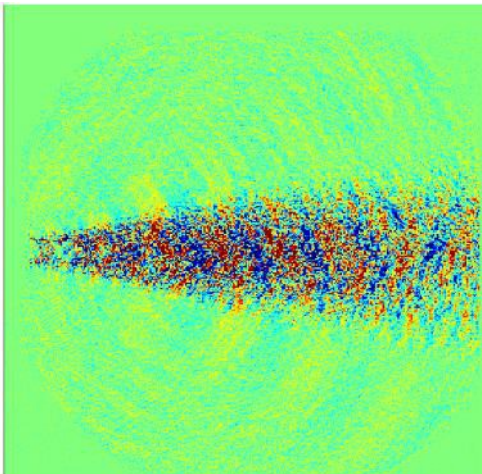


Figure 2: SPOD for Baseline $M = 1.35$, $St = 0.51$.
On Major Axis (Left) and Minor Axis (Right) Planes

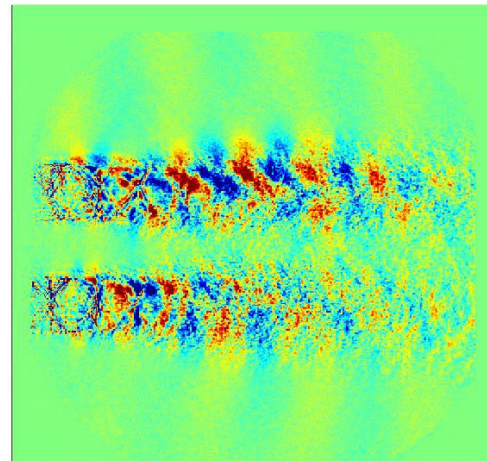
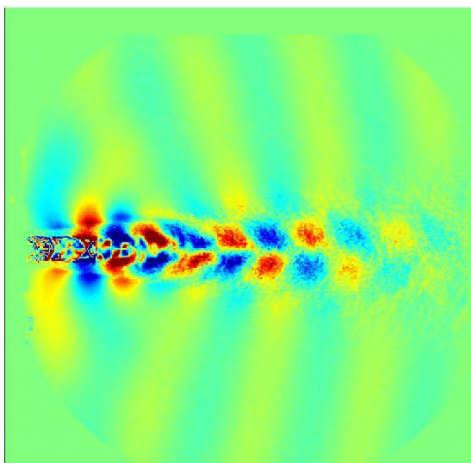


Figure 3: SPOD of Baseline $M = 1.35$ at $St = 0.41$

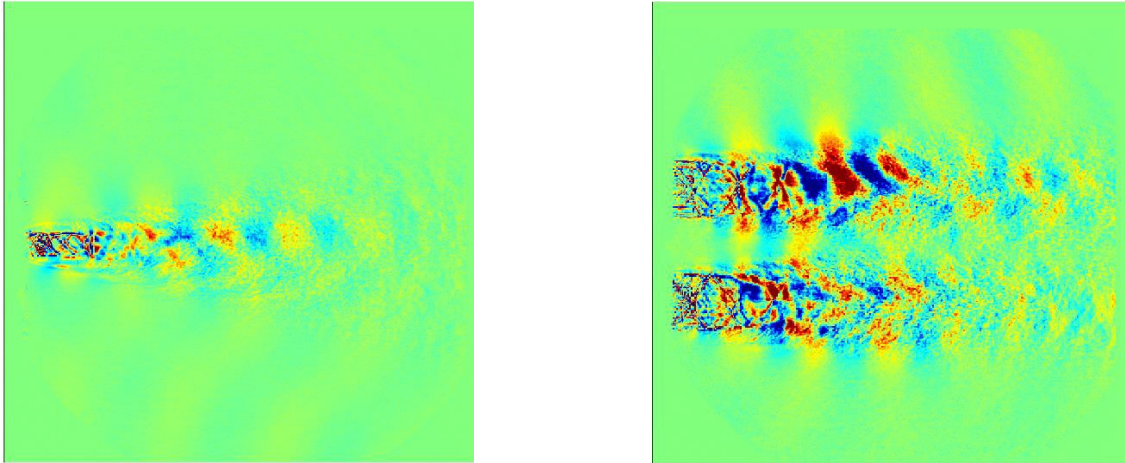


Figure 4: SPOD of $M = 1.35$ at $fe = 0.41$

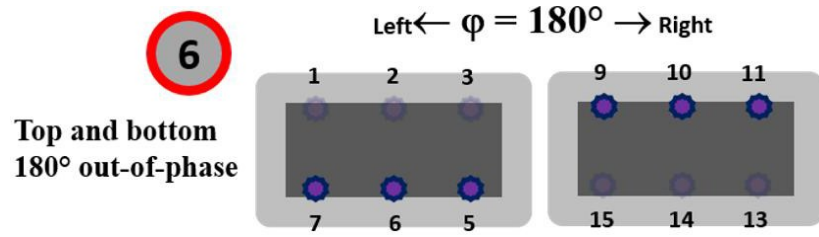


Figure 5: Actuation Pattern 6

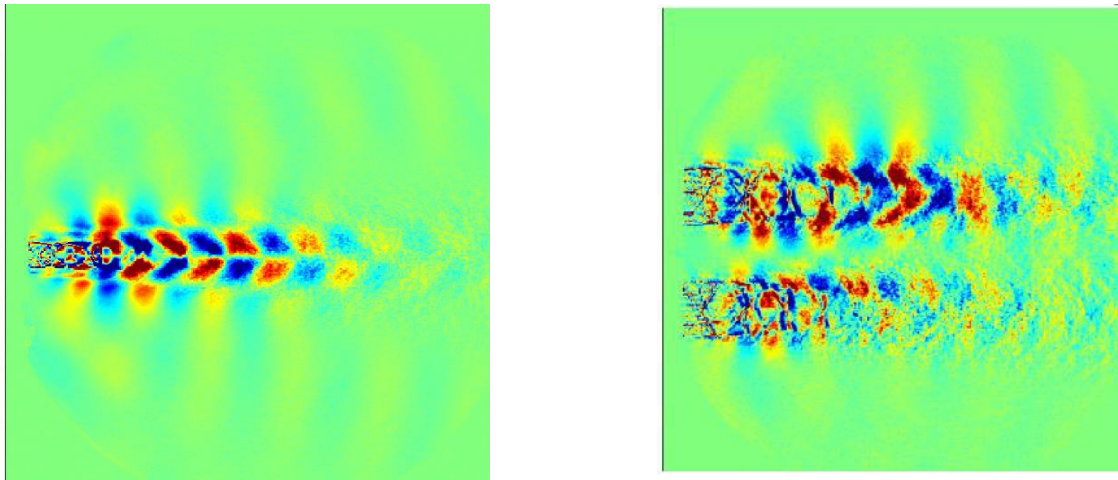


Figure 6: SPOD of $M = 1.35$ at $fe = 0.51$

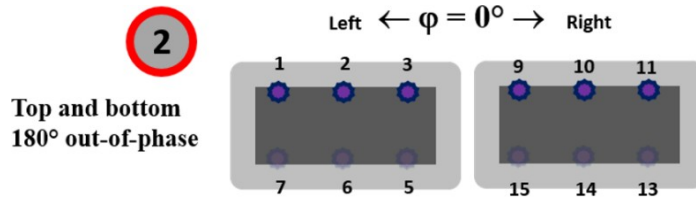


Figure 7: Actuation Pattern 2

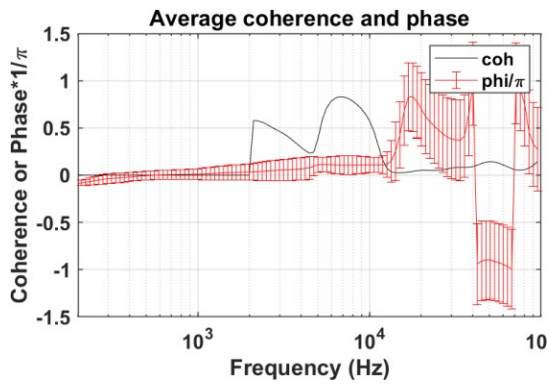


Figure 8: Baseline Average Coherence and Phase between the jets, $M = 1.35$

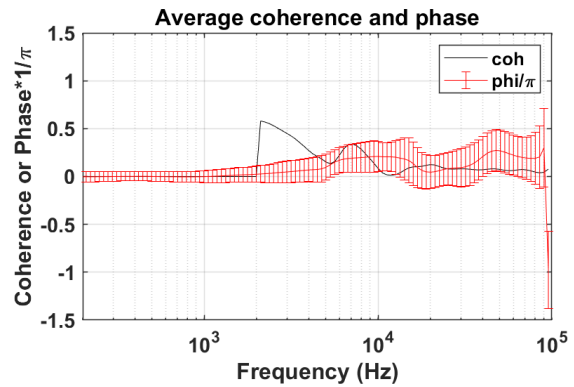


Figure 9: Average Coherence and Phase between the jets, $M = 1.35$, excitation frequency, $f_e = 0.41$

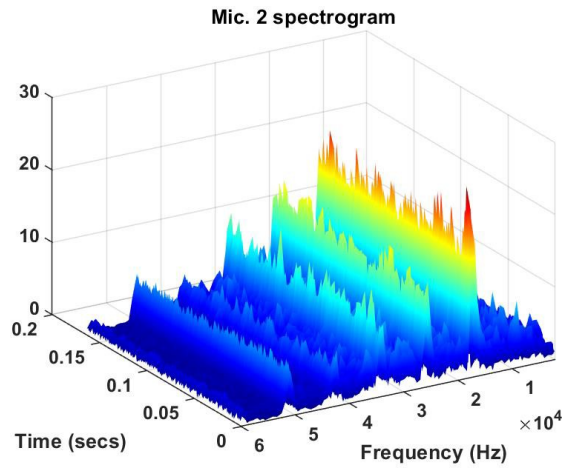
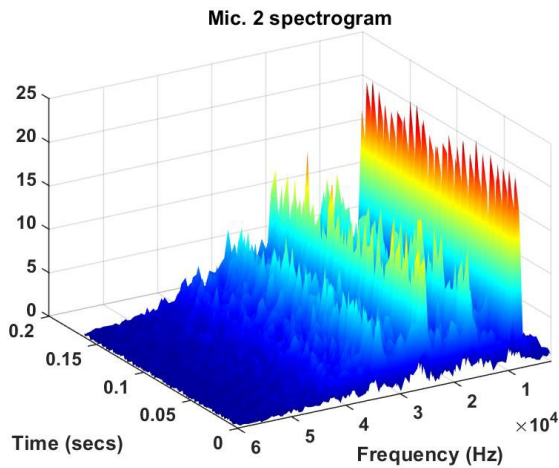


Figure 10: Spectrogram from single near-fields mic before excitation (Left) and after excitation (Right) for $M = 1.35$, excitation frequency, $f_e = 0.41$

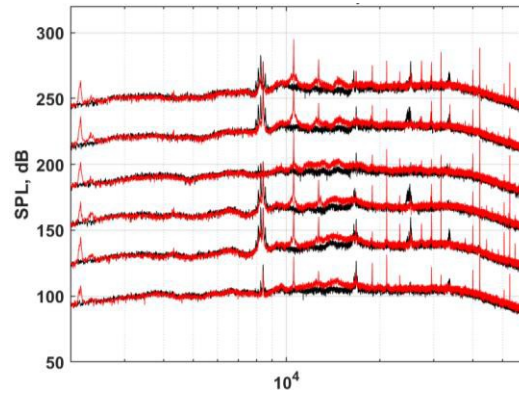


Figure 11: Near-field spectra for $M = 1.35$, excitation frequency, $f_e = 0.51$

Acknowledgments and References

1. Edgington-Mitchell, D. (2019). "Aeroacoustic resonance and self-excitation in screeching and impinging supersonic jets – A review." *International Journal of Aeroacoustics*, 18(2–3), 118–188. <https://doi.org/10.1177/1475472x19834521>
2. Schmidt, Oliver T., and Tim Colonius. "Guide to Spectral Proper Orthogonal Decomposition." *AIAA J*, vol. 53, no. 3, Mar. 2020, doi:<https://doi.org/10.2514/1.J058809>.
3. Github: https://github.com/SpectralPOD/spod_matlab

I would like to acknowledge Dr. Mo Samimy, along with Dr. Nathan Webb, Ata Esfahani, and Jack Tyszkiewicz, whose kindness and generosity of experience, knowledge, and time have helped me understand what it means to investigate the world we inhabit.

Impacts of Shift Work on People with Chronic Conditions

Student Researcher: Hayley D. Shasteen

Advisor: Dr. Rachael Blasiman

Kent State University
Department of Psychological Sciences

Abstract

In this project, we aim to understand how shift work impacts people with chronic conditions, such as systemic lupus erythematosus or multiple sclerosis, as compared to people without chronic conditions. Current research efforts have revealed that shift work is a risk factor for developing numerous chronic conditions and that shift work in general leads to dysfunction in cognition as well as an increase in physiological maladies. However, there remains a lack of research regarding how shift work impacts those who already have a chronic condition. We examine differences in objective and subjective cognition, physical symptoms, sleep, and sleep-wake activities between shift workers with chronic conditions and those without. We also compare shift workers to non-shift workers both with and without chronic conditions.

Objective

The purpose of this project was to understand the potential negative impacts that shift work has on people with chronic conditions. Shift workers, defined as people who work outside the hours of 07:00 and 18:00 and may be required to routinely rotate their hours of service, are often at risk for a variety of chronic conditions, such as cardiovascular and gastrointestinal diseases as well as metabolic disorders.¹ There is also evidence that shift work is a risk factor for developing autoimmune diseases, such as rheumatoid arthritis, multiple sclerosis, and autoimmune hypothyroidism.^{2,3,4} In addition to physiological impacts, shift work also has noted detrimental impacts to cognition, including producing deficits in executive functioning.⁵ Despite growing evidence that shift work is a risk factor for chronic conditions, there remains a lack of research concerning the negative impacts of shift work on people with previously diagnosed chronic conditions. The objective of this study is to understand impacts to physiological health and cognition in shift workers with chronic conditions as compared to shift workers without chronic conditions and how shift workers compare to non-shift workers with and without chronic conditions. We are interested in understanding if shift work negatively impacts those with chronic conditions more than those without. We hypothesized that people who are shift workers with a chronic condition will differ significantly from shift workers without chronic conditions, non-shift workers with chronic conditions, and non-shift workers without chronic conditions on variables of short term memory (STM), working memory (WM), general health, sleep, and pain specifically that shift workers with chronic conditions will report negative scores in these domains.

Methodology

We recruited participants via email, social media platforms, and organizations specific to shift workers and chronic conditions, as well as university students recruited from research subject pools. Participants were asked to complete an online survey that included demographic questions, asked their shift worker status, and asked if they had ever been diagnosed with a chronic condition(s), and if yes, which chronic condition(s) they had been diagnosed with. Participants then were asked to complete the RAND-36 Measure of Health-Related Quality of Life, a modified version of the Pittsburgh Sleep Quality Index, the Bodily and Emotional Perception of Pain Scale, the Sleep-Wake Activity Inventory, and a modified

inventory of subjective cognitive symptoms.^{6,7,8,9,10} After completing the online survey, participants were then asked to complete an assessment of STM and WM. The STM task consisted of a backwards digit span task in which participants are asked to read a series of numbers and repeat them from memory starting with the last digit they read, and the WM consisted of a reading span task in which participants are asked to read and answer a series of true or false statements, remember the last word of each statement, and type the last words of each statement from memory.^{11,12}

Results Obtained

We surveyed 125 participants ranging in age from 14-74 ($M = 33.08$, $SD = 13.61$), were 75% female, and 64% of participants reported being diagnosed with one or more chronic conditions. Of those participants diagnosed with a chronic condition, 33.6% self-identified as shift workers. 12.8% of participants self-identified as shift workers without a chronic condition, while 23.2% of participants identified as non-shift workers with no chronic conditions.

To test our hypotheses, we utilized a Oneway ANOVA. We found significant differences between groups in mean scores of overall general health ($F(3, 118) = 11.71$, $p = .001$), mean bodily pain reported in the past 4-weeks ($F(3, 119) = 22.13$, $p = .001$), the number of health limiting activities reported ($F(3, 117) = 5.34$, $p = .002$) (Table 1), the number of pain limiting activities reported ($F(3, 63) = 7.79$, $p = .001$) (Figure 1, Table 2), quality of sleep during the past month ($F(3, 116) = 7.65$, $p = .001$), scores on the WM task ($F(3, 121) = 3.04$, $p = .032$), and self-reported severity of pain rated during the time in which the survey was taken ($F(3, 95) = 12.89$, $p = .001$) (Figure 2). Interestingly, we found no significant differences between groups on scores on the STM task ($F(3, 121) = 0.357$, $p = .784$) or subjective cognitive symptoms ($F(3, 59) = 1.07$, $p = .367$), which we have reported in previous studies.¹³ We performed a post hoc test (Tukey) to determine the differences between groups. Significant differences were found between the shift worker without chronic conditions and shift workers with chronic condition groups in overall general health ($p = .034$), bodily pain reported in the past four weeks ($p = .001$), quality of sleep ($p = .041$), health limiting activities ($p = .041$), pain limiting activities ($p = .043$), and the severity of pain rated in the moment the survey was taken ($p = .001$). Interestingly, significant differences were only found between shift workers without chronic conditions and non-shift workers without chronic conditions on scores of the WM task ($p = .001$).

We additionally ran correlation analyses to determine the relationships between our variables of interest. Notably, we found negative correlations between WM and past month pain ($r = -.318$, $p = .001$) (Figure 3), past month sleep ($r = -.296$, $p = .001$) (Figure 4), pain limiting activities ($r = -.302$, $p = .001$), and pain in the current moment ($r = -.279$, $p = .005$) (Figure 5). We also found relationships between the number of cognitive symptoms reported and pain in the past month ($r = .564$, $p = .001$) (Figure 6), pain limiting activities ($r = .427$, $p = .002$) (Figure 7), and general health ($r = .362$, $p = .004$).

Significance and Interpretation of Results

Our results indicate that shift workers with chronic conditions report significantly worse general health than shift workers without a chronic condition and report significantly more bodily pain. Additionally, shift workers with chronic conditions report significantly poorer sleep quality. Shift workers without chronic conditions performed significantly worse on the WM task than non-shift workers without chronic conditions; no significant differences were found in either WM performance or STM performance between shift workers with chronic conditions and shift workers without chronic conditions. Additionally, shift workers with chronic conditions report more pain limiting activities than shift workers without chronic conditions; however, shift workers without chronic conditions report more health limiting activities than shift workers with chronic conditions. From these results, we can

generally conclude that shift workers with chronic conditions experience more health-related issues than shift workers without chronic conditions but do not experience more cognitive issues as predicted.

Our results regarding poor WM performance in shift workers is aligned with previous research on the topic with the same results.^{14,15} Intriguingly, a large body of literature exists that reports that those with inflammatory chronic conditions experience deficits in WM performance that we did not observe in this study; this could possibly be explained by the large amount of chronic conditions represented in our sample.^{16,17} Additionally, results showing that pain influences WM performance and cognitive symptoms are similar to previous results in the literature.^{18,19} Finally, our results indicating that shift workers with chronic conditions experience more health and pain limiting activities aligns with research that chronic conditions relate to lower quality of life.²⁰

One of the main limitations of our study is the small sample size of shift workers. Additionally, this study took place during the ongoing COVID-19 pandemic which possibly could have impacted participants' ratings of overall health, pain, and sleep quality, especially if they were a shift worker working in essential settings, such as a hospital. Utilizing one time point may have also been detrimental to this study as shift workers often rotate shifts which can contribute to fluctuations in cognitive performance and health related domains.

Overall, our study begins to investigate how shift work can impact those with chronic conditions. This study attempts to answer some preliminary questions about shift work and chronic conditions as the field currently lacks research understanding the complex relationship between shift work and chronic conditions. Future research should continue to investigate potential deficits in cognition in shift workers with chronic conditions as well as how shift work contributes to physiological manifestations of disease in those with chronic conditions. Finally, future research may benefit from using a longitudinal design to investigate fluctuations in cognition and health as workers rotate shifts.

Figures

Figure 1. Differences between groups on pain limiting activities.

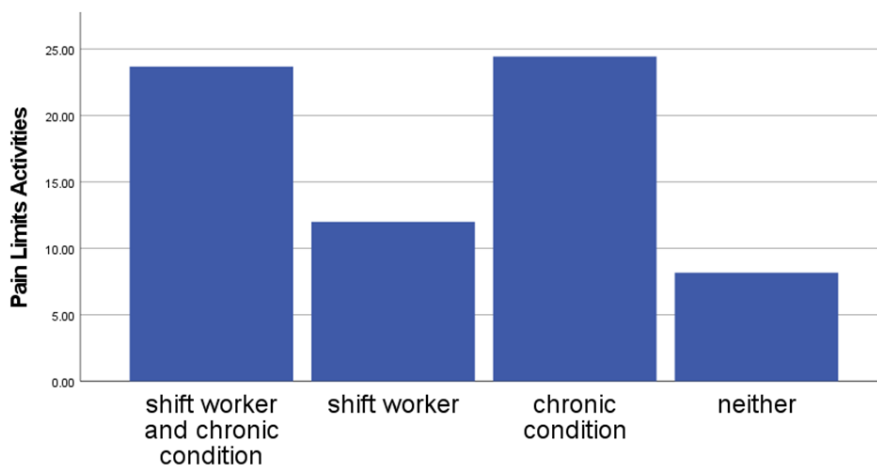


Figure 2. Differences between groups on pain felt in the moment taking the survey.

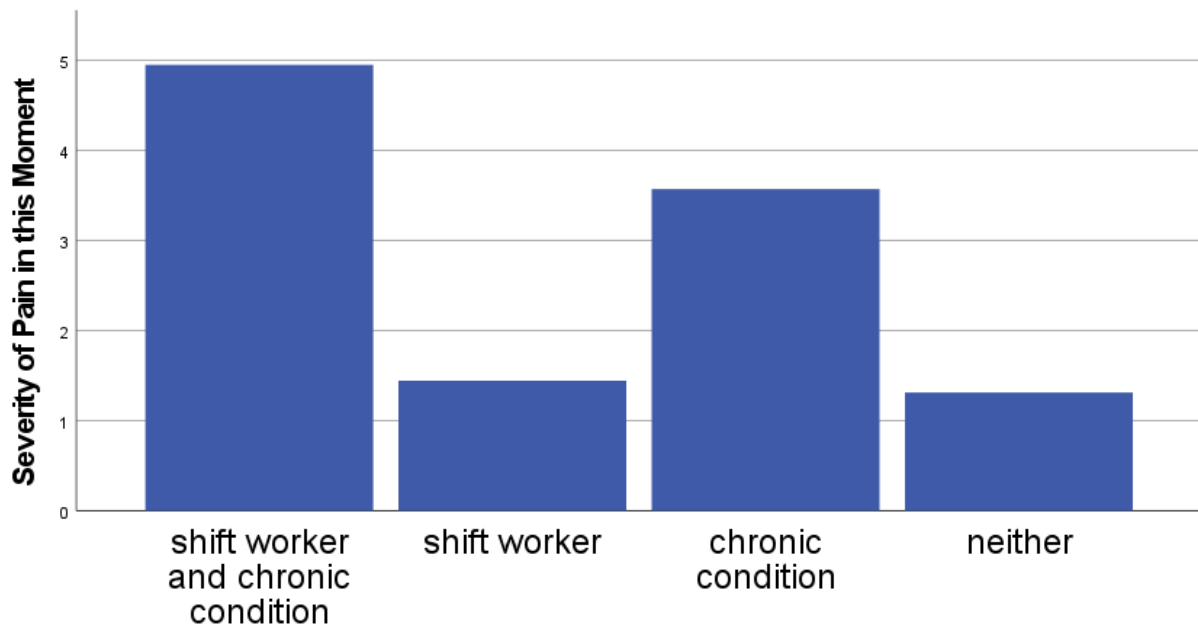


Figure 3. Differences between groups on pain reported in the past month.

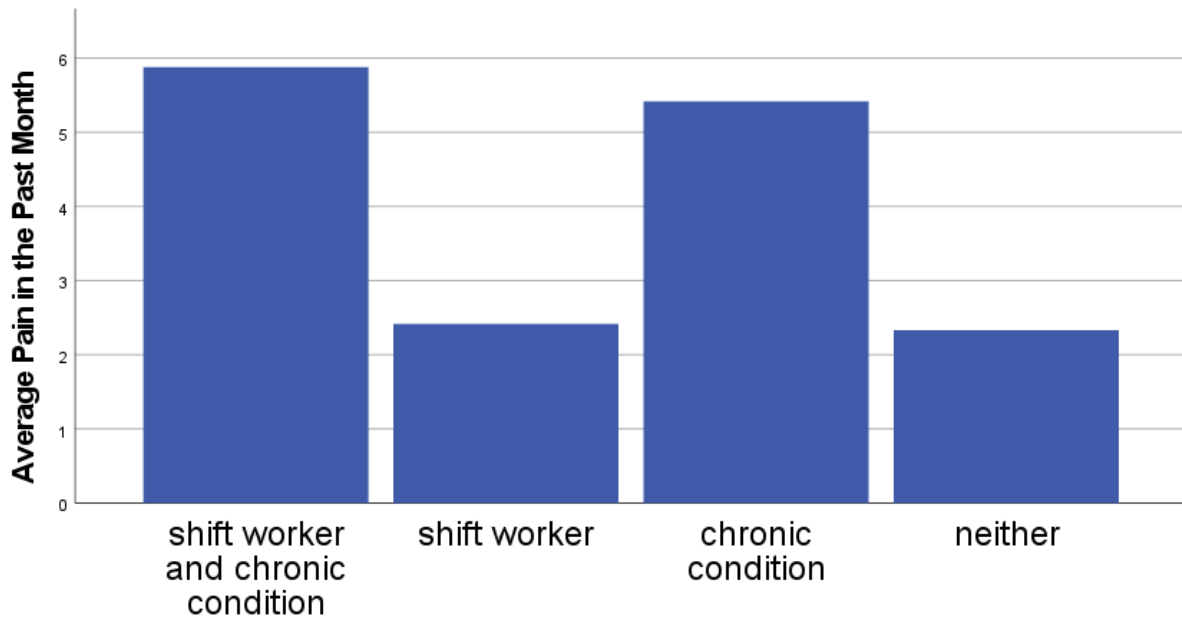


Figure 4. Correlation between WM performance and past month sleep quality.

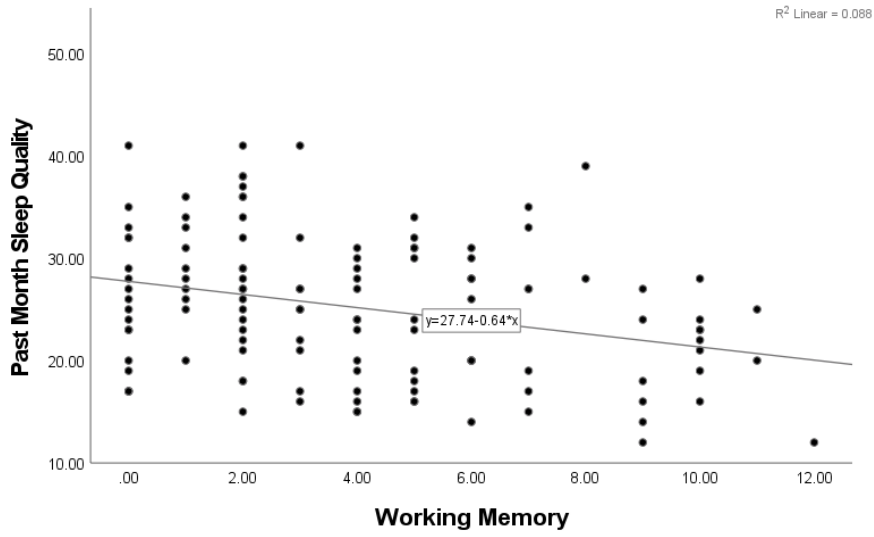


Figure 5. Correlation between WM performance and pain reported in the moment.

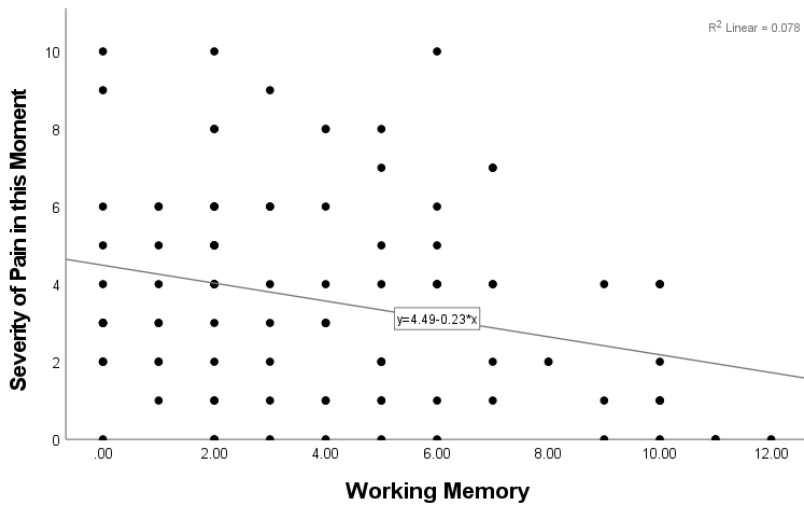


Figure 6. Correlation between cognitive symptoms reported and pain in the past month.

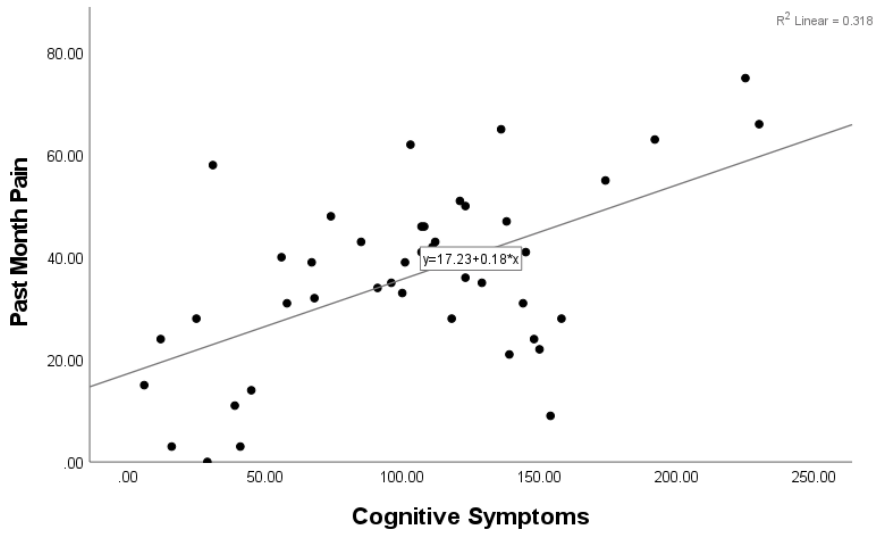
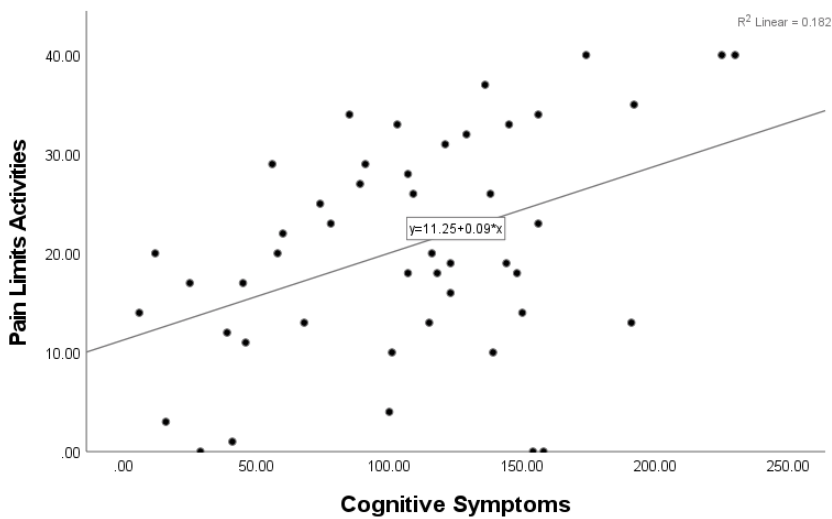


Figure 7. Correlation between cognitive symptoms reported and pain limiting activities.



Tables

Table 1. Health limiting activities.

Health Limiting Activities
Vigorous activities, such as running, lifting heavy objects, participating in strenuous sports
Moderate activities, such as moving a table, pushing a vacuum cleaner, bowling, or playing golf
Lifting or carrying groceries
Climbing several flights of stairs
Bending, kneeling, or stooping
Walking more than one mile
Walking one block
Bathing or dressing yourself

Table 2. Pain limiting activities.

Pain Limiting Activities
Working performance
Capability to move
Social role
Sports activity
Mood
Interpersonal relationships
Sleep
Pleasure of living

References

1. Moreno, C.R.C., Marqueze, E.C., Sargent, C., Wright Jr., K.P., Ferguson, S.A., & Tucker, P. (2019). Working Time Society consensus statements: Evidence-based effects of shift work on physical and mental health. *Industrial Health, 57*, 139-157.
2. Puttonen, S., Oksanen, T., Vahtera, J., Pentti, J., Virtanen, M., Salo, P., & Kivimäki, M. (2010). Is shift work a risk factor for rheumatoid arthritis? The Finnish Public Sector study. *Annals of the Rheumatic Diseases, 69*, 679-680.
3. Hedström, A.K., Åkerstedt, T., Hillert, J., Olsson, T., & Alfredsson, L. (2011). Shift work at young age is associated with increased risk of multiple sclerosis. *Annals of Neurology, 70*, 733-741.
4. Magrini, A., Pietroiusti, A., Coppeta, L., Babucci, A., Barnaba, E., Papadia, C., ... & Bergamaschi, A. (2006). Shift work and autoimmune thyroid disorders. *International Journal of Immunopathology and Pharmacology, 19*, 31.
5. Elhami Athar, M., Atef-Vahid, M., & Ashouri, A. (2020). The influence of shift work on the quality of sleep and executive functions. *Journal of Circadian Rhythms, 18*.
6. Hays, R.D. & Morales, L.S. (2001). The RAND-36 measure of health-related quality of life. *Annals of Medicine, 33*, 350-357.
7. Buysse, D.J., Reynolds III, C.F., Monk, T.H., Berman, S.R., & Kupfer, D.J. (1988). The Pittsburgh Sleep Quality Index: A new instrument for psychiatric practice and research. *Psychiatry Research, 28*, 192-213.
8. Preti, A., Stocchino, S., Pinna, F., Deidda, M.C., Musu, M., Sancassiani, F., ... & Carta, M.G. (2019). BEEP – Bodily and emotional perception of pain. A questionnaire to measure reaction to pain in chronic pain disorders. *Frontiers in Psychology, 10*, 480.
9. Rosenthal, L., Roehrs, T.A., & Roth, T. (1993). The Sleep-Wake Activity Inventory: A self-report measure of daytime sleepiness. *Biological Psychiatry, 34*, 810-820
10. Ottati, A., & Feurestein, M. (2013). Brief self-report measure of work-related cognitive limitations in breast cancer survivors. *Journal of Cancer Survivorship, 7*, 262-273.
11. Wechsler, D. (1981). Wechsler Adult Intelligence Scales – Revised (WAIS-R), Psychological Corporation, New York.
12. Daneman, M. & Carpenter, P.A. (1980). Individual differences in working memory and reading. *Journal of Verbal Learning and Verbal Behavior, 19*, 450-466.
13. Shasteen, H.D. & Blasiman, R.N. (2020). The role of sunlight exposure in tasks of inhibition in patients with systemic lupus erythematosus. *NASA/Ohio Space Grant Consortium 2019-2020 Annual Student Research Symposium Proceedings XXVIII*, 261-265.
14. McHill, A.W. & Wright Jr., K.P. (2019). Cognitive impairments during the transition to working at night and on subsequent night shifts. *Journal of Biological Rhythms, 34*, 432-446.

15. Cheng, P., Tallent, G., Brender, T.J., Tran, K.M., & Drake, C.L. (2017). Shift work and cognitive flexibility: Decomposing task performance. *Journal of Biological Rhythms*, *32*, 143-153.
16. Shucard, J.L., Parrish, J., Shucard, D.W., McCabe, D.C., Benedict, R.H.B., & Ambrus Jr., J. (2004). Working memory and processing speed deficits in systemic lupus erythematosus as measured by the paced auditory serial addition test. *Journal of the International Neuropsychological Society*, *10*, 35-45.
17. Kennedy, P.J., Clarke, G., O'Neill, A., Groeger, J.A., Quigley, E.M.M., ... & Dinan, T.G. (2014). Cognitive performance in irritable bowel syndrome: Evidence of a stress-related impairment in visuospatial memory. *Psychological Medicine*, *44*, 1553-1566.
18. Smith, A. & Ayres, P. (2014). The impact of persistent pain on working memory and learning. *Educational Psychology Review*, *26*, 245-264.
19. Attridge, N., Noonan, D., Eccleston, C., & Keogh, E. (2015). The disruptive effects of pain on n-back task performance in a large general population sample. *Pain*, *156*, 1885-1891.
20. Zheng, D.D., McCollister, K.E., Christ, S.L., Lam, B.L., Feaster, D.J., & Lee, D.J. (2020). Chronic condition patterns in the US population and their association with health related quality of life. *Preventive Medicine: An International Journal Devoted to Practice and Theory*, *136*.

Investigating Technology Leading to the Design of a High Altitude Ballooning Platform

Student Researcher: Armani D. Shelton

Advisor: Augustus Morris, Jr., Ph.D., P.E.

Central State University
Manufacturing Engineering

Abstract:

Exploration of the upper atmosphere and near space has become increasingly affordable for students at all levels over the last 20 years. Thanks to modern technology, instrumentation and communications needed to support scientific ballooning missions have become miniaturized, reliable, and affordable. Dubbed by some as the poor man's space program, it is now possible to conduct real science at near space altitudes for less than \$1000. Central State University is revisiting high altitude ballooning as a means to attract students toward, and choose careers in, the STEM fields. Working toward this goal, understanding the basic instrumentation necessary to measure key atmospheric variables is required if custom payloads are designed with such instrumentation. Knowing the range of environmental conditions encountered during a flight at altitudes up to 100,000 feet is necessary in order to protect the instrumentation on such missions.

Project Objectives:

There are several objectives to accomplish for this project:

1. Understanding of the variation of the Earth's atmosphere from sea level to an altitude of 100,000 feet.
2. A listing of key atmospheric variables to be monitored during a balloon flight.
3. Development of appropriate sensors and supporting electronics needed to build instrumentation with the capacity to measure the full range of variation of atmospheric variables during the flight.

Methodology Used:

A search through appropriate literature and references has provided a good foundation on the changes that occur in temperature and pressure in the troposphere and stratosphere of the Earth. Near space is defined at altitudes in the stratosphere beginning around 30 km.

Key variables used in weather monitoring and other atmospheric research include temperature and air pressure. These are the chosen variables to be monitored on balloon missions at Central State University.

A number of sensors are available capable of measuring temperature and pressure. However, these sensors require supporting electronics to ensure its measurements are calibrated and spans the range of the desired variables.

Results Obtained:

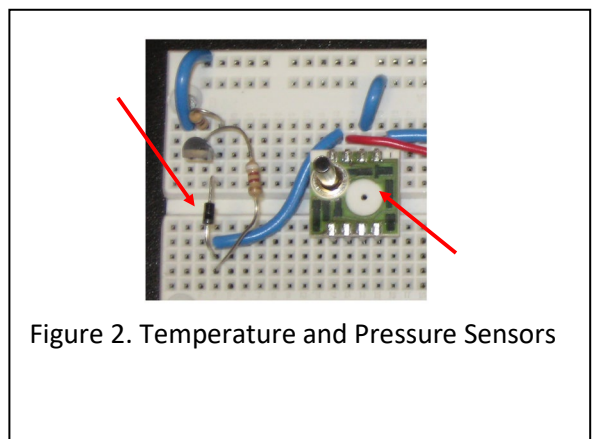
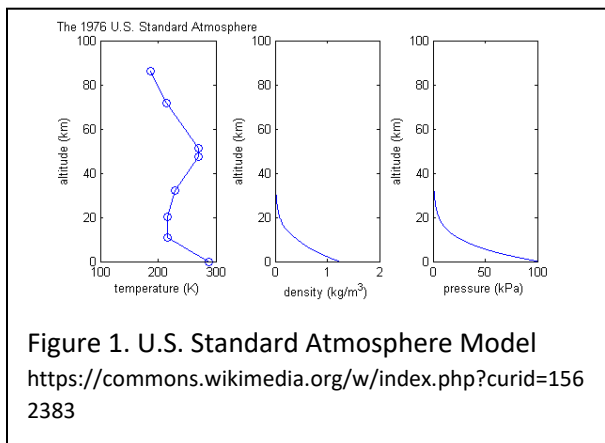
Figure 1 shows how temperature, pressure, and density changes as the altitude increases from sea level. Air density decreases with altitude. Air pressure ranges from around 1000 mbars at sea level to nearly 0 mbars at near space altitudes. In contrast, the temperature decreases with altitude near the Earth's

surface, but then temperature begins to increase in the stratosphere. Of particular note, the temperature during a journey to near space can reach lows of -40C. Figures 2 shows a temperature and pressure sensor along with supporting circuitry and instrumentation.

Significance and Interpretation of Results:

The next phase of this effort will focus on designing payload structures to enclose and protect the instrumentation from the extremes in atmospheric conditions. An embedded system will be considered to coordinate the instrumentation and provide storage of the data collected. When an appropriate communication and tracking system is decided on, the critical instrumentation is in place to plan and execute a high altitude balloon mission.

Figures/Charts:



Acknowledgments:

This work would not be possible without the support of the Ohio Space Grant Consortium, the Manufacturing Engineering Department at Central State University, and my advisor, Dr. Augustus Morris.

References:

Larson S.L., Armstrong J.C. and W. A. Hiscock. The First Frontier: High Altitude Ballooning as a Platform for Student Research Experiences in Science and Engineering, American Journal of Physics 77(489) June 2009.

Thrust Generation Due to Turbofan Fan Blade Assembly as It Relates to Free-Stream Velocity

Student Researcher: Branden S. Stoeffler

Advisor: Dr. Jed E. Marquart

Ohio Northern University
Mechanical Engineering

Abstract

The vast majority of commercial aircraft today utilize turbofan engines. A turbofan engine works by using a fan to draw air into the engine. The air is then compressed by using an axial-flow compressor. Next, the compressed air is passed into the combustion chamber where it is mixed with jet fuel and combusted. The exhaust from the combustion is then passed through a turbine, which makes the turbine capable of rotating, which rotates the compressor and the fan. Finally, the exhaust is passed out through a nozzle in the rear of the engine. This process allows the turbofan engine to create thrust.

Project Objective

This project will examine how much trust is created by the fan portion of the turbofan engine based on the free-stream velocity of air entering into the turbofan engine while the fan is rotating at a constant angular velocity.

Methodology

The ability of a turbofan engine to create thrust is given by the relationship between mass flowrate and fluid velocity at various locations in the turbofan engine. The total thrust of a turbofan engine is given by Equation 1 [1].

$$F_T = \dot{m}_e v_e - \dot{m}_0 v_0 + BPR(\dot{m}_c v_f) \quad (1)$$

Where:

\dot{m}_e is the mass flowrate of the fluid exhaust after combustion

v_e is the velocity of the fluid exhaust after combustion

\dot{m}_0 is the mass flowrate of the fluid entering the turbofan engine

v_0 is the free-stream velocity of the fluid entering into the turbofan engine

BPR is the bypass ratio of turbofan engine

\dot{m}_c is the mass flowrate of the fluid entering in the core of the engine

v_f is the velocity of the fluid that bypasses the engine core

In order to determine the thrust generated by the fan itself, several manipulations of Equation 1 were made. Firstly, because only the trust generated by the fan was being examined, the mass flowrate and the velocity of the fluid exhaust after combustion could be neglected. Secondly, the definition of the bypass ratio was substituted into Equation 1. These manipulations yield Equation 2.

$$F_T = -\dot{m}_0 v_0 + \left(\frac{\dot{m}_f}{\dot{m}_c}\right)(\dot{m}_c v_f) \quad (2)$$

Where:

\dot{m}_f is the mass flowrate of the fluid that bypasses the engine core

Simplifying Equation 2 yields Equation 3 which can be used to calculate the thrust generated by the fan itself.

$$F_{T_{fan}} = \dot{m}_f v_f - \dot{m}_0 v_0 \quad (3)$$

In order to determine mass flowrate and velocity of the fluid after it passes through the fan, a CFD analysis was used. The first step in this process was to create a CFD grid using a 3D model obtained through GrabCad [2]. In order to accomplish that, a mesh generating software called *Pointwise* was used. Once the turbofan blade grid was constructed, a wake field and flow box were created around the turbofan blade. Next, a series of boundary conditions were assigned to the grid. The turbine blades were set to be "Wall (general no slip)" and the flow box was set to be "Farfield (modified Riemann)". The grid file was then exported to be run in the flow solver, *Cobalt*. In order to determine the relationship between the thrust generated by the fan and the free-stream velocity, two separate cases were run. The Turbulent Navier Stokes Equations were used to solve each case. Each case was also run with an angle of attack of zero degrees and an angle of side slip of zero degrees. The temperature for each case was set at 288.15 Kelvin and the pressure was set at 101.325 kPa. The fan blade was rotating at a constant 3,000 rpm for each case. The free-stream velocities for each of the two cases were Mach 0.405 and Mach 0.660, respectively. The results were then examined in the post-processing software, *Fieldview*.

Results Obtained

When a free-stream velocity of Mach 0.405 entered into the fan blade assembly, the outlet velocity decreased slightly to Mach 0.376. The density of the fluid decreased from $1.23 \frac{kg}{m^3}$ at the inlet to $1.15 \frac{kg}{m^3}$ at the outlet of the fan assembly. The resulting generated thrust was approximately 5,530 Newtons. When a free-stream velocity of Mach 0.660 entered into the fan blade assembly, the outlet velocity decreased to Mach .585. The density of the fluid decreased from $1.23 \frac{kg}{m^3}$ at the inlet to $1.11 \frac{kg}{m^3}$ at the outlet of the fan assembly. The resulting generated thrust could be calculated to be approximately 22,015 Newtons.

Significance and Interpretation of Results

As the free-stream velocity increases, the thrust generated by the turbofan blade assembly increases as well. However, the relationship between free-stream velocity and thrust generated is not linear. A 63% change in the free-stream velocity resulted in a 298% change in the generated thrust. In order to further this research, it would be necessary to generate a function that relates free-stream velocity with the generated thrust by this particular fan assembly. However, many more cases would have to be run with various free-stream velocities. While this information is pertinent when designing an engine that produces an adequate amount of thrust to support its mission, it would be quite difficult to develop a generalized relationship for all types of fan blade assemblies due to the fact that the geometry and angle of attack of the blades also has a great deal of effect on exit velocity of the air as it passes through the fan.

Acknowledgements

I would like to thank the Ohio Space Grant Consortium for presenting me with the opportunity for conducting this research. I would also like to thank Dr. Marquart for providing guidance and expertise throughout the entirety of this project.

References

- [1] N. Hall, "Turbofan Thrust," National Aeronautics and Space Administration, 05 May 2015. [Online]. Available: <https://www.grc.nasa.gov/www/k-12/airplane/turbfan.html>. [Accessed 13 March 2021].
- [2] C. Shakal, "high bypass turbofan front fan (10:1 ratio)," GrabCad, 11 February 2012. [Online]. Available: <https://grabcad.com/library/high-bypass-turbofan-front-fan-10-1-ratio>. [Accessed 21 November 2020].

Wind-Resilience Via Physical Modeling Of Tornado Flows In Laboratory

Student Researcher: Kevin C. Stropki

Advisor: Dr. Zhiqiang Gao

Cleveland State University
Electrical Engineering and Computer Science

Abstract

In recent years, wind-related hazards in the United States have caused record-setting economic damage. Tornadoes have been the primary cause of this damage, with more personal and property damage being attributed to them than earthquakes and hurricanes combined. Traditional methods for testing wind loads on buildings and other structures are performed in low-speed boundary-layer wind tunnels that generate straight-line winds. To better understand the complex nature of tornado wind flow patterns on civil structures, Cleveland State University is designing a tornado simulator capable of producing tornado-like vortices. An existing tornado simulator at Iowa State University was identified as the basis of our design. The Iowa State Tornado Simulator (ISU-TS) was chosen based on its ability to reproduce full-scale data collected from established tornado research accurately. Through extensive literature reviews of the ISU-TS, a limitation was discovered in its ability to change the generated tornado-like vortex's diameter. To solve this problem and serve as a point of differentiation, the tornado simulator being designed at Cleveland State University will contain an advanced control system.

Project Objectives

This project's main objective is to have a working tornado simulator to be used for expanding the knowledge of the effects of tornado wind flow patterns on buildings and other structures. This research's starting point was to conduct literature reviews on existing tornado simulators and discover how well they can replicate an actual tornado's physics. Three simulators were identified as potential candidates to serve as the design framework, the Iowa State Tornado Simulator (ISU-TS), WindEEE Dome at Western, and Texas Tech University Simulator. Ultimately, it would be the ISU-TS's simplistic design coupled with its ability to recreate tangential and radial wind profiles similar to that measured in full-scale data that would deem it as the basis of our design. Currently, the focus of this project is on conducting literature reviews on airflow control systems.

Methodology

Due to the COVID-19 pandemic, the extent of this project's development was limited. Being unable to use the laboratories on campus, the physical development of this project has yet to begin; however, the project is currently conducting literature reviews to further the conceptual development.

Results

After a thorough review of literature on each of the three simulators, the ISU-TS provided the best framework for which we could implement an advanced closed-loop control system. The ISU-TS design is simple in nature, and it creates tornado-like vortices by mimicking a phenomenon of tornadogenesis called rear-flank-downdrafts. This is achieved by a dual concentric duct system in which a centrally

located fan forces air up through turning vanes and is then forced downward through the downflow duct. As the airflows out of the downflow duct, it converges towards the center, creating a rotating downdraft[1]. The rotating downdraft is then sucked up by the fan through a honeycomb section positioned directly below the fan, straightening the incoming air. The ISU-TS is suspended over a ground plane by a crane, allowing the tornado-like vortices to be translated across the surface up to 0.61 m/s. Having these capabilities is useless if the simulator is unable to accurately replicate data found from field studies, so our research team is looking into how well the ISU-TS could replicate data collected from the VORTEX Project[2]. The findings came from a paper by Haan Jr et al., in this study, they set to replicate radar data collected from the Spencer and Mulhall tornados. It was concluded that the ISU-TS is capable of creating tangential and radial velocities similar to that measured from the full-scale data[1]. The ISU-TS relatively inexpensive and straightforward design coupled with its ability to re-create flow conditions from full-scale data was the distinguishing factor in choosing this design for our simulator.

Significance and Interpretation of Results

Having the capability of creating tornado-like vortices in a laboratory can provide researchers and engineers with valuable information, particularly concerning the effects of tornado-like winds and aerodynamic loads on buildings.

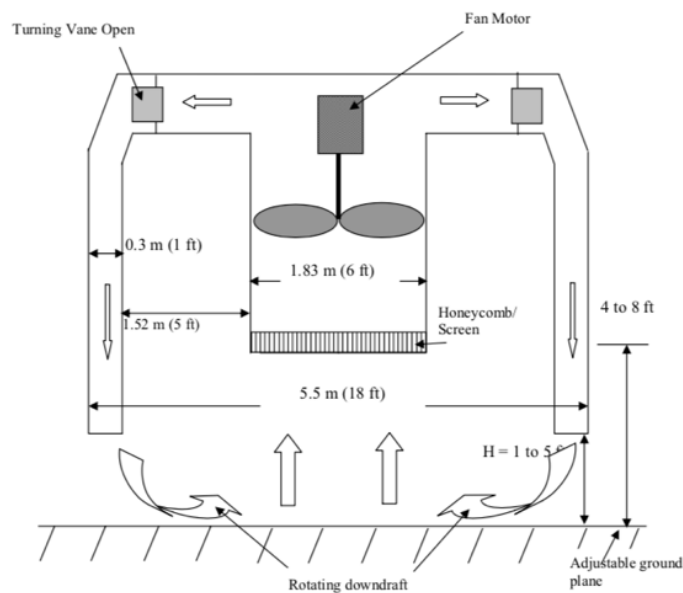


Figure 1. Schematic illustration of the ISU-TS[2]

References

- [1] F. L. Haan, P. P Sarkar, W. A. Gallus, "Design, Construction and performance of a large tornado simulator for wind engineering applications," *Engineering Structures*, Volume. 30 no. 3, Sept., pp. 116-1159, 2008.
- [2] Y. Fangping, et al, "Numerical simulation of laboratory tornado simulator that can produce translating tornado-like wind flow," *Journal of Wind Engineering & Industrial Aerodynamics*, Volume. 190, April, pp. 200-217, 2019.

Investigation Of Proper Scaling Of Screech Frequency For Low Aspect Ratio Supersonic Rectangular Jets

Student Researcher: Jack C. Tyszkiewicz

Advisors: Dr. Mo Samimy and Dr. Nathan Webb

The Ohio State University
College of Engineering

Abstract

Screech is a high amplitude, highly directional discrete frequency in the acoustic signature of supersonic jets issued from circular or rectangular nozzles. Strouhal number, St , is a dimensionless unit used to express screech frequencies and if scaled properly, it allows comparison of data between facilities and various geometry nozzles. Throughout literature on screeching rectangular jets, various characteristic length scales have been used in expressing St without clear agreement on which should offer the best collapse of data. An empirical investigation of three commonly used scaling lengths was performed. It was found that geometrical equivalent diameter (D_e) and pressure loss equivalent diameter (D_{ep}) offered the best collapse of data among low aspect ratio rectangular nozzles, while another scaling length such as nozzle exit height (h_e) may be preferred for high aspect ratio nozzles.

Project Objectives

Screech is a high amplitude acoustic tone seen in both circular and rectangular supersonic jets. Screech is formed by a four component feedback loop consisting of (i) a downstream propagating hydrodynamic perturbation, (ii) a generation process (often considered to occur at the third or fourth or fifth shock cell) in which an upstream propagating acoustic wave is generated from the formerly downstream propagating hydrodynamic wave, (iii) the upstream propagation of an acoustic wave to a point where the base flow is sensitive to perturbation (i.e. where the shear layer is thinnest at the nozzle lip), and (iv) the production of new downstream propagating Kelvin-Helmholtz instability waves at the nozzle lip where the shear layer is highly sensitive to perturbation at a specific frequency. This forms a self-sustaining feedback loop that adopts a specific frequency and generates high amplitude, highly directional discrete-frequency acoustic tones [1]. Much of the work done at the Gas Dynamics & Turbulence Lab (GDTL) at the Ohio State University is done to control various components of this screech feedback cycle and mitigate noise from screeching supersonic jets.

In analyzing acoustic signatures across the frequency domain, fluid dynamitists employ the use of a dimensionless parameter, St , or Strouhal number. Strouhal number is given as below,

$$St = \frac{fL}{U} \quad (1)$$

where f is frequency, L is characteristic length, and U is flow velocity. While in a circular jet the characteristic length is the nozzle exit diameter, various characteristic length scales have been used across literature for rectangular jets, with no clear agreement on what should provide the best collapse for comparison between facilities. There is nothing more paramount in research than consistent and repeatable results, and it is crucial for these results to be universal to any facility. An empirical investigation of the proper characteristic length scale for low aspect ratio (AR) screeching rectangular nozzles was performed with the ultimate goal of verifying the accuracy of data obtained for a screeching converging-diverging rectangular nozzle of AR 2 and design Mach number of 1.5 being studied at the GDTL.

Methodology Used

A converging-diverging rectangular nozzle of AR 2 and design Mach of 1.5 with nozzle height (the smaller dimension), h_e , of 12.065 mm was studied. A Mach sweep of fully expanded Mach numbers, M_j , from 1.10 to 1.85 in increments of 0.05 was performed and a near-field microphone array was used to measure the screech frequency. Six microphones were located at $x/D_e = 0$ and $r/D_e = 4$ (7.3 cm from nozzle centerline) and were oriented as seen in Figure 1a. The signals obtained were processed using a signal conditioner with a gain of 1 mV/Pa. 100 blocks of 32,768 samples at 200 kHz were acquired for each case. It was found that screech began at M_j of 1.20 and continued throughout the rest of the Mach sweep. From the microphone data, spectra of SPL (sound pressure level) vs. frequency were generated at each Mach number (an example spectrum is provided in Figure 1b). Screech peaks were then identified and the discrete frequency at which screech occurred in each Mach number was recorded. A data set of screech frequency vs. fully expanded Mach number was thus obtained.

Stagnation temperature, T_0 , data was recorded throughout the Mach sweep, allowing calculation of fully expanded temperature as follows,

$$T_j = \frac{T_0}{1 + 0.2M_j^2} \quad (2)$$

From this, fully expanded jet velocity, U_j , could then be calculated as,

$$U_j = M_j \sqrt{1.4 * 287 * T_j} \quad (3)$$

All screech frequency (f_s) data in Hz was then converted into dimensionless Strouhal form as,

$$St_L = \frac{f_s L}{U_j} \quad (4)$$

where L is the characteristic length scale used in collapsing the data. Three length scales were studied: h_e , D_e , and D_{ep} . These length scales will be discussed below.

The geometrical equivalent diameter, D_e , represents the diameter of a circular shape with the same area as the rectangular shape and is found as,

$$D_e = 2 \sqrt{\frac{h_e * w}{\pi}} \quad (5)$$

where h_e is the dimension along minor axis and w is the dimension along major axis of the rectangular nozzle at the nozzle exit.

D_{ep} is based on the Huebscher definition of the diameter a circular duct that for equal flow gives the same pressure loss as an equivalent rectangular duct such that,

$$D_{ep} = \frac{1.30(h_e * w)^{0.625}}{(h_e + w)^{0.25}} \quad (6)$$

Data provided in literature from other labs where rectangular nozzles had been studied was compiled and reduced back into screech frequency (f_s in Hz) vs. Mach number data. Each of these data sets was then converted into three Strouhal data sets with different characteristic length scales used: St_{h_e} , St_{D_e} , and $St_{D_{ep}}$. All data sources were then plotted on the same St_L vs. M_j graphs to find which length scale offered the best collapse of data.

Results Obtained

From the Mach sweep, screech peaks were identified at each fully expanded Mach number from M_j of 1.20 to 1.85 using spectra obtained from the near-field microphone array data. Screech frequencies, f_s , were then recorded in Hertz for each respective fully expanded Mach number and are provided in Table 1. Data sets of screech frequency vs. Mach number were likewise obtained for other various geometry rectangular nozzles using data found in references [2] through [7]. The results from all the gathered data sets are shown in Figures 2 and 3. The data sets from the references were obtained from Figures 4a through 4f using the *grabit* MATLAB function. Each data set was then converted into non-dimensional Strouhal number data using each of the three possible characteristic length scales: h_e , D_e , and D_{ep} . The data sets for each St_L vs. M_j were plotted on the same graph to search for which length scale provided the best collapse. These plots are provided in Figure 2.

In looking at Figure 2, it is clear to an observer that characteristic length scales of D_e and D_{ep} offer a much better collapse of data across facilities and nozzles geometries than does h_e . In particular, low aspect ratio rectangular nozzles offer a great collapse of data when a characteristic length scale of D_e or D_{ep} is used. High aspect ratio nozzles, however, resist collapse for these cases but offer a better collapse to the use of jet exit height, h_e . In the cases of St_{D_e} and $St_{D_{ep}}$, disagreement of high aspect ratio nozzle data with low aspect ratio nozzle collapsed data tends to increase as aspect ratio is increased. Figure 3 shows only low aspect ratio rectangular nozzles using D_e as the collapsing length scale.

Significance and Interpretation of Results

Across literature, various characteristic length scales are used in characterizing screech from rectangular nozzles, seemingly at the discretion of the author. No clear agreement on the proper length scale for screeching rectangular nozzles had previously been established, making it difficult in comparing data from various geometry rectangular nozzles and among facilities that offer slightly different conditions.

This empirical study has helped to answer many of those concerns in demonstrating that characteristic length scales of D_e and D_{ep} offer an excellent collapse of low aspect ratio rectangular nozzle screech data. Importantly, this collapse occurs for data including a wide host of facilities and geometries including data from both converging and converging-diverging nozzles ranging from aspect ratio of 2 to 5. The data from this study was likewise critical in verifying the baseline data obtained from the GDTL nozzle is consistent with other studies before moving on to further experiments.

This author hopes that use of equivalent diameter, D_e , will become most common practice for St normalization in the future among low aspect ratio screeching rectangular nozzles to allow easier comparison of screech data for labs studying low aspect ratio nozzles. As for higher aspect ratio nozzles, jet exit height, h_e , or another length scale may offer the best collapse. Until further analysis is completed, the proper collapsing length scale for high aspect ratio rectangular nozzles remains unknown.

Figures

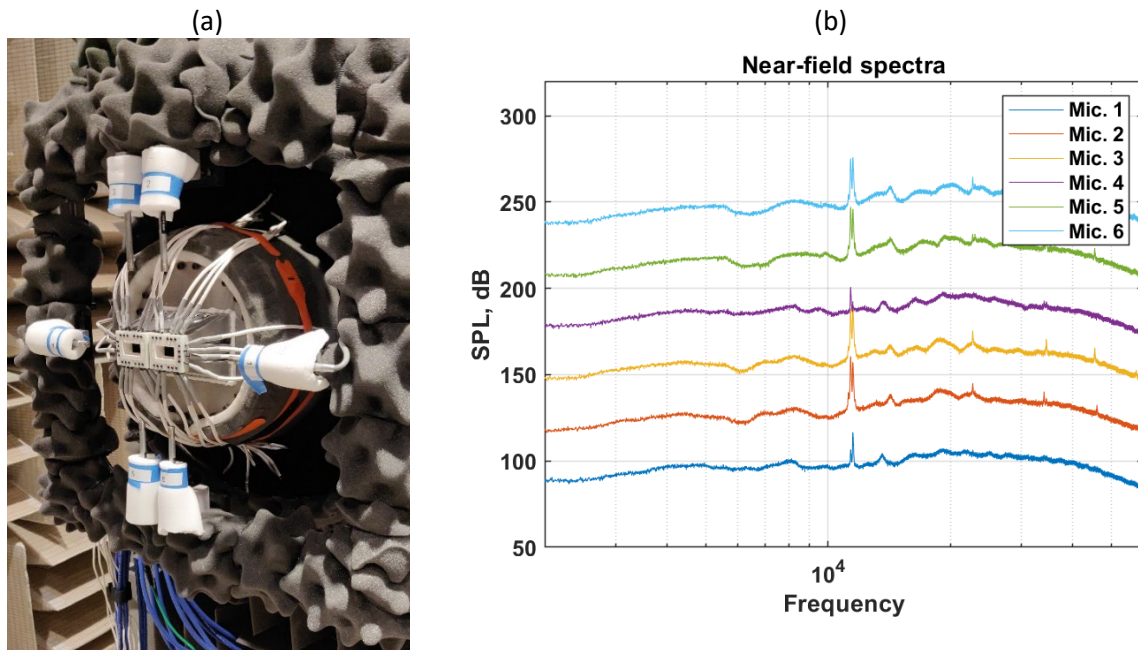
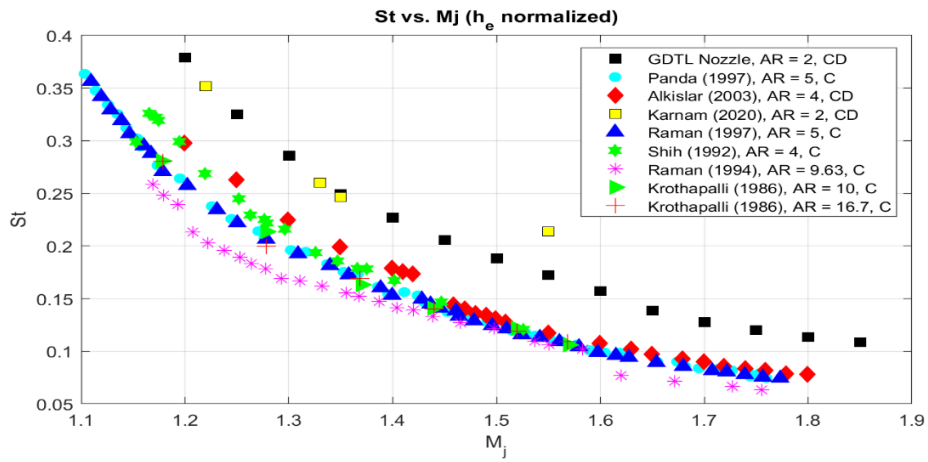


Figure 1: (a) Near-field microphone setup and (b) example spectra for $M_j = 1.20$

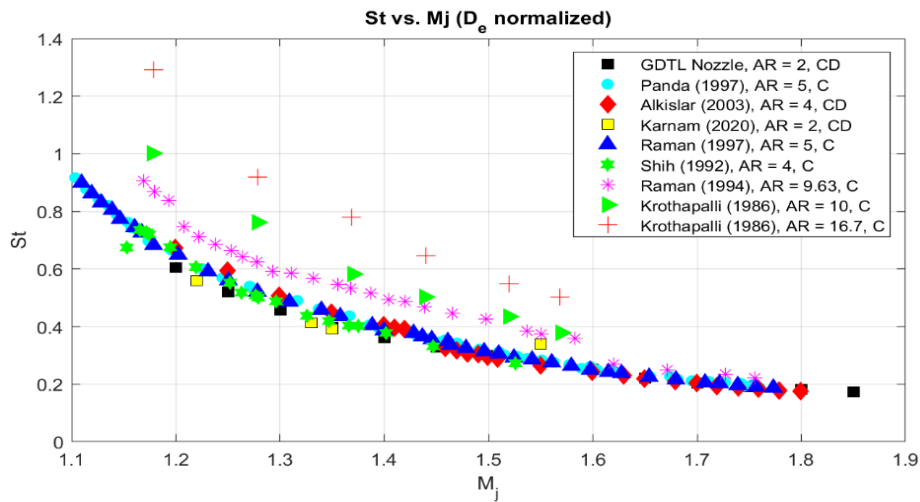
Table 1: GDTL Converging-Diverging Nozzle Data ($AR = 2$, $M_d = 1.5$)

M_j	F_s (Hz)	T_0 (in Celsius)
1.20	11,360	18.2
1.25	10,060	17.9
1.30	9,097	17.4
1.35	8,151	17.1
1.40	7,611	16.9
1.45	7,074	16.5
1.50	6,616	16.2
1.55	6,201	15.9
1.60	5,783	15.8
1.65	5,185	15.5
1.70	4,886	15.4
1.75	4,660	15.2
1.80	4,486	14.9
1.85	4,358	14.6

(a)



(b)



(c)

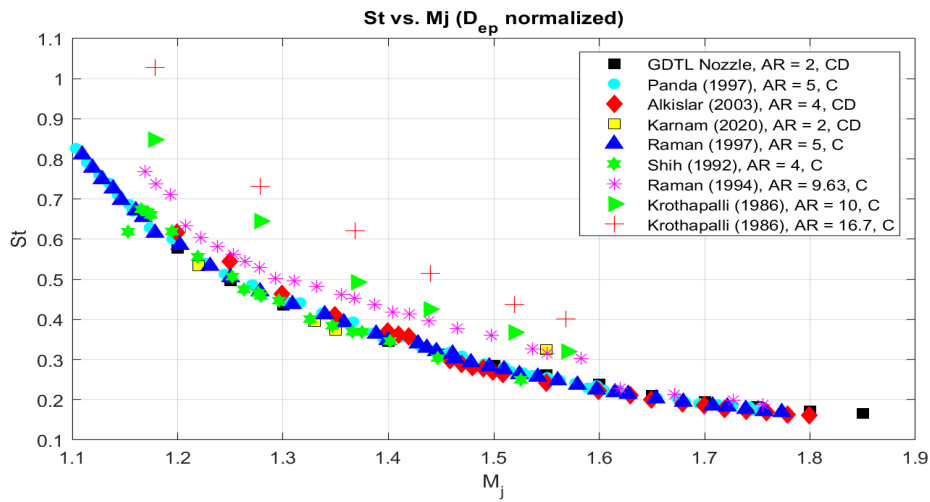


Figure 2: Strouhal number vs. fully expanded Mach number normalized with characteristic length scale of (a) jet exit height, (b) geometrical equivalent diameter, and (c) equivalent diameter based on pressure loss (Huebscher)

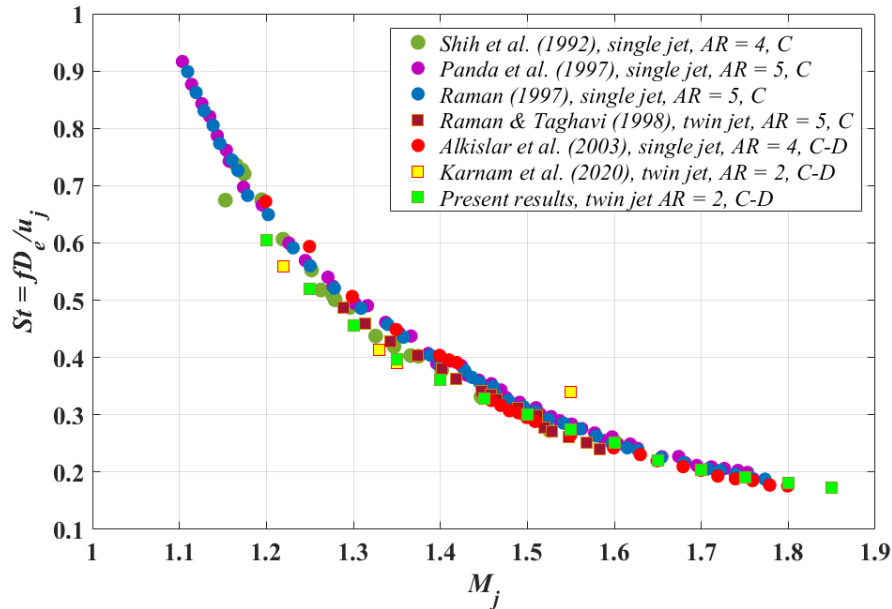


Figure 3: Low aspect ratio screeching rectangular nozzle data collapse with geometrical equivalent diameter as characteristic length scale

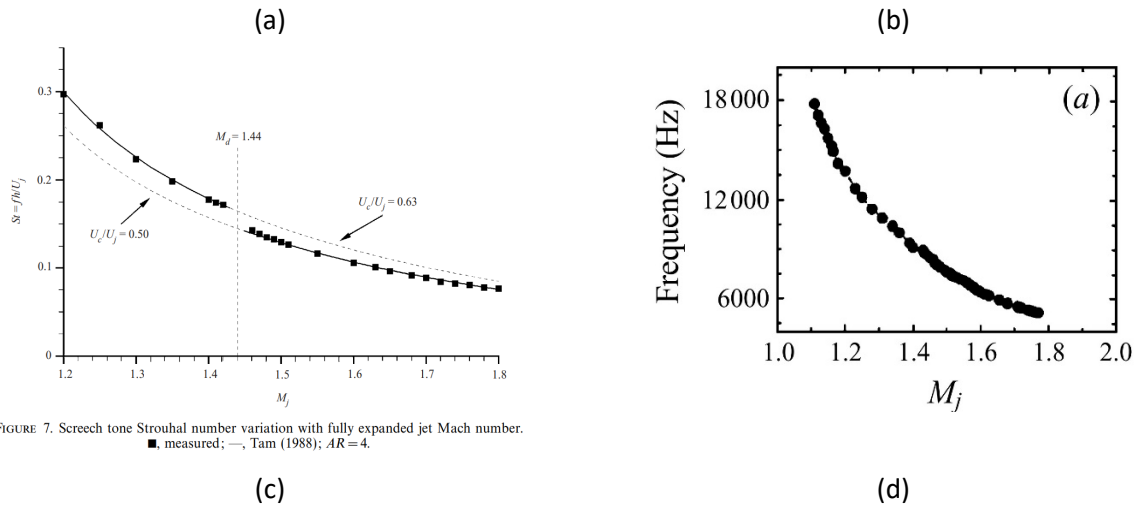


FIGURE 7. Screech tone Strouhal number variation with fully expanded jet Mach number. ■, measured; —, Tam (1988); AR=4.

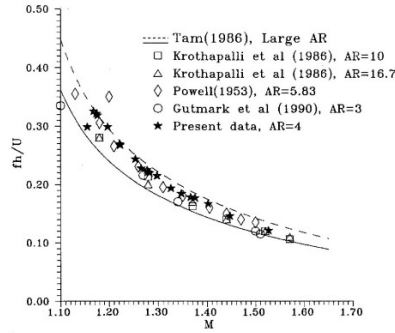


Fig. 18 Variation of the screech tone Strouhal number with the jet exit Mach number.

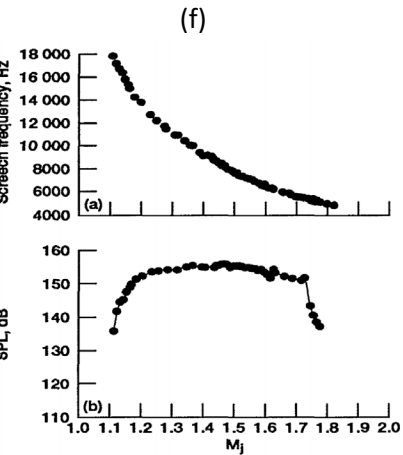
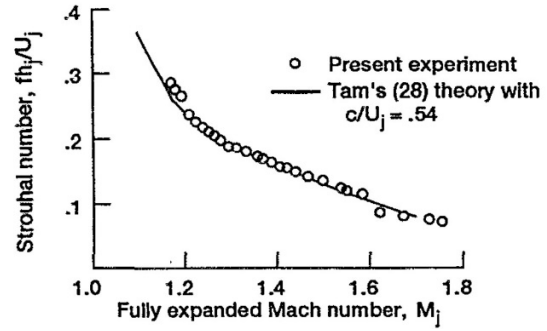


Figure 7. The variation of the fundamental frequency with pressure ratio. O, 3 mm nozzle; Δ, 5 mm nozzle; —, $St = R^{-3/2}$.

Figure 3.—(a) Screech frequency and (b) relative amplitude levels from a 5:1 aspect ratio rectangular nozzle.

- (a) Alkisar (2004) [2]; CD with AR = 4
- (b) Raman (1997) [3]; C with AR = 5
- (c) Shih (1992) [4]; C with AR = 4
- (d) Raman (1994) [5]; C with AR = 9.63
- (e) Krothapalli (1986) [6]; C with AR = 10, 16.7
- (f) Panda (1997) [7]; C with AR = 5

Figure 4: Data from different facilities and geometries used in St collapse comparisons

Acknowledgements and References

- [1] Edgington-Mitchell, Daniel. "Aeroacoustic Resonance and Self-Excitation in Screeching and Impinging Supersonic Jets – A Review." *International Journal of Aeroacoustics*, vol. 18, no. 2-3, 2019, pp. 118–188., doi:10.1177/1475472x19834521.
- [2] Alkisar, Mehmet B., et al. "Structure of a Screeching Rectangular Jet: a Stereoscopic Particle Image Velocimetry Study." *Journal of Fluid Mechanics*, vol. 489, 2003, pp. 121–154., doi:10.1017/s0022112003005032.
- [3] Raman, Ganesh. "Cessation of Screech in Underexpanded Jets." *Aeroacoustics Conference*, 1997, doi:10.2514/6.1996-1719.

- [4] Shih, Chiang, et al. "Experimental Observations of Instability Modes in a Rectangular Jet." *AIAA Journal*, vol. 30, no. 10, 1992, pp. 2388–2394., doi:10.2514/3.11238.
- [5] Raman, Ganesh, and Edward Rice. "Instability Modes Excited by Natural Screech Tones in a Supersonic Rectangular Jets." *15th Aeroacoustics Conference*, 1994, doi:10.2514/6.1993-4321.
- [6] Krothapalli, A., et al. "The Role of Screech Tones in Mixing of an Underexpanded Rectangular Jet." *Journal of Sound and Vibration*, vol. 106, no. 1, 1986, pp. 119–143., doi:10.1016/s0022-460x(86)80177-8.
- [7] Panda, J., et al. "Underexpanded Screeching Jets from Circular, Rectangular and Elliptic Nozzles." *3rd AIAA/CEAS Aeroacoustics Conference*, 1997, doi:10.2514/6.1997-1623.
- [8] Karnam, Aatresh, et al. "Nature of Flow Field & Acoustics of Twin Supersonic Rectangular Jets." *AIAA Scitech 2020 Forum*, 2020, doi:10.2514/6.2020-0500.
- [9] Zaman, K. "Spreading Characteristics and Thrust of Jets from Asymmetric Nozzles." *34th Aerospace Sciences Meeting and Exhibit*, 1996, doi:10.2514/6.1996-200.

I would like to acknowledge and thank Dr. Mo Samimy, Dr. Nathan Webb, Ata Esfahani, and Andrew Sais. Their support and belief in me throughout the duration of this project has been unparalleled. Through their actions, I have learned what is required in the ever-lasting search for the truth and that we never stop learning. I would also like to thank OSGC for their financial support throughout this experience and their continued support of STEM.

Disruptions of the Oxytocin System Impacts Social Discrimination Behavior in Adult Mice

Student Researcher: Christopher P. Vadala

Advisor: Dr. Heather Caldwell

Kent State University
Biomedical Sciences

Abstract

Oxytocin (Oxt) is a nine amino acid neuropeptide produced in the paraventricular nucleus (PVN) and the supraoptic nucleus (SON) of the hypothalamus, the latter of which is part of the brain important to the regulation of behaviors critical for an animal's survival. Oxytocin is released at the level of the posterior pituitary to act peripherally and within the brain Oxt is released via its projections originating in the aforementioned brain regions. Oxt promotes social behaviors, including aggressive and maternal behaviors, and has only one identified receptor, the Oxtr. The Oxtr is a G-protein coupled receptor that is found in many locations important for the regulation of social behavior.

There are numerous brain regions that are important to the neural regulation of social behavior. Collectively, they are referred to as the social behavior neural network (SBNN). The Oxtr is one of the receptors found throughout this network, including regions such as, the lateral septum (LS), the bed nucleus of the stria terminalis (BNST), and the medial amygdala (MeA). Data from many species suggests that Oxt signaling through the Oxtr in many of these brain regions is important to the neural regulation of social behavior. For example, studies in mice with genetic, lifelong disruptions, of the Oxtr (Oxtr $-/-$) mice, have heightened intermale aggression. However, in these studies a resident-intruder test was used, which gives the experimental animal the "home cage" advantage as a new stimulus animal is placed into the experimental animal's cage. Thus, this test predominantly evaluates territorial aggression. What has not been specifically tested is whether or not Oxtr $-/-$ males will display heightened aggression in another type of behavioral context, such as a neutral arena. In this test, there is no "home-cage advantage", and offensive aggression can be separated from territorial aggression.

Beyond aggressive behavior, the Oxt system has a key role in social memory, with mice lacking Oxt or the Oxtr "forgetting" mice they have previously encountered. These data suggest that the Oxt system has to function in order for a social memory to function. While we know that Oxt action within the MeA is critical for the effective formation of social memory, previous work has not compared Oxt knockouts directly with

Oxtr $-/-$ mice, nor have there been comparisons made between the sexes, in measures of neuronal activation during social memory recall.

Based on the role of the Oxt system in both aggression and social memory, two research questions were generated. The first was whether proper functioning of the Oxtr was necessary for the modulation of aggression across social contexts. Based on this question, we hypothesized that Oxtr $-/-$ males would display heightened aggression in a neutral arena compared to wildtype controls (Experiment 1). The second was what brain regions are activated when a social memory is being recalled in mice with disruptions in their Oxt system. We hypothesized that there would be a decrease in neuronal activation in Oxt $-/-$ and Oxtr $-/-$ animals, as compared to controls, as well as a difference between males and females (Experiment 2).

Methodology

In Experiment 1, a neutral arena aggression test was used. Oxtr $-/-$ and control male mice, along with a stimulus animal were placed in a neutral cage and allowed to interact for five minutes on three consecutive days. The behaviors of the experimental animals were then scored and statistically analyzed. In Experiment 2, a modified social discrimination test was used. The experimental mouse was exposed to a stimulus mouse for five minutes, separated for 30 minutes, then exposed again for five minutes. The brains were then taken and stained for the immediate early gene c-Fos, which will measure neuronal activation during recall of social memory. Due to time constraints, only the MeA was analyzed for c-Fos expression, but there are plans to examine more areas.

Results Obtained

In Experiment 1, there was a significant decrease in anogenital contact in Oxtr $-/-$ males compared to controls, as well as a significant increase in nonsocial behaviors in Oxtr $-/-$ males. Both of these were only significantly different from controls on the first day of testing. We hypothesize that in a neutral arena the Oxtr is necessary for understanding of social context, so a disruption leads to a decrease in social behaviors, possibly due to fear of the stimulus animal. It will be important to examine fear and anxiety-like behaviors in future studies in order to understand the nuanced action of the Oxtr further.

In Experiment 2, there were no genotypic or sex differences in c-Fos expression within the MeA. This could possibly be due to a small sample size, so there are plans to add more animals and increase statistical power. An examination of more areas, including the BNST and the LS, is going to be conducted to elucidate the full extent of the Oxt system's action on neuronal activation.

Noncovalent Complexation and Assembly of Boron Nitride Nanotubes Using Biomolecules

Student Researcher: Jacob C. Vitale

Advisor: Dr. Geyou Ao

Cleveland State University
Department of Chemical and Biomedical Engineering

Abstract

Boron nitride nanotubes (BNNTs) are one-dimensional (1D) nanostructures with a cylindrical shape similar to that of carbon nanotubes. BNNTs are mechanically robust, stable under air oxidation up to 1173K, and absorb ultraviolet light. These features make BNNTs an ideal material for potential applications, such as thermal coatings for medical devices. Establishing stable dispersions of the synthetic BNNT material is a prerequisite to translating distinct properties of individual nanotubes into assembled structures via liquid phase processing.

In this work, aqueous dispersions of BNNTs will be prepared by probe tip ultrasonication utilizing various biomolecules including single-stranded DNA, lysozyme, bovine serum albumin, and acylase, respectively. The biomolecule:BNNT mass ratio will be varied for a broad range from 0.5:1 up to 20:1 to determine the optimal ratio for each dispersion. BNNT dispersions will be characterized by UV-vis absorption spectroscopy and zeta-potential measurement. A least squares regression method will be applied to determine the absorbance value of BNNTs at 205 nm peak. Furthermore, stable dispersions of biomolecule-BNNTs will be utilized to create thin films using a layer-by-layer assembly method. UV-vis absorbance measurement and scanning electron microscope imaging will be utilized to characterize BNNT films. Research findings of this work will enable the development of new technologies utilizing BNNTs in biological applications. Potentially, techniques learned from BNNT processing will be used to process stable dispersions of 2D boron nitride nanosheets and emulsions.

Project Objectives

The ultimate goal of this work is the formation of aligned BNNT thin films through layer-by-layer assemblies. The creation and alignment of these films will then allow for distinct BNNT properties, namely high thermal conductivity and electrical insulation, to be applied to a wide variety of products. In order to create these thin films, it is necessary to first optimize the aqueous dispersions of BNNTs with biomolecules such as Lysozyme (LSZ) and DNA. These biomolecules offer enhanced biocompatibility to the BNNTs and themselves carry the charges necessary for layer-by-layer assemblies.

Methodology Used

Aqueous dispersion of BNNTs were created using the following procedures. First, raw BNNT material are combined with biomolecules at various mass ratios in one milliliter of distilled water. This solution is then tip sonicated for one hour at 8W in an ice bath. This sonication forms an aqueous dispersion of the biomolecules and BNNTs. Centrifugation is then used to remove BN impurities and non-dispersed nanotubes from the solution. Solutions can then be further purified by precipitation with NaSCN and PEG or through centrifugal membrane filtration. Finally, the samples are characterized via UV-vis spectrometry, and concentrations can be calculated from absorbance measurements using the extinction coefficient at 205 nanometers found by Kode et al.¹

In order to use the BNNT extinction coefficient there must be a strong and well absolved peak at 205nm. It has been found that a majority of the free biomolecules remaining in our aqueous dispersions also absorb light in the ultraviolet region. This makes it nearly impossible to get accurate concentration measurements without the use of purification methods that remove biomolecules. These purification methods, however, also remove BNNTs from the solutions and lower concentrations significantly. For this reason, we have proposed and developed a least squares linear regression method; this allows for the deconvolution of the supernatant absorbance into the biomolecule and BNNT absorbances that compose the supernatant. The use of this method allows for the BNNT concentration to be calculated without the need for further purification.

BNNT thin films are formed using a procedure developed by Nepal et al. for carbon nanotube thin films.² Briefly, layer-by-layer (LbL) thin films are formed due to electrostatic interactions between oppositely charged materials. In this case, negatively charged DNA-BNNTs and positively charged LSZ-BNNTs. First, either a silicon or UV-quartz slide is selected as the base for the LbL film (these are based on the type of characterization performed on the slide). The LSZ-BNNT solution is then placed on the slide for several minutes and dried off using pressurized air from a uniform direction. This achieves two goals as it both dries the slide and aligns the BNNTs. This procedure is then repeated with DNA-BNNTs, and alternating dispersions are used until the desired film thickness is reached. At this point the thin films can be characterized by either UV-vis spectrometry to determine the film nanotube concentration or scanning electron microscopy to determine the alignment of the nanotubes.

Results Obtained

Thus far, we have optimized both LSZ-BNNT and DNA-BNNT dispersions using single-strand (GT)₃₀ in distilled water. In addition to this we have created initial thin films of BNNTs on both UV-quartz and silicon substrates. From initial SEM images we have also shown alignment of BNNTs on the silicon substrates.

Future work includes the optimization of other biomolecule-BNNT dispersions, the creation of additional BNNT thin films, optimization of BNNT film thickness, quantification of BNNT thin film alignment, and measurement of thin film thermal conductivity.

Significance and Interpretation of Results

This work has determined optimal biomolecule-BNNT mass ratios for aqueous dispersion that can be used in further work biological BNNT applications. In addition to this, it has been shown that BNNTs can be used to form thin films in a similar way to carbon nanotubes, opening the emerging material to a broad range of applications in both the medical and electronic fields.

Figures/Charts

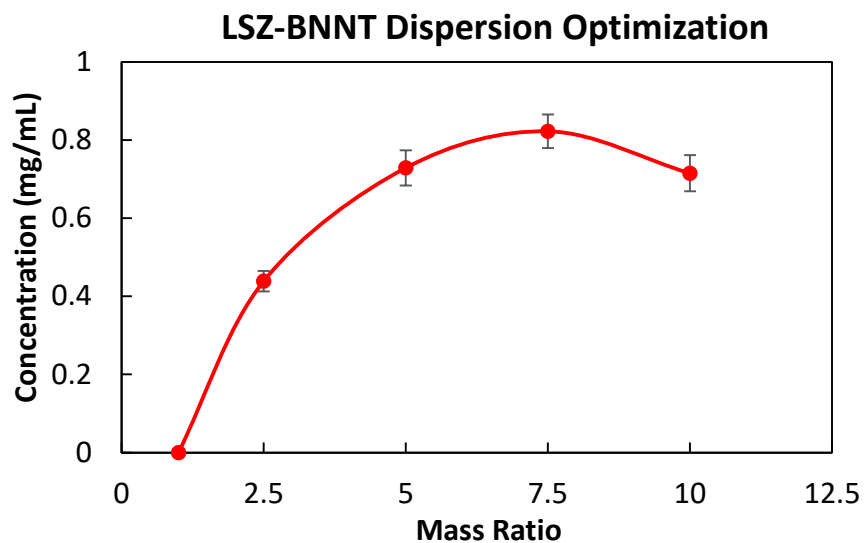


Figure 1. Concentration of LSZ-BNNT complexes as a function of BNNTs:LSZ mass ratios in the initial dispersion.

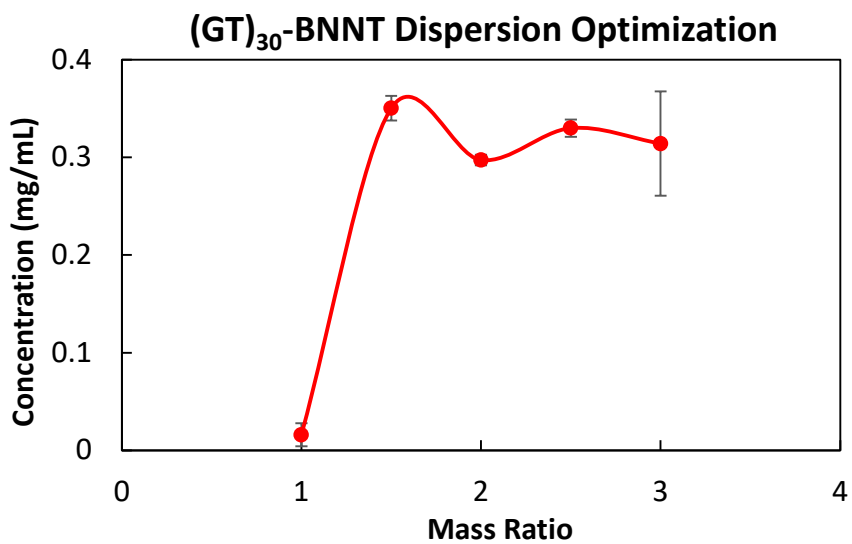


Figure 2. Concentration of (GT)₃₀-BNNT complexes as a function of BNNTs:DNA mass ratios in the initial dispersion.

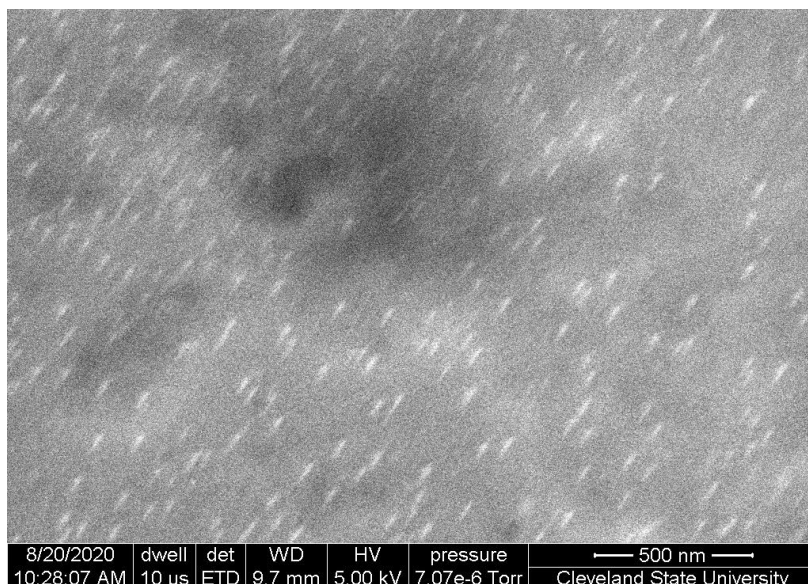


Figure 3. Initial SEM image of four-layer LbL Assembly of BNNTs obtained from aqueous dispersions of LSZ-BNNTs and DNA-BNNTs.

Acknowledgments

The author acknowledges the NASA OSGC Undergraduate STEM Scholarship and the CSU Undergraduate Summer Research Award. Additionally, we acknowledge Dr. Shawn Ryan for useful discussions.

References

- (1) Kode, V. R.; Thompson, M. E.; McDonald, C.; Weicherding, J.; Dobrila, T. D.; Fodor, P. S.; Wirth, C. L.; Ao, G. Purification and Assembly of DNA-Stabilized Boron Nitride Nanotubes into Aligned Films. *ACS Appl. Nano Mater.* **2019**, 2 (4), 2099–2105. <https://doi.org/10.1021/acsnm.9b00088>.
- (2) Nepal, D.; Balasubramanian, S.; Simonian, A. L.; Davis, V. A. Strong Antimicrobial Coatings: Single-Walled Carbon Nanotubes Armored with Biopolymers. *Nano Lett.* **2008**, 8 (7), 1896–1901. <https://doi.org/10.1021/nl080522t>.

Free-Stream Mach Number Effect on Aerospike Nozzle Performance

Student Researcher: Ryan T Watts

Advisor: Jed E. Marquart, Ph.D., P.E.

Ohio Northern University
Department of Mechanical Engineering

Abstract

In spacecraft, bell nozzles are typically used to control the flow exiting the rocket's engines. Bell nozzles have a major flaw, however, when compared to other nozzles like the aerospike nozzle. Bell nozzles are only optimally efficient at one altitude, whereas aerospike nozzles are nearly optimal for all altitudes. The purpose of this analysis is to study the thrust produced and the engine efficiency of the aerospike nozzle at different free-stream velocities. Three cases will be run, each with a different free-stream air velocity. The results showed that when the Mach number increases, the nozzle efficiency decreases. Though, the efficiency decreases much less than a bell nozzle would.

Project Objectives

The objective of this project is to determine the change in thrust and efficiency of an aerospike nozzle with differing free-stream velocities. This will help to understand the relationship between the flight speed of the vehicle and the efficiency of the engine.

Methodology Used

A computational fluid dynamics (CFD) analysis was completed on the aerospike nozzle in order to simulate the flow of the nozzle. The nozzle was first modeled using a software called Pointwise. The grid for the model along with the boundary conditions were also created using this software. With the model created, three different cases were run using the CFD software called Cobalt. The three cases studied used free-stream velocities of Mach 1.2, 0.8, 0.2. In order to complete this analysis, the Turbulent Navier-Stokes equation set was used. The aerospike was assumed to be flying at an altitude of 15000 meters and a speed of Mach 1.2, 0.8, or 0.2. Thus, the air surrounding the nozzle was set to match the temperature and density of the atmosphere at this altitude and the freestream velocity in that case.

Results Obtained

The first case looked at for this analysis used a free-stream velocity of Mach 1.2. As seen in Figure 1, the flow coming out of the nozzle naturally forms the typical bell shape due to the atmospheric pressure.

Figures/Charts

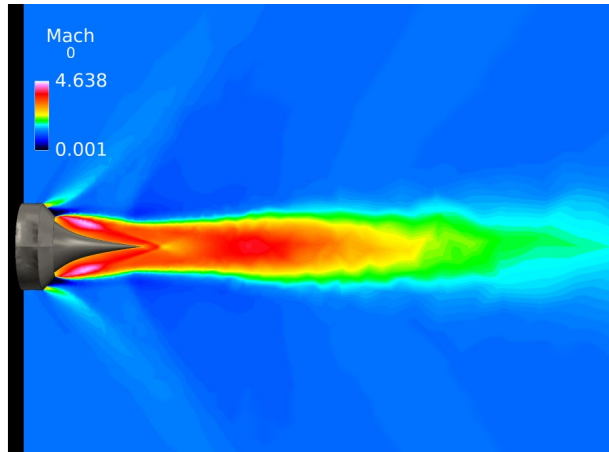


Figure 1. Mach Plane for Free-Stream Velocity of Mach 1.2

The second case looked at used a free-stream velocity of Mach 0.8, and the third case used a velocity of Mach 0.2. The thrust produced from the aerospike nozzle in the three cases can be seen in Table 1. The thrust of the nozzle varied from 124.7 kN to 130.75 kN in this analysis.

Table 2. Nozzle Thrust at Differing Free-Stream Velocities

Free-Stream Velocity (Mach)	Thrust Produced (N)
1.2	124,700
0.8	128,000
0.2	130,750

The efficiency of the nozzle was also found in each of the three cases. [1] A plot of the nozzle efficiency versus the Mach number can be seen in Figure 2. The nozzle efficiency was found to vary from 57.3% at Mach 0.2 to 54.6% at Mach 1.2.

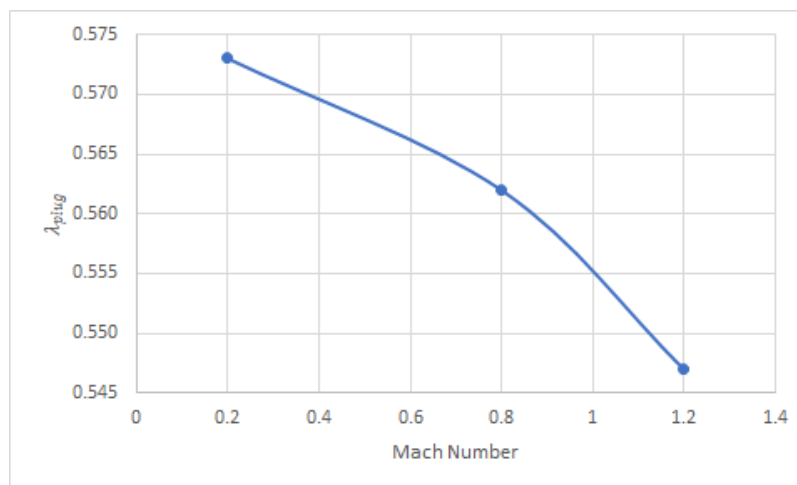


Figure 2. Nozzle Efficiencies of Aerospike Nozzle

Significance and Interpretation of Results

It is important to note that in this analysis only the free-stream velocity of the nozzle was changed, and not the free-stream pressure. This allowed the relationship between the thrust output and the free-stream velocity to be analyzed without the additional variable change of air pressure. Looking at the thrust output of the aerospike nozzle in the three cases, as in Table 1, it can be seen that as the free-stream velocity of the nozzle increased, the thrust produced decreased. Similarly, as the free-stream Mach number of the nozzle increased, the nozzle efficiency decreased. The efficiency of the nozzle only decreases about 2.7% from Mach 0.2 to Mach 1.2, however. This shows that the freestream velocity of the aerospike nozzle has a relatively small effect on the output thrust of the nozzle. Comparing this data to a similar analysis that alters the free-stream pressure rather than the velocity would be beneficial.

Acknowledgements

I am sincerely thankful to my research advisor Dr. Jed Marquart for his help and guidance during the process of this research.

References

[1] Wilson, A., Clark, J., Besnard, E. and Baker, M., 2020. CFD Analysis of a Multi-Chamber Aerospike Engine in Over-Expanded, Slipstream Conditions. *AIAA*,

Open Source Axial Compressor Mean-Line Design Tool for Supercritical Carbon Dioxide

Student Researcher: Kaden C. Wells

Advisor: Mark G. Turner

University of Cincinnati
Aerospace Engineering

Abstract

Interest in Supercritical CO₂ (S-CO₂) as the working fluid for closed loop Brayton cycles has increased over the past decade due to theoretical high cycle efficiencies. S-CO₂ with the compression phase near the critical point results in a cycle that possesses favorable qualities of both the closed loop water Rankine Cycle and the traditional open loop air Brayton Cycle [1]. This project deals only with analysis of a Compressor in the Brayton Cycle or a novel heat energy charging cycle [2], ETES. The design of compressors that use S-CO₂ as the working fluid require advanced assessment to accurately calculate the properties of the fluid and specifications of the compressor.

CO₂ is a gas of interest because it is cheap, inert, non-toxic, and its critical temperature of 304K (31 C) is near ambient temperature, 294K (21 C). In addition, the S-CO₂ Brayton cycle features high power densities due to the high fluid density that occurs because of the high pressures throughout the cycle and the high molecular weight of CO₂ when compared to water or air [1]. These high density and high pressures result in higher structural loading of the compressor components and generate many design difficulties that counter many benefits S-CO₂ initially allows; because of this, no compressors currently utilize S-CO₂ as the working fluid. However, technological advancements in structural loading and seal leakage have given the capability to design safer power cycles that utilize S-CO₂ [1].

Project Objectives

As a result, the design of an axial compressor with a mean-line code with S-CO₂ properties increases in importance. If correctly done, axial compressor designs utilizing S-CO₂ can be improved using mean-line computation as a starting step in optimization; furthermore, the mean-line code will calculate the expected conditions on a compressor design before the compressor is physically tested. The code created for this project does exactly that. Using input conditions such as mass flow rate, inlet pressure, inlet temperature, flow angles, and more; the code created can simulate the properties that the compressor will create with CO₂ as the working fluid. Furthermore, the code can calculate the properties at each stage of the compressor, as well as at each rotor and stator. (One stage is made up of a moving rotor, and a stationary stator) The full output of variables is supplied in **Table 1**.

Methodology Used

In order to account for the real gas properties (not just using the perfect gas assumption) property tables are needed so the full spectrum of properties that S-CO₂ undergoes can be mapped. This is done by utilizing capabilities from *National Institute of Standards and Technology's REFPROP (Reference Fluid Thermodynamic and Transport Properties Database)* [6]. REFPROP is a code that provides accurate thermophysical property models for a variety of industrially important fluids and fluid mixtures, including accepted standards [6].

By linking REFPROP with MATLAB, a double loop code creates a 300:300 property table based on two independent property variables. For instance, an entire map of the enthalpy variation of S-CO₂ is created within a range of 300-800K and 1-35 MPa. **Figure 1** shows the table in an easy-to-read format. The tables are imported into a python script where they are then interpolated with the bi-cubic spline routine `interp2d` in `scipy`. The function created from this then are used in each stage to accurately calculate the S-CO₂ properties.

Each stage and rotor/stator pair use thermodynamic equations to find total and static properties of the fluid. Bi-section method for root finding is also used when finding flow velocity and Mach number.

Results Obtained

The code ran using the input properties from a non-optimized compressor design. With the hub radius remaining constant, a full output of variables was calculated. The 8-stage compressor design ended with an adiabatic efficiency of 0.905, a total pressure ratio of 3.747, and a total temperature ratio of 1.327 using S-CO₂ as the working fluid. A few of the output graphs are supplied in **Figure 2**.

Significance and Interpretation of Results

The real properties of S-CO₂ were able to be accurately calculated throughout an 8-stage compressor design. Because of the variation of S-CO₂ in high pressure situations, the properties varied far from the perfect gas assumption, proving the need for real property computations when dealing with S-CO₂. The python code created during this project can be used as the first step in an optimization loop for creating efficient compressors that use S-CO₂. The author(s) are continuing work on this design system.

Figures/Charts

X-AXIS Prop.	Y-AXIS Prop.
S [J/(kgK)]	H [J/kg]
P_t [kPa]	T_t [K]
P_s [kPa]	T_s [K]
Φ	Ψ
P_t [kPa]	γ
T_t [K]	γ
Stage Num.	P_t [kPa]
Stage Num.	T_t [K]
Stage Num.	ρ [kg/m ³]
Stage Num.	S [J/(kgK)]
Stage Num.	Ψ
Stage Num.	Φ
Stage Num.	Leading Edge α [deg]
	Trailing Edge α [deg]
Stage Num.	Leading Edge β [deg]
	Trailing Edge β [deg]
Stage Num.	Abs. Angle Turning (<i>Rotor</i>) [deg]
Stage Num.	Abs. Angle Turning (<i>Stator</i>) [deg]
Stage Num.	Diffusion Factor
Stage Num.	Total Pressure Ratio
Stage Num.	Per Stage Pressure Ratio
Stage Num.	Total Temperature Ratio
Stage Num.	Per Stage Temperature Ratio
Stage Num.	Efficiency Per Stage []
Stage Num.	Value of Reaction []
Station Num.	S [J/(kgK)]
Station Num.	ρ [kg/m ³]
Station Num.	V_r, V_s, V_θ [m/s]
Station Num.	$\alpha, \beta, \text{angle turning}$ [deg]
Station Num.	<i>Mach</i>
Station Num.	<i>Pitch Radius</i> [m]
	<i>Hub Radius</i> [m]
	<i>Tip Radius</i> [m]
Station Num.	γ
Station Num.	C_p
Station Num.	μ [uPa/s]

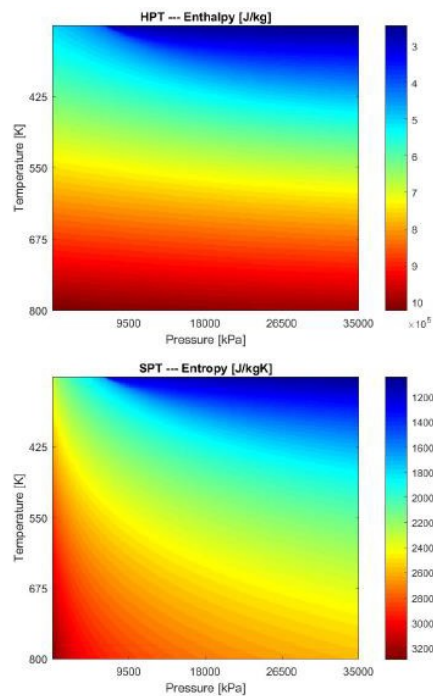


Table 1. All properties in output file **Figure 1.** Property Tables Created from REFPROP

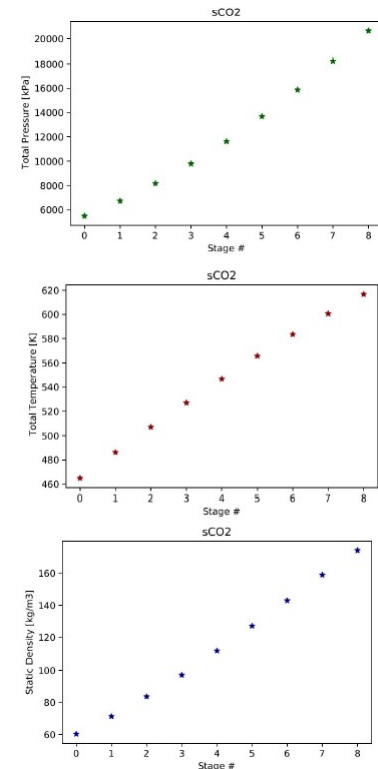


Figure 2. Some output properties per stage

Acknowledgments and References

- 1) Schroder, A. U., 2016. "A study of power cycles using supercritical carbon dioxide as the working fluid". PhD thesis, University of Cincinnati.
- 2) Held, T. J., 2019. Advanced compressors for co₂-based power cycles and energy storage systems. Tech. rep., Echogen Power Systems (DE), Inc.
- 3) Lemmon, E. W., Bell, I. H., Huber, M. L., and McLinden, M. O., 2018. "nist standard reference database 23: Reference fluid thermodynamic and transport properties-refprop, version 10.0, national institute of standards and technology." website.

Lead (Pb) Speciation In Soil

Student Researcher: Madison M. Wood

Advisor: Dr. David Singer

Kent State University
Department of Geology

Abstract: Lead (Pb), a versatile metal, is commonly present in urban soils because of its wide range of industrial uses and its resistance to degradation. One way to identify if Pb is present in soils is through the use of scanning electron microscopy with electron dispersive spectroscopy which can be used to identify Pb and other elements present, assisting in understanding the phases Pb is bound in. The identification of Pb-bearing phases present in soils will aid in identifying potential bioaccessible Pb, which can assist in future targeted remediation.

Project Objectives: The U.S. Environmental Protection Agency has set a standard of 400 mg/kg of Pb in bare soils in residential areas to limit human exposure, however exposure to lower Pb concentrations (100-200 mg/kg) can still result in serious health consequences particularly for children. Exposure to Pb and potential bioavailability is dependent not just on total concentration, but also speciation; the chemical and physical form(s) of Pb present in soils and sediments. This project aims to identify physical and chemical speciation.

Methodology: One method to determine Pb speciation is scanning electron microscopy with electron dispersive spectroscopy (SEM-EDS) analyses. This approach can determine grain-scale particle size, shape, morphology, texture, and elemental composition. Soil and sediment samples were analyzed from locations within two neighborhoods in Akron, Ohio and two industrial sites in Israel. Notably, although leaded gasoline was used in Israel, little to no lead paint was used, whereas in Akron both have been used.

Results Obtained: Preliminary results indicate that physical speciation ranged from discrete Pb-bearing micrometer- to millimeter-scale grains to Pb-bearing mineral surface coatings, where composition was dependent on morphology and texture. For example, a soil samples from Akron contained: (1) a discrete grain with a smooth surface that is ~30 μm wide with its composition dominated by PbS-Ca-Mg; and (2) a discrete grain with a rough surface and cubic structure that is ~10 μm and a composition dominated by Pb-S in an aggregate of Fe-Mn oxides. The samples from Vulcan Automotive Industries Ltd. in the industrial area of Tefen, Israel contained: (1) a coated grain that is rough and 15-20 μm with a composition dominated by Pb-S- PO_4 -Cl; and (2) a group of hexagonal platy discrete grains that are <10 μm in size with a composition dominated by Pb-S-Al-Si. The samples from the Hakurnas Lead Works Ltd. in the city of Ashdod, Israel contained: (1) a large coated grain that is >200 μm in length with a rough surface and a composition dominated by Pb- SO_4 - PO_4 ; and (2) a smooth discrete grain with a cubic structure that is ~20 μm wide and a composition dominated by Pb- PO_4 -Cl. Physical and chemical speciation need to be analyzed in tandem going forward to fully predict potential bioavailability.

Significance and Interpretation of Results: Physical speciation like the grain size can affect potential bioavailability with larger grains being more immobile and therefore having a lower potential for bioaccessibility, and coated grains potentially being more bioaccessible than discrete grains. Chemical speciation can also affect potential bioavailability. Grains with the primary composition of Pb-S-Ca-Mg

like in some Akron samples are less mobile and therefore have a lower potential bioavailability than a grain with the primary composition of $\text{Pb-SO}_4\text{-PO}_4$ like in Hakurnas soils.

Acknowledgments: This project is being done in collaboration with Dr. Bridget Mulvey (Kent State University), Dr. Nadya Teutsch (The Geological Survey of Israel), and Dr. Katrina Halasa (Akron Public School District). Thank you to the Ohio Space Grant Consortium for supporting this project.

The Early Earth: Cool and Clement or Hot and Hadean? An Investigation into the Geology and Surface Environments on Ancient Earth

Student Researcher: Sarah N. Worrell

Advisor: Dr. Daniel K. Holm

Kent State University
Department of Geology

Abstract

The current research on Earth's modern-day geology and surface environments has coincided with a renewed interest about Earth's initial early environment – from 4.4 to 3.6 billion years ago, during Earth's first gigayear. The long-held view of a hot and "hell-like" (Hadean) early Earth with molten magma oceans maintained by heat released from inside the Earth has been challenged by recent geological evidence, which favors a calmer early Earth cool enough to support liquid water, proto-continental crust, and possibly even life. This paper synthesizes the evidence that earth materials have provided for a cool, clement early Earth, with an emphasis on the evolution of the mineral, rock, and isotopic record. These evidences taken from the research literature have important implications for the formation of ancient continental crust, the onset of plate tectonics, the existence of liquid water, and the origin of life on Earth. A major part of this evidence comes from the discovery of 4.4 billion-year-old zircons determined to have formed from a granitic magma in the presence of liquid water. Water-deposited sedimentary rocks in Greenland have further supported the existence of a hydrosphere by 3.85 Ga. Carbon isotopes in metacherts from this same region in Greenland suggest that primitive life may have also existed by this time. There is also discussion of the nature and composition of the first proto-continental crust and the beginning of plate tectonics.

Conclusion

The Earth has a complex, dynamic history; the earliest of which has been challenging to decipher from the surviving rock record. Water-lain and chemically precipitated sediments observed in the sedimentary rock record of Isua, along with the isotopically "light" carbon in metacherts in these rocks, suggest a hydrosphere and biosphere on Earth by 3.85 Ga. The earliest life was likely carbon-based, siliceous organisms that began in Earth's primordial oceans. The formation of rigid lithospheric plates, accompanied by the transition from a thin mafic crust to a thicker intermediate crust, set in motion the system of plate tectonics between 3.2-2.5 Ga. Most of the rock record older than 4 billion years is poorly exposed on the surface, either having been eroded or buried under kilometers of sediment at continental cratons. Any existing exposures of rocks this ancient are often highly metamorphosed to the point of migmatization (partial melting), which are difficult to study and date. The Isua supracrustal belt is our best source of well-preserved, low-strain sedimentary rocks that date back to the Eoarchean. There are no rock samples yet discovered that pre-date 4.0 Ga. Mineral samples, however, particularly the 4.4 billion-year-old Jack Hills zircons, hold a surprising wealth of information about the early Earth. The zircons provide strong evidence for liquid water, silica-rich magma, and low surface temperatures a mere 150 million years after the formation of the planet. These zircons remain the oldest materials yet discovered from the early Earth. Perhaps with time and technological advancements, geologists will uncover more samples to piece together the story of our planet's distant past.

Figure 1. Valley, 2005 – Oxygen isotope ratios in >4 billion-year-old Jack Hills zircons compared to typical mantle-sourced zircons.

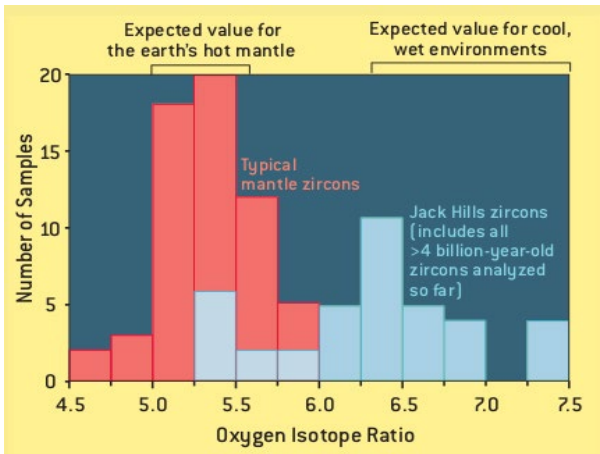


Figure 2. Cawood et al., 2018 – Nature of the Earth’s early lithosphere and upper mantle, in which the lithosphere transitioned from a thin, predominantly mafic crust >3.2 Ga to a thicker, intermediate crust that began to form stable continental cratons around 2.5 Ga.

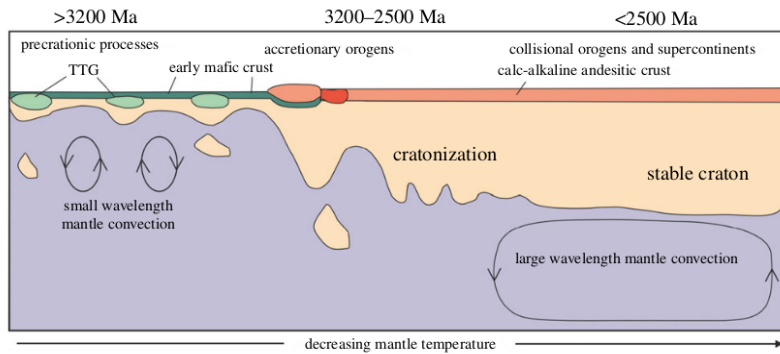


Figure 3. Cawood et al., 2018 – Lithospheric growth model, where a shift in the composition of juvenile crust from mafic to more intermediate compositions, occurring between 3.2-2.5 Ga, is accompanied by an inferred growth in lithospheric thickness.

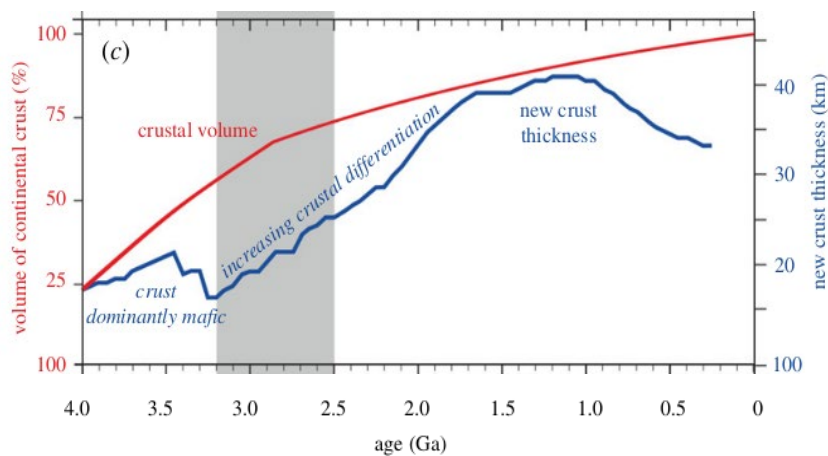
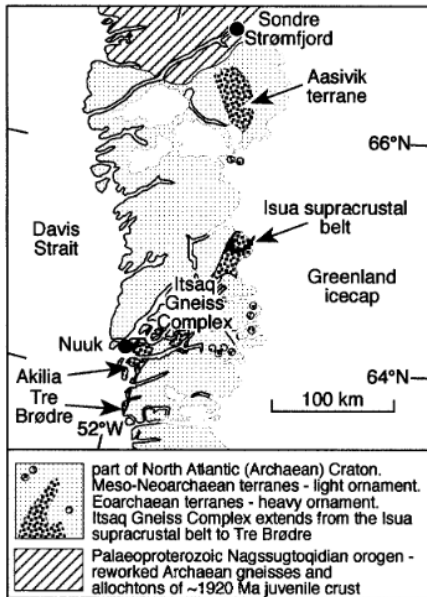


Figure 4. Nutman et al., 2001, Figure 1 – Location of known Eoarchean rocks in West Greenland. They are probably from one or more (Neoarchean) allochthonous bodies, extending for >400 km.



References

Cawood Peter A., Hawkesworth Chris J., Pisarevsky Sergei A., Dhuime Bruno, Capitanio Fabio A., Nebel Oliver, 2018. *Geological archive of the onset of plate tectonics*. Philosophical Transactions of the Royal Society A: Mathematical, Physical, and Engineering Sciences, 376.

Nutman Allen P., Friend Clark RL, Bennett Vickie C., 2001. *Review of the oldest (4400–3600 Ma) geological and mineralogical record: Glimpses of the beginning*. Episodes 24(2), 93-101.

Nelson, 2004. *The early Earth, Earth's formation and first billion years*. In: Eriksson, P.G., et al. (Eds.), *The Precambrian Earth: Tempo and Events*. Elsevier, Amsterdam, p. 3-27.

Peck and Valley, 2009. *Archean environments*. In: Gornitz, V. (Ed.), *Encyclo. of Paleoclimatology and Ancient Environments*. Springer, Dordrecht, The Netherlands. p. 34-38.

Valley, John W. *A cool early Earth?* *Scientific American* 293.4 (2005): 58-65.

Valley John L., Peck William H., King Elizabeth M., Wilde Simon A., 2002. *A Cool Early Earth*. *Geology* 30, 351-354.

A Hybrid Fuel Cell/Battery/Capacitor Power Source for UAS Laboratory Flight Test Demonstration

Student Researcher: Matthew Zirckel

Advisor: D. Blake Stringer, Ph.D.

Kent State University

College of Aeronautics and Engineering

Abstract

Rapid advancements have been made in UAS technology, specifically electric Vertical Takeoff and Landing (eVTOL). These efforts include Urban Air Mobility (UAM) and cargo applications. Autonomous and near-autonomous operations are currently in production as well as commercial use. With this expansion in the use of eVTOL aircraft, electric motors are being used in applications previously powered by unconventional gas turbine engines.

Project Objectives

The objectives of the project are to interface the new power cell technology with the existing test stand and to simulate flight conditions of a UAS powered by the new power source. Due to scheduling constraints and delays, the fitting of the power source has yet to occur, although data has been taken using a traditional battery system with similar output capabilities in preparation for interfacing the new system.

Methodology

The test stand software's internal scripting software takes user defined throttle settings and simulates a profile like that shown in Figure 1. The throttle settings are experimentally obtained, based on the desired mechanical power output of the rotor-motor combination. The test stand is capable of recording parameters such as the thrust output, torque, rotational speed, power, voltage, current and temperature. Once the test has been completed, the collected data is tabulated into a spreadsheet for analysis.

Results Obtained

The 15-minute tests that were completed showed that the motor-rotor combination initially chosen would not be sufficient for the needs of the UAS. The flight profile of this test is shown in Figure 2. The expected power output exceeds the capability of the initial motor-rotor combination. A critical failure in the motor occurred in the first attempted 1-hour test. Smoke was recorded exiting the motor, as the test exceeded the manufacturer's limitations. The test was ended prematurely due to motor damage.

Significance and Interpretation of Results

Due to the critical failure in the motor, it was determined that a larger motor was necessary, as well as a three-bladed rotor, as opposed to a two-bladed rotor. The power output is greater with this combination and higher temperatures can be maintained without damaging the motor. The new combination will more closely replicate the desired output in preparation for the fitting of the hybrid-electric power source.

Figures/Charts

Figure 1. The Mission Profile of a 1-hour Flight Demonstration Using Approximate Power Values

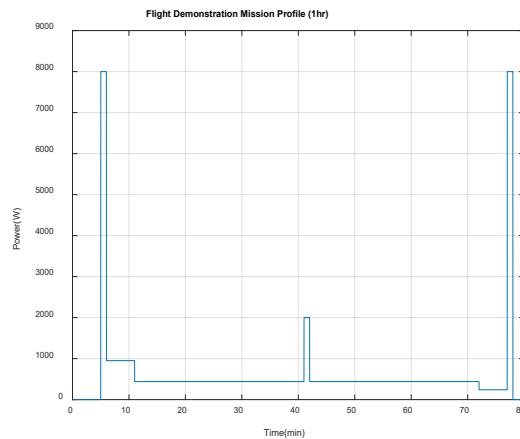
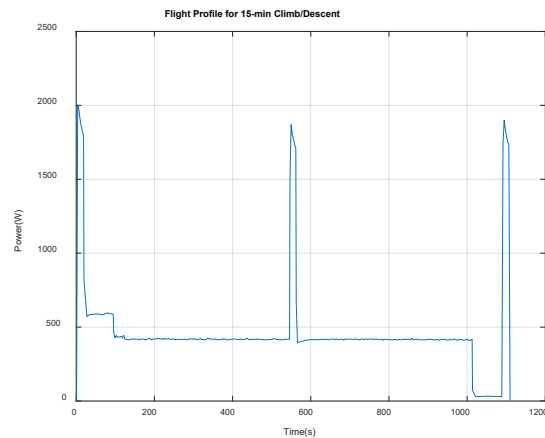


Figure 2. The Flight Profile of a 15-minute Test



Acknowledgements and References

Edmonds, K. Stringer, D., Valco, M., “Experimental Results of Transient Variable Speed Rotor Performance for Small UAS Propulsion Scalability,” Vertical Flight Society 76th Annual Forum, October 6-8, 2020, Virtual.

Edmonds, K., and Stringer, D., “Unmanned VTOL Propulsion Research – Scalability of Quadcopter Rotor-Motor Configurations Outside the sUAS Regime,” Final Report, ARL-CR-0848, Grant No. W911NF-18-2-0024, May 2020, <https://apps.dtic.mil/sti/pdfs/AD1102551.pdf>.

Edmonds, K. Stringer, D., “Unmanned VTOL Propulsion Research – Scalability of Quadcopter Rotor-Motor Configurations Outside the sUAS Regime,” AUVSI Xponential, April 29 – May 2, 2019, Chicago, Illinois.

Stringer, D., and Edmonds, K., “sUAS Propulsion Scalability,” Ohio UAS Academic Summit, Dayton, Ohio, September 17, 2019.

Community College

Electroplating Gold onto an iPhone 12 Pro Max

Student Researcher: Muhammad Z. Ali

Advisor: Harry Kestler, Regan Silvestri, Aaron Weiss

Lorain County Community College
Science and Math Department

Abstract

A vital manufacturing process known as electroplating involves the use of an anode and electrically conductive object placed in a solution of a metallic salt and acid. This process was intended to be used in place of vapor deposition for prototyping supercapacitors to compete with lithium-ion batteries. As a baseline test, a layer of gold was successfully plated onto an iPhone 12 Pro Max.

A standard process to plate gold onto an unknown alloy of stainless steel was tested. The steel was the outer casing of an iPhone 12 Pro Max. The steel was mirror polished with polishing compound. It was cleaned with an ultrasonic cleaner and then an alkaline electro cleaning solution was used to clean it further. The phone was plated using a standard Wood's Nickel Strike. The strike was then plated with the final layer of 24 karat gold. The gold layer was between 2.5 and 3.5 microns thick. The gold layer was able to withstand pulling from packaging tape and further polishing. The layer thickness was determined based on which polishing compound was able to remove the gold layer from the steel.

Project Objectives

The original project was to create a sputtering machine. Due to a lack of access to high strength vacuum pumps and a location to build, the idea was partially scrapped. The sputtering machine would have been used to create thin film supercapacitors designed with carbon nanostructures to compete with lithium-ion batteries as an electric storage device.

As mentioned, the idea was partially scrapped due to cost and a lack of access to resources caused by the rapid spread of Covid-19 in the U.S. The intention of the new project was to gold plate the latest iPhones and sell them to cover costs towards the original intended idea of a sputtering machine.

The project would be successful if the gold plating is visibly reflective and shiny in appearance rather than cloudy. The gold layer must also have a decent level of adhesion to be considered a usable (therefore sellable) product. Finally, the iPhone must be able to survive the plating processes, otherwise, the result would be a defective iPhone.

Methodology Used

The methodology of the study varied greatly for the two iPhones that were plated. First, an iPhone 7 back housing was used as a test. During this, access to proper texts and procedures was not available so the tests were rather random. Initially the part was in rough shape showing scratches and scuff marks significant enough to remove damage the black anodized layer. A handheld circular sander was initially used to remove the anodization. The sander was used in grits 80,120,180, and 240. The finer polishing was done with a rotary tool. A series of four abrasive buffs was used with WD-40 as a lubricant. The rated abrasive grit of the buffs was 80,120,160,240 and used in that order respectively. The polishing compounds used were sold as "Diamond" polishes. Those that contained "diamonds" of various sizes in

order to be used as a polishing paste. A dedicated hard felt buffing wheel was available for each grit of buffing compound to prevent contamination. The polishing compound was loaded onto the buffing wheel and the iPhone 7 back housing was polished. The polishing compound was cleaned off using a blue shop towel and 70 percent isopropanol. The blue shop towels were used as they do not leave behind lint and could be thrown out after each use to prevent contamination into the next polishing grit. This process was repeated until a mirror polish was achieved. The polishing grits used were 325, 650, 950, 1400, 1750, 2800, 4500, 6000, 9000, 13000, 14000, 60000, and 100000 in that order.

The iPhone 7 back housing was placed in a sulfuric acid based surface activator solution and then plated with acid copper. The surface activator was from Gold Plating Services and the acid copper was purchased from Caswell. The plating lacked adhesion and did not adhere to the iPhone 7 back housing. The phone was repolished with the method above and the plate was attempted again. This time with a zincation solution also purchased from Caswell. The zincate was concentrated and diluted with distilled water as per the instructions that came with the bottle. The process was repeated, this time with the surface activator first, then zincation, then the copper plate. The process was mixed up several times in a different order and attempted with no good adhesion for either method. The best adhesion came from a homemade alkaline solution added in place of the sulfuric acid activator. The solution was made with one tablespoon of sodium hydroxide and distilled water. This plating was tested with a piece of tape placed on the phone and pulled back.

The process was modified after more research was conducted. A good source on this method was Lawrence J Durney's *Electroplating Engineering Handbook*. After consulting the book, the process was modified and attempted on a new iPhone.

The iPhone 12 Pro Max came polished so if done correctly the first time, should not require a series of polishing compounds. For this experiment the stainless steel (silver) version was selected. The entire phone was dipped in the solutions to allow for equal plating thicknesses. Initial tests proved failures as the proper solutions were not being used. Because of this the phone had to be repolished to a mirror finish using the process of polishing compounds mentioned before. The hard abrasive pads and abrasive buffing wheels were not used. Only the polishing compounds were used with the hard felt pads. Once a satisfactory finish was achieved the phone was cleaned with 70% Isopropyl Alcohol. It was cleaned again with brake cleaner and then put in an ultrasonic cleaner for 8 minutes in a degreasing solution. The phone was then placed in a homemade plating tank consisting of a Rubbermaid lunch container and flat sheets of 316 steel that were cut and bent around the inside perimeter of the lunch container to act as the anode.

The first tank contained a solution of equal parts sodium hydroxide and sodium bicarbonate totaling 5% of the solution and the remaining 95% was made with distilled water. This solution was mixed until uniformly clear. The stainless steel anodes were placed along the perimeter and the positive alligator clip was attached at 7 volts. The phone was covered with a set of wires connected to the negative terminal of the rectifier. The phone was put in this tank for 2 minutes. The process was checked with a spray of distilled water. As highlighted by Durney, if the water sticks to the surface then it is ready for the next plating bath.

The next plating bath was a solution of hydrochloric acid 17% and one tablespoon of nickel chloride. This was mixed until uniform in color and no solute was left. This solution was plated with a nickel anode (thin 2cm x 15cm sheet of nickel). The anode was covered with a fresh small piece of blue shop towel

previously mentioned for their use in cleaning the parts. This was placed in order to hold the solution and to prevent contact between the two metals. The rectifier was set at 6.5 volts. The phone remained in the solution with the negative alligator clip and the positive nickel anode was rotated around the perimeter for 3 minutes. The phone was sprayed again with distilled water to remove the nickel strike solution.

The phone was placed back in the alkaline activator solution as before to activate the surface. It was cleaned with a spray of distilled water and then plated with gold.

Originally the gold solution was to be a bath but since it wasn't concentrated enough the solution was concentrated by heating the liquid. The evaporation increased the concentration of the solution and was still plateable. However, concentrated 24k Gold solution was purchased from Gold Touch Inc in Cleveland Ohio. This was then plated with a custom-made anode wrapped with a blue shop towel at the tip. The anode was made from 316 steel tweezers. The positive alligator clip was put on the tweezers and the negative lead was placed on the phone. This was plated at 2.7 volts.

Results Obtained

The iPhone 7 was not plateable with any of the methods tested and showed signs of pitting when observed closely. The phone did not pass a tape adhesion test and the copper eventually flaked off by rubbing it gently.

The iPhone 12 Pro Max was successfully partially plated in 24k gold. There were sections of the phone that could not be plated and had to be retouched. The activating solution did not work well in those sections. The touch screen and all components worked fine when the phone was removed from the solutions. The phone stopped working after it was charged again. The plating was tested with tape and none of it peeled off. The plating was removed in certain areas with varying polishing compounds to test the thickness of the plate. The 3.5 micron (6000 grit) polish was able to remove the gold plating. The 2.5 micron (9000 grit) was not able to remove the gold.

Significance and Interpretation of Results

The results showed that the iPhone 7 can be plated with relatively poor adhesion using the method above. The phone backing is made from aluminum and aluminum is known to be difficult to plate. A proposed solution to increase adhesion is to dip the backing in dilute nitric acid and then into zincate. Back and forth twice. According to Durney, this is known as double zincation. This should help remove the other metals that are in the aluminum and make it easier for the zinc to bond to the aluminum and thus allow for better adhesion to the metal. The flaking is most likely due to the other metals in the aluminum as pure aluminum is hardly ever used as a production metal.

The iPhone 12 Pro Max showed promising results of being plateable. A strong bond between the plate and the metal means it could be plated with this method. The lack of adhesion in certain areas could be due to a lack of proper materials. The homemade plating solutions include the alkaline cleaner and the nickel strike solution. Since both are critical steps in getting a plate that can adhere well, a commercially available solution should be used, as there would be less variability in the results.

The iPhone stopped working once it was charged. The screen had a greenish tint and then slowly turned into a green screen and then stopped working. This could be due to a few reasons. Most likely, the

mixture of solutions entered the phone in a minute amount and damaged the connector cable between the digitizer and the logic board. This could also have happened to the battery connector and would explain the lack of vibration and charging that is usually present when the phone is connected to a charger. If it was just the screen that was damaged an audible sound should have been present. Another problem could be the strong solution of acids and bases alternating against the adhesive used to hold the digitizer to the main frame of the phone could have penetrated the digitizer layers and damaged the screen. This would make sense as the screen is unresponsive.

The only way to truly tell would be to open the phone and check the components individually. The easiest component to check would be the battery. If voltage is present at 3.7v then the battery works and other components should be checked.

Figures/Charts



Figure 1. Initial Condition of iPhone 7



Figure 2. iPhone 7 polished to 280 Grit



Figure 3. iPhone 7 Polished to 40 micron (325 Grit)



Figure 4. iPhone 7 Polished to .25 micron (100,000 Grit)



Figure 5. Poor adhesion of zincate solution on scrap aluminum



Figure 6. Copper plate tests on iPhone 7



Figure 7. Acid Copper plating on iPhone 7 after alkaline dip



Figure 8. Adhesion test on iPhone 7

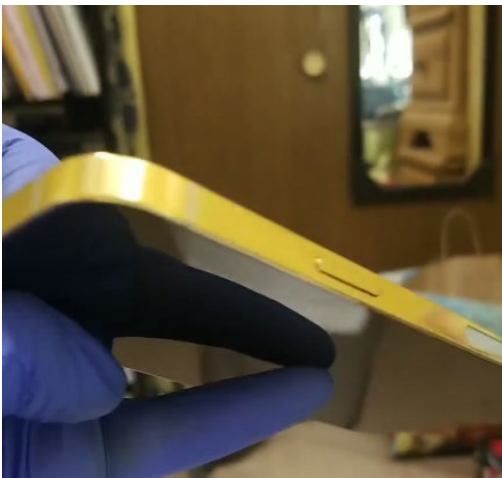


Figure 9. Gold plate on iPhone 12 Pro Max



Figure 10. Poor gold plate on iPhone 12 Pro Max



Figure 11. Homemade Anode of 316 steel tweezer and blue shop cloth



Figure 12. Homemade plating tanks

Acknowledgments and References

Durney, L. J. (1984). *Electroplating engineering handbook*. New York: Van Nostrand Reinhold.

Comparative Study of Resilient and Green Building Practices and Applications Used in the Construction Field

Student Researcher: Grace A. Ciminillo Delamotte

Advisor: Dean M. Bortz, M.A., CSI, CDT, CCPR

Columbus State Community College

Design, Construction and Trades Department
Construction Management

Abstract

Conduct a comparative study through a literature review examining resilient and green building practices and applications within the built environment.

Introduction of key terms

Green building practices involve the use of sustainable sites, water and energy efficiency, including the reduction of waste and emissions, commitment to eco-friendly building materials, that ultimately improves indoor environmental quality more efficiently than conventional designs.

Project Objectives

The purpose of this study is to research the different green building practices and consider their impact within the construction field.

Methodology Used

The foundation used to conduct this study were my college courses and various resources that included research articles, trade publications, construction textbooks, and specifications related to different products.

Results Obtained

According to Roodman and Lensson, building and construction activities worldwide consume 3 billion tons of raw materials each year or 40 percent of total global use. Therefore the construction industry must consider its impact in the world.

The results of this research has led to a deeper understanding of different products used within the construction field and the different qualities for consideration that include renewability, sustainability, and environmental impact.

Significance and Interpretation of Results

Using green building materials and products promotes conservation of dwindling nonrenewable resources globally. In addition, integrating green building materials into building projects can help reduce the environmental impacts associated with the extraction, transport, processing, fabrication, installation, reuse, recycling, and disposal of these building industry source materials.

Along with those considerations, research also reveals health benefits. According to Fisk and Rosenfeld, recent studies reveal that buildings with good overall environmental quality can reduce the rate of respiratory disease, allergy, asthma, sick building symptoms, and enhance worker performance creating substantial financial benefits.

The construction industry has a long history of great builds and can continue building into the future as long as it actively works to protect future resources through green practices.

Acknowledgments

My professors, Dean Bortz, Dr. Owens, Kolton Wilson, David Busch and others have introduced me academically to the construction field and fostered my curiosity of the built environment. This research project has reinforced all that is important to me. Caring for the natural world and building with it instead of against it is my responsibility as a world citizen and future construction manager. Thank you OSGC for this opportunity to grow as a learner.

References

"Buildings Can Become a Global CO2 Sink If Made out of Wood Instead of Cement and Steel." ScienceDaily, ScienceDaily, 27 Jan. 2020, www.sciencedaily.com/releases/2020/01/200127134828.htm.

Dennehy, Kevin. "Using More Wood for Construction Can Slash Global Reliance on Fossil Fuels." YaleNews, Yale, 2 Apr. 2014, news.yale.edu/2014/03/31/using-more-wood-construction-can-slash-global-reliance-fossil-fuels.

Fisk, W. and Rosenfeld, A. Potential Nationwide Improvements in Productivity and Health from Better Indoor Environments, Lawrence Berkeley National Laboratory, May 1998.

Froeschle, Lynn. "Environmental Assessment and Specification of Green Building Materials," The Construction Specifier, October 1999,

Green, Michael, director. Why We Should Build More Wooden Skyscrapers. TED, 2013, www.ted.com/talks/michael_green_why_we_should_build_wooden_skyscrapers/transcript.

Ike. "Recycling Timber: Wasting Away." Building, 28 Oct. 2015, www.building.co.uk/focus/recycling-timber-wasting-away/5078393.article.

Mehta, Madan, et al. Building Construction: Principles, Materials, and Systems. Pearson, 2018.

Lenssen and Roodman, A Building Revolution: How Ecology and Health Concerns are Transforming Construction, Worldwatch Paper 124, Worldwatch Institute, Washington, D.C., March 1995, p. 5

Oliver, Chadwick Dearing. "Carbon, Fossil Fuel, and Biodiversity Mitigation with Wood and Forests." Taylor & Francis, 28 Mar. 2014, www.tandfonline.com/doi/full/10.1080/10549811.2013.839386.

Petersen, K A, and B Solberg. "Greenhouse Gas Emissions, Life-Cycle Inventory and Cost-Efficiency of Using Laminated Wood Instead of Steel Construction." Ohiolink, 2002, rave.ohiolink.edu/ejournals/article/322357757.

Super Conductors, From One Extreme to Another

Student Researcher: Tyler J. Dorsey

Advisor: Abigail Yee

Cincinnati State Technical Community College
Mechanical Engineering

Abstract

Last year a team of physicists in New York created the first material to be classified as a superconductor at room temperature (59°F). This was a major breakthrough as the previous record was more than 50° cooler. The biggest downfall of this however was the pressure needed to maintain the superconductive properties. The pressure needed is close to 2.5 million times atmospheric pressure. The biggest issue with implementing superconductors into practical uses before this breakthrough was the fact they were only found to be superconductive at very low temperatures. While we could take advantage of the bizarre properties superconductors exert, there was no practical way to keep the temperature low enough to make it a reality.

Project Objectives

The overall objective was to see impact, if any, this new discovery could lead to. The main questions I wanted to answer were, could we implement this into society, what did we learn to better our understanding, and what does this mean going forward?

The thought of a superconductor is an interesting one. A perfect material, conducting with zero resistance. A perfect condition always seems impossible, with superconductors it really is no different. In order to achieve this the conditions must be extreme. The most common way to achieve this state is with liquid nitrogen bringing the material down to around 195°C, or more recently room temperature with a pressure measuring upwards of 267 GPa.

Being able to harness the properties a superconductor exerts would change the world. The technology we have today not only be able to be improved on, but there would most likely be a whole new system of technology innovated. Everything could be more efficient, more powerful, and lead to a much greener world. They could be used as electromagnets to power trains, replace copper wiring all together, and create very powerful magnets.

Methodology Used

The method to achieve superconductor properties was interesting. Sulfur and Carbon were infused using a one-to-one ratio and then put under immense pressure. Hydrogen was then slowly added to the mix until the properties started showing superconductivity. A high-powered laser was then used on the material for hours to break down any bonds between electrons.

Results Obtained

The material was then superconductive at room temperature, but unless the pressure was extremely high, it was not stable.

The chemistry behind why this reaction happens is still not understood fully. With a better understanding of what is happening during this reaction could lead to the possibility of optimizing the reactions in order to improve the stability at lower pressures.

While going to one extreme to another may not seem to bring the world any closer to harnessing the properties of superconductor, I would have to disagree. This is a major breakthrough for science and for the world. Since the recent discovery in 2020, it has since been recorded of achieving superconductive properties at room temperature with the pressure as low as 187 GPa. While this is still incredibly high and not ideal for implementing this technology, it shows a vast improvement over a short time.

Significance and Interpretation of Results

Making this new discovering as led to new methods of achieving the properties. With this comes a bigger base knowledge of the materials themselves. Which can then be modified for improvement. It sparks new ideas and new hypotheses to form, which can provide insightful information on this project which has been growing for years. The technique that has been being used most recently is doping Sulfuric Hydride with Carbon.

In short, in the middle of the fourth revolution, we may see another one start to form. Where we can harness energy without waste, replace the power grid that we have today, improve the tools of the medical field, and be inspired by new innovations that would inevitably follow.

Acknowledgments and References

“Room Temperature Superconductor? Rochester Lab Sets New Record toward Long-Sought Goal.”
NewsCenter, 31 Mar. 2021, www.rochester.edu/newscenter/rochester-sets-new-record-for-room-temperature-superconductor-455722/.

Coauthors on the papers include lead author Elliot Snider '19 (MS), Nathan Dasenbrock-Gammon '18 (MA), Raymond McBride '20 (MS), Kevin Vencatasamy '21, and Hiranya Vindana (MS), all of the Dias lab; Mathew Debessai of Intel Corporation, and Keith Lawlor of the University of Nevada Las Vegas.

Oasis in the Food Desert: Using the Internet of Things to Support Community-Organized Groceries

Student Researcher: Brandon L. Dunson

Advisor: Dr. Derek A. Petrey

Sinclair Community College

Electronics Engineering Technology

Abstract:

This project fulfilled the capstone project in the Internet of Things (IoT) Cyber Technician Associates of Applied Science (CETT.S.AAS) degree. The Gem City Market (**Figure 1**), is an innovative community project to create a “vibrant, community-centered grocery store... [that] will restore grocery service to Northwest Dayton for the first time in over a decade.” (<https://gemcitymarket.com/about-us/>)

We examined the technological needs of the Gem City Market and determined that we could provide Gem City Market with a low-cost data management and loss prevention tool for large-scale electronic store inventory (microwaves, stoves, mobility scooters, cash registers, etc.) (**Figures 2 and 3**)

Project Objectives:

Each item will receive a radio-frequency identification (RFID) sticker with identification of the inventory item. The database with this information for each item will be stored on a Raspberry Pi mini-computer. This computer will be connected to a wall unit and placed under lock and key. The data from the stickers is to be read either using a PN532 NFC reader (**Figure 4**), or with a mobile device with the free Linktree app. With this system in place, Gem City Market will be able to track and record these large-scale items and possibly identify them if they are removed from the store. We researched the best logistics management software to use and decided to use Sortly.

Methodology Used:

We discussed needs with the President of the Gem City Market Community Board, did a walk-through of the Gem City Market to determine which items would benefit from being inventoried. We then researched the most inexpensive means of meeting this need. We then presented a proposal to the Board. Upon approval, we will proceed with installation and testing.

Results Obtained:

Gem City will have the technology to track up to \$8000 worth of merchandise using technology that costs less than \$150. The technology in this project will benefit the Gem City Market by providing the store with the equipment needed to monitor the inventory they will be using in the store.

Significance and Interpretation of Results:

It was a great opportunity to work with the Gem City Market. I appreciated the experience to show this business how using this technology will allow them to benefit from logistics management as well as saving money for their organization.

Figure 1. Photo (by author) of Gem City Market Exterior.



Figure 2. Photo (by author) of one of the microwaves to be inventoried



Figure 3. Photo (by author) of the stoves to be inventoried



Figure 4. Photo (by author) of the hardware (NFC Hat installed on top of Raspberry Pi)



Acknowledgments:

For my acknowledgments I would like to thank Professor Amaha Sellassie for providing access to the Gem City Market / Community Board for considering my request and thanks to my mentors: my advisor, Dr. Petrey; Mr. Kenzie, my EET Advisor; my EET Capstone Professor, Mr. Hance; my brother Willie Lovelace; and my mother Regina.

References:

Gem City Market. (<https://gemcitymarket.com/about-us/>)
Sortly. (<https://www.capterra.com/p/169199/Sortly-Pro/>)

Microstructure, Heat Treatment, and Applications of Inconel 718 in Aerospace

Student Researcher: Kyle H. Frith

Advisor: Dr. Adele Wright

Columbus State Community College
Mechanical Engineering Technology

Abstract

Inconel 718 is a superalloy that has been in use for over 70 years. There are currently more than a dozen designated Inconel alloys produced by metal manufacturers with applications including furnaces, gas turbines, rocketry, and nuclear facilities. Heat treatment has been critical to the successful use of this alloy, as has an understanding of the microstructure evolution that occurs by altering the heat treatment. With the advent of additive manufacturing Inconel 718 has found continued viability into the future. This project will serve as an examination through existing research of various heat treatments and their applications in aerospace of Inconel 718.

Project Objective

The purpose of this project was to investigate the microstructure mechanisms of heat treatment of Inconel 718 and the specific aerospace problems that are solved by the material science applications of heat treatments.

Methodology Used

Several recent Inconel alloy symposiums were consulted, from which several more specific microstructure scientific papers were considered. The NASA technical reports server was also accessed for historical contractor papers that focused on Inconel 718. Additional information was gleaned from scientific journals as well.

Results

Heat treatment of Inconel 718 consists of an annealing phase and a two-step aging process to produce the combination of strengthening precipitates. For wrought and cast specimens, heat treatments for Inconel 718 have coalesced into two types: sub δ solvus and super δ solvus. In the sub δ solvus heat treatment, the material is heated to 1750°F during the annealing process to create a solid solution with the precipitates fully dissolved into the lattice, which creates a higher strength material. The super δ solvus anneal brings the material to 1900° F. The remaining steps of the treatment are the same as the sub δ solvus anneal but the material post treatment has increased impact resistance and ductility at cryogenic temperatures. Below are reproduced yield strength, percent elongation, and ultimate strength charts of IN718 sheet using data from a NASA contractor report. Table 1 highlights the increased ductility induced by the super delta solvus anneal (Treatment B) while tables 2 and 3 highlight the overall increased strength of the sub delta solvus anneal (Treatment A).

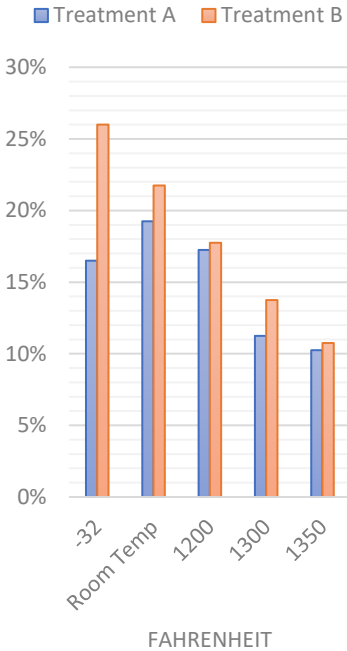


Table 1: Percent Elongation

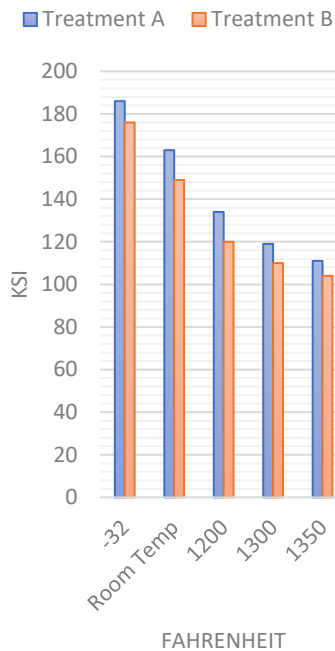


Table 2: Yield Strength

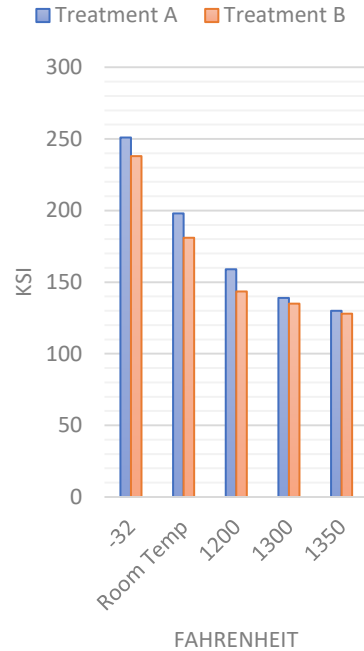


Table 3: Ultimate Strength

Additive manufacturing produces a grain structure that is anisotropic with equiaxed grains in the direction of building. Heat treatment of additive manufactured parts involves a different method than has historically been applied to wrought and cast IN718. The solvus temperature is raised to at least 1976° F for 1 hour followed by the traditional two-part aging process. Below this temperature the material does not get hot enough to fully recrystallize and produces a large coarse grain structure. This is a still actively researched process.

Parts currently produced of Inconel 718 are rocket engine jacketing, liquid hydrogen fuel lines, turbo pump casings, turbo pump rotors, gas turbine rotor hubs, SCRAM jet flame holders, reaction control system nozzles, and aerospike nozzles. Depending upon the heat treatment rotor fatigue and creep can be reduced, the effect of hydrogen embrittlement can be mitigated, and the operational temperature range can be increased by inducing more ductility in low temperatures or higher strength at elevated temperatures.

Conclusion

Heat treatment should vary depending upon operating temperatures and method of manufacture. By altering the heat treatment the operational capabilities of a part can be greatly improved. Additive manufacturing has increased part complexity and an optimum heat treatment is still evolving. Current aerospace vehicle designs utilize Inconel 718 in wrought and cast form and future designs are applying additively manufactured parts.

References

1. Black, J.T. And Ronald A. Kohser. *DeGarmo's Materials and Processes in Manufacturing*. Wiley, 13th ed., 2019.
2. "Inconel alloy 718." *Special Metals*, www.specialmetals.com/assets/smc/documents/alloys/inconel/inconel-alloy-718.pdf. Accessed 30 October 2020
3. "Why Choose Inconel 718 for Aerospace Additive Manufacturing?" *Farinia Group*, www.farinia.com/additive-manufacturing/3d-materials/inconel-718-aerospace-additive-manufacturing. Accessed 11 November 2020.
4. Kracke, Art. "Superalloys, The Most Successful Alloy System of Modern Times – Past, Present, and Future." *Proceedings of the 7th International Symposium on Superalloy 718 and Derivatives*. Edited by E.A. Ott, J.R. Groh, A. Banik, I. Dempster, T.P. Gabb, R. Helmink, X. Liu, A. Mitchell, G.P. Sjöberg, and A. Wusatowska-Sarnek. 2010. pp. 32-33
5. Mahadevan, Sundararaman, Sachin Nalawade , Jung Bahadur Singh , Amit Verma , Bhaskar Paul, and Kishore Ramaswamy. "EVOLUTION OF d PHASE MICROSTRUCTURE IN ALLOY 718." *Proceedings of the 7th International Symposium on Superalloy 718 and Derivatives*. pp. 737-748.
6. Galliano, Florian, Benoit Ter-Ovanessian, Eric Andrieu, Jean-Marc Cloué , Christine Baret-Blanc , Grégory Odemer. "On the influence of temperature on the hydrogen embrittlement susceptibility of alloy 718." *Proceedings of the 7th International Symposium on Superalloy 718 and Derivatives*. . pp. 933-944.
7. Patel, Shailesh, John deBarbadillo and Stephen Coryell. "Superalloy 718: Evolution of the Alloy from High to Low Temperature Application." *Proceedings of the 9th International Symposium on Superalloy 718 & Derivatives: Energy, Aerospace, and Industrial Applications*. Edited by Eric Ott, Xingbo Liu, Joel Andersson, Zhongnan Bi, Kevin Bockenstedt, Ian Dempster, Jon Groh, Karl Heck, Paul Jablonski, Max Kaplan, Daisuke Nagahama, and Chantal Sudbrack. 2018 pp. 23-46.
8. Aoki, Chuuya, Satoru Kobayashi, Tomonori Ueno and Masao Takeyama. "Dependence of Creep Strength on Cooling Rate After Subsolvus Solution Treatment in Wrought Alloy 718." . " *Proceedings of the 9th International Symposium on Superalloy 718 & Derivatives: Energy, Aerospace, and Industrial Applications*. pp. 449-459.
9. Inouye, F. T., V. Hunt, G. R. Janser, mu? V. Frick. "Application of Alloy 718 in M-1 Engine Components." *NASA Contractor Report CR-788*. June 1967
10. Halchack, J.A., R.P. Jewett. "Use of Alloy 718 in the Space Shuttle Main Engine." *Superalloys 718, 625 and Various Derivatives*. Edited by Edward A. Loria. 1991
11. Segersäll, Mikael. *Nickel-Based Single-Crystal Superalloys - the crystal orientation influence on high temperature properties*. 2013. Linköping University Institute of Technology, PhD dissertation.
12. Deng, Donyong. *Additively Manufactured Inconel 718 : Microstructures and Mechanical Properties*. 2018. Linköping University Institute of Technology, PhD dissertation.
13. Bayha, Thomas D., David S. Bergstrom. "Properties and Microstructure of Allvac® 718PLUS™ Alloy Rolled Sheet." *Superalloys 718, 625, 706 and Derivatives 2005*. Edited by E.A. Loria TMS (The Minerals, Metals & Materials Society), 2005
14. Solberg K, Wan D, Berto F. "Fatigue assessment of as-built and heat-treated Inconel 718 specimens produced by additive manufacturing including notch effects." *Fatigue Fract Eng Mater Struct*. 2020;1–11. [https:// doi.org/10.1111/ffe.13300](https://doi.org/10.1111/ffe.13300)

Uncovering the Recipe for Synthetic Mineral Water

Student Researcher: Mystal E. Jackson

Advisor: Regan Silvestri

Lorain County Community College
Department of Chemistry

Abstract

Mineral waters may contain various salts including sodium chloride, potassium chloride, calcium chloride and magnesium chloride. Furthermore, mineral waters may contain various sulfates and bicarbonates. Atomic Absorption (AA) spectroscopy and Inductively Coupled Plasma (ICP) spectroscopy are being used to identify and quantify the various minerals in selected commercially available mineral waters. Further, blind taste tests are being conducted on the mineral waters to identify user preference for flavor. Ultimately, a statistical correlation will be drawn between the analytical data and user preference, identifying what minerals are preferred for taste and in what quantities.

Project Objectives

Sodium, commonly known as salt, comes in many forms including but not limited to table salt, Himalayan pink salt, kosher salt, sea salt and Celtic salt. Sodium is a common element that is important to the human body, needed to control fluid levels, maintain blood pressure and for nerve and muscle function. The flavor of mineral water is important because people will repeatedly choose what tastes good to them. Taste tests are being carried out by multiple test subjects on campus and the data is being recorded; this tells us which water the majority think tastes better. Spectroscopy is being used to analyze and quantify the minerals in various water samples, -to tell us what's in it and specific amounts. The analytical data is being compared to the taste test results and a correlation drawn, which in turn tells us what people prefer to taste in their water. We are de-formulating the recipe for the best tasting mineral water and using this information to create synthetic mineral water.

Methodology Used

The waters studied were among various commercial brands, including spring water, filtered water, alkaline water, soda water and tap water. The subjects used to test for preferred flavors were among various students and faculty. The results were recorded and analyzed. Spectroscopy was then carried out on the samples to find which raw minerals they contained. The quantities needed to obtain these user preference tastes, were also obtained by using methods of spectroscopy. Following the results, an external study was performed by [American Analytical Laboratories, INC](#) to confirm our results.

Results

The commercially available samples contained all or some of the following ingredients, Calcium, Magnesium, Potassium, Sulfate as SO_4 , Selenium and sodium. From the results obtained, we are able to accurately and successfully produce a synthetic mineral water that contains the ingredients to synthesize mineral water preferred by users.

Table 1. Concentrations of Metals

Metals				
Metals	Reporting limit	Reporting Limits	Units	Dilution
Calcium	0.05	0.29	mg/L	1
Magnesium	0.05	0.25	mg/L	1
Potassium	0.5	0.8	mg/L	1
Selenium	0.002	BRL	mg/L	2
Sodium	0.5	35	mg/L	10

Figure 1. Commercial Mineral water and dilution.

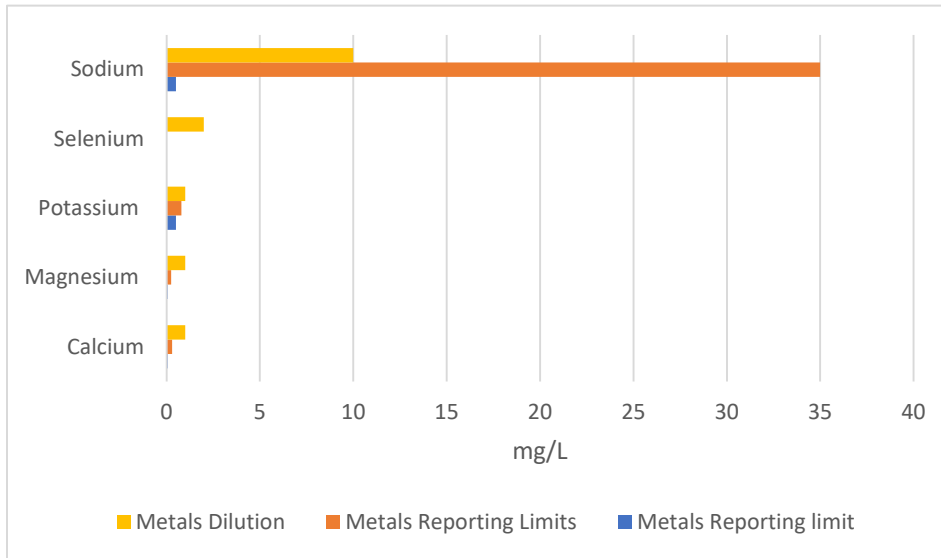
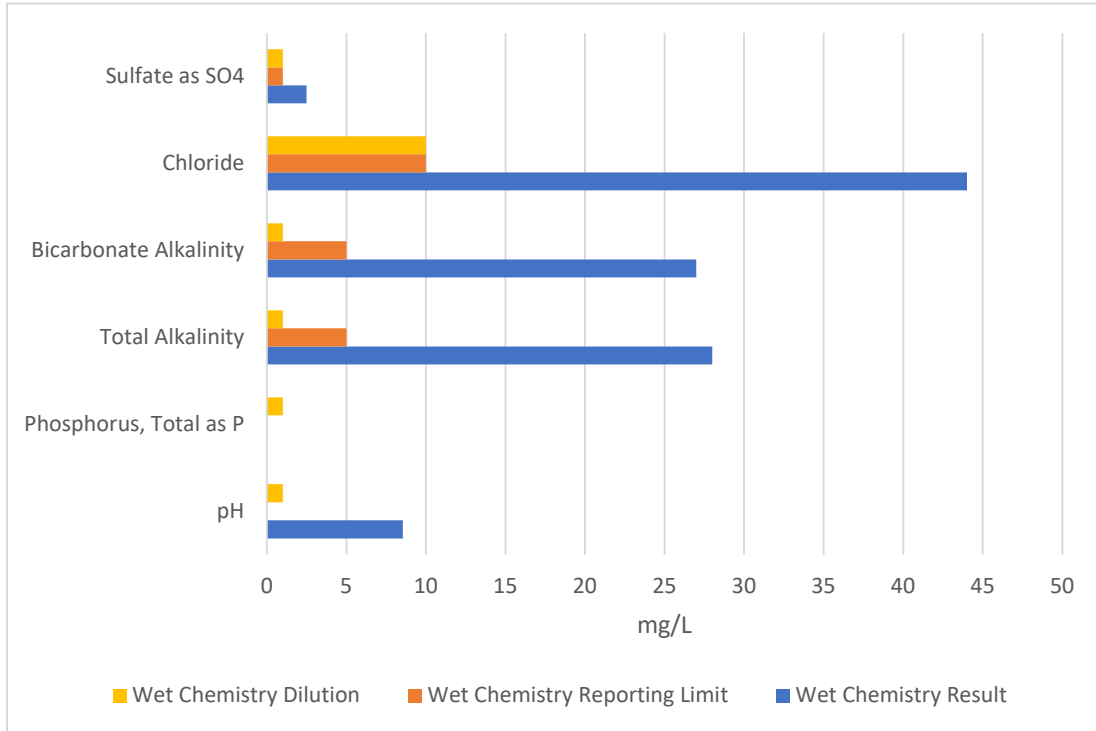


Table 2. Wet Chemistry results.

Wet Chemistry				
	Result	Reporting Limit	SU	Dilution
pH	8.55			1
Phosphorus, Total as P	BRL	0.01 mg/L		1
Total Alkalinity	28		5 mg/L as CaCO ₃	1
Bicarbonate Alkalinity	27		5 mg/L as CaCO ₃	1
Chloride	44		10 mg/L	10
Sulfate as SO ₄	2.5		1 mg/L	1

Figure 2. Wet Chemistry Properties.



Reduction of Voiding in Pb-Free Solder Joints on PCBs Processed in Varying Thermal Profiles of a Solder Reflow Oven

Student Researcher: Ryan M. Palmer

Adviser: Johnny Vanderford

Lorain County Community College
Micro Electro-Mechanical Systems (MEMS)

Abstract

Solder voids are defects common in Pb-free solder joints that are caused by many factors, the most notable of which is the reflow process. Reflow variables that affect void formation were changed while observing the percentage of voids formed with an X-ray system. Results showed that peak temperature had the largest effect on voiding whereas varying soak time had the least amount of change.

Introduction

What are solder voids, why are they undesirable, and how can they be reduced? Solder voids are the result of a bubble of gas being trapped within the solder [1]. These gases are mainly formed during the reflow process by evaporating solvents and flux compounds contained in solder paste. These gasses can remain in the solder joint due to a number of factors: surface tension, partially solidified solder blocking escape, parts of the component or pad that have been unwetted by the solder or trapped by the component itself. Voids contribute too many undesirable qualities in solder joints: they reduce the structural reliability of the connection, they reduce the ability to transfer heat out of components, and to a lesser extent they affect the electrical resistance of the joint. The IPC-A-610 standard considers a solder joint to be defective if more than 30% of its area in an X-ray image is made up of voids. [3] Typically, the reflow profile is one of the biggest variables that contributes to the formation of voids. [1] Various parts of the reflow profile can be altered to reduce the amount of voiding, these parts are profile length, heating ramp rate, preheat/soak time, peak temp, reflow time (Temperature Above Liquidus, TAL), and cooling ramp rate.

Objective

The objective of this paper is to study the effect of different reflow profiles on solder voiding, to create a better understanding of how the reflow process effects solder voiding, and to document any findings.

Experiment

Seven identical custom PCBs (printed circuit boards) will be made for this test by JLCPCB. These boards will be processed identically up until the reflow oven. The test PCBs will be printed with a Panasonic SPG stencil printer using FCT's Amp One low voiding Pb-free solder paste and inspected with an Omron VP5200-V stencil print inspection unit for accuracy of print. They will then be populated by a Panasonic NPM-W2 high-volume SMT pick & place machine with a variety of standard SMT components including a BGA component, and finally visually inspected. These boards will then be separated into seven tests. The control test will use the recommended linear profile from the solder paste datasheet [2]. The next six tests will change the peak temperature, time at liquidus (TAL), and soak times from the stock reflow profile Table 1. After the boards have been reflowed in a Heller 1826 MK5 eight zone reflow oven, they will be tested for voids with a Creative Electron TruView Prime X-ray microscope and visually inspected with an AmScope SM-4NTP stereo microscope. The part from which the voiding measurements will be taken will be a WBGA package part number (W9751G6KB-25). Visual inspection will be taken from an SOIC-8 NE555DR Integrated Circuit (IC) and will be judged on visual quality under 16x magnification. A solder joint is considered visually passing if it has: visually reflowed, wetted and bonded to the pad and lead, and does not contain any anomalies. Proprietary software from Creative Electron will be used to take automated measurements of BGA voiding.

Table 1: List of temperatures of each reflow zone for one control and six test reflow profiles.

Temp in C	Parameter changed	preload	Heating	Heating	Heating	Heating	Heating	Heating	Heating	Heating	cooling	Cooling
	time/s	0	33.75	67.5	101.25	135	168.75	202.5	236.25	270	302	334
	cm	0	33.75	67.5	101.25	135	168.75	202.5	236.25	270	302	334
	Zone	zone 0	zone 1	zone 2	zone 3	zone 4	zone 5	zone 6	zone 7	zone 8	zone 9	zone 10
Control	N/A	25	65	115	150	175	200	220	245	220	175	125
Test 1	Peak Temp Increased	25	65	115	150	175	200	220	275	220	175	125
Test 2	Peak Temp Decreased	25	65	115	150	175	200	220	220	220	175	125
Test 3	TAL Increased	25	65	115	150	175	220	235	245	220	175	125
Test 4	TAL Decreased	25	65	115	150	175	200	200	245	200	175	125
Test 5	Soak Time Increased	25	65	150	160	175	200	220	245	220	175	125
Test 6	Soak Time Decreased	25	65	115	140	170	200	220	245	220	175	125

Results

Test one reflowed properly but had the largest amounts of voiding of all the tests. Test two had low voiding but did not visually reflow properly. Test three had higher voiding than test four but also passing visual quality. Best results were found with test number four, it had the lowest voiding of all the passing tests and was visually passing. Test five had higher voiding than test four or six and passing visual quality. Test six had lower voiding than test 5 and had passing visual quality. Summary of results is listed in Table 2. Additional results and images of voids and more can be found at:

<https://drive.google.com/drive/folders/101DOW9I42UH2x26UsagTEqPHxslDr2Ft?usp=sharing>



Table 2: Results of experiment including X-Ray void measurements and visual inspection

Test #	Parameter Changed	Highest voiding% BGA	Top 5 Average voiding %	IPC Voiding Pass/Fail	Objective Visual Quality of SOIC-8
Control	N/A	11.2%	7.06%	Pass	Passing
1	Peak Temp Increased	12.64%	10.4%	Pass	Passing
2	Peak Temp Decreased	3.46%	2.79%	Pass	Incomplete reflow
3	TAL Increased	6.9%	5.79%	Pass	Passing
4	TAL Decreased	4.6%	1.9%	Pass	Passing
5	Soak Time Increased	9.89%	3.54%	Pass	Passing
6	Soak Time Decreased	6.56%	2.69%	Pass	Passing

Conclusion

Highest voiding for both top voiding and top 5 voiding average was test one, the temperature increase may have increased the amount of volatile components that became gaseous, increasing the amount of voiding. Best voiding result was found with the peak temperature decrease test (test 2), but the lack of good reflow suggests that the balls on the BGA did not have enough time and or heat to melt. Since the balls didn't melt they could not have trapped any gas. In the X-ray image of test two there are few to zero voids present in the center of the joint suggesting that the pre applied ball on the BGA did not melt. The best voiding result with a visually passing reflow was test 4. This test had a lower time above liquidus, but the longer soak time that was inherently created could have driven off a large portion of the volatile components in the solder paste, leading to less voiding. Test five had a relatively high amount of voiding, this might be to the flux being driven off to early in the reflow process. Test six had less voiding than test five, suggesting that there was sufficient flux at TAL for a good joint.

References

[1] Keith Sweatman, Takatoshi Nishimura, Kenichiro Sugimoto, Akira Kita, Controlling Voiding Mechanisms in the Reflow Soldering Process, https://www.circuitinsight.com/pdf/controlling_voiding_mechanisms_reflow_soldering_process_ipc.pdf, 2-15-2021, Nihon Superior Co., Ltd.

[2] <https://fctsolder.com/wp-content/uploads/2020/10/Amp-One-Solder-Paste-TDS.pdf>

Special thanks to FCT for donating solder paste for this experiment.

[3] IPC-A-610 "Acceptability of Electronic Assemblies", IPC-Association Connecting Electronic Industries, Bannockburn, IL 60015, USA: Article 8.3.12.4

Microcystin Detoxification Through Glutathione Conjugation

Student Researcher: Blaine C. Thompson

Advisors: Dr. Kathryn Durham & Michelle Neudeck

Lorain County Community College & Bowling Green State University
Department of Biology

Abstract

Algal blooms have become a major public health concern within the past several decades. Although algal blooms are seen universally, our research is focused on the blooms in Lake Erie and the Sandusky Bay. These blooms are driven by two types of cyanobacteria: *Microcystis aeruginosa* and *Planktothrix agardhii* respectively. The underlying cause is excess runoff of nutrients from nearby farm fields post-fertilization. During bloom periods, these cyanobacteria release toxic amounts of the hepatotoxin, microcystin, which can cause permanent liver damage in living organisms exposed to the contaminated water.

Once ingested, microcystin binds and inhibits protein phosphatases 1 and 2A that are found within liver cells. These phosphatases are important for maintaining the cytoskeleton and when inhibited causes collapse and ultimate death of the cells. In response to microcystin exposure, the hepatocytes produce a molecule called glutathione which can also bind to microcystin. Once bound by glutathione, the microcystin molecule is converted into a nontoxic substance called mercapturic acid and subsequently eliminated renally from the body. Unfortunately, with exposure to high amounts of microcystin, the liver cannot produce adequate amounts of glutathione to neutralize the toxin.

Project Objectives

Although the algal bloom crisis is being researched by many different universities worldwide, to date the primary focus has been on how to eradicate the blooms. At Lorain County Community College, the focus of our research is to create an antitoxin that will treat individuals exposed to the toxin. In this study, human liver cells will be exposed to a known amount of microcystin, and then treated against a concentration curve of varying amounts of glutathione. This will determine the concentration of glutathione required to neutralize the microcystin.

Methodology Used

This research project is currently on-going. The methodology used in the entirety of this project is being assessed after each individual phase has been performed, and results obtained. As of the typing of this preview, an immunofluorescent antibody assay has been performed and results from the assay are currently being assessed. This method was chosen in order to determine the binding affinity between the microcystin toxin, the glutathione, and the protein phosphatases within the hepatocytes.

Significance and Interpretation of Results

In light of the COVID-19 pandemic, much of the laboratory work and progress required for this project has been hindered, but work is still being done. With an abundance of determination, the future results from this research will at minimum provide more light on the binding properties of microcystin within the cellular environment, and at maximum provide a credible *in vitro* study displaying the neutralizing capabilities of glutathione on microcystin.

A Study on Solder Fume Inhalation and the Long-Term Health Effects on Industry Workers

Student Researcher: Emily T. Williams

Advisor: Johnny Vanderford

Lorain County Community College

Engineering Information Business Technology - MicroElectroMechanical Systems (MEMS)

Abstract

Lead soldering is a common electronic manufacturing process used in many companies that requires the use of equipment to create safe and healthy work environments. With minimal recognition of regulation and prioritization in the United States to protect the manufacturing workforce from the severe consequences of rosin core flux intake and lead poisoning, most easily obtained from direct inhalation, workers in industries that use lead solder materials and components are unknowingly subjecting themselves to long term damage without proper knowledge and safety precautions. Lead poisoning is capable of being cured but is easier to prevent. Fume extractors are one of several types of equipment used to minimize and prevent the particulates and airborne toxins generated from lead solder being in liquid state with activated fluxing agents used with it. The goal of this experiment is to monitor and inspect a fume extractor for the quantity and quality of extracted lead particulates and flux residue while keeping lead and lead-free solder at liquid state with the activated fluxes. Results showed that after 40 hours of solder at liquid state, the fume extractor filtered a significant amount of materials that was observable using time-lapse photography.

Introduction

The human body is a complex and resilient ecosystem that is capable of healing itself over time, with trillions of cells working together in order to maintain a healthy equilibrium. The immune system detects bacteria and viruses, but from the gradual deterioration of white blood cells due to exposure to lead and other toxic substances, the immune system is less efficient in its ability to fight off infections and other diseases. Lead is a soft and malleable material with many manufacturing benefits that have previously outweighed the environmental and health related costs in the United States; because of the accessibility, low cost, and predominant use in US military electronic products, it has continued to be used in everyday production, whereas regulations and limitations of lead use have been adopted across Europe. Occupational exposure, including but not limited to the electronics manufacturing industry, is a major source of lead poisoning in adults with an estimated 3 million workers in the United States potentially exposed to lead in the workplace according to the National Institute of Occupational Safety and Health (NIOSH). [1] Sentry Air Systems reports that, Fume extraction utilizes fans to pull the fumes and particulates as small as 0.12 microns into the filtration system to create a recirculating airflow. [2] The particulate filters use efficiency fiberglass and intercept particles, smoke, and other airborne particulate to prevent asthma and allergies. The size of the particles filtered in fume extractors is similar in size to that of the particulates produced by tobacco smoke. [3] Activated carbon filters are used to absorb organic vapors to collect odors and chemical fumes. Based on research and practical studies, preventing lead and flux fumes from being inhaled is as important to someone's health as the prevention of tobacco smoke. For best efficiency of these carbon filters, once they become oversaturated they are typically replaced annually or as necessary based on accumulation of contaminants blocking airflow.

Objective

The main objective of this project is to produce visual documentation of the quality of a fume extraction filter over the course of 40 hours of lead solder in heated liquid state and activated fluxing agent producing fumes. RoHS compliant solder is also used in conjunction with the lead-based solder for rosin core fume production. With the equipment utilized to heat the flux and solder to the point of liquidation, the substances that become liquid will also experience vaporization due to the Ideal Gas Law. These fumes are produced regardless of safety precautions and fume extraction being present, so it becomes the responsibility for both the heads of departments exposed to these toxic fumes to implement safety measures for their workforce and enforce their use, as well as the employees who make the conscious decision of protecting their bodies and health against the overwhelming evidence showing the inhalation of lead and flux fumes is detrimental to the human body. The use of a fume extractor significantly reduces the number of airborne lead particles and flux fumes typically caused by soldering, limiting the potential of these toxins being inhaled and absorbed by a human body as they are diverted through the fume extractor's hose.

Experiment

The environment in which the experiment was conducted was in an isolated lab with standard ventilation flow via HVAC at Lorain County Community College. A soldering pot model CT-21C was used to melt Kester rosin core leaded solder wire SN63PB37-.025 and AIM flux core unleaded solder wire SN100C-.032 in conjunction with activating ChipQuik SMD4300TF10 no-clean tack flux and Amtech MC-559-V2-TF no-clean tack flux. A Metcal fume extractor model BVX-201-KIT was able to collect the particulates through one hose and distribute flux and solder fumes onto the filter. The solder pot was continuously supplied with approximately 1 mL of flux and variable amounts of solder periodically while the contents in the solder pot remained in molten state and continuously evaporated. Every three hours, the filtering components of the fume extractor were observed; specifically, the carbon filter was photographed while continuing to observe the particulates collected over 40 hours - in intervals of photos being taken at 3 hours each up until 39 hours of data was collected, with one additional photo taken at 40 hours.

Results

The results initially collected from the experiment were not prominent until comparing the photos next to each other. By doing this, seeing the intricate changes between the filter at different time intervals showed the development of color and the size of the location and distribution of particles expanding. With a collection of all fourteen photos together, there is a steady development both of the darkening of color and expansion of size. Figure 1 shows the images taken of the filter at 0 hours, 15 hours, and 40 hours which demonstrate the steady accumulation of solder particles and activated fluxing agent fumes. All pictures and additional information can also be found here:

<https://drive.google.com/drive/folders/1EP-15ZvaUdWILJodXJuN02EWI21d743I?usp=sharing>

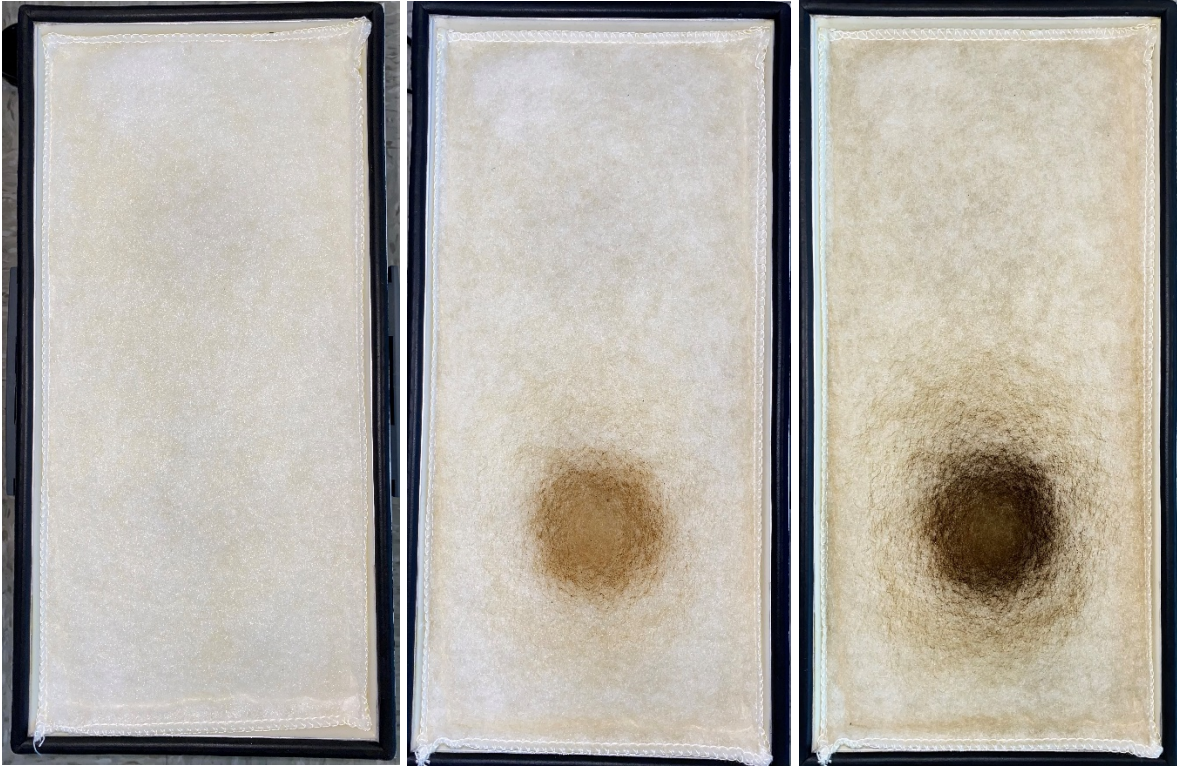


Figure 1: Filters showing accumulation of extracted lead solder particles and activated flux fumes taken at the following times throughout experiment: 0 hours (left), 15 hours (middle) and 40 hours (right)

Conclusion

Based on the data collected there is significant evidence that a majority of the fluxing agent fumes and solder particles are collected in the fume extractor filter. Without the fume extractor and filters these particles would be airborne and in close proximity to an operator to breathe them in. The conclusive data suggests that ventilation equipment such as fume extractors or other types of personal protective equipment (PPE) such as masks are recommended to be required by anyone performing soldering using Pb based solder or using fluxes in a solder process. The amount of material collected and photographed in the fume extractor only represents an average workweek for someone employed in electronic manufacturing working with lead solder materials. It is worth taking into consideration that a substantial amount of additional materials would be collected if this experiment were run for a typical one year. Additionally, it is alarming to consider that without a fume extractor that someone employed in electronic manufacturing would be incidentally subject to breathing in these materials if it weren't for the fume extractor, thus deteriorating the immune system due to lead poisoning. Based on the results of this experiment, anyone currently using Pb based solder or fluxes in an electronic manufacturing environment discuss the use of PPE or fume extraction methods with their management or supervisors and that management consider investment of funds to purchase proper fume extractors to mitigate any health issues.

1. <https://www.ncbi.nlm.nih.gov/pmc/articles/PMC4961898/>
2. <https://www.sentryair.com/blog/product-review/fume-extractors/what-is-a-fume-extractor/>
3. <https://www.sciencedirect.com/science/article/pii/S0095852260900374#:~:text=From%20these%20measurements%20it%20was,between%200.2%20and%200.25%20micron>

Flavor Profile of Moonshine Homemade from Apples and Double Distilled

Student Researcher: Andrea L. Zirkle

Name of Advisor(s): Dr. Regan Silvestri

Lorain County Community College
Science and Mathematics

Biography:

Andrea Zirkle is currently a student at Lorain County Community College pursuing an Associates of Science degree. Following completion of her Associates degree she will continue her education through Lorain County Community College's University Partnership with Bowling Green State University, to pursue a Bachelor's of Science in biology with a minor in chemistry. Andrea has been conducting independent research at Lorain County Community College for two years under the direction of Professor Regan Silvestri on the science of the flavor of whiskey. Andrea presented her work on the flavor of apple moonshine as influenced by the distillation process at the Society for Applied Spectroscopy May Conference in spring 2019, and will also present her work at the Ohio Academy of Science annual conference in spring 2020.

Abstract:

Homemade moonshine prepared from fermented apples and double distilled was analyzed by gas chromatography-mass spectroscopy (GC-MS). The volatile compounds thus identified serve as a flavor profile of the spirit. As the moonshine has been fermented from apples, it was anticipated a-priori that the flavor profile would contain a wealth of pleasant aroma fruity esters. However, it was found that the flavor profile of the apple moonshine consists mainly of longer chain alcohols, butanols, pentanols and hexanols, which serve as off-flavors. Overall, it was found that the flavor of the apple moonshine is dominated by 3-methyl-1-butanol which imparts a fusel, alcoholic, and fermented flavor often described as pungent. It is hypothesized that the fruity ester flavors were unfortunately removed during the double distillation process, which brought the spirit to 170 proof.

Publications:

"Flavor Profile of Moonshine Homemade from Apples and Double Distilled", Proceeding from Society for Applied Spectroscopy 63th Annual May Conference, May 22, 2019

"Flavor Profile of Moonshine Homemade from Apples and Double Distilled", The Ohio Journal of Science, Volume 120, No. 1, April 2020

Education Scholars

Seventh Graders in Space

Student Researcher: Lillian C. Brautigam

Advisors: Dr. Todd France & Dr. Tena Roepke

Ohio Northern University
School of Science, Technology, and Math

Abstract

This lesson is geared toward seventh grade math students. This math lesson incorporates activities from the NASA lessons “How Big is Our Solar System?” and “Exploring Your Weight Across the Solar System.” A key part of the seventh-grade math standards is learning and applying ratios and proportional relationships. Students will learn how to form a proportion in order to convert different measurements and weights from Earth to different planets in our solar system. Students will convert different measurements to different units, find weights on different planets, and create scale drawings of the planets. Incorporating the NASA lessons into these state learning objectives allows the students to apply their new knowledge in a real-world situation. This lesson is geared to spark interest in the mathematics of space and our solar system.

Project Objectives

The objective of this lesson is for seventh grade students to learn how to apply ratios and proportions to space inspired activities around weight conversions. Students should feel like they are traveling through space as they travel around the classroom from planets to moons and find the weights of different objects at each of these different locations.

Methodology Used

Students will need to know different units. On Earth, we typically measure our weight in pounds. A weight (measured in Newtons) is determined by the multiplication of a mass (measured in kilograms) multiplied by the acceleration of gravity (measured in meters per second squared). These labels may be difficult for seventh grade students to understand, but it is most important that they realize that each measurement used must be in the appropriate units before applying in the equations. Students will be provided different measurement ratios so they can convert their measurements appropriately.

Results Obtained

The main activity of this lesson asks students to convert the weights of three objects on Earth to the appropriate weight on different planets and moons using the provided gravity for each location. The students will be provided the mass of each object in kilograms. They will create a chart that lists each object’s weight on each selected location. The classroom should be decorated with different pictures of the planets and moons and their corresponding gravities. Students will travel from planet to planet to obtain their results. Although I have not taught this lesson in a classroom yet, I intend for students to work together although they will all have three different objects with different masses. At the end of this activity, students will be able to accurately use the conversion factors and the appropriate equations to find the weight of each object on a variety of planets and moons.

Significance & Interpretation of Results

It is important for students to have a math activity that allows them to move around the room and apply their knowledge to a new topic. Students will be inspired by this space themed lesson because it will be

different than what they are used to in their math classes. This lesson not only teaches students about different mathematical conversions and equations, but it allows them to understand how gravity effects the weight of objects on different planets and moons.

Figures & Charts:

This is an example of the chart students will create to keep their data from the activity. This example is for an object with a mass of 85 kilograms.

Location	Gravity (meters/sec ²)	Weight (Newtons)	Weight (pounds)
Earth	9.8 m/sec ²	833 N	187 lbs

Acknowledgements & References

This lesson was inspired by the NASA lessons “How Big is Our Solar System?” and “Exploring Your Weight Across the Solar System.” Many extensions can be created to this lesson with information from these resources.

Density as a Representation of Layers of the Earth

Student Researcher: Savannah E. Carter

Advisor: Dr. William Theisen

Ohio Northern University
Physics & Secondary Science Education

Abstract

Density is a basic concept of science which in which students must understand the relationship between mass and volume. Science and mathematics are often concepts which students fail to see the purpose or “bigger picture”. They wonder why phenomena such as density impact their life or why they should care about them. In this middle school lesson, students combine the mathematical basis of the density formula with an understanding of how density resembles the layers of the Earth. Students will solve the density formula for several household liquids such as honey, dish soap, vegetable oil, etc. They will then predict which substances are most dense based on their calculations. The students can then test their predictions by putting all the substances in a graduated cylinder and watching them settle based on density. After students analyze their data and observations, they can draw conclusions and compare their finding to the layers of the Earth and how the layers differentiate based on density. In gaining a further understanding of the layers of the Earth, students can more fully grasp the characteristics of their home planet. Further studies could be completed with students to compare the density and composition of Earth with other planets to greater understand outer space as well. In combining mathematics, hands-on demonstrations, and real-world applications, the goal is for students to develop a more complete understanding of a complex scientific topics both here on Earth and beyond.

Project Objectives

The key for students throughout the lab is to not only reflect on their prior knowledge of mathematical practices in their use of formulas, but to also incorporate what they know about data collection and formula trends to draw conclusions about an unfamiliar scientific phenomenon. Students will further develop their understanding of the physical earth and its component through scientific inquiry and research-based methods. Students will gain an understanding of the relationships between mass, volume, and density, and then use this knowledge to carry out research in a lab setting. In their acquisition of data, students will be able to formulate predictions based on their calculations and observations throughout the lab. With these predictions, students will be able to interpret the relationships between density and real-world phenomena such as the layers of the earth and apply their conclusion to conceptual questions or hypothetical scenarios.

Methodology Used

Students were given their data packets prior to entering the class on the day of the lab. They were tasked with looking into the details of the procedure and then told to come to class with any questions they had pertaining to the lab. As students enter, they had an opportunity to ask questions to address any misconceptions they might have prior to beginning their research. Students then broke up into small lab groups in which they worked together to acquire data. The students began by finding the mass of their graduated cylinder, which would later be utilized in calculating the density. The students then asked for five milliliters for one of the substances they were working with. Students were given a list of all the substances prior to entering the class on the day of research. Students were then tasked with finding the mass of the substance with the graduated cylinder and using subtraction to find the mass of

just the substance. After students calculated both mass and volume, they could use their density formula to solve for the density of the substance. After they calculated the density for all six substances, the class was responsible for predicting how the substances would settle if they were all put into one large graduated cylinder. After showing their predictions to the instructor, they could test their theory by putting all their substances into a large graduated cylinder. After analyzing how the substances settle, the students were able to draw conclusions about the accuracy of their predictions. Once finished with the data collection portion, students were responsible for completing a series of conceptual question which connected the idea of density to both their research within the lab as well as real-world scenarios. The class period was finished with students working through the computations and conceptual questions and discussing ideas with their lab group to build on each other's knowledge of the unfamiliar material. The students used this time also as a final opportunity to ask the instructor any questions they may have regarding their data or the questions prior to leaving the class.

Results Obtained

Students obtained a variety of results depending on the accuracy of their density calculations. Most students struggled to obtain accurate mass and volume calculations, which led to inaccurate interpretation of density for a specific substance. Thus, when the students went to predict the order the substances would settle in the large graduated cylinder, their predictions were often incorrect. However, some students were able to find the correct order of substances which was, from least dense to most dense, rubbing alcohol, vegetable oil, water, dish soap, syrup, and honey. For the students who did not get this result, though, most were able to explain their results and draw conclusions about what should have ideally happened throughout the experiment even if their results did not match the theoretical results.

Significance and Interpretation of Results

From the results it can be seen that the students need more practice acquiring accurate measurements within a lab setting. Since most of the students were able to correctly apply the density formula to the variables and use the density to predict the order the substances would fall within the graduated cylinder, it became clear that the student errors within the lab lied in the accuracy of their measurements. Thus, moving forward, students will receive more opportunities to practice data measurement both in lab activities and through simple assessments in order to further develop students' research skills.

Figures/Charts

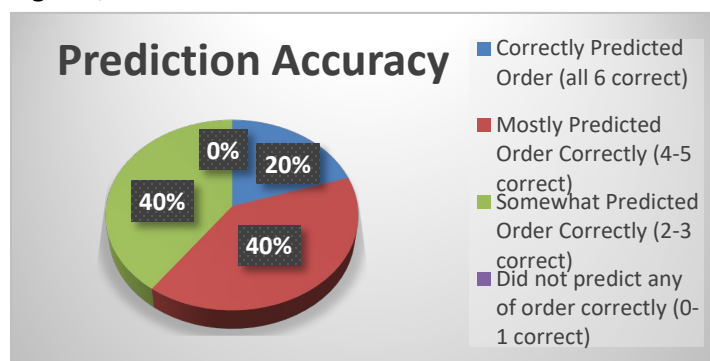


Figure 1. Prediction Accuracy

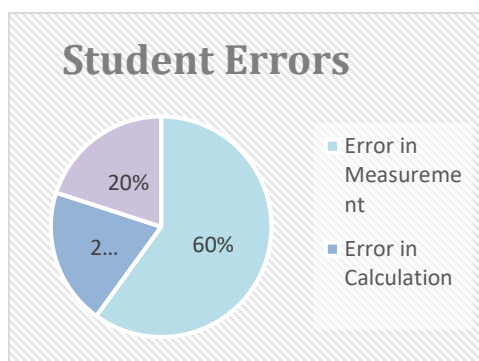


Figure 2. Student Errors

Acknowledgments and References

A special thanks to Dr. Theisen for his support in the theory and research of the lab in understanding content for a specific age group, as well as my cooperating teacher from Lima Sci Tech for her support in the classroom. Thanks to the Ohio Northern University Education department as well for their support in development of appropriate education practice, and their encouragement for me as I learn and further develop as an educator.

Exploration of the Elements and Space Craft

Student Researcher: Emma N. Christman

Advisor: Dr. Morwer

Marietta College
Department of Education

Abstract

Students learn in a variety of different ways including hands on experience, observation, self-exploration, auditory, visual, collaborative projects, as well as much more. It can be difficult for students to fully comprehend and apply information until experienced and encountered in multiple different ways. The purpose of this project is to make meaningful connections between the periodic table of elements and rocket fuel used in space craft. Students will be introduced to the following: the history of different combustible elements (such as hydrogen seen in the Hindenburg Disaster of 1937), real world application of elements in the rocket fuel of spacecraft, and some of the women who helped pave the way for space exploration. Additionally, students will be asked to explore elements and families on the periodic table to make their own connection between elements and real-world applications. By making connections between real-world-application and the periodic table of elements, students will be able to better understand chemistry by changing their perception of the elements from purely abstract to more concrete thought.

Objectives and Pedagogy

The main objectives of this lesson were for students to be able to understand why certain elements are used in rocket fuel, to infer similar logic to other uses of certain groups/families on the periodic table, to summarize their findings of real-world applications of elements, to identify the family's location on the periodic table, and to present findings about assigned family of elements to the class. An additional goal of this lesson is for students to see themselves better reflected within science, particularly those who identify as female or come from various cultural backgrounds that remain underrepresented within the field of science. This lesson is geared toward a physical science class and aligns with Ohio's State Standards to "explain why elements are grouped into families" (PS.M.3) and to "identify metals, nonmetals, metalloids, alkali metals, alkaline earth metals, halogens and noble gases based on their positions on the periodic table" (PS.M.3) [1]. Educational theory within this lesson includes scaffolding, Bloomsburg Taxonomy, an interactive lesson whereby students receive dual coding through a variety of sources and a synthesis task which allow students to make connections to outside content [5].

Required Resources

The resources for this lesson include: teacher and student access to internet, online bingo review game (<https://bingobaker.com/view/3888416>), group research worksheet (Figure 1), Hindenburg disaster video (<https://youtu.be/rWeO1q0gHJE>), and exit slip (Figure 2).

Lesson Methodology

The lesson began with a review activity (Bingo Identification) to help support the various vocabulary words listed above related to prior academic knowledge. This activity involved students playing a game of bingo or "atom." Students were then reminded of the location of the different families and how valence electrons may play a role in family properties. The main portion of the lecture then began with a discussion about the uses of oxygen, aluminum, nitrogen, and hydrogen in rocket fuel [2, 3]. The Hindenburg disaster video was presented to further reinforce the combustible nature of hydrogen when

reacting with oxygen to form water. Within the next section of the lecture, students were introduced to Claudia Alexander who was an African American woman born in Canada and worked within NASA's Jet Propulsion Laboratory [4]. Students were also given the example of radioactivity by introducing Marie Curie's research. After the lecture portion was completed, the class was released into smaller groups to do a worksheet on an assigned family of elements from the periodic table. Once completed, students presented their findings orally to the class. At the end of presentations, an exit slip was completed by the students to evaluate overall understanding of specific topics within the lecture portion.

Results and Conclusions

The lesson was presented to two different classes. One was a 9th grade physical science class, and the other was an 11th grade chemistry class. In the physical science class, students were able to make meaningful first encounters with the families of the periodic table but had some issues citing sources on the worksheet. In the chemistry class, the lesson was more of a review with some new concepts related to element application which allowed the chemistry to make deeper connections with the material. Both classes showed a significant increase in understanding related to periodic families and real-world application of elements. However, due to time constraints neither class was able to complete exit slip within the same class period after the worksheet presentations.

Based on these results it can be concluded that students were able to make meaningful connections with the lesson materials and infer similar logic to other families on the periodic table. Future use of this lesson can be further improved by turning the worksheet into a group-homework assignment or by turning the exit slip into a quiz to be completed at a later date. Additionally, increased instruction on utilizing and citing web sources would prove beneficial for most students.

Figures

Assigned Family Name:

Group Members:

1. What elements are included in this family?
2. Do the elements in this family have similar properties? If so, what are the properties? Why do you think they might have these similar properties?
3. What are some real-world applications of at least 2 elements within this family?

Name:

1. What is made by burning rocket fuel in reactions that provide energy?
 - a. water vapor
 - b. ammonium perchlorate
 - c. carbon monoxide
 - d. oxygen gas
2. Hydrogen led to the Hindenburg disaster because it has what property?
 - a. lighter than air
 - b. extremely low boiling point
 - c. highly combustible
 - d. helium caused the explosion (not hydrogen)
3. Which scientists pioneered research on radioactivity?
4. What 3 things did you find most interesting from this lesson?

Figure 2. Example Worksheet

Figure 1. Example Exit Slip

References

1. Ohio's Learning Standards for Science. (2019). <http://education.ohio.gov/getattachment/Topics/Learning-in-Ohio/Science/Ohios-Learning-Standards-and-MC/SciFinalStandardsMC060719.pdf.aspx?lang=en-US>
2. Perry, B. (2016a). We've got (rocket) chemistry, part 1. <http://blogs.nasa.gov/Rocketology/2016/04/15/weve-got-rocket-chemistry-part-1/>
3. Perry, B. (2016b). We've got (rocket) chemistry, part 2. <http://blogs.nasa.gov/Rocketology/2016/04/21/weve-got-rocket-chemistry-part-2/>
4. Smith, Y. (2018). Claudia Alexander and her life well-lived. <http://www.nasa.gov/image-feature/claudia-alexander-and-her-life-well-lived>
5. Using Interactive Pedagogy. (n.d.). Retrieved 2021, from <https://schoolguide.caseli.org/focus-area-3/classroom/integration-of-sel-and-instruction/using-interactive-pedagogy/>

Comparing and Contrasting the Planets

Student Researcher: Nicolette M. Hoon

Advisor: Erica Miller Arpajian

Cleveland State University
Department of Teacher Education

Abstract

This written report for the NASA/ Ohio Space Grant Consortium Education Scholarship focuses on my Comparing & Contrasting the Planets Special Education Unit Plan. I will refer to this unit plan in my response along with my personal experiences to complete this written report. The topics covered include the rocky planets, the gas planets, and comparing/contrasting.

Keywords: the rocky planets, the gas planets, and comparing/contrasting

Our classroom is learning about earth/space science, focusing on the solar system, in science through a three-lesson unit plan. My Mentor Teacher (Ms. L) and Paraprofessional (Mrs. M) stated that they would like my NASA/ Ohio Space Grant Consortium Education Scholarship to encompass the topic comparing and contrasting the planets. After collaborating with them and speaking with Susan Kohler (NASA EPDC Educator Specialist); I gathered resources/ideas to create my own PowerPoint. This unit plan will focus on comparing and contrasting planets within the solar system. The student will learn to correlate the rocky planets (inner planets) with Mercury, Venus, Earth, and Mars. Along with correlating the gas planets (outer planets) with Jupiter, Saturn, Uranus, and Neptune. This includes recognizing and sorting the inner and outer planets on the provided venn-diagram pre/post assessment. The unit plan will introduce how to determine the planets place within the solar system, recognize the similarities and differences between the inner/outer planets, how the moon orbits around the sun, the stages of the lunar cycle, and how the earth's tilt causes seasons.

My placement is in a 6th-8th grade Multiple Disabilities/Autism Unit. Our classroom is broken up into two groups for differentiation as organized by Mrs. L at the beginning of the academic year. The Cavaliers (struggling learners) group includes four scholars in the class, while the group Lakers (excelling learners) group consists of the other four scholars. Thus, the Cavaliers and Lakers group will complete activities based on their comprehension level. Each lesson will involve a pre/post assessment of matching the inner/outer planets in a venn diagram. The scholars will engage in a KWL chart at the beginning and the end of the unit to reflect on their knowledge. To begin the lesson, scholars will be prompted to draw what they think the solar system looks like. The scholars will share their visuals and engage in a discussion regarding what they know about the solar system and what they want to learn. Afterwards, we will explore the NASA solar system online experience. The scholars will review the Planetary Posse Space School Musical (produced by NASA JPL Edu). At the end of the unit, the scholars will complete a Play-doh scale model of the solar system.

The first lesson will focus on the rocky planets (inner planets) Mercury, Venus, Earth, and Mars. A student will be assigned to each planet to present the findings. This will include how long a year is, the size compared to earth, the color, origin of the name, and the temperature. A scholar will be chosen from the wheel of names. They will present the rock planets poster to provide a review to their classmates. The scholars will engage with the venn diagram as a post-assessment. The second lesson will focus on the gas planets (outer planets) Jupiter, Saturn, Uranus, and Neptune. A scholar will be assigned to each planet to present the findings. This will include how long a year is, the size compared to earth, the color, origin of the name, and the temperature. A scholar will be chosen from the wheel of names.

They will present the gas planets poster to provide a review to their classmates. The scholars will engage with the venn diagram as a post-assessment. The third lesson will focus on bringing all of the acquired knowledge together regarding the solar system. By the end of the unit, scholars will be able to determine the planet's place within the solar system, recognize the similarities and differences between the inner/outer planets, how the moon orbits around the sun, the stages of the lunar cycle, and how the earth's tilt causes seasons. A review will be accomplished through a variety of video models created by the intern. I will create a video with planet manipulatives to describe general information about both the rocky and gas planets. This will provide a visual model of the order of planets within our solar system. I will scaffold how the moon orbits around the sun with the models. As well as, how the earth's tilt causes seasons. The lunar cycles of the moon will be explained utilizing the manipulatives and pictures of each phase. The scholars will review the acronym visual to remember the order of the solar system. A smart board activity will be provided to match the name of the planets to their place in the solar system. The wheel of names will be spun to choose a scholar to engage with the solar system poster to review the concepts with their classmates. The scholars will engage in the venn diagram as a post-assessment. Scholars should be at mastery level (100%) of sorting inner versus outer planets. The post-assessment plan will include a Play-doh scale model activity. The scholars will compare the Play-doh scale models. At the end of this lesson, the scholars will engage in a class discussion around the following questions: how did you complete the activity, what problems did you face during this activity, and how did you solve the problems? The overarching themes/topics covered in the NASA/ Ohio Space Grant Consortium Education Scholarship include comparing and contrasting the planets.

When given an instructional-level earth and science unit plan the scholars will identify the planets place within the solar system, recognize the similarities and differences between the inner/outer planets, how the moon orbits around the sun, the stages of the lunar cycle, and how the earth's tilt causes seasons. The learning targets will include: I can explain how the planets are similar, I can explain how the planets are different, I can name the rocky and gas planets, I can explain how the moon orbits around the sun, I can discuss the lunar cycle, I can explain how the earth tilts to cause seasons, and I can order the planets in the solar system. The essential questions will include: how are the inner and outer planets the same, how are they different, what order are the planets arranged in, how did you complete the activity, what problems did you face during this activity, and how did you solve the problems? Every scholar in the class has a modification to their IEP that states their planning will be done using the Ohio Extended Standards (Grade 7 Earth and Space Science Section). An instructional level science curriculum will be utilized as aligned with the extended standard chosen due to the scholars PLOP on their IEP. This states that scholars require an instructional leveled science lesson due to their current comprehension level. For each standard, I chose to differentiate instruction by using two levels (B/C) of complexity for their extended standard. My Mentor Teacher (Mrs. L) utilizes two groups: The Cavaliers (struggling learners) and The Lakers (excelling learners). Middle Complexity (Lakers/excelling learners) will focus on: 7.ESS.4b Recognize different stages in the lunar cycle (e.g., full moon, new moon) and 7.ESS.5b Model the tilt of the Earth towards or away from the sun. Low Complexity (Cavaliers/ struggling learners) will focus on: 7.ESS.4c Recognize that the moon orbits around the Earth and 7.ESS.5c Recognize that the patterns we call seasons.

My unit plan follows the constructivism theory of learning since the scholars are constructing their own knowledge through independent learning experiences. Self-regulated learning occurs when scholars personally adapt to a learning environment. Setting goals, strategies, monitoring progress, self-evaluation, and adapting to methods is the backbone of the constructivism theory. Each of my lessons affords scholars the opportunity to collaboratively share their knowledge attained with their classmates. Thus, when scholars are motivated by themselves, they can collaboratively work with their peers towards a common learning goal. The results obtained from the comparing and contrasting the planets unit plan shows evidence of student growth. The following results were interpreted from the pre/post assessment, scholars' individual planet assignments, and the end of unit activity. Comparing the assessment scoring of the Venn diagram of inner and outer planets, eight out of eight students' assessment scores improved from the beginning to the end of the unit. While, each scholar was assigned to a planet in the solar system to study outside of class. During the following presentations the scholars

presented one slide show discussing their findings in detail. Each scholar was successful in collecting scientific information about their assigned planet. The end of the unit activity focused on a Play-doh scale model. The scholars discussed how they completed the activity, the problems they faced, and how they solved the problem. My areas of strength throughout this unit plan included differentiation, higher order thinking skills, and the depth of knowledge wheel. In conclusion, the scholars utilized constructivism theory of learning continuously throughout the comparing and contrasting planets unit plan.

Acknowledgements & References

Resources courtesy of: Susan Kohler (Susan.m.Kohler@nasa.gov) NASA Glenn Research Center: EPDC Education Specialist & NASA & the Ohio Aerospace Institute in Cleveland, OH

Space School Musical

https://www.google.com/url?q=https://www.jpl.nasa.gov/edu/teach/activity/space-school-musical/&sa=D&source=editors&ust=1616076056461000&usg=AOvVaw3t6aGXztilC6DDecRgp_hc

Solar System Exploration

<https://solarsystem.nasa.gov/solar-system/our-solar-system/overview/>

Play-Doh Scale Models

<https://stereo.gsfc.nasa.gov/img/scales.pdf>

PowerPoint Free Resources courtesy of Teacherpayteachers.com

Compare and Contrast Visuals

<https://www.teacherspayteachers.com/Product/Compare-and-Contrast-Visuals-1448672>

The Planets Digital Research Templates

<https://www.teacherspayteachers.com/Product/The-Planets-Digital-Research-Templates-Google-Slides-Distance-Learning-6170957>

Solar System Comparison: Inner and Outer Planets

<https://www.teacherspayteachers.com/Product/Solar-System-Comparison-Inner-and-Outer-Planets-1525703?st=0fc052e4d6db73ccfcf3e63a9fd37fe8>

Solar System KWL

<https://www.teacherspayteachers.com/Product/Solar-System-KWL-2309620?st=238956c4e79aca9011f568d4efb4db94>

Solar System Activity: Planets Sorts

<https://www.teacherspayteachers.com/Product/Solar-System-Activity-Planets-Sorts-3-Freebie-2534317?st=ad65cf8aa4a48ec2c1255d13fa5fcd9e>

Solar System Order of Planets Poster / Anchor Chart

<https://www.teacherspayteachers.com/Product/Solar-System-Order-of-Planets-Poster-Anchor-Chart-4634602?st=cfd4f3f6c8fbba8cd697aee04c945abd>

Solar System: Order of Planets Activity Sheet

<https://www.teacherspayteachers.com/Product/Solar-System-Order-of-Planets-Activity-Sheet-6588624?st=0677e6309ad01e705e5fb831bb84e442>

Google slide presentation created by Nicolette M. Hoon for the scholars

https://docs.google.com/presentation/d/1oPJw9wFA4H3PeytO0iL7YomPN4f5DzYhBLz_PaWQJKI/edit?usp=sharing

Google slide presentation created by Nicolette M. Hoon for the OSGC presentation

<https://docs.google.com/presentation/d/1WjgM9In1NIV4coraArxpAPXAtTEBRQsh9WQRK72VCsk/edit?usp=sharing>

A Picture is Worth a Thousand Words: NASA's Database on the Planets

Student Researcher: Derek G. Joy

Advisor: Karen Henning, Kathleen Cripe

Youngstown State University
Department of Teacher Education

Abstract

The goal of science education in 2021 focuses on modeling the process of scientific inquiry. Inquiry-based education focuses on student interaction with the content as opposed to a lecture/teacher centered approach. This requires the development of strong supporting materials and clear directions for student activities. The learning segment created for this purpose centers around the usage of NASA resources and the development of activities around the data provided there. The activity plan was designed for the 8th graders because of the opportunity to pilot the plan during a student teaching semester. However, the plans and activities can be extrapolated to higher levels of educational instruction as needed. The plan is broken down into five segments, each corresponding with a day. In order, the five segments cover a survey of the planets in the solar system, determination of the origin and properties of the planets based on the data provided, current events in the imaging of celestial objects, Newton's laws as applied to astronomy, and Hertzsprung-Russell diagrams. All five sections of the plan have students collect and interpret data while focusing on the methodology that allows scientist to collect the data they use. The underlying theme of the unit is scientific literacy, with many scientific releases being used as additional information.

Lesson or activity plan that integrates science or technology into the learning activity

One of the goals of the learning segment was to incorporate current scientific practice and technology into every lesson. All five of the lesson plans are attached with this report. Lesson 1 and 2 directly use the Solar System Exploration page with the students. Lesson 1 incorporates a Planetary Scavenger Hunt where students use the database to gather information about the planets to begin to build profiles on the planets in the solar system. Lesson 2 has students continue to gather information on the planets but has them using charts and tables to organize this information. Students will then interpret the information they gathered to determine the composition and origin of the planets. Lesson 3 has students use current scientific articles to understand how imaging in space works. This incorporates a vital skill that students need to develop of the course of their scientific education. Lesson 4 is a survey of Newton's laws that uses online simulations for students to use and collect data from. Good scientific practice is the continuous collection of data and the interpretation of that data that allows for the continued development of the student's knowledge base. Lesson 5 focuses on diagram reading that helps student develop the skill that they will certainly use in high school and is invaluable for being an informed citizen. All five lessons connect online resources with the scientific process to allow for a truly student-centered approach to astronomy.

Statement and explanation of the learning objectives

1. Students will determine and explain the origin of characteristics of celestial objects based on their appearance and location in the solar system with at least 70% accuracy

- a. In lesson 1, students will collect data on each of the planets in the solar system and begin to build connections between location, size, and composition in relation to how the planet interacts with the rest of the solar system.
2. Students will determine the composition of each planet's surface and atmosphere based on the characteristics they observe from photos of the planet with at least 70% accuracy.
 - a. In lesson 2, students will continue to define and explain the origin of the properties of the planets using observational data that mimics how astronomers create inferences about planets. This requires students to form the connections based on the data they collect.
3. Students will synthesize and report the reasoning for the struggles scientists experience with distant objects and determine a reasoning for those difficulties with at least 70% accuracy.
 - a. In lesson 3, students will read two articles on the imaging of Pluto and of a blackhole in order to understand and explain the fundamental hardships associated with those actions and to continue to build their scientific literacy.
4. Students will connect the concepts of motion on Earth and motion in the universe by observing how celestial bodies move and comparing the two with at least 70% accuracy.
 - a. In lesson 4, students will complete a series of simulations that allow students to begin to understand Newton's laws and how they act at the cosmic scale. The most important simulation has students work with the gravity equation and the modeling of orbits.
5. Students will identify the aspects of the H-R diagram and make predictions on the properties of stars based on the diagram with at least 70% accuracy.
 - a. In lesson 5, students will practice reading diagrams in order to better understand how scientific data is often presented. This allows them to begin to understand the lifetime of stars as well.

Description of alignment with the Ohio Academic Content Standards

8.PS.1 Objects can experience a force due to an external field such as magnetic, electrostatic or gravitational fields.

- The state of Ohio mainly focuses on forces in the standards for 8th grade. Because of the importance of forces to how celestial objects, the learning segment clearly discusses the magnetism and gravity in respect to this. These two forces are intimately related to the properties each planet has. The standards also discuss the need for data collection and interpretation, which is present throughout.

8.PS.2 Forces can act to change the motion of objects.

- Lesson 4 thoroughly discusses Newton's laws and the impact they have on the motion of celestial objects. The first four lessons define and explain the importance of force in the formation of planets and how forces drive the interactions of objects in place. Lesson 3 defines a blackhole and has students focus on its impact on the universe.

Discussion of the underlying pedagogy or learning theory

As previously discussed, the learning segment focuses on the philosophy of science education by inquiry. Students are presented with problems or phenomenon and are tasked with explaining or describing them. Each of the five lessons are classified as guided inquiry. Guided inquiry outlines the methods and resources students should use for the learning to occur but allows them to take the lead and interact with the content at their own pace. The activities are student directed and are made in an open-minded manner. This allows students to make their own connections and understanding of the content. The guided aspect gives students direction for what they are to be looking for, but they have discretion on what they find. After the exploration is completed, students are brought back to questioning to make sure they achieved the particular goal of the lesson.

Discussion of type and level of student engagement involved

Students are targeted to be engaged throughout the learning segment. Because of the nature on inquiry, a respectable level of the learning to occur is the responsibility of the student. Guided inquiry means each student is going through the material on their own with assistance of the instructor. This looks like active student participation and interaction with the materials they are given. The unit is relatively self-paced but requires several checkpoints of understanding from the instructor. Students will lead their own learning but will be scaffolded by the instructor. Students will be collecting data for a large portion of the instruction and analyzing it with a lot of the rest of time. The instructor will provide background information and discussion for deeper learning as needed, and as part of the activity.

Resources required

The activities are included on a separate accompanying document. These include the Planetary Scavenger Hunt for Lesson 1, Composition of the Planets Activity for Lesson 2, Telescopes (Planetary of Pocket-Sized) for Lesson 3, Newton's 3 Laws for Lesson 4, and the H-R Diagram for Lesson 5. Each of these activities are designed to for data collection, interpretation, and assessment of student learning. Other resources included are the NASA Solar System Exploration database for Lesson 1 and 2, scientific press releases on the imaging of Pluto and the blackhole for Lesson 3, the University of Colorado's PHet simulations for Lesson 4, and H-R diagrams for Lesson 5.

Lesson or activity implementation results

Due to the timing and structure of the 8th grade curriculum at the school where this will be implemented, the learning segment will not be implemented until April to properly coincide with the Physics/Astronomy unit students will go through. Further data will be collected then.

Description and results of an assessment element

Lesson 4 focuses on Newton's laws and how they apply to the previous three lessons and the cosmos as a whole. The activity students will complete has them go through a series of simulations designed to demonstrate each of the three laws. Students will collect data on each of the simulations they are designated to go through and interpret what this data means and which law it relates to. The final simulation applies the three laws to gravitational orbits of planets and students will create their own scenarios and explain the relationships they observe as they manipulate the variables on the simulation. This will assess how well students understand the laws and how well they understand how forces work at a cosmic scale. Since the learning segment has not yet been implemented, there are no results.

Critique and conclusion of the project

Overall, the project was designed to create a guided inquiry of astronomy for students that has strong aspects of data collection, manipulation, and interpretation. The finished project has incorporated all of the desired aspects. Because of the timing of the curriculum of the school where it will be taught, no results could be provided yet. That remains the biggest hole in the project. In the future however, I would like to do more of this kind of instruction. Students love to work at their own pace and make sense of interesting phenomenon that the universe has. This was the first guided inquiry learning segment I designed from the ground up and I believe it to be very promising. One other note I wanted to make is the importance of scientific literacy. All of the lessons, but particularly Lessons 3 and 5, have learning tasks that are designed to get students reading, writing, and talking about science. This is a huge topic I believe in and is what I believe to be at the core of effective science education. Scientific literacy is the biggest takeaway from science education and the learning tasks get students to begin to develop those skills by utilizing the amazing beauty and power of science. NASA and its resources are an absolutely amazing starting point for this.

We're Going On A Road Trip

Student Researcher: Margaret M. Kaminski

Advisor: Julie Wilcox

Kent State University
College of Education

Abstract

For my lesson plan I chose to use the human exploration and operations mission directives. I thought this could provide an interesting project at the end of an Earth science or Life science class. My objectives for this two weeklong project is for students to be able to identify and articulate what an exoplanet is and why they are important to us as humans, have students debunk artificial gravity in famous space movies, and finally work with the students to better understand the price and difficulties of deep space travel, such as building a ship and the many essential human needs once on the trip. They will do all of this while playing along to the project topic of our Earth is dying so we need to find a new one and figure out a way to get there. Hopefully by the end of this project the groups of students will have chosen an exoplanet, designed a spaceship and figured out the means of survival for their journey to our new home.

Objectives

My objectives were for student to be able to identify and articulate what an exoplanet is. They should also be able to describe why they are important to us as students. They should be able to identify and describe why artificial gravity in movies are false. Finally, they should be able to list four different things humans need to survive in space.

Methodology

I would present this lesson as a two-week inquiry unit or unit plan. The unit will be split into four different units, exoplanets, artificial gravity, life in space and spaceships. This unit will culminate in a final presentation that summarizes all the other points of the unit. Unfortunately, since COVID I have not been able to actually teach this lesson, but I am hopeful to implement it in the fall semester.

Results obtained

Once again I haven't been able to truly teach this lesson but hopefully by the Fall I will be able to use this lesson in my classroom.

Figures

Here is a table I use for students to craft their spacecrafts. They can choose one option per row and that will help them make their spaceship.

Farming	Fresh food farming More space/cheaper	Freeze dried food Less space/costs more
Energy	Laser satellites Costs less/needs many to be effective	Microwave satellites Costs more/only a few needed but installed by astronauts
Oxygen	Already installed	
Water	Already installed	
Gravity	Ring structured ship Costs less/worse for the body	High tech artificial gravity Costs more/better for the body.

Acknowledgements and References

I want to thank NASA and the Space Grant Consortium for giving me this opportunity to plan this really fun lesson. I also want to thank Sydney Jordan and Julie Wilcox who both helped me revise and type up this lesson. I want to thank the NASA website where I got most of my information for this project. I want to thank Real Engineering on YouTube for a great video on artificial gravity. I want to thank Bill Macarthur for his video on water and oxygen recycling on the International Space Station and the Department of Energy's site on solar energy in space.

Hidden Figures: Helping Students Realize Their Capability

Student Researcher: Kaitlyn D. Lafferty

Advisor: Dr. Cathy Mower

Marietta College
Department of Education

Abstract

Hidden Figures brought to light the many mathematical wonders that were accomplished by the women of color behind the John Glenn Mission. Since the anniversary falls in February, these lessons will be a combination of Black History and the mathematical feats. While the vast majority of the math computed was above a high school level math class, these lessons will focus on the fundamental skills that students learn in high school, and how that can lead to great scientific accomplishments. Students will be able to learn about why math can be such an important skill, but most of my students are females, several of which who are considering stem related college majors. The overall hope of the lesson is to not only educate students on some amazing people, but show them that no matter who they are, they can be in a stem field. I am from the same hometown as John Glenn, and my hometown shaped my confidence in being able to be a math major as a woman, and I hope that this can spark some of that confidence in my students.

Project Objectives

The objective of this project was for students to see their ability to be in a stem field. The project first introduced students to different mathematicians, both men, woman, and people of color. I picked people who were the first to do something, inventors, overcame barriers, and many others in between. This is how we started every lesson, and how we will continue, but featuring students as the mathematicians in the last month. The goal of these lessons is to show the students that while they may only be in high school, they are still doing great mathematical feats.

Methodology Used

We first had discussion about how students felt being in a stem field. This was before we started discussing a mathematician every day. I wanted to have a baseline for how they felt before, to see if this had any affect on their thoughts. Most of my students gave me responses that they were not strong, or not intelligent enough to work in a stem field. We then started every day with a mathematician. Towards the middle of March, we watch Hidden Figures in class. We discussed the many feats of the women in the movie, and how they overcame barriers. The students enjoyed this far more than I expected. Unpromoted, many of my students did their own research, and came to the discission we had with interesting facts. They debunked some of the scenes in the movie, informed me of updates about the women, and many others who weren't centered in the film, and even reactions from some of the astronauts. I realized then that this project had more of an impact that I initially thought it would have. The students then completed a reflection to reevaluate how they felt about their own math capabilities. This gave them space to put any thoughts they were not comfortable sharing in a class discussion, and spend time thinking about their roles. Lastly, students filled out a survey that gave me the same information I presented to them about other mathematicians. This is turned into a mathematician of the day, but now our mathematicians will be the students in the class.

Results Obtained

I was thoroughly impressed by the responses I received. They truly engaged in the questions, and I was able to see the changes in their opinions of their own capability. The students were asked to talk about how the math the women were doing in the movie related to the math we do in class, and the students gave me examples I hadn't even noticed. They mentioned graphing, finding points on a graph, finding area, exponents, radicals, adding, multiplying, writing equations, and so much more. They also saw themselves as more capable. Now, instead of just feeling like they are bad at math, they talked about how they are able to do whatever they want, and they will do what they are passionate about. One student in particular decided that she wanted to become a journalist, and that the movie helped them realize that it doesn't matter that journalism is struggling and getting backlash. The student noted that no matter what they chose, people would have opinions and that they want to do what makes them happy. Other students discussed how they struggle, but they could overcome anything if these women overcame what they had. Every one of my female students noted they felt empowered, capable, and motivated.

Significance and Interpretation of Results

I never thought I would have gotten the responses I did. While not every student wants to go into STEM, they now feel that they could. Only one student wanted to be in a STEM field before we started this project, and now, out of the 24 students I asked, 16 of them expressed desire to go into STEM. Additionally, in class I noticed a change in their confidence. They are not as afraid to be wrong, and they ask questions. I've had the bell ring, and an entire class of students ask me to finish the example because they wanted to see if they got it correct. As a student teacher, I was so astounded and ecstatic that they have developed a love for math much like the one I have. I know that as a female in stem, seeing successful women kept me going, and wanting to be successful. I can confidently say that at least for this school year, many of my female students feel the same way. I've had email exchanges, lunch conversations, and students who stay after class just to keep asking questions about mathematicians, women in stem, and their career endeavors. They see that while rocket science takes a lot of brain power, they are capable of learning and strengthening their brain.

Acknowledgments

I would like to thank my cooperating teacher, Mrs. Deana Dye, for helping me create a classroom climate that allowed the levels of honesty and vulnerability for students to be successful in building their confidence. I would like to thank all of the people at the Ohio Aerospace Institute for giving me the opportunity to share what I worked on. I would like to thank all of the amazing mathematicians that I used to inspire my students. Lastly, I would like to thank all of my students for going on this journey with me and inspiring me to do better every day. None of this would have been possible without them. If anyone would like to have the materials, or have any questions, feel free to contact me. I'd be happy to share.

The Orbiting Water Balloon

Student Researcher: Grace S. Lockwood

Advisor: Dr. Kevin Jones

Cedarville University
Middle Childhood Science Education

Abstract

This lesson, geared towards upper Middle School Students (7th-8th grade), is focused on orbits and the concept of gravity and allows for interdisciplinary content in mathematics. The instruction manual that the students would receive is modified from the “The Great Escape Activity” lesson plan in NASA’s Aerospace Education Services Project.

Project Objectives

The goal for these lesson activities is for the students to be able to calculate and use the concepts of physics such as release velocity, and gravity and apply them to real world scenarios

- Students can calculate the release velocity of an object based on the revolutions, time and distance using the circumference formula and a stopwatch.
- Students can convert units.
- Students can critique their experimental process and identify experimental error

Methodology Used

This lesson is based on a constructivist learning approach¹. This theory suggests that students’ gain knowledge and meaning from their sensory experiences. The students throughout this lesson will construct new knowledge about orbits, gravitational pull, and release velocity through hands on experimentation. Students will collaborate with peers, draw on prior knowledge and develop their own techniques to calculate for release velocity of a water balloon. This lab requires students to integrate both math and science content from prior knowledge to construct new schema and develop meaningful learning. They will use the hands on experiment to define release velocity while incorporating math calculating skills.

Results Obtained

I have not yet been able to use this lesson with students. However my plan is for students to work in groups of 3-4 people to complete the inquiry activity. Students will simulate planetary orbit with each group having one member who will represent a planet. As they work through this lab activity they are to take note of observations and track their calculations. Students will start by having each member of the group assigned a role in the lab. One will be the time keeper, another will count the rotations, another will be the planet, and if there is a fourth they will record the results. This lab requires students to practice converting units of measurement as well as calculating for velocity. It also helps them to become familiar with the concept of gravity and what it means to orbit. At the end of the lab students are to analyze the scientific process they used.


Significance and Interpretation of Results

The purpose of this lab activity would be for students to work together to determine the release velocity

of the water balloon from their own planetary orbit. Students will use the data found to calculate the release velocity using conversions and units taught in class instruction. Students will repeat this experiment several times with different lengths of string and determine how that affects the release velocity. Students will then work together as a group to fill out the reflection portion of the worksheet to analyze the results they received. Students will examine which variable affects the release velocity-length of string? Size of human/planet? Size of water balloon? Etc.

Figures/Charts

Orbiting Water Balloons Workshop



	First Speed	Second Speed	Third Speed	Fourth Speed
Student	# of Rotations	# of Rotations	# of Rotations	# of Rotations

Name: _____
 Pre-lab: <https://history.nasa.gov/conghand/traject.htm>
 What is Orbit? What forces are in play for orbit to exist?

https://www.nasa.gov/audience/forstudents/k-4/dictionary/Escape_Velocity.html
 What is release velocity? What is the unit connected to velocity?

Today you are a planet!
 You must determine the velocity required for a water balloon to escape the orbit around you.

Materials:

- 5 ft. length of twine
- Clothespin(attached to the end of the twine)
- small water filled balloon.

Procedures:

1. Each member of your group will take turns attaching a water balloon to the string and swinging it around.
2. The first student should start off very slow (swinging the balloon just fast enough to keep it off the ground).
3. While swinging the balloon, another student should use a stopwatch to count 10 second, and the other students should count how many times the balloon goes around in the 10 second intervals.
4. Record the number of rotations in the "First Speed" column in the table below.
5. Then speed up the rotation slightly, and count the number of rotations again, this time putting the results in the "Second Speed" column.
6. Keep increasing the speed and recording the results until the balloon releases from the clothes pin. Take the last recorded number of rotations and use the table at the bottom to calculate the escape velocity.
7. If time permits, repeat activity for each group member, and calculate the escape velocity for each person's swinging results.

	# of Rotations	Final Speed	/	Time	x	Circumference		=	Escape Velocity	
						Diameter	Pi			
Escape Velocity 1			/	10 seconds	x	10 feet	x	3.14	=	
Escape Velocity 2			/	10 seconds	x	10 feet	x	3.14	=	
Escape Velocity 3			/	10 seconds	x	10 feet	x	3.14	=	
Escape Velocity 4			/	10 seconds	x	10 feet	x	3.14	=	
Escape Velocity 5			/	10 seconds	x	10 feet	x	3.14	=	

Reflection:
 Describe release velocity in your own words(include the words atmosphere and gravity):

What experimental errors affected your data in this experiment? What could you change for future experiments? How would that change help improve accuracy?

How did your results compare the rest of the class? Use inference skills to predict why each of your classmates might have gotten different velocities? What factors may have affected your results?

Figure 1. The Orbiting Water Balloon Worksheet

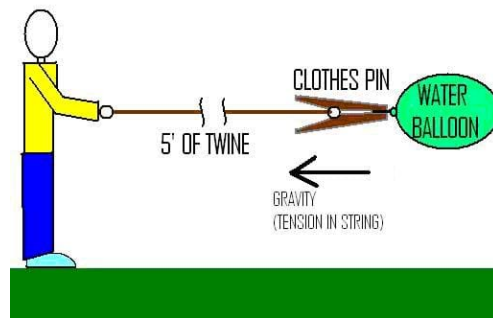


Figure 2. A model of format of how students will position all of the elements in this lab

Acknowledgments and References

I would like to thank my advisor Dr. Jones, Dr. Chasnov, and the Ohio Space Grant Consortium, NASA, for all of their help.

¹ Saunders, W. L. (1992). The Constructivist Perspective: Implications and Teaching Strategies for Science.

Sending a Rocket to the Moon

Student Researcher: Josephine M. Palmer

Advisor: Dr. Todd France

Ohio Northern University

Department of Engineering and Department of Teacher Education

Abstract

Within this activity, the students will use the engineering design process to think through how to build a makeshift rocket. The students will be given a wide variety of materials that are able to be used, and they will have to work together to brainstorm, sketch, design, and create a solution. Their final product will be tested, results calculated, revised, and then tested again. They will be determining how position, velocity, acceleration, and time are all related to each other and how they all can affect one another. The overall arching purpose of this activity is to get the students to use all six steps of the engineering design process and see, in practice, how they can implement the process into any problem or task they are working on.

Objectives

By the end of this activity, students should be able to:

1. Calculate the velocity of the rocket while traveling, $V = \frac{\Delta x}{\Delta t}$
 - a. V , velocity
 - b. Δx , change of distance
 - c. Δt , change of time
2. Determine how the position and time of the rocket affects the velocity and acceleration
3. Create a data chart to show correspondence between position, velocity, acceleration, and time of rocket
4. Appropriately sketch a design that can be followed and designed

Methodology Used

Using the engineering design process is a very important skill to understand in the engineering world and in general. This process is very similar to the scientific method used in science classes, but a big difference is that the engineering design process undergoes a step in which the engineer uses specific requirements given by the client to create a solution to their proposal. Once they have this idea for a possible solution, the engineers will then team up with other engineers in the specific fields they are dealing with to build and test the solution.

Incorporating this into secondary classroom, I can get my students to learn about this process in a fun and engaging activity to show them first-hand how this process works. Explaining the steps at the

beginning of the activity, and then helping them work through all nine steps to get a complete understanding of how they can incorporate this into process into any problem they are given.

Assessments/ Results

Throughout this activity I asked my students eliciting questions to help spark discussion and promote thoughtful insight on their creations. Once the students finished their buildings, we tested all the builds as a class. Part of their assessment was how well their builds worked during testing, how their improvements helped their testing, how well their data table turned out, and how well the students worked as part of a team. After doing this activity, I was able to see all the students making great progress towards using the engineering design process. Having them take things step by step really helped them get a good grasp of how intricate the process can be sometimes and the fact that it is a continuous process. The students, while working in their groups, were able to communicate with each other to design and create their rockets, and then tested them. When I had them go back and revise their builds, they realized how much of a continuous process engineering a design can be, they learned that there will always be that one little something that can be adjusted to be more accurate or to make it more optimized.

Conclusion

This activity allows students from any age range to learn how to use the engineering design process, and how it can be used in everyday life. Although this activity is aimed for lower high school students, it can easily be adjusted to become beneficial to all age ranges depending on the student's skill level and what the curriculum is asking of the students. This activity was a great way to get the students interacting with one another and using their math skills for something interactive and related to a real-world example. After using this process in this activity, my students will be able to keep going forward and improving all of their future work to the best of their ability with the help and knowledge from others as needed.

Finding Math in Every Space

Student Researcher: Emily Sukalac

Advisor: Katie Adkins

Baldwin Wallace University

Department of Education

Abstract

This lesson is focused on learning how to carry out unit conversions while gaining more information about various topics in space. The appropriate age for this activity would be junior high to high school students. The main idea of the lesson is that unit conversions are an important part of our everyday lives and can be applicable to different aspects. Within the lesson students will have the chance to carry out appropriate challenging unit conversion problems to increase their problem-solving skills. The lesson will begin by students measuring out various distances in different units. In groups of 3-4 students will then travel the distance they selected and time how long it takes for each member to do so, in seconds. Once they have collected the various times, I will have each group convert their distance/time in varying units, to see who was the fastest. After students remember how to carryout unit conversions, students will be given the Unit Challenge packet. The goal of this packet is to have students complete master unit conversion questions of varying difficulty while learning valuable information about outer space. Each question will have a corresponding letter that students will then match to the correct spot. The letters will spell out the names of the three black women who helped with John Glenn's flight. Students will then have a short presentation that they will need to complete based on these three women. The goal is to bring attention to the fact that there is a place for women in science.

Lesson

The lesson designed to have students further master their knowledge on unit conversions while also learning interesting facts about outer space. Students begin the lesson by refreshing their prior knowledge of unit conversions by converting the data they collected from the "races." To set up the races, the students will be given measuring tapes of different units such as centimeters, inches, feet, and meters. Students will then record the distance their team of 3-4 chose and time how long it takes each person in their group to travel said distance. Each group will then convert the fastest time to feet/second, to determine the fastest person in the class.

Once students have completed the warmup races, they will receive a packet of 22 space related questions that require them to use their knowledge of unit conversions to complete. Students will stay in the same groups that they completed the races in. As the students work through the packet of questions, they will find that for each question, there is a corresponding letter to the answer they find. After they have solved all questions, they will be able to match the corresponding letter the correct number. After the groups place the correct letter with the correct number students will see the name of the three black women, Mary Jackson, Katherine Johnson and Dorothy Vaughn, who helped with the mathematics of John Glenn's flight will be written. They will then have to create a small 5 to 10-minute presentation on who they are and what they did, and why they are so important. Students will then present these to the class, and we will have open discussions as to what interesting things they had learned during the lesson.

Objectives

- Construct data real time data by using a stopwatch and google sheets.
- Apply conversion factors to convert data into different units by hand and in google sheets.
- Identify which units can be used as conversion factors in a specific problem.

Standards

- N.Q.1 Use units as a way to understand problems and to guide the solution of multi-step problems; choose and interpret units consistently in formulas; choose and interpret the scale and the origin in graphs and data displays.
- N.Q.2 Define appropriate quantities for the purpose of descriptive modeling.

Educational Theories

- Constructivist Theory: During this lesson students will use their prior knowledge of multiplying and dividing numbers in order to help them convert measurements of one unit to another. Students will start with doing single step conversions and then work their way up to multiple step conversions. Students will also be taught how to do this in a scaffolding way.
- Kohn 3C's of Intrinsic Motivation: This lesson will provide students with engaging content from the very beginning when students are to create their own data by timing how long a student takes to travel a certain distance. Throughout the entire lesson students will also be able to collaborate and work together with their team.
- Marzano's Finding Patterns: Students will quickly realize that the conversion of units is very similar for each problem. There will be a pattern that students will follow in order to get the correct units.

Resources

Students will need a few different resources for this lesson. The first few will be a measuring tape, masking tape and a stopwatch. These will be used for the "races" at the beginning of the lesson in order to have a stop and start spot as well as the measure between the stop and start spots, and being able to capture the time it took for a student to travel that distance. They will also need paper and pencil to record their data of their "races." The last two materials the students will need are the guided notes and the Unit Challenge packet, which the students will work in teams to complete.

Expected Results

This activity was not performed within the classroom, so no results were found. However, there are some results that are possible.

Examples: After solving each question, they are unable to find their answer on the list that contains the matching letter. This would mean that the students got an incorrect answer. Another possible result is that the students place the incorrect letter on a line. This would mean that the students got an answer that was incorrect for the problem but correct for a different question. It is also expected that students will be made aware of new information about outer space.

Assessment

The assessment for students to complete will be the Unit Challenge packet. Within this packet will be single and multiple step unit conversions problems. All conversions will be based on information gathered from NASA's website. This information can range from how hot Venus is in Fahrenheit, or how long it would take for a radio signal to travel once around the earth, at the speed of light. Once students have completed all 22 problems, they will then match their answers with the corresponding letter and place it on the line with the matching problem number. If students have done the problems correctly, it should then spell out the names of the three black women who helped with the mathematics of John Glenn's flight. They will then need to create a short presentation on who they are and what they helped do.

Conclusion

This lesson allows for students to learn to apply what they have learned prior with single step conversions to solve some complex multistep unit conversions. In addition, this can be a cross content lesson since they will also be introduced to information about space and other interesting science topics. This allows for the students to see real life applications of what they are learning in the classroom. The activity allows for students to work collaboratively and in a positive environment.

The Defense Mechanism of Animals

Student Researcher: Jenna L. Vollmar

Advisor: Laura Dell, Ed. D

University of Cincinnati
Department of Early Childhood Education

Abstract

This lesson is designed for grades second and third. The focus is why animals have defense mechanisms and how that is important for survival. Part one of this lesson focuses on student's understanding as to what defense mechanisms are. Students will read a book and watch a video about this. The second part of this will include a presentation and an instructional activity. This is fun and exciting for grades second and third to learn about animals and their defense mechanisms. By the end of the lesson(s), the students will be able to understand the common defense mechanisms and they will be able to create one of their own to show the class.

Lesson

This activity is focused on students understanding to why animals have defense mechanisms and how camouflage is used for survival. Students will start by reading a book and watching a video. Students will read *Camouflage: Changing to Hide* and they will watch *Avoiding Predators: How to Avoid Being Eaten*. Students will then have time to discuss what they read and watched and have the opportunity to ask questions about the topic. The teacher will then ask students questions to check understanding. For the second part of the lesson, the teacher will have a presentation and instructional activity. The teacher will provide a presentation these questions:

- Why do you think animals would want to blend in with their environment?
- What are defense mechanisms?
- Why do animals use camouflage?
- How can animals use this for survival?
- What different kinds of animals use camouflage?
- How are these animals alike and different?

After the presentation, the students will then participate in an instructional activity. This activity includes students creating their own camouflage. Students will be shown an example of an animal that they will be creating. Students will be given the option to choose from many different animals they can cut out or they can create their own animal. Then students can create a pattern using the color pencils, crayons or markers to create the camouflage of the animal. During this activity, students can talk amongst themselves and share their ideas with others. Open communication will be allowed during this activity. When closing this lesson, the teacher will summarize what camouflage is and the teacher will also ask the students to show their creation to the class.

Objectives

- Students will have a better understand of how and why animals camouflage themselves.
- Students will be able to identify animals that use camouflage as defense mechanisms.
- Students will be able to explain why animals have defense mechanisms and how they use it for survival.

Methodology

Vygotsky's Theory of Learning: During this activity, students will be able to interact with each other and share their ideas. Students will be able to share ideas with one another and it will help them create better understanding of their animal they selected or created and what kind of camouflage that animal might use according to their environment they live in. This shows that social learning will occur.

Piaget's Theory: Piaget's theory states that children learn best when they are actually doing the work themselves and when students are creating their own understanding. In this lesson, students are learning through a hands-on activity where they can select create their own animal and create their own understanding of why that animal might use a defense mechanism.

John Dewey's Theory: Dewey believes that when students are engaged in their learning and are interested then their process of learning becomes enjoyable. In this activity, students will be engaged when actively creating their own animal and creating their own camouflage for that animal.

Expected Results

Since this activity wasn't performed within the classroom because I am not in my student teaching practicum currently, there are possible and expected results that could occur at the end of this activity. The expectation is that students understand the topic and are able to meet the lesson objectives.

Example of an Expected Result: After reading the book and watching the short video, students will be able to understand and comprehend that animals use camouflaging for safety and survival. Students will then be able to identify some animals that use these defense mechanisms and explain why they use it.

Interpretation of Expected Results

The significance and interpretation of expected results are that students will be able to understand how and why animals camouflage themselves. Students will be able to identify animals that use camouflage as defense mechanisms. Students will be able to explain why animals have defense mechanisms and how they use it for survival.

References

Inc., E. (n.d.). Camouflage: Changing to Hide. Retrieved March 25, 2021, from <https://www.getepic.com/app/read/7651>

Avoiding predators: How to avoid being eaten. (2012, June 05). Retrieved March 25, 2021, from <https://youtu.be/B2JdRPKYyTc>

Mooney, C. G. (2013). *Theories of childhood: An introduction to Dewey, Montessori, Erikson, Piaget, and Vygotsky*. St. Paul, MN: Redleaf Press.

Third Graders Explore Space

Student Researcher: Alexa E. Wallbrown

Advisor: Shannon Logsdon

Kent State University
Early Childhood Education

Abstract

Following the Ohio Learning Standards, I created a space-themed mini-unit for students. With a variety of COVID-19 protocols, I had to make a few accommodations regarding my lesson plans. In this mini-unit students will meet their goal of using space-related vocabulary as they learn about planets and the Space Race. For the whole unit, we are setting the time-period back in 1969 during the Space Race as we learn. The students will have goals each day to learn about space before they launch, then build a rocket to get there. Once they learn about the moon up in space, they will come back down to Earth and share the big news that the United States was the first to the moon!

Project Objectives

In the third-grade Ohio Learning Standards, there is not any space-related content, so I worked with writing standards to teach space. I chose a standard that would allow for students to convey what they had learned which is: *W.3.2 Write informative/explanatory texts to examine a topic and convey ideas and information clearly.* In this objective, I can utilize the value of ability to examine informative topics as well as incorporating recently learned vocabulary words.

On the board, we have the learning objectives for the students. These objectives are in the form of a question so they can ask themselves if they are comprehending different topics. For the mini unit about space, the question was "Can I write an article about the moon-landing?"

Methodology Used

Before beginning the mini unit about space, I asked the students what they knew about it to gain an understanding of their background knowledge of the content. I took their schema plus what their interests about space are and turned it into lesson plans. The students are interested in the planets, moon, Mars, and aliens. I took their interests and built a space unit around it. I wanted to focus more on the moon landing, however, there was a snow day plus a pre-planned day off so it was a little rushed. Day 1 was about planets and students researched one planet then created their own planet. Day 2 was all about the moon landing. The students worked in pairs to create a packing list to the moon and created a rocket. Day 3 was a Martian Mission on Mars. This was an interactive Google Slides that required research about Mars to help find the Martian. Later in the day, students then created a news article about the moon landing.

Results Obtained

Based upon this data, I notice that the student's writing needs more attention. I see that 90% of the students met the objective of using 2 or more space-related vocabulary, but only 70% of students were

able to examine a topic and convey the information clearly. Science seems to a strong subject for the student from the experience working with them and the data reflects this. The students have been remote for a few months this school year and were required to only type out work at the beginning of the school year to prevent germs. Now, they are writing using pencil and paper more. I am happy with the 70% of students able to convey information as they have grown tremendously.

Significance and Interpretation of Results

To assess what the students had learned, I had created an informal assessment. I tried to keep the dramatic play/pretend theme of us set in the year 1969. With this in mind, students created news articles sharing what they saw and other information they had learned about the moon.

If I were to change anything about this space unit, I would have extended it. From a teacher standpoint, it felt rushed so from the student standpoint, I know they wanted more out of it. The topic of space is not directly in the third-grade standards and for my lesson, I needed to abide by incorporating some standards within it. I chose an English/Language Arts standard instead: *W.3.2 Write informative/explanatory texts to examine a topic and convey ideas and information clearly.* This standard allows for students to tell a reader through their writing all about different informative texts and in this case, all about the moon landing.

I also would love to have gone with my original idea of using recyclables as the rocket as I know the students would have retained more from the topic and enjoyed the STEM activity more. I recognize the COVID-19 safety protocols taken within the district and respect them so allowing students to have separate sheets of paper and work in pairs is perfect. For future lesson plans, I would have made this more STEM-like and used more than three days for the lesson if the districts or school's curriculum map allows for it.

From this mini space-unit I have learned the value of STEM in the classroom. I am taking this information I learned into future lesson within my last month of student teaching and into my future classroom. STEM is important as it applies a higher order of thinking. Theorist, Robin Fogarty, shared that learning is emotional, constructed, and experimental. Within this experimentation and hands-on learning approach, we can transfer this learned knowledge through reflection.

Figures/Charts

Below I have created a table based upon the learning objectives of this space unit. Objective One is based upon the ELA Standard: *W.3.2 Write informative/explanatory texts to examine a topic and convey ideas and information clearly.* Since there is not a space-related social studies standard for third grade, I am basing the second objective around space-related vocabulary used in their writing.

Green: Met Objective

Yellow: Partially Met Objective

Red: Did Not Meet Objective

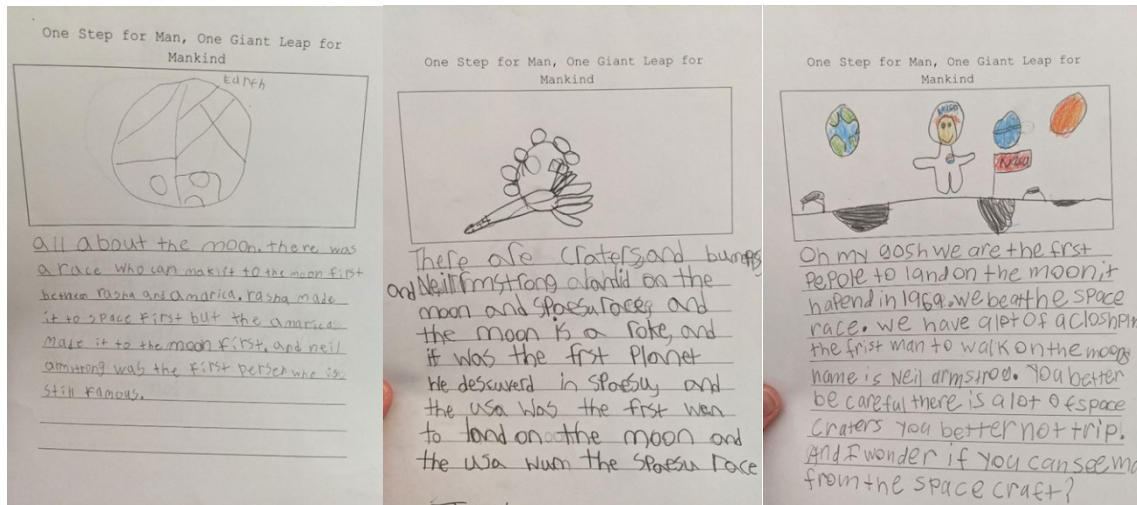
Students:	Criterion One:	Criterion Two:
-----------	----------------	----------------

Numbered to hold confidentiality	Student can examine a topic and convey the information clearly.	Student uses 2 or more space-related vocabulary in their writing.
1	Theatric and informatic	
2 *SR		
3		
4	Conveyed an engaging article using schema from previous writing prompts	
5	Student wrote one sentence.	
6 *SW	Student did not fully meet the requirement of conveyed information	
7		Student did not use grade-level vocabulary expected
8		
9 *SR		
10	Created an opinion piece, not an informative piece	Used more than 2 space-related vocabulary

*SR = Struggling Reader

*SW = Struggling Writer

Sample Work:



Acknowledgments and References

W.3.2 Write informative/explanatory texts to examine a topic and convey ideas and information clearly.

<http://education.ohio.gov/getattachment/Topics/Learning-in-Ohio/English-Language-Art/English-Language-Arts-Standards/ELA-Learning-Standards-2017.pdf.aspx?lang=en-US>

How Space Travel Affected Me: The Integration of Aeronautics Into an English Language Arts Classroom

Student Researcher: Adison M. Wright

Advisor: Dr. Romena Holbert

Wright State University
Middle Childhood Education

Abstract

Students will research the effects of microgravity and space radiation on the human body for the duration of a six-month space exploration mission. Upon collecting data, students will compose six (one per month) descriptive, first-person journal entries about the effects of space travel on the human body using figurative language and sensory details based on their scientific data and research. The goal of this lesson is to show the level of mastery that can be achieved through cross-curricular instruction and how the integration of writing in science can enhance the learning experience for students. The multidisciplinary teaching methodology used in this activity supports student mastery, holistic material comprehension, and accurate interpretation of scientific research.

Project Objectives

This lesson is designed to align with the following Ohio Learning standards: CCSS.ELA-Literacy.CCRA.W.7 - *Conduct short as well as more sustained research projects based on focused questions, demonstrating understanding of the subject under investigation* and W.7.3 *Write narratives to develop real or imagined experiences or events using effective technique, relevant descriptive details, and well-structured event sequences*. A student will prove to have mastered the standards/objectives previously stated if their completed work shows adequate knowledge and usage of sensory details and figurative language to interpret their research in a first-person narrative.

Methodology Used

This lesson uses a variety of teaching methodologies. First and foremost, the educator will be using a multidisciplinary approach to the curriculum, incorporating both science and language arts concepts into the lesson (Kramer, 2013). Specifically, during the research process, the educator will be using a facilitator teaching methodology, as they will guide the students in their aeronautics research by providing scholarly articles and utilizing online NASA databases. The educator will also be implementing the five-part process model approach to writing, explained in figure 1. In combination, these methodologies create a cross-curricular lesson that is developmentally responsive for middle-level students. Students' knowledge will then be assessed by grading their journal entries based on the "How Space Travel Affected Me" rubric shown in figure 2.

Figures and Data

Figure 1 portrays the different parts of the Process Model Approach to Writing discussed in chapter six of *Essentials of Integrating Language Arts* by David Yellin and Beverly A. DeVries. Figure 2 portrays the scoring rubric used to assess student comprehension and interpretation of research to develop six mock journal entries. Table 1 displays the level of mastery achieved by students upon the conclusion of the activity. Excerpt 1 is a portion of an entry from an anonymous student who completed the assignment and received a mastery score.

Excerpt 1. Student Entry

“Today is my third day on the mission. After finally getting a few consecutive hours of sleep, I felt like I had hit the lottery. That was until my stomach started to feel like it had a hurricane inside it. The lack of gravity made my stomach leap from my insides like a frog from a pond. I had heard that most people had nausea for the first few days, but I never imagined it would be this bad. As I swam through the cabin like a lost fish at sea, I groggily sit down in a seat, close my eyes, and try to imagine that I am as still as a statue.”



Figure 1. The Writing Process

CATEGORY	4	3	2	1
Focus on the Effects of Microgravity and Space Radiation	All entries are related to the assigned topic and allows the reader to understand much more about the effects of microgravity and space radiation.	Most of the entries are related to the assigned topic. Some entries wanders off at one point, but the reader can still learn something about the effects of microgravity and space radiation.	Some of the entries are related to the assigned topic, but a reader does not learn much about the effects of microgravity and space radiation.	No attempt has been made to relate the entries to the effects of microgravity and space radiation.
Accuracy of Facts	All facts/data presented in the entries are accurate.	Almost all facts/data presented in the entries are accurate (at least 90%).	Most facts/data presented in the entries are accurate (at least 70%).	There are several factual/data errors in the entries.
Requirements	All of the written requirements (# of entries, # of facts, # of figurative language techniques, etc.) were met.	Almost all (about 90%) the written requirements were met.	Most (about 75%) of the written requirements were met, but several were not.	Many requirements were not met.
Sensory Details & Figurative Language	All 6 entries contain 2-3 sensory details and/or figurative language techniques per entry.	4-5 entries contain 2-3 sensory details and/or figurative language techniques.	4-6 entries contain 1-2 sensory details and/or figurative language techniques.	3-6 entries contain 1-0 sensory details and/or figurative language techniques.
Writing Process	Student devotes a lot of time and effort to the writing process (prewriting, drafting, reviewing, editing, and publishing). Works hard to make the story wonderful.	Student devotes sufficient time and effort to the writing process (prewriting, drafting, reviewing, editing, and publishing). Works and gets the job done.	Student devotes some time and effort to the writing process but was not very thorough. Does enough to get by.	Student devotes little time and effort to the writing process. Doesn't seem to care.

Figure 2. "How Space Travel Affected Me" Rubric

Table 1. Levels of Mastery Achieved

Points Earned on Rubric	Percentage Grade Earned	Number of Students	Percentage of Class
Mastery (17-20)	85-100	18	72%
Near Mastery (14-16)	70-84	4	16%
Developing (11-13)	55-69	2	8%
Remedial (0-10)	0-50	1	4%

Significance and Interpretation of Results Obtained

The data collected shows the benefits of a multidisciplinary approach to learning by incorporating both science and English language arts topics into one lesson activity. The majority of students expressed a mastery level understanding of both the effects of space travel on the human body and descriptive and figurative writing used in first-person narratives. To show mastery, students needed to earn 17-20 points (85%-100%) in the rubric displayed in figure 2. This scoring correlates to a "B" or higher on a typical middle school grading scale. In a class of 25 students, the breakdown of their levels of mastery

can be viewed in table 1 of the Figures and Data section. 75% of the students scored an 85% or higher on the assignment and 88% were near mastery or higher.

Conclusion

The integration of figurative writing into aeronautics research provides students with a holistic learning experience. Students not only learn how to conduct scientific research but also learn how to interpret data into a mock narrative, which aligns with the previously stated Ohio Learning Standards for seventh grade English Language Arts. Though this research provided insightful results, adaptations can be made to provide a more inclusive learning experience and accurate data. This activity can be adapted to appeal to more learning styles (not just linguistic learners) in accordance with Gardner's theory of multiple intelligences (Gardner, 1993). More accurate data can also be obtained by using a larger sample size.

Acknowledgments and References

Gardner, H. (1993). *Multiple Intelligences : The Theory in Practice*. Basic Books.

Kramer, Tracy (2013). Middle-Level Curriculum Approaches Handout. Wright State University. Dayton, OH.

Ohio Department of Education. "Ohio Learning Standards English Language Arts." *Ohio.gov*, ODE, 2017, Yellin, & DeVries (2015). *Essentials of Integrating Language Arts* (5th Ed.) New York, NY: Routledge.